# Inaugural-Dissertation

**submitted to the**

**Combined Faculty of Mathematics,
Engineering and Natural Sciences**

**of**

**Heidelberg University, Germany**

**for the degree of
Doctor of Natural Sciences**

**put forward by
M.Sc. Dmitrij Sitenko
born in Rubzowsk, Russia**

**Date of oral examination:**

# Nonlocal Graph-PDEs and Riemannian Gradient Flows for Image Labeling

Advisor: Prof. Dr. Christoph Schnörr

# Zusammenfassung

Diese Arbeit befasst sich mit dem Problem der Bildsegmentierung, was die Aufgabe darstellt ein Bild durch eindeutige Pixel-Label Zuweisungen zu vereinfachen und die darin enthaltenden redundanten Informationen zu reduzieren. Darüberhinaus basiert diese Thesis auf dem kürzlich eingeführten geometrischen Ansatz für Datenlabeling mit Assignment-Flows [ÅPSS17] welches ein glattes dynamisches System für die Datenverarbeitung auf gewichteten Graphen darstellt. Dabei werden zwei Forschungsziele verfolgt, um neue Einblicke in die Anwendung und Theorie der zugrunde liegenden Segmentierungsaufgabe zu geben.

Am Beispiel der Optical Coherence Tomography (OCT), welche die am häufigsten verwendete nicht-invasive Erfassungsmethode volumetrischer Abtastung von menschlichem Netzhautgewebe ist, wird demonstriert wie das Einschränken der Geometrie auf einer statistischen Mannigfaltigkeit zu einem rein datengetriebenen *geometrischen Ansatz* zur ordnungsgebundenen Segmentierung volumetrischer Daten in einem beliebigen metrischen Raum führt. Aus der Sicht der diagnostischen Analyse menschlicher Augenkrankheiten werden entscheidende Informationen in Form einer exakten Messung der Netzhautschichtdicke benötigt, welche für jeden Patienten separat durchgeführt werden muss und eine anspruchsvolle und zeitaufwändige Aufgabe darstellt. Deswegen, zur Erleichterung der klinischen Diagnose, wird ein vollautomatischer, parallelisierbarer Algorithmus mit hoher Segmentierungsgenauigkeit vorgestellt. Im Gegensatz zu vielen etablierten Segmentierungsansätzen von retinaler Schichten, werden als Eingabe nur lokale Informationen verwendet ohne jegliche Annahmen über die globale Form der Schichtverläufe. Stattdessen wird die physiologische Ordnung der retinalen Zell- und Membran-Schichten durch Einbeziehung einer neuen Formulierung von geordneten Verteilungen in einen Energieterm erreicht. Dies reduziert systematische Verzerrungen vom retinalen Formverlauf und eignet sich zur Erkennung anatomischer Veränderungen der Struktur des Netzhautgewebes. Die Effizienz der präsentierten Methode wird durch eine Gegenüberstellung mit zwei etablierten Segmentierungmethoden auf einem manuell annotierten Datensatz von 3D OCT-Volumina der gesunden menschlichen Netzhaut sowie durch einen direkten Abgleich mit manueller Annotierung unter Verwendung verschiedener Metriken ausgewertet.

Zusätzlich wird eine Verallgemeinerung von Ergebnissen der Arbeit [SS21] zur Variationsperspektive auf Zuweisungsflüsse erzielt, welche auf eine neue nichtlokale partielle Differenzengleichung (G-PDE ) zur Kennzeichnung metrischer Daten auf Graphen führt. Die G-PDE wird als nichtlokale Reparametrisierung des Assignment Flow-Ansatzes abgeleitet, der in *J. Math . Imaging & Vision* 58(2), 2017 eingeführt wurde . Aufgrund dieser Parametrisierung wird gezeigt, dass die numerische Lösung der G-PDE äquivalent ist zur Berechnung des Riemannschen Gradientenflusses in Bezug auf ein nicht-konvexes Potential. Wir entwerfen eine Entropie-regulierte Differenz-von-Konvex-Funktionen (DC)-Zerlegung dieses Potentials und zeigen, dass das grundlegende geometrische Euler-Schema zur Integration des Zuweisungsflusses gleichwertig ist.

# Abstract

In this thesis, we focus on the image labeling problem which is the task of performing unique pixel-wise label decisions to simplify the image while reducing its redundant information. We build upon a recently introduced geometric approach for data labeling by assignment flows [ÅPSS17] that comprises a smooth dynamical system for data processing on weighted graphs. Hereby we pursue two lines of research that give new application and theoretically-oriented insights on the underlying segmentation task.

We demonstrate using the example of Optical Coherence Tomography (OCT), which is the mostly used non-invasive acquisition method of large volumetric scans of human retinal tissues, how incorporation of constraints on the geometry of statistical manifold results in a novel purely data driven *geometric* approach for order-constrained segmentation of volumetric data in any metric space. In particular, making diagnostic analysis for human eye diseases requires decisive information in form of exact measurement of retinal layer thicknesses that has be done for each patient separately resulting in an demanding and time consuming task. To ease the clinical diagnosis we will introduce a fully automated segmentation algorithm that comes up with a high segmentation accuracy and a high level of built-in-parallelism. As opposed to many established retinal layer segmentation methods, we use only local information as input without incorporation of additional global shape priors. Instead, we achieve physiological order of retinal cell layers and membranes including a new formulation of ordered pair of distributions in an smoothed energy term. This systematically avoids bias pertaining to global shape and is hence suited for the detection of anatomical changes of retinal tissue structure. To access the performance of our approach we compare two different choices of features on a data set of manually annotated 3D OCT volumes of healthy human retina and evaluate our method against state of the art in automatic retinal layer segmentation as well as to manually annotated ground truth data using different metrics.

We generalize the recent work [SS21] on a variational perspective on assignment flows and introduce a novel nonlocal partial difference equation (G-PDE) for labeling metric data on graphs. The G-PDE is derived as nonlocal reparametrization of the assignment flow approach that was introduced in *J. Math. Imaging & Vision* 58(2), 2017. Due to this parameterization, solving the G-PDE numerically is shown to be equivalent to computing the Riemannian gradient flow with respect to a nonconvex potential. We devise an entropy-regularized difference-of-convex-functions (DC) decomposition of this potential and show that the basic geometric Euler scheme for integrating the assignment flow is equivalent to solving the G-PDE by an established DC programming scheme. Moreover, the viewpoint of geometric integration reveals a basic way to exploit higher-order information of the vector field that drives the assignment flow, in order to devise a novel accelerated DC programming scheme. A detailed convergence analysis of both numerical schemes is provided and illustrated by numerical experiments.

# Acknowledgements

This thesis would have not been possible without the guidance and support of the people who accompanied me on my academic journey until the final submission. First of all, I would like to express my gratitude to my supervisor Prof. Christoph Schnörr who sparked my interest for information geometry and image processing, and guided me throughout my PhD by giving advises and instructive meetings which encouraged me to develop my own path of research. I especially appreciate his instinctive feeling for selecting appropriate literature and his fast responses at any time and from any place.

I also would like to thank Dr. Stefan Schmidt and Dr. Julian Weichsel from Heidelberg Engineering who their collaboration, who have introduced me through various insightful discussions into the topics of medical research by sharing with me their expertise.

Many thanks to Bastian Boll for proofreading this thesis and for the illuminate discussions that resulted in a number of new ideas and findings. In addition, I show appreciation to Bastian Boll and Artjom Zern for opening me new perspectives on CUDA and Cython-programming which served for me as an extra source of inspiration. Moreover, I extol the help of Alexander Zeilmann who introduced me into new research area and for his blackboard advises and explanations.

I would like to mention my colleagues who has contributed to my work in a various ways: Jonas Cassel, Felix Draxler, Ecaterina Bodnariuc, Fabian Rathke, Fabrizio Savarino, Daniel Gonzales, Jan Plier, Matthias Zisler, Jonathan Schwarz, Lukas Kiefer, Ruben Hühnerbein, and Stefania Petra who have contributed to this thesis through informative discussions, comments and regenerative coffee breaks. Great thanks to Barbara Werner and Evelyn Wilhelm for supporting me throughout my studying time in all kinds of administrative matters and the pleasant conversations in the mathematical corridors of Mathematikon.

I would finally like to thank all of the people outside Heidelberg who have helped me complete the dissertation. I would like to express my deep gratitude to my parents, my mother Veronika, my father Vladimir, my uncle Juri Loukachev, and to my grandmother Erna for their excessive support throughout my life and their attendance in helping at any situation. I also would like to thank my sister Alexandra for her visits which gave me an extra motivation on my PhD journey. I am especially grateful to my wife Sol for her encouragement, motivation and unlimited backing who shared with me bad and good stages and was always on my side by giving me extra strength and pushing towards the right directions. I also thank Rula Mukarker and Suleiman Mukarker for their assistance in coffee and patience to the end of my studies.

# Table of contents

# List of Symbols

## Basic Conventions

| Symbol | Description |
|---|---|
| $\mathbb{N}$, $\mathbb{N}_0$ | natural numbers, natural numbers including 0 |
| $\mathbb{R}$, $\mathbb{R}_+$, $\mathbb{R}_{++}$ | real numbers, nonnegative real numbers, positive real numbers |
| $\overline{\mathbb{R}}$ | extended real line $\overline{\mathbb{R}} = \mathbb{R} \cup \{\infty\}$ |
| $\operatorname{int} S$ | interior of a set $S$ |
| $\operatorname{bd} S$ | boundary of a set $S$ |
| $\operatorname{dom} F$ | domain of a convex function $F\colon \mathbb{R}^n \to \overline{\mathbb{R}}$ |
| $\partial F$ | subdifferential of a convex function $F\colon \mathbb{R}^n \to \overline{\mathbb{R}}$ |
| $F^*$ | Fenchel conjugate of a function $F\colon \mathbb{R}^n \to \overline{\mathbb{R}}$ |
| $\delta_C(x)$ | indicator function w.r.t. a convex set $C \subset \mathbb{R}^n$ |
| $D_f(x, y)$ | Bregman divergence induced by $f$ of Legendre type |
| $D_{\mathrm{KL}}(p, q)$ | Kullback-Leibler (KL) divergence for $p, q \in \Delta_c$ |
| $\mathcal{M}$ | smooth manifold |
| $(\mathcal{M}, g)$ | Riemannian manifold |
| $C^\infty(\mathcal{M})$ | set of all smooth real-valued functions $f\colon \mathcal{M} \to \mathbb{R}$ |
| $T_p\mathcal{M}$ | tangent space at $p \in \mathcal{M}$ |
| $T\mathcal{M}$ | tangent bundle |
| $T_p^*\mathcal{M}$ | cotangent space at $p \in \mathcal{M}$ |
| $T^*\mathcal{M}$ | cotangent bundle |
| $\mathfrak{X}(\mathcal{M})$ | set of all smooth vector fields on $\mathcal{M}$ |
| $\mathfrak{X}^*(\mathcal{M})$ | set of all smooth covector fields (one-forms) on $\mathcal{M}$ |
| $dF_p(v)$ | differential of a smooth function $F\colon \mathcal{M} \to \mathcal{N}$ at $p \in \mathcal{M}$ |
| $g_p(v, u)$ | Riemannian metric, alternative notation $\langle v, u \rangle_g$ |
| $\|v\|_g$ | induced norm on $T_p\mathcal{M}$ of a Riemannian metric $g$ |
| $d_g(p, q)$ | Riemannian distance between $p, q \in \mathcal{M}$ |
| $\operatorname{grad} f$ | Riemannian gradient of $f \in C^\infty(\mathcal{M})$ |
| $\operatorname{Exp}_p(v)$ | exponential map at $p \in \mathcal{M}$, $v \in T_p\mathcal{M}$ |
| $\operatorname{Log}_p(q)$ | logarithmic map at $p \in \mathcal{M}$, i.e. inverse exponential map |
| $[n]$ | integers $\{1, 2, \ldots, n\}$ |
| $\lvert S \rvert$ | cardinality of a finite set $S$ |
| $\langle \cdot, \cdot \rangle$ | standard inner product in $\mathbb{R}^n$ |
| $\| \cdot \|$ | Euclidean and Frobenius norm for vectors and matrices |
| $I_c$ | identity matrix of $\mathbb{R}^{c \times c}$ |
| $\operatorname{tr}(A)$ | trace of a matrix $A \in \mathbb{R}^{n \times n}$ |
| $\operatorname{rank}(A)$ | rank of a matrix |
| $A \otimes B$ | Kronecker product |
| $\operatorname{vec}(A)$ | vector $\mathbb{R}^{mn}$ representation of a matrix $A \in \mathbb{R}^{m \times n}$ |
| $\nabla^2 F$ | Hessian of a twice differentiable function $F\colon \mathbb{R}^n \to \mathbb{R}$ |

| | |
|---|---|
| $e_i$ | $i$-th unit vector of $\mathbb{R}^n$ |
| $\mathbb{1}_n$ | constant vector of ones $(1, 1, \dots, 1)^\top \in \mathbb{R}^n$ |
| $\mathbb{R}_+^{n\times c}$ | set of nonnegative $n \times c$ matrices |
| $\mathcal{P}_d$ | set of symmetric positive definite $n \times n$ matrices |
| $\mathrm{GL}(n)$ | general linear group of invertible $n \times n$ matrices |

## Chapter 3

| Symbol | Description |
|---|---|
| $\mathcal{P}_\mu, \mathcal{P}_\theta$ | space of probability density functions and parametric probability density functions on $\mathcal{X}$ |
| $l(x), \partial_i l(\theta)$ | log-likelihood function on $\mathcal{X}$, score functions on parameter space $\Theta$ |
| $\nabla^\alpha$ | one parameter family of $\alpha-$ connections |
| $(\mathcal{F}, d_\mathcal{F})$ | feature space as a metric space |
| $f_i \in \mathcal{F}_n$ | data points and set of given data |
| $f_j^* \in \mathcal{F}_*$ | prototypes and set of prototypes |
| $\mathcal{G} = (\mathcal{I}, \mathcal{E})$ | undirected graph |
| $\mathcal{I}$ | index set of data points |
| $n$ | number of data points $n = \lvert\mathcal{I}\rvert$ |
| $\mathcal{J}$ | index set of prototypes |
| $c$ | Number of labels $c = \lvert\mathcal{J}\rvert$, one of which is uniquely assigned to each data point. |
| $\Delta_c$ | Probability simplex in $\mathbb{R}^c$ of dimension $c - 1$. |
| $\mathcal{S}$ | Relative interior of the probability simplex $\Delta_c$, forming the factors of the product manifold $\mathcal{W}$. |
| $\mathcal{N}_i$ | neighborhood of a vertex $i, \mathcal{N}_i = \{k \in \mathcal{I} \colon ik \in \mathcal{E}\} \cup \{i\}$ |
| $w_{i,k}$ | edge weights for $k \in \mathcal{N}_i$ |
| $\Omega$ | weighted adjacency matrix on $\mathcal{G}$ with $\Omega_i = \big(w_{i,k}\big)_{k\in\mathcal{N}_i}^\top$ |
| $\rho$ | selectivity parameter, $\rho > 0$ |
| $D_\mathcal{F}$ | field of distances, $D_\mathcal{F} \in \mathbb{R}_+^{n\times c}$ with $D_{\mathcal{F};i.j} = d_\mathcal{F}(f_i, f_j^*)$ |
| $L(W), L_i(W)$ | likelihood map, likelihood vector |
| $S(W), S_i(W)$ | similarity map, similarity vector |
| $\mathcal{W}$ | assignment manifold, $\mathcal{W} = \mathcal{S} \times \cdots \times \mathcal{S}$ ($n$ factors) |
| $W$ | assignment matrix, $W \in \mathcal{W}$ |
| $\mathcal{W}, \mathcal{T}_0$ | Assignment manifold and the corresponding tangent space at the barycenter $\mathbb{1}_\mathcal{W}$. |
| $T_0$, | tangent space of $\mathcal{S}$ |
| $T\mathcal{S}, T\mathcal{W}$ | tangent bundle of $\mathcal{S}$ and $\mathcal{W}$, $\mathcal{T}_0 = T_0 \times \cdots \times T_0$ ($n$ factors) |
| $\Pi_0$ | orthogonal projection onto $T_0$ or $\mathcal{T}_0$ |
| $R_p$, $R_W$ | replicator map defined on $\mathcal{S}$ and $\mathcal{W}$ |
| $\exp_p$, $\exp_W$ | lifting map, $\mathrm{Exp}_p \circ R_p$ and $\mathrm{Exp}_W \circ R_W$ |
| $\mathcal{H}_\mathcal{W}$ | negative entropy |
| $S_+^n$ | space of symmetric nonnegative matrices |

## Chapter 4

| Symbol | Description |
|---|---|
| $\tilde{\Theta}$ | cost matrix penalizing deviation from the ordering constraint |
| $K$ | pointed convex cone on $\mathbb{R}^c$ |
| $\Pi(\omega_i, \omega_j)$ | set of coupling measures between two probability distributions $\omega_i, \omega_j \in \Delta_c$ |
| $L_{\text{ord}}(W)$ | generalized likelihood matrix |
| $\phi$ | smooth approximation of the indicator function $\delta_C$ |
| $E_{\text{ord}}(W)$ | ordering energy parametrized directly on the assignment manifold $\mathcal{W}$ |

## Chapter 5

| Symbol | Description |
|---|---|
| $\mathcal{G} = (\mathcal{V}, \mathcal{E}, \Omega)$ | A graph with vertex set $\mathcal{V}$, edge set $\mathcal{E}$ and weights $\Omega$. |
| $\mathcal{V}$ | Set of vertices representing the discrete domain $\mathcal{V} \subset \mathbb{Z}^d$. |
| $n$ | Total number $n = \lvert\mathcal{V}\rvert$ of nodes in the graph $\mathcal{G}$ |
| $d$ | Dimension of the discrete domain associated with $\mathcal{V}$. |
| $\Omega$ | Weighted symmetric adjacency matrix of the graph $\mathcal{G}$. |
| $\mathcal{N}(x)$ | Neighborhood of $x \in \mathcal{V}$ induced by $\Omega$. |
| $E$ | Subset of an Euclidean space. |
| $\mathcal{F}_{\mathcal{V}}, \mathcal{F}_{\mathcal{V},E}$ | Space of one-point functions defined on $\mathcal{V}$, taking values in $\mathbb{R}$ resp. $E$. |
| $\mathcal{F}_{\mathcal{V}\times\mathcal{V}}, \mathcal{F}_{\mathcal{V}\times\mathcal{V},E}$ | Space of two-point functions defined on $\mathcal{V} \times \mathcal{V}$, taking values in $\mathbb{R}$ resp. $E$. |
| $\alpha \in \mathcal{F}_{\overline{\mathcal{V}}\times\overline{\mathcal{V}}}$ | Antisymmetric mapping that defines the interaction of nodes $x, y \in \mathbb{Z}^d$. |
| $\Theta \in \mathcal{F}_{\overline{\mathcal{V}}\times\overline{\mathcal{V}}}$ | Nonnegative scalar-valued symmetric mapping that parametrizes the introduced nonlocal diffusion process. |
| $\mathcal{V}_{\mathcal{I}}^{\alpha}$ | Nonlocal interaction domain which represents the connectivity of nodes $x \in \mathcal{V}$ to nodes $y \in \mathbb{Z}^d \setminus \mathcal{V}$. |
| $\overline{\mathcal{V}}$ | Extension of the discrete domain associated with $\mathcal{V}$ by the nodes in $\mathcal{V}_{\mathcal{I}}^{\alpha}$. |
| $\mathcal{D}^{\alpha}, \mathcal{G}^{\alpha}$ | Nonlocal divergence and gradient operators parametrized by the mapping $\alpha$. |
| $\mathcal{N}^{\alpha}$ | Nonlocal interaction operator parametrized by the mapping $\alpha$. |
| $\mathcal{L}_{\omega}$ | Nonlocal Laplacian with weight function $\omega$. |
| $\mathcal{X}_n$ | Data on the graph $\mathcal{G}$ taking values in a metric space $\mathcal{X}$. |
| $X(x)$ | Data point $X \in \mathcal{X}_n$ given at $x \in \mathcal{V}$. |
| $\mathcal{X}^*$ | Set of labels $\{X_j^* \colon j \in \mathcal{J}\} \subset \mathcal{X}$. |
| $S, W \in \mathcal{W}$ | Points on the assignment manifold taking values $S(x), W(x) \in \mathcal{S}$ at $x \in \mathcal{V}$. |
| $S^*, W^* \in \overline{\mathcal{W}} \setminus \mathcal{W}$ | Integral vectors on the boundary of $\mathcal{W}$. |
| $V \in \mathcal{T}_0$ | Points in the tangent space taking values $V(x) \in T_0$ at $x \in \mathcal{V}$. |

# 1 Introduction and Overview

## 1.1. Motivation

Since the dawn of mankind, our vision system guides us through everyday life situations by giving aid to the perception of the world around us. This supports our decision-making by learning and adopting to current environment when encountering various objects such as trees, animals and buildings, on different types of landscapes. To do so in a correct and secure manner, fast processing of occular information and subsequent automatic categorization of the current image scene are two essential aspects that highlight the superiority of our vision system. Carrying over these fundamental properties to the machine world resulted in a substantial technological progress in language processing, cognitive radio, speech recognition, search engines, robotic motion and stock mark analysis. In general, this poses a difficult tasks that is accompanied by a presence of noise and missing information of data and limited capacity of computational power.

To describe the object being observed while alleviating the aforementioned challenges, image analysis has become an interdisciplinary area of research that has united scientific efforts from fields of computer science, physics and mathematics. This resulted in a rapid development of image processing methods aimed towards image regularization, inpainting and optical flow problems that progress the recent advents in application specific scenarios of medical imaging: by visualizing biological processes, observing cell structures for cancer study, (b) remote sensing: by tracking of earth resources and using satellite scan images for studying stars, planets and space.

Among them, the image segmentation task amounts to partition given data into individual objects which is key to obtain alternative representation which is easier to analyze. This led to a broad array of methods starting from earliest binary approaches such as thresholding [PSA88], k-means clustering [Teb07], random walks [Gra06] and more advances methods of graph cuts [BJ01] and dynamical conditional Markov random fields [WJ05]. Over the past years, progressing research of deep learning-based approaches provided a new paradigm of algorithmic design in numerous image segmentation tasks, see [MBP+21] and references therein. Despite their striking empirical performance and a high representation power these methods lack of mathematical underpinning and thus fall into a ”black box”. In this context, the recently proposed assignment flow framework [Sch20; ÅPSS17] for large scale data processing on graphs offers a new perspective on the design of deep learning-based algorithms by relating the nonlocal nonlinear transformations with geometric integration steps of a continuous-time model. Potential applications of the aforementioned approaches include detection of pedestrians on different street scenes for autonomous driving and extraction of tissue boundaries within the human retina for medical diagnosis.

Among these, data labeling constitutes particular subclass of low-level segmentation problems that exhibit a graph-like structure. That is, given a finite set of sample data that forms a vertex set of an undirected graph $(\mathcal{V}, \mathcal{E})$ along with a contextual interrelation (regularization) encoded by

the weights on $\mathcal{V} \times \mathcal{V}$, the labeling task aims to infer unique assignments of labels, representing prior knowledge characteristic category properties or disparities within the data, to nodes on the graph in an optimal data-consistent fashion.

In this thesis we deal with the specific task of image labeling which includes categorization of semantic objects by introducing proper objectives whose global minima leads to favorable pixel-label decision. In contrast to classification of whole images where each image is assigned to one label, the image labeling operates at a pixel-level which is due to its combinatorial nature generally more involved NP-hard task and thus computing global optima represents a formidable challenge. A way out is provided by tight relaxations of the underlying problems that are feasible in the sense that the solution can be achieved in a polynomial computation time. In practice, preferentially convex relaxations are taken into account which can be conveniently solved by established convex programming routines. However, despite being highly effective this results in global minima corresponding to convex functional which not necessarily carries over to the original nonconvex functional of interest.

### 1.1.1. Assignment Flows

Recently, motivated by the seminal work on relaxation labeling and aided by the mathematical results from the field of information geometry the authors [ÅPSS17; Sch20] presented the mathematical approach tailored to the data labeling problem that is aimed to alleviate the difficulties of above mentioned classical approaches. The basic idea is to represent label assignments to data by a smooth dynamical system, the 'assignment flow', by coupling local flows at edges across the graph.

In contrast to dynamical formulations such as the Beltrami [KMS97] and the curvature flow [CFSS16] which defines processes in the space underlying the data, the assignment flow entirely evolves on an elementary statistical manifold by decoupling the underlying feature space at each node on the probability simplex each equipped with Fisher-Rao metric (information metric). Tracking the integral curve of the underlying ODE through geometric integration performs discrete label decisions and results in a regularized labeling with a low entropy state after a final rounding step. Within this particular geometric setting, replacing the Levi Cevita connection by a one parameter family of $\alpha$-connections introduced by Amari and Chentsov [AN00] enables to carry out basic geometric operations in a numerical tractable way. Figure 1.1 graphically illustrates the main concepts of data labeling approach from viewpoint of regularization: Given finite discrete data set which lives in the underlying feature space (RGB), associating each data point with vertex on a graph with connectivity prescribed by the size of neighborhoods $\mathcal{N}_i$ which drives the assignment of labels to data by parameters $\Omega$ that are chosen to preserve the spatial structure at a certain spatial scale (Section 3.2.2). These parameters can be determined either directly in a data-driven way through via plugin replacements [BCM10] or learned offline in a supervised way. This can be achieved by using symplectic numerical integration [HSPS21a] or, alternatively and quite efficiently, using exponential integration of linearized assignment flows [ZPS21; ZPS22]. In particular, deep parametrizations of assignment flows do not at all change the mathematical structure which enables to exploit recent progress on PAC-Bayes bounds in order to compute a statistical performance certificate of classifications performed by deep linearized assignment flows in applications [BZPS22].

Stability and convergence to integral solutions of assignment flows hold under mild conditions [ZZS20]. A wide range of numerical schemes exist [ZSPS20] for integrating geometrically assignment flows with GPU-conforming operations. Generalized assignment flows for unsuper-

vised and self-supervised scenarios [ZZPS20a; ZZPS20b] are more involved computationally but do not essentially change the overall *mathematical* structure.

**Figure 1.1.:** Data labeling by assignment flows. Data points (pixels) reside on underlying feature space (RGB) forming the vertex set of an undirected graph (image grid graph). **Left:** Noisy input data. **Middle:** Geometric integration of the flow using local-graph connectivity $\mathcal{N}_i = 5$ produces spatially regularized labeling at a small scale. **Right:** Enlarging the neighborhood sizes to $\mathcal{N}_i = 11$ increases the effect of regularization at a larger scale which leads to more context sensitive label assignments.

### 1.1.2. Segmentation in Medical Imaging

In the interim time, the term *medical imaging* encompasses a wide scope of imaging modalities and different techniques which serve to support evaluation and interpretation of experimental and clinical data. Thus, acquisition of images from scanning devices finds its application in a number of different medical tasks including examination of internal structures, diagnosis and treatment of diseases, identification of pathological abnormalities, and guidance of medical treatment and therapy. Motivated by this line of reasoning, the first part of this work is dedicated to extend the assignment flow framework [Sch20] to ordered labeling especially suitable for problems indicating a particular structure such as segmentation of tree rings and arterial walls (cf. Figure 1.2).

In this thesis we confine ourselves to the problem of detecting retinal layers along with corresponding tissue boundaries from volumetric optical coherence tomography (OCT) data which fits the aforementioned shape of ordered labeling. In particular, elaboration of automatic approaches for multi cell layer segmentation comprises a high clinical potential in real life applications, such as detection of fluid regions and reconstruction of vascular structures. The effectiveness of these approaches mainly relies on the access to automatic feature extraction techniques that accurately represents the information of the underlying OCT data. The difficulty of these tasks lies in the challenging signal-to-noise ratio which is influenced by multiple factors including physical eye movement during registration and the presence of speckle noise. This can be remedied by taking into account recent developments of deep neural networks that possess a striking ability to discover informative features which capture even very subtle patterns in data. However, despite their apparent expressiveness, such features are notoriously hard to interpret by humans. While

neural networks often generalize surprisingly well to unseen data, their lack of interpretability makes it hard to anticipate or otherwise reason about specific failure cases. Concerning medical applications this fact is of particular relevance because deep networks may produce predictions which appear plausible even in cases where they fail to generalize. Additionally, the aquisition of high-quality labeled data for training is laborious and may require the expertise of skilled medical professionals such that data availibility is limited compared to other problem domains.

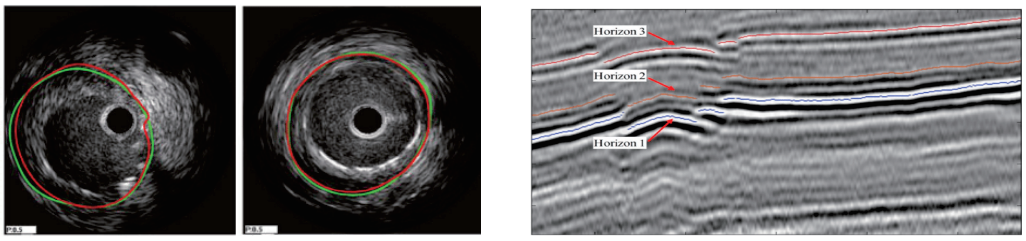


**Figure 1.2.:** Order-preserving labeling on example of two particular application scenarios. **Left:** Coronary cross-sectional images with circular ordering constraint [EX17]. **Right:** A sectional scan of an volumetric seismic data set depicting surfaces corresponding to different horizons [YS20].

### 1.1.3. PDEs in Image Processing

Since their first appearance in the works of Leonhard Euler, Partial Differential Equations (PDEs) are ubiquitous in mathematical modeling of various natural processes in physics and engineering. From practical perspective, first valuable numerical approaches were made by Neumann in the mid-1940s with ongoing analysis resulted in more advanced numerical solvers which remain, efficient in the presence of nonlinearities. Indeed, besides establishing theoretical results, the development of alternative PDE schemes for facilitating numerical computations has led to a surge of research that has altered the kind of experiments performed and have expanded the scope of theory. Over the past years, PDE-based methods become a significant tool in the field of computer vision and were successfully applied for purposes of image smoothing, inpainting and segmentation. In practice, these methods comprises local computations which limits their ability to be applied on data that exhibits nonlocal interrelations across single data points. In this regard, recent progress in parallel-processing guided hardware makes it possible to enhance the expressiveness of PDE-based approaches by instead relying on nonlocal iterative operations for discrete data processing that underlie many major image and data processing frameworks, including variational methods and PDEs on graphs for denoising, morphological processing and other regularization-based methods of data analysis [GO07; ELB08; GO09; BCM10; ETT15]. This includes deep networks [GBC16] and time-discretized neural ODEs [CRBD18] whose layers generate sequences of nonlocal data transformations. Building upon [ÅPSS17] in this thesis we focus on a particular type of PDEs for the task of image labeling and introduce a novel nonlocal class of graph-based partial differential equations (G-PDEs). Hereby, we work out how these new G-PDEs connect to the underlying local formulation proposed in [SS21].

## 1.2. Contribution and Organization

Based on the information geometric framework of assignment flows, the aim of this work is twofold, (1): extension of [Sch20] to the application specific task of retinal layer segmentation by

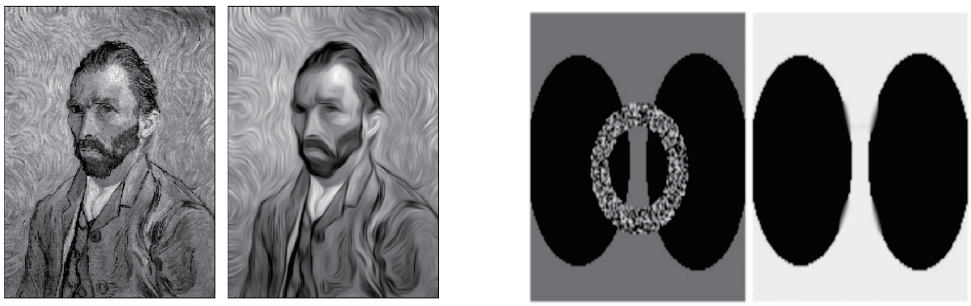

$\partial u(x,t) = \mathrm{div}(D\nabla u)(x,t)$ $\qquad$ $\partial u(x,t) = \nabla^{\perp} u \cdot \nabla \Delta u + v\nabla \cdot (g(|\nabla u|)\nabla u)$

**Figure 1.3.:** Two instances of PDE-based image processing tasks. **Left:** Image regularization through iterative coherence enhanced diffusion (bottom part) proposed in [Wei98]. **Right:** Outcome of the transport equation as stated in applied on the image inpainting problem [BS15].

geometric assignment, and (2): formulation of a novel class of nonlocal PDEs on graphs for image labeling that exposes the assignment flow as a particular instance. Regarding this objectives, the outcome of this thesis are summarized by the following contributions.

**(1): Ordered segmentation of OCT-volumes by assignment flows**

- We derive a geometric continuous characterization of layer ordering that allows to simultaneously perform local regularization and includes the global topological ordering constraint in a *single smooth* labeling process.
- Making use of the particular property of assignment flows: decoupling label decisions from the data feature space, we show how incorporation of voxel-wise local features results in a high-quality cell layer segmentations of OCT volumes. This is in contrast to competing deep learning approaches which explicitly aim to incorporate as much global context into the feature extraction process as possible. Moreover, we indicate how the use of local features reduces bias caused by limited data availability in training process and makes it possible to use three-dimensional information without limiting runtime scalability.
- Building upon the former point, we present two local feature extraction approaches. *The first* is based on identifying each voxel with a covariance descriptor [TPM06] and finding prototypical descriptors as cluster centers. Additionally, we provide a detailed qualitative performance evaluation of the labeling accuracy and of computational efficiency by utilizing various mean retrieval approaches including the Riemannian mean [BI13] and its approximation distance like divergence functions.

  *The second* is based on training of a relatively shallow convolutional neural network that classifies small patches around each voxel. In this context, we discuss the impact of feature locality and of variance in the reference segmentations used for training.
- As a main theoretical contribution we establish a novel relation of the continuous notion of geometric ordering to the existence of particular mass transportation maps that opens alternative ways for segmenting retinal tissues.
- Finally, we present a segmentation pipeline that differs from common deep learning methods which explicitly aim to incorporate global context into the feature extraction process.

This allows for a queue of practical benefits including higher regularization resulting in smoother transitions of layer boundaries along the B-scan acquisition axis similar to the effect in [RSS14] where the used smooth global Gaussian prior leads to limitations for pathological applications.

**(2): Labeling by nonlocal graph-based partial difference equation (G-PDE)**

The main outcome of the second part of this thesis is a presentation of a novel graph-partial differential equation (G-PDE) for the purpose of image labeling. In detail, this fundamentally includes two main contributions, illustrated by Figure 5.2:

(a) Given an undirected weighted regular grid graph $\mathcal{G} = (\mathcal{V}, \mathcal{E}, \Omega)$, we show that solving a particular parametrization of the assignment flow is equivalent to solving the *nonlocal nonlinear* partial *difference* equation (*G-PDE*) on the underlying graph $\mathcal{G}$,

$$\partial_t S(x,t) = R_{S(x,t)}\Big(\frac{1}{2}\mathcal{D}^\alpha\big(\Theta\mathcal{G}^\alpha(S)\big) + \lambda S\Big)(x,t), \qquad \text{on } \mathcal{V}\times\mathbb{R}_+, \tag{1.1a}$$

$$S(x,t) = 0, \qquad \text{on } \mathcal{V}_{\mathcal{I}}^\alpha \times \mathbb{R}_+, \tag{1.1b}$$

$$S(x,0) = \overline{S}(x)(0), \qquad \text{on } \overline{\mathcal{V}}\times\mathbb{R}_+, \tag{1.1c}$$

where the vector field $S$ takes values at $x \in \mathcal{V}$ in the relative interior of the probability simplex and corresponding geometry as specified in Section 3.1. In (1.1) $\mathcal{V}_{\mathcal{I}}^\alpha$ takes the roles of the discrete counterpart of the continous interaction domain $\Omega^\delta$. $\mathcal{D}^\alpha$ and $\mathcal{G}^\alpha$ are nonlocal divergence and gradient operators based on established calculus [DGLZ12; DGLZ13]. The linear mapping $R_{S(x,t)}$ is the inverse metric tensor (3.35), expressed in ambient coordinates.

The G-PDE (1.1) confirms and provides a generalized *nonlocal* formulation of a PDE that was heuristically derived by [SS21, Section 4.4] in the continuous-domain setting. In particular, (1.1) addresses the data labeling problem *directly* without any further pre- or postprocessing step and thus contributes to the line of PDE-based research of image analysis initiated by Alvarez et al. [AGLM93] and Weickert [Wei98].

(b) The particular parametrization of the assignment flow that we show in this chapter to be equivalent to (1.1), constitutes a Riemannian gradient flow with respect to a non-convex potential [SS21, Section 3.2]. We consider a *Difference-of-Convex (DC)* function decomposition [HT99] of this potential and show

  (i) that the simplest first-order geometric numerical scheme for integrating the assignment flow can be interpreted as basic two-step iterative method of DC-programming [HAPD05];

  (ii) that a corresponding tangent-space parametrization of the assignment flow and second-order derivatives of the tangent vector field can be employed to *accelerate* the basic DC iterative scheme.

  Due to result (a), both schemes (i) and (ii) also solve the G-PDE (1.1). In addition, we point out that while a rich literature exists on accelerated *convex* optimization, see e.g. [BT12; KBB16; FRMP18] and references therein, methods for accelerating *nonconvex* iterative optimization schemes have been less explored.

The remaining chapters of this thesis are organized as follows.

In **Chapter** 2 we collect basic mathematical material from convex analysis, differential geometry and machine learning. We conclude the chapter we gather anatomical background biological to comprehend the medical terms and techniques required throughout the thesis.

In **Chapter** 3 we recap the main information geometric background and introduce the Fisher-Rau geometry on the probability simplex. Subsequently, we summarize key ingredients of assignment flow approach by adding detailed comments of main properties of this framework.

In **Chapter** 4 we first introduce the general problem of ordered segmentation by taking a closer look looking at its formulation on graphs. We then relate the resulting discrete graphical model to a local polytope relaxation which motivates the result of Theorem 4.3.1. Building upon this knowledge we derive a generalized notion of order preservation by specifying a geometric continuous characterization of a pair of ordered assignments (cf. Definition 4.3.1). Armed with new concept of ordering we state the main mathematical result of this chapter: An equivalent representation of the ordering constraint by the existence of mass transportation maps between two ordered discrete distributions. Relying on this novel result we make the first step towards including ordering as a global constraint by constructing a proper energy functional. Due to the beneficial parametrization of the energy directly on the assignment manifold we subsequently present a novel labeling algorithm given by an adoption of the approach [ÅPSS17]. After formulating the final pipeline of the proposed *ordered assignment flow* (Definition 4.3.2) we apply this novel approach to the challenging task of segmenting retinal tissues. To achieve an informative representation of noisy OCT-data volumes we discuss various Riemannian metrics on the manifold of symmetric positive definite matrices from the viewpoint of computational efficiency of clustering. We then evaluate the resulting features against local features extracted by a convolutional network with limited small of view, see A for further details. To access the accuracy of our approach we leverage various performance measures and compare the proposed OCT segmentation approach with two other state-of-the-art methods with available standalone software. We conclude the chapter by discussing the access to appropriate ground truth data and the impact of feature locality underlying our approach.

In contrary to Chapter 4 where we have shown how a variant of [ÅPSS17] emerges as competitive segmentation approach in the field of imaging, in **Chapter 5** we follow another direction and link the assignment framework to a generalized families of nonlocal G-PDEs. To do so, in the beginning of the chapter we gather basic mathematical material and notational conventions that is commonly used in the framework of nonlocal PDEs [Du19]. Subsequently, y taking use of the *S-flow-parametrization* presented in [SS21] we focus on a certain subclass of assignment flows that are Riemannian gradient descent flows of an explicitly given nonconvex potential. We then identify the underlying geometric ODE as a particular instance of nonlinear partial difference equations on graphs (G-PDEs) with a specific boundary configuration and consider a broader class of labeling processes that are governed by the novel nonlocal G-PDE formulation. In this regard, by choosing several instances of averaging matrices we demonstrate how imposition boundary conditions along with a choice of different nonlocal boundary configurations affects the segmentation outcome. In addition, we report new mathematical insights on the corresponding evolutionary processes by stating novel non local balance laws for image labeling. In the second part of Chapter 5 we investigate the proposed (G-PDE) from the context of nonconvex optimization and investigate how particular geometric integration schemes emerges within the context of DC-programming. Hereby, we focus our attention on the first order explicit Euler iterations and indicate how incorporation of higher order derivatives can accelerate geometric integration process by including of tools such as line-search and adaptive step size selection policies. To support our findings, we provide theoretical results on the convergence along with an exhaustive experimental study in the end of this chapter.

In **Chapter** 6 at the end of this thesis we summarize the main results and give an outlook for potential research directions.

## 1.3. List of Publications

Parts of this thesis have been published in international journals and have been presented at conferences.

1. Sitenko, D. and Boll, B. and Schnörr, C., "Assignment Flow for Order-Constrained OCT Segmentation," in *GCPR*, 2020, pp. 58–71
2. D. Sitenko, B. Boll, and C. Schnörr, "Assignment Flow For Order-Constrained OCT Segmentation," *Int. J. Computer Vision*, vol. 129, pp. 3088–3118, 2021
3. D. Sitenko, B. Boll, and C. Schnörr, "Assignment Flows and Nonlocal PDEs on Graphs," in *DAGM GCPR*, ser. LNCS, Springer, 2021
4. D. Sitenko, B. Boll, and C. Schnörr, "A Nonlocal Graph-PDE and Higher-Order Geometric Integration for Image Labeling," *SIAM J. Imaging Science, in press*, 2023

# 2 Preliminaries

In this chapter we gather basic concepts and notational conventions that are required for a concise treatment of the main topics presented in this thesis. In Section 2.1 we give a brief, systematic review of fundamental mathematical notions of *Convex analysis*. Section 2.2 provides a short excursion into the fields of *Differential*-and *Riemannian geometry*. Section 2.3 gives theoretical background on the geometry of symmetric positive definite matrices and reviews two algorithmic schemes for numerically approximating the Riemannian means. In Section 2.4, we briefly introduce the concept of clustering along with basic iterative schemes that will be used for prototype recovery in experimental part of Chapter 4. Introductory material regarding the physiological structure of the eye and optical coherence tomography are presented in Section 2.5.1.

## 2.1. Convex Analysis

In this section we recapitulate some basic results in convex analysis. For a more detailed exposition we refer to classical works [Roc70; RW10] and [BV12].

We consider *extended real valued* mappings $F : \mathbb{R}^n \to \overline{\mathbb{R}}$ taking values on the *extended real line* $\overline{\mathbb{R}}$

$$\overline{\mathbb{R}} := (-\infty, \infty], \tag{2.1}$$

and denote the *effective domain* of $F : \mathbb{R}^n \to \overline{\mathbb{R}}$ by

$$\operatorname{dom} F = \{x \colon F(x) < \infty\}. \tag{2.2}$$

A function $F : \mathbb{R}^n \to \overline{\mathbb{R}}$ is called *proper* if its effective domain which is not the empty set, i.e. $\operatorname{dom} F \neq \emptyset$ and *improper* if $\operatorname{dom} F = \emptyset$. We say $F : \mathbb{R}^n \to \overline{\mathbb{R}}$ is *lower semicontinuous (lsc.)* at $x \in \mathbb{R}^n$ if for any convergent sequence $\lim_{k\to\infty} x^k \to x$ it holds

$$F(x) \leq \liminf_{k\to\infty} F(x^k), \tag{2.3}$$

and *lower semicontinuous* on $\mathbb{R}^n$ if inequality (2.3) is satisfied at each $x \in \mathbb{R}^n$. Replacing lim inf by lim sup in (2.3) analogously defines the notion of *upper semicontinuity (usc.)*. We call $F : \mathbb{R}^n \to \overline{\mathbb{R}}$ a *coercive* function if

$$F(x) \to \infty \quad \text{as} \quad \|x\| \to \infty. \tag{2.4}$$

Given a subset $C \subseteq \mathbb{R}^n$ an important instance of a mapping with properties specified above is given by the associated *indicator function* $\delta_C : \mathbb{R}^n \to \overline{\mathbb{R}}$ through

$$\delta_C : \mathbb{R}^n \to \overline{\mathbb{R}}, \qquad \delta_C(x) = \begin{cases} 0 & x \in C, \\ \infty & x \notin C. \end{cases} \tag{2.5}$$

Moreover, (2.5) provides a convenient way to extend any constrained function $F : C \to \mathbb{R}$ on

$\mathbb{R}^n$ by

$$F(x) + \delta_C(x) = \begin{cases} F(x) & x \in C, \\ \infty & x \notin C. \end{cases} \tag{2.6}$$

In particular, simply adding (2.5) to $F$ amounts to restricting its effective domain to $C$.

## Convexity

We proceed with the introduction of convex sets and convex functions. A set $C \subseteq \mathbb{R}^n$ is *convex* if for any pair of points $x \in C$ and $y \in C$ the line segment between these two points is contained in $C$, i.e.

$$x + \lambda(y - x) \in C, \qquad \forall \lambda \in [0, 1]. \tag{2.7}$$

A function $F : C \to \overline{\mathbb{R}}$ is said to be a *convex* function if $C \subseteq \mathbb{R}^n$ is a convex set and for $x, y \in C$ it holds

$$F\big(x + \lambda(y - x)\big) \leq F(x) + \lambda\big(F(y) - F(x)\big), \qquad \forall \lambda \in [0, 1]. \tag{2.8}$$

More generally, the convexity property of a function $F$ (2.8) admits an equivalent representation in terms of the *Jensen inequality*, that is $F : C \to \overline{\mathbb{R}}$ is convex if and only if

$$F\left(\sum_{i=1}^{N} \lambda_i x_i\right) \leq \sum_{i=1}^{N} \lambda_i F(x_i) \quad \text{for} \quad \lambda_i \geq 0, \quad \sum_{i=1}^{N} \lambda_i = 1, \quad \forall x_i \in \operatorname{dom} F. \tag{2.9}$$

Returning to (2.5) convex sets are characterized by convex functions $F : C \to \overline{\mathbb{R}}$ as follows

- $C \subset \mathbb{R}^n$ is convex if and only if $\delta_C$ is an extended real-valued convex function.
- If in addition $C \subseteq \mathbb{R}^n$ is a closed set, then $\delta_C$ is lsc.

If in (2.8) strict inequality holds, then $F : C \to \overline{R}$ is a *strictly convex* function. The function $F : C \to \mathbb{R}^n$ is *concave* and *strictly concave* if $-F$ is convex and strictly convex respectively. If $F : C \to \overline{\mathbb{R}}$ is differentiable then $F$ satisfies (2.8) if and only if

$$F(y) > F(x) + \langle \nabla F(x), (y - x) \rangle, \qquad x, y \in C, \tag{2.10}$$

and equivalently if $F$ is twice differentiable, then $F$ is convex if and only if

$$\nabla^2 F(x) \geq 0, \qquad \forall x \in C. \tag{2.11}$$

Note that while (2.10) is true for strict convexity, the inequality in (2.11) does not hold in general, that is not any strict convex function satisfies $\nabla^2 F(x) > 0$.
An important relation between convex functions and convex sets is given in terms of the *epigraph*

$$\operatorname{epi} F = \{(x, \beta) \in \mathbb{R}^n \times \mathbb{R} \colon x \in C \text{ and } F(x) \leq \beta\}. \tag{2.12}$$

More precisely a function $F : C \to \mathbb{R}$ is convex if and only if its epigraph (2.12) is a convex set.

An important class of mapping is given by $\mu$-*strongly convex* functions characterized by

$$F(x) \ \mu\text{-strongly convex} \quad \Leftrightarrow \quad F(x) - \mu\|x\|^2 \text{ convex}, \tag{2.13}$$

or equivalently, if $F$ is differentiable

$$F(y) - F(x) \geq \langle \nabla F(x), y - x \rangle + \frac{\mu}{2}\|y - x\|^2. \tag{2.14}$$

Convexity is preserved by various operations as specified next

**Lemma 2.1.1.** *Let $(F_i)_{i \in \mathcal{J}}$ be a collection of proper convex functions on $\mathbb{R}^n$ with $\mathcal{J} \subseteq \mathbb{N}$ and let $(a_i)_{i \in \mathcal{J}}$ be a positive sequence number. Then $F = \sum_{i \in \mathcal{J}} a_i F_i$ is convex.*

**Theorem 2.1.1.** *Let $(F_i)_{i\in\mathcal{J}}$ be as in Lemma 2.1.1, then*

$$F(x) = \inf_{x\in\mathbb{R}^n} \left\{ \sum_{j\in\mathcal{J}} F_j(x_j) \colon x_j \in \mathbb{R}^n, \sum_{j\in\mathcal{J}} x_j = x \right\} \tag{2.15}$$
$$\text{and} \quad F(x) = \sup_{j\in\mathcal{J}} F_j(x)$$

*are convex functions on $\mathbb{R}^n$.*

## Subdifferential

Convex functions may not be differentiable everywhere. Let $F : C \to \overline{\mathbb{R}}$ be convex. $F$ is called *subdifferentiable* at $x \in C$ if there exists $\xi \in \mathbb{R}^n$ such that the *subgradient inequality*

$$F(y) - F(x) - \langle \xi, y - x\rangle \geq 0, \qquad \forall y \in \operatorname{dom} F, \tag{2.16}$$

holds at $x$. We call the vector $\xi \in \partial F(x)$ satisfying (2.16) the *subgradient* of $F$ at $x$ where

$$\partial F(x) = \{\xi \in \mathbb{R}^n \colon F(y) - F(x) - \langle \xi, y - x\rangle \geq 0 \quad \forall y \in \operatorname{dom} F\} \tag{2.17}$$

is denoted as the *subdifferential* of $F$ at $x$. If $F$ is not finite at $x$ then we write $\partial F(x) = \emptyset$. If $\partial F(x)$ is a singleton then $F(x)$ is differentiable at $x$. An important special case is the subdifferential of the indicator function $\delta_C$ of a convex set $C$, i.e. $\xi \in \partial\delta_C(x)$ if and only if

$$\langle \xi, y - x\rangle \leq 0, \qquad \forall y \in C, \tag{2.18}$$

which is equal to the *normal cone* to $C$ at $x \in C$. Moreover, from optimization point of view the set (2.17) generalizes various properties of smooth derivatives to nondifferentiable functions.

- For a family of proper lower semicontinuous convex functions $(F_j)_{j\in\mathcal{J}}$ it holds

$$\partial \sum_{j\in\mathcal{J}} F_j(x) = \sum_{j\in\mathcal{J}} \partial F_j(x), \qquad x \in \bigcap_{j\in\mathcal{J}} \operatorname{rint} F_j. \tag{2.19}$$

- If for $F : \mathbb{R}^n \to \overline{\mathbb{R}}$ and some $A \in \mathbb{R}^{n\times n}$ it holds $Ax \in \operatorname{rint} F$ for some $x \operatorname{dom} F$, then

$$\partial(F \circ A) = A^T \partial F(Ax), \qquad \forall x \in \operatorname{dom} F. \tag{2.20}$$

**Theorem 2.1.2** (*Fermat's rule*)**.** *Let $F : \mathbb{R}^n \to \overline{\mathbb{R}}$ be a convex function. Then $x^*$ is the global minimizer of $F$ if and only if $0 \in \partial F(x^*)$.*

Moreover, if $C \subseteq \mathbb{R}^n$ is a closed convex set then Theorem 2.1.2 yields an optimality condition

$$x^* \in \operatorname{argmin}_{x\in C} F(x) \quad \Leftrightarrow \quad 0 \in \partial F(x^*) + \partial\delta_C(x^*) \tag{2.21}$$

that is

$$\exists \xi \in \partial F(x^*) \quad \text{with} \quad \langle \xi, y - x^*\rangle \geq 0 \qquad \forall y \in C. \tag{2.22}$$

## The Fenchel Conjugate

To each function $F : \mathbb{R}^n \to \overline{\mathbb{R}}$ we can associate a function $F^* : \mathbb{R}^n \to \overline{\mathbb{R}}$ defined by

$$F^*(\xi) = \sup_{x\in\mathbb{R}^n} \{\langle \xi, x\rangle - F(x)\}, \qquad \xi \in \mathbb{R}^n, \tag{2.23}$$

which is the *(Fenchel) conjugate* function of $F$. The induced operation $F \to F^*$ in (2.23) is denoted as *conjugation* and can be interpreted geometrically as the intercept of supporting hyperplane to epi $F$ with normal vector $(\xi, -1) \in \mathbb{R}^{n+1}$. Applying (2.23) twice defines the *biconjugate* function

of $F$

$$F^{**}:\mathbb{R}^n\to\overline{\mathbb{R}},\qquad F^{**}(x)=\sup_{\xi\in\mathbb{R}^n}\{\langle\xi,x\rangle-F^*(\xi)\}. \tag{2.24}$$

If $F:\mathbb{R}^n\to\overline{\mathbb{R}}$ is proper, the Fenchel conjugate (2.23) is lsc. and convex as the pointwise supremum of affine functions by Theorem 2.1.1. Moreover if dom $F$ is closed then (2.24) agrees with $F$, i.e. $F^{**}=F$. An important special case is the conjugate of indicator function (2.5) which defines the *support* function of the set $C\in\mathbb{R}^n$

$$\sigma_C(\xi)=\sup_{x\in\mathbb{R}^n}\{\langle\xi,x\rangle-\delta_C(x)\},\qquad \xi\in\mathbb{R}^n, \tag{2.25}$$

and if in addition $C$ is a closed set then $\sigma_C(x)=\partial\delta_C(x)$. In connection with conjugation we have the following inequalities

$(i)$ For $F,G:\mathbb{R}^n\to\overline{\mathbb{R}}$ we have

$$F\geq G\quad\Rightarrow\quad F^*\leq G^* \tag{2.26}$$

$(ii)$ The *Fenchel inequality* holds

$$F^*(\xi)+F(x)\geq\langle\xi,x\rangle\qquad\text{for all}\qquad x,\xi\in\mathbb{R}^n \tag{2.27}$$

$(iii)$ $F^{**}\leq F(x)$ for all $x\in\mathbb{R}^n$.

The following fundamental result highlights the role of conjugation in connection with subdifferential and optimality conditions.

**Theorem 2.1.3** (Subgradient Inversion Rule)**.** *Let $F:\mathbb{R}^n\to\overline{\mathbb{R}}$ be proper lsc. function. Then for $x\in\mathbb{R}^n$ it holds*

$$\xi\in\partial F(x),\qquad\Leftrightarrow\qquad\langle\xi,x\rangle=F(x)+F^*(\xi). \tag{2.28}$$

*In addition, if $F$ is convex then the subgradient inversion rule holds*

$$\xi\in\partial F(x)\qquad\Leftrightarrow\qquad x\in\partial F^*(\xi), \tag{2.29}$$

*and*

$$\partial F(x)=\operatorname{argmax}_{\widetilde{\xi}\in\mathbb{R}^n}\{\langle\widetilde{\xi},x\rangle-F^*(\widetilde{\xi})\}\qquad\partial F^*(\xi)=\operatorname{argmax}_{\widetilde{x}\in\mathbb{R}^n}\{\langle\xi,\widetilde{x}\rangle-F(\widetilde{x})\}. \tag{2.30}$$

## Divergence Functions

In this section we present distance-like functions that serve as surrogates for intractable problem-specific distances such as Riemannian distance, see Section 2.2. To do so we consider an important subclass of convex functions that are specified below and refer to [Bre67; BB97] and [CZ97] for a more detailed exposition.

**Definition 2.1.1 (convex functions of Legendre type [Roc70, Chapter 26]).** Let $f:\mathbb{R}^n\to\overline{\mathbb{R}}$ be a lower-semicontinuous proper convex function with nonempty open domain $C=\operatorname{int}(\operatorname{dom}f)\neq\emptyset$. Then $f$ is called

(i) *essentially smooth*, if $f$ is differentiable on $C$ and for every sequence $(x_k)_{k\in\mathbb{N}}\subset C$ with $x_k\to x^*\in\overline{C}\setminus C$ converging to a boundary point for $k\to\infty$, it follows $\|\nabla f(x_k)\|\to\infty$;

(ii) *Legendre type function*, if $f$ is essentially smooth and strictly convex on $C$.

Convex functions $f$ of Legendre type yield a class of *Bregman divergence functions* $D_f$ through

$$\begin{aligned} D_f \colon \overline{C} \times C &\to \mathbb{R}_+, \\ (x, y) &\mapsto f(x) - f(y) - \langle \nabla f(y), x - y \rangle. \end{aligned} \tag{2.31}$$

The Bregman divergence is a linear function in $f$ that is for $f, g : C \to \mathbb{R}$ of Legendre type 2.1.1 and $\alpha, \beta \in \mathbb{R}$ (2.31) it holds

$$D_{\alpha f + \beta g} = \alpha D_f + \beta D_g. \tag{2.32}$$

By strict convexity of $f$ and Jensen's inequality (2.9) the distance surrogate (2.31) has the following properties:

- For all $(x, y) \in \overline{C} \times C$ it holds
$$D_f(x, y) \geq 0 \quad \text{and} \quad (D_f(x, y) = 0) \;\Leftrightarrow\; (x = y). \tag{2.33}$$
- The mapping $x \to D_f(x, y)$ is strictly convex.
- $D_f(x, y)$ is *jointly* continuous in both arguments.

In other words, $D_f$ behaves like a distance except for al lack of symmetry and triangle inequality. Moreover, in the case of $f : \mathbb{R}^n \to \overline{\mathbb{R}}$ being twice continuously differentiable the following representation of the Bregman divergence indicates how $f$ induces $D_f$ that locally reflects the geometry of a particular problem of interest, i.e.

$$D_f(x, y) = \frac{1}{2} \langle x - y, \nabla^2 f(z), x - y \rangle, \quad \text{for some} \quad z \in \{(1 - \lambda)x + \lambda y \colon \lambda \in [0, 1]\}. \tag{2.34}$$

A canonical example is given by $f(x) = \|x\|^2$ which recovers the basic Euclidean distance $D_{\|\cdot\|^2}(x, y) = \|x - y\|^2$. Moreover, in this thesis we will use the *Kullback-Leibler (KL) divergence* (a.k.a. *relative entropy, information divergence*) $D_{\mathrm{KL}} = D_f$ that is induced through (2.31) by the negative discrete entropy function (with the convention $0 \cdot \log 0 = 0$)

$$f(s) = \langle s, \log s \rangle + \delta_{\Delta_c}(s) \tag{2.35}$$

where $s \in \Delta_c$ encodes a state on the probability simplex

$$\Delta_c = \{s \in \mathbb{R}^c \colon s_i \geq 0, \langle s, \mathbb{1}_c \rangle = 1\}. \tag{2.36}$$

In this setting (2.31) reads

$$D_{\mathrm{KL}} \colon \Delta_c \times \operatorname{int}(\Delta_c) \to \mathbb{R}_+, \qquad D_{\mathrm{KL}}(s, p) = \left\langle s, \log \frac{s}{p} \right\rangle. \tag{2.37}$$

## 2.2. Differential Geometry

In this section we introduce the basic tools from differential geometry. This will include notions of smooth manifolds which are geometric objects locally resembling the Euclidean space $\mathbb{R}^d$. Moreover, we gather relevant results from Riemannian geometry with some emphasis on the manifold of symmetric positive define matrices that are required for later treatment of local feature extraction techniques in Section 4.4. The introductory material and basic notations used in this thesis are adopted according to [Lee13; Bis64] and [Jos17] . For the proofs of the presented results and more detailed exposition into the topics of Riemannian Geometry we refer the reader to [Car13] and [GHL04] and references therein.

## Manifolds, Tangent Spaces and Derivatives

Let $\mathcal{M}$ be a topological space that is Hausdorff, second countable where each $p \in \mathcal{M}$ possesses a neighborhood $U$ that is homeomorphic to an open subset of $\mathbb{R}^d$. In this case we say $\mathcal{M}$ is a *topological $d-$manifold*. Let $U$ be an open subset of $\mathcal{M}$ and $\phi : U \to \mathbb{R}^d$ a homeomorhism that maps $U$ into an open subset of $\mathbb{R}^d$, then the pair $(U, \phi)$ is called a *chart* on $\mathcal{M}$. We refer to *local coordinates* of $p$ with respect to the chart $(U, \phi)$ by the mapping

$$\phi(p) = \big(x^1(p), \dots, x^d(p)\big) \in \mathbb{R}^d. \tag{2.38}$$

A *smooth atlas* $\mathcal{A}$ for a manifold $\mathcal{M}$ is a collection of charts $(U_\alpha, \phi_\alpha)_{\alpha\in\mathcal{A}}$ which satisfy:

$(i)$ : The domain of $U_\alpha$ constitutes an open cover of $\mathcal{M}$, i.e. $\mathcal{M} = \bigcup_{\alpha\in\mathcal{A}} U_\alpha$.

$(ii)$ : For each pair $(U_\alpha, \phi_\alpha), (U_\beta, \phi_\beta) \in \mathcal{A}$ the mapping $\phi_\alpha \circ \phi_\beta^{-1} : \phi_\beta(U_\alpha \cap U_\beta) \to \phi_\alpha(U_\alpha \cap U_\beta)$ is a diffeomorhism.

A *smooth structure* on $\mathcal{M}$ is a maximal atlas $\mathcal{A}$ with respect to conditions $(i)$ and $(ii)$. If in addition $\mathcal{M}$ is topological $d$-manifold then we call $\mathcal{M}$ a *smooth manifold* of dimension $d$. From now on we assume $\mathcal{M}$ to be a smooth manifold of dimension $d$ and denote by $C^\infty(\mathcal{M})$ the set of all smooth real valued functions on $\mathcal{M}$. Let $\gamma : (-\epsilon, \epsilon) \to \mathcal{M}$ be a differentiable curve. Then the *tangent vector* to $\gamma$ at $t = t_0$ is the linear functional that acts on $C^\infty(\mathcal{M})$ through

$$\dot\gamma(t_0) f = \frac{d}{dt}\bigg|_{t=t_0} (f \circ \gamma(t)), \qquad f \in C^\infty(\mathcal{M}). \tag{2.39}$$

A *tangent vector* $v$ at a point $p \in \mathcal{M}$ is a linear functional $v : C^\infty(\mathcal{M}) \to \mathbb{R}$ that is a tangent vector to some curve $\gamma : (-\epsilon, \epsilon) \to \mathcal{M}$ with $\gamma(0) = p$ and $\dot\gamma(0) = v$. With respect to local coordinates (2.42) the tangent vector (2.39) at $p \in \mathcal{M}$ with $(x^1, \dots, x^d) = \phi(p)$ is equivalently represented by adopting the Einstein summation convention

$$\frac{d}{dt}\bigg|_{t=0} \big(f \circ \gamma(t)\big) = \frac{d}{dt}\bigg|_{t=0} \big(f(x^1(t), \dots, x^d(t))\big) = \dot x^i(0)\, \frac{\partial}{\partial x^i}\bigg|_p f \tag{2.40}$$

where the local *coordinates vectors* on the r.h.s. of (2.40) are given by

$$\frac{\partial}{\partial x^i}\bigg|_p = \frac{d}{dt}\bigg|_{t=0} (\phi^{-1} \circ \tilde x^i(t)), \quad \text{with} \quad \tilde x^i(t) = (x^1, \dots, x^i + t, \dots, x^d). \tag{2.41}$$

The *tangent space* at $p \in \mathcal{M}$ is a set of all tangent vectors at $p \in \mathcal{M}$ which forms a vector space denoted by $T_p\mathcal{M}$. Given a chart $(U, \phi)$ around $p \in \mathcal{M}$ using $\phi \circ \gamma(t) = (x^1(t), \dots, x^d(t))$ each function $f \in C^\infty(\mathcal{M})$ is expressed along a curve $\gamma(t) \in \mathcal{M}$ in terms of local coordinates (2.38) through

$$f \circ \phi^{-1}(q) = f(x^1, \dots, x^d), \qquad q = \phi^{-1}(x^1, \dots, x^d) \in U. \tag{2.42}$$

If the Jacobian matrix of $\phi^{-1}$ has a maximum rank $d$ then the coordinate vectors (2.41) form a basis of $\mathcal{T}_p\mathcal{M}$ in which each tangent vector $v \in \mathcal{T}_p\mathcal{M}$ is uniquely represented by

$$v = v^i \frac{\partial}{\partial x^i}\bigg|_p, \qquad v^i = \dot x^i(0). \tag{2.43}$$

The *cotangent space* at $p \in \mathcal{M}$ is the dual space of the tangent space, i.e. $(T_p\mathcal{M})^*$, denoted by $T_p^*\mathcal{M}$. The *tangent bundle* and the *cotangent bundle* of $\mathcal{M}$ are given by disjoint union of tangent spaces and cotangent spaces at each $p \in \mathcal{M}$ respectively via

$$T\mathcal{M} = \dot\bigcup_{p\in\mathcal{M}} \{p\} \times T_p\mathcal{M}, \qquad T^*\mathcal{M} = \dot\bigcup_{p\in\mathcal{M}} \{p\} \times \mathcal{T}_p^*\mathcal{M}, \tag{2.44}$$

which both form $2d$-dimensional manifolds. The elements of $T_p^*\mathcal{M}$ are called *covectors* at $p \in \mathcal{M}$. If $\mathcal{M}$ is embedded into $\mathbb{R}^N$ then the tangent space can be identified with the set of all directional derivatives along directions which are tangent to $\mathcal{M}$ at $p \in \mathbb{R}^N$. Given smooth manifolds $\mathcal{M}, \mathcal{N}$ and a smooth map $F : \mathcal{M} \to \mathcal{N}$, the *differential* (pushforward) at $p \in \mathcal{M}$ of $F$ is the linear mapping $dF_p : T_p\mathcal{M} \to T_{F(p)}\mathcal{N}$ between the tangent spaces satisfying

$$dF_p(v) = \frac{d}{dt}\,(F \circ \gamma(t))|_{t=0}\,, \tag{2.45}$$

where $\gamma : (-\epsilon, \epsilon) \to \mathcal{M}$ is a smooth curve with $\gamma(0) = p$ and $\dot\gamma(0) = v \in T_p\mathcal{M}$. Alternatively, the map (2.45) can be defined in terms of the its action on $C^\infty(\mathcal{M})$ via

$$dF_p(v)(g) = v(g \circ F), \qquad \text{for all} \qquad v \in \mathcal{T}_p\mathcal{M}, \quad g \in C^\infty(\mathcal{N}). \tag{2.46}$$

For any $f \in C^\infty(\mathcal{M})$ the differential of $f$ induces a covector $df_p \in T_p^*\mathcal{M}$. As a consequence, the differential of coordinate functions $x^i = (\phi(p))_i$ yields the *dual basis* of cotangent space $T_p^*\mathcal{M}$ where each cotangent vector $\omega \in T_p^*\mathcal{M}$ admits a representation

$$\omega = \omega_i\, dx^i\big|_p \in T_p^*\mathcal{M}. \tag{2.47}$$

## Vector Fields and Flows

A smooth *vector field* on $\mathcal{M}$ is a smooth mapping that assigns to each point $p \in \mathcal{M}$ an element $X_p \in T_p\mathcal{M}$ which is a smooth *section* of the tangent bundle, that is

$$\pi_1 \circ X(p) = \mathrm{id}_{\mathcal{M}}, \qquad \pi_1 : \mathcal{T}\mathcal{M} \to \mathcal{M}, \qquad \pi_1(p, v) = p. \tag{2.48}$$

If $\gamma : (-\epsilon, \epsilon) \to \mathcal{M}$ is a smooth curve, then we call the continuous map

$$X : (-\epsilon, \epsilon) \to \mathcal{T}\mathcal{M} \qquad \text{with} \qquad X(t) \in T_{\gamma(t)}\mathcal{M}, \quad t \in (-\epsilon, \epsilon), \tag{2.49}$$

the *vector field along* $\gamma$. The union of all smooth vector fields along $\gamma$ is denoted by $\mathfrak{X}(\gamma)$ i.e. $X \in \mathfrak{X}(\mathcal{M})$ evaluates to a tangent vector $X_p \in T_p\mathcal{M}$ smoothly depending on $p$. For a fixed chart $(U, \phi)$ the vector field $X$ on $U$ admits an expression in terms of local coordinate vectors (2.41) and corresponding coordinate functions $X^i = X(x^i)$

$$X_p = X^i(p)\,\frac{\partial}{\partial x^i}\bigg|_p, \qquad x^1, \ldots, x^d \in C^\infty(U). \tag{2.50}$$

We denote the set of all vector fields and cotangent vector fields (one-forms) on $\mathcal{M}$ by $\mathfrak{X}(\mathcal{M})$ and by $\mathfrak{X}^*(\mathcal{M})$ respectively. Given a smooth vector field $X \in \mathfrak{X}(\mathcal{M})$ on $\mathcal{M}$ a differentiable curve $\gamma : (-\epsilon, \epsilon) \to \mathcal{M}$ that satisfies

$$\dot\gamma(t) = X(\gamma(t)), \qquad \gamma(0) = p, \tag{2.51}$$

is called an *integral curve* of $X \in \mathfrak{X}(\mathcal{M})$ that passes through $p \in \mathcal{M}$ at $t = 0$. Let $\mathcal{D}$ by an open subset $\mathcal{D} \subseteq \mathbb{R} \times \mathcal{M}$ containing the set $\{0\} \times \mathcal{M}$. A *flow* on $\mathcal{M}$ is a continuous map $\Phi : \mathcal{D} \to \mathcal{M}$ on $\mathcal{D}$ that satisfies the group laws for any $p \in \mathcal{M}$

$(i)$: $\Phi(0, p) = p$

$(ii)$: $\Phi(t, \Phi(s, p)) = \Phi(t + s, p)$ for all $s, t \in \mathbb{R}$ with $(s, p), (t, \Phi(s, p)), (s + t, p) \in \mathcal{D}$.

In particular, a collection of integral curves (2.51) associated to a vector field $X \in \mathfrak{X}(\mathcal{M})$ that pass though each point on $\mathcal{M}$ induces a flow on $\mathcal{M}$. Each flow $\Phi : \mathcal{D} \to \mathcal{M}$ defines an associated vector field on $\mathcal{M}$

$$X_p = \frac{d}{dt}\,\Phi(t, p)|_{t=0}\,, \qquad X \in \mathfrak{X}(\mathcal{M}). \tag{2.52}$$

which is called the *infinitesimal generator* of the flow $\Phi$. Moreover, there is a direct link between smooth vector fields that are generated by (2.52) and integral curves (2.51) whose domain can not be extended to a larger open interval.

**Theorem 2.2.1** (Fundamental Theorem of Flows). *[Lee13, Thm.9.12] Let $X$ be a smooth vector field on $\mathcal{M}$. There is a unique smooth maximal flow $\Phi : \mathcal{D} \to \mathcal{M}$ such that for each $p \in \mathcal{M}$ the map $\Phi^{(p)} : \mathcal{D}^{(p)} \to \mathcal{M}$ defined on open interval $\mathcal{D}^{(p)} = \{t \colon (t, p) \in \mathcal{D}\}$ with $0 \in \mathcal{D}^{(p)}$ by $\Phi^{(p)}(t) = \Phi(t, p)$ is the unique maximal integral curve of $X$ starting at $\Phi(0, p) = p$.*

If $\mathcal{D} = \mathbb{R} \times \mathcal{M}$ the map $\Phi$ is denoted as the *global flow* or the *one parameter group action* on $\mathcal{M}$. We call $X \in \mathfrak{X}(\mathcal{M})$ a *complete* vector field if the corresponding mapping $\Phi : \mathcal{D} \to \mathcal{M}$ in theorem 2.2.1 is global. The following Lemma characterizes a subclass of complete vector fields in terms of the trajectories of maximal integral curves.

**Lemma 2.2.1** (Escape Lemma). *[Lee13, Lemma 9.19] Let $X \in \mathfrak{X}(\mathcal{M})$ be a smooth vector field on $\mathcal{M}$ and let $\gamma : (-\epsilon, \epsilon) \to \mathcal{M}$ be the maximal integral curve of $X$ as in Theorem 2.2.1. If the interval $I$ admits an upper bound, i.e. $b = \sup I < \infty$, then for any $t_0 \in I$ the path $\gamma([t_0, b])$ is not contained in any compact subset of $\mathcal{M}$.*

A direct consequence of Lemma 2.2.1 is that the maximal integral curve starting at $p \in \mathcal{M}$ that is induced by a vector field with compact support is globally defined on $\mathbb{R}$.

### Affine Connections and Parallel Transport

A key property of tangential derivative (2.39) of a smooth curve $\gamma(t) \in \mathcal{M}$ is that its well defined *velocity* tangent vector $\dot{\gamma}(t)$ does not depend on the choice of a particular chart $(U, \phi)$. However, this property does not carry over to the corresponding *acceleration vector* $\ddot{\gamma}(t)$. To generalize the notion of directional derivative of a vector field in a chart-independent way we introduce the concept of connections on a manifold $\mathcal{M}$.

Given smooth vector fields $X, Y, Z \in \mathfrak{X}(\mathcal{M})$ and $f, g \in C^\infty(\mathcal{M})$ an *affine connection* on a smooth manifold $\mathcal{M}$ is given by the mapping

$$\nabla \colon \mathfrak{X}(\mathcal{M}) \times \mathfrak{X}(\mathcal{M}) \to \mathfrak{X}(\mathcal{M}), \qquad (X, Y) \mapsto \nabla_X Y, \tag{2.53a}$$

which satisfies the following properties:

$(i)$ $\nabla$ is linear over $C^\infty(\mathcal{M})$ in its first argument

$$\nabla_{fX+gY} Z = f \nabla_X Z + g \nabla_Y Z. \tag{2.53b}$$

$(ii)$ $\nabla$ is linear over $\mathbb{R}$ in its second argument

$$\nabla_X (a_1 Y + a_2 Z) = a_1 \nabla_X Y + a_2 \nabla_X Z, \qquad a_1, a_2 \in \mathbb{R}. \tag{2.53c}$$

$(iii)$ The following product like rule holds

$$\nabla_X (fY) = X(f) Z + f \nabla_X Z. \tag{2.53d}$$

The resulting vector field $\nabla_X Y \in \mathfrak{X}(\mathcal{M})$ is denoted as the *covariant derivative* of vector field $Y$ in the direction $X$. Given $X, Y \in \mathfrak{X}(\mathcal{M})$ at each $p \in \mathcal{M}$ the covariant derivative can be expressed in terms of the coordinate vectors (2.41) on a small neighborhood $U$

$$\nabla_X Y = \left( X(Y^k) + \Gamma^k_{ij} X^i Y^j \right) \frac{\partial}{\partial x^k}, \qquad X = X^i \frac{\partial}{\partial x^i} \qquad Y = Y^j \frac{\partial}{\partial y^j}, \tag{2.54}$$

where $\Gamma_{ij}^k \in C^\infty(\mathcal{M})$ are $d^3$ *Christoffel symbols of the second kind* that completely determine the affine connection $\nabla$ by expansion

$$\nabla_{\frac{\partial}{\partial x^i}} \frac{\partial}{\partial x^j} = \Gamma_{ij}^k \frac{\partial}{\partial x^k}. \tag{2.55}$$

The *torsion tensor* of an affine connection $\nabla$ is the mapping $T : \mathfrak{X}(\mathcal{M}) \times \mathfrak{X}(\mathcal{M}) \to \mathfrak{X}(\mathcal{M})$ that assigns to each pair $X, Y \in \mathfrak{X}(\mathcal{M})$ the vector field

$$T(X,Y) = \nabla_X Y - \nabla_Y X - [X,Y], \tag{2.56}$$

where $[\cdot,\cdot] \colon \mathfrak{X}(\mathcal{M}) \times \mathfrak{X}(\mathcal{M}) \to \mathfrak{X}(\mathcal{M})$ is the *Lie bracket* defined by

$$[X,Y](f) = X(Yf) - Y(Xf), \qquad \text{for} \qquad X, Y \in \mathfrak{X}(\mathcal{M}), \quad f \in \mathcal{C}^\infty(\mathcal{M}). \tag{2.57}$$

Using (2.57) the *curvature tensor* is the map that assigns to a triple $X, Y, Z \in \mathfrak{X}(\mathcal{M})$ a vector field $R(X,Y)Z$ given by

$$R(X,Y)Z \coloneqq \nabla_X \nabla_Y Z - \nabla_Y \nabla_X Z - \nabla_{[X,Y]} Z. \tag{2.58}$$

This is conveniently expressed in terms of the coordinate function by leveraging notation (2.55)

$$R_{ijk}^l = \frac{\partial}{\partial x^i}\Gamma_{jk}^l - \frac{\partial}{\partial x^j}\Gamma_{ik}^l + \Gamma_{jk}^m \Gamma_{im}^l - \Gamma_{ik}^m \Gamma_{jm}^l. \tag{2.59}$$

Given a smooth curve $\gamma : (-\epsilon, \epsilon) \to \mathcal{M}$ and a vector field $X \in \mathfrak{X}(\gamma)$, definition (2.53a) induces the mapping $\nabla_{\dot\gamma} : \mathfrak{X}(\gamma) \to \mathfrak{X}(\gamma)$ called the *covariant derivative along* $\gamma$. Expressing $X$ and $\dot\gamma$ in local coordinates (2.38) via $X = (x^1, \dots, x^d)$ and $\dot\gamma = (\gamma^1, \dots, \dots \gamma^d)$ respectively and taking into account properties (2.53) along with identity (2.54) the covariant derivative $\nabla_{\dot\gamma} X$ is expressed in terms of coordinates by

$$\nabla_{\dot\gamma(t)} X(t) = \left(\dot X^k(t) + \dot\gamma^i(t) X^j(t) \Gamma_{ij}^k(\gamma(t))\right) \frac{\partial}{\partial x^k}\bigg|_{\gamma(t)} \in T_{\gamma(t)}\mathcal{M}. \tag{2.60}$$

If $\nabla_{\dot\gamma(t)} X(t) = 0$ then the vector field $X(t) \in T_{\gamma(t)}\mathcal{M}$ is called *parallel along* $\gamma$. For any $V \in T_{\gamma(0)}\mathcal{M}$ there exists a parallel vector field $X^V$ along $\gamma$ which is uniquely determined as a solution to a system of linear first order ODEs (2.60) with initial condition $X(0) = V$. For points $p, q \in \mathcal{M}$ that are connected by a curve $\gamma$ via $\gamma(t_0) = p, \gamma(t_1) = q$ the *parallel transport* between tangent spaces at $p$ and $q$ along $\gamma$ is the linear isomorphism

$$\Pi_{t_0 t_1}^\gamma : T_{\gamma(t_0)}\mathcal{M} \to T_{\gamma(t_1)}\mathcal{M}, \qquad \text{with} \qquad \Pi_{t_0 t_1}^\gamma(V) = X^V(t_1), \tag{2.61}$$

with the inverse map given by $\Pi_{t_1 t_0}^\gamma$. Any connection $\nabla$ that is evaluated at two smooth vector fields $X, Y \in \mathfrak{X}(\mathcal{M})$ can be recovered from the concept of parallel transport via the following rule

$$\nabla_X Y|_p = \lim_{t_1 \to t_0} \frac{1}{t_1 - t_0}\left(\Pi_{t_1 t_0}^\gamma Y(\gamma(t_1)) - Y(\gamma(t_0))\right), \tag{2.62}$$

where $\gamma(t) \in \mathcal{M}$ is any smooth curve with $\gamma(t_0) = p, \gamma(t_1) = q$ and $\dot\gamma(t_0) = X_p$. We denote $\nabla$ as a *flat* connection if at each $p \in \mathcal{M}$ there is a chart $(U, \phi)$ and local coordinates $(x^i)_{i=1}^d$ such that $\Gamma_{ij}^k = 0$ in (2.55) or equivalently if the curvature tensor vanishes, i.e. $R_{ijk}^l = 0$. In this case we refer to $(x^i)_{i=1}^d$ as $\nabla$*-affine coordinates.*

### Geodesics and Exponential Map

If $X \in \mathfrak{X}(\gamma)$ is the velocity vector $\dot\gamma$, then (2.60) boils down to *geodesic equation*:

$$\ddot\gamma(t) = \nabla_{\dot\gamma(t)}\dot\gamma(t) = \left(\ddot\gamma^k(t) + \dot\gamma^i(t)\dot\gamma^j(t)\Gamma_{ij}^k \circ \gamma(t)\right) \frac{\partial}{\partial x^k}\bigg|_{\gamma(t)} \in T_{\gamma(t)}\mathcal{M}, \tag{2.63}$$

which defines the *acceleration* $\ddot{\gamma}$ of $\gamma(t)$. Given initial condition $\gamma(0) = p$ and $\dot{\gamma}(0) = v \in T_p\mathcal{M}$ a *geodesic* on $\mathcal{M}$ with respect to connection $\nabla$ is a smooth curve $\gamma : I^v \to \mathcal{M}$ with zero acceleration that is uniquely defined through coordinate functions $(\gamma^j(t))_{j=1}^d$ that solve the system of second order ordinary differential equations (2.63) on maximal open interval $I^v$ with $0 \in I^v$. Simply put, a geodesic is a smooth curve $\gamma : I \to \mathcal{M}$ for which the tangent vector field $\dot{\gamma}(t)$ (2.39) is parallel along $\gamma(t)$. If $I^v = \mathbb{R}$ for each $p \in \mathcal{M}$ and $v \in T_p\mathcal{M}$, then $\nabla$ is called a *complete* connection on $\mathcal{M}$.

The *exponential map* at $p$ is defined on some neighborhood $V_p \subseteq T_p\mathcal{M}$ of $0$ in the tangent space to $\mathcal{M}$ at $p$ by

$$\begin{aligned} \exp_p \colon V_p \supseteq T_p\mathcal{M} &\to U_p \subseteq \mathcal{M}, \\ v &\mapsto \exp_p(v) := \gamma(1), \end{aligned} \tag{2.64}$$

with smooth curve $\gamma : [0,1] \to \mathcal{M}$ starting at $\gamma(0) = p$ with initial direction $\dot{\gamma}(0) = v$. This mapping is a diffeomorphism of $V_p$ and its inverse map $\exp_p^{-1} \colon U_p \to V_p$ exists on a corresponding open neighborhood $U_p$ and is called the *logarithmic map* denoted by $\log_p(q) = \exp_p^{-1}(q)$ for $p, q \in \mathcal{M}$. The exponential map on $\mathcal{M}$ is the mapping $\mathrm{Exp} : \mathcal{S} \to \mathcal{M}$ defined at each $(p, v) \in \mathcal{S}$ through (2.64) where $\mathcal{S} = \{(p, v) \in T\mathcal{M} \colon 1 \in I^v\} \subseteq T\mathcal{M}$ is a star-shaped domain with respect to $0 \in T_p\mathcal{M}$ in the sense that if $t \in I^v$ then $\gamma([0, t]) \in \mathcal{S}$. A manifold $\mathcal{M}$ is called geodesically complete if in (2.64) it holds $V_p = T_p\mathcal{M}, p \in \mathcal{M}$.

## Riemannian Geometry

Next, we collect few concepts from Riemannian Geometry and refer to [Lee13; Jos17] for background reading.

A *Riemannian metric* on a smooth manifold $\mathcal{M}$ is a mapping that assigns to each point $p \in \mathcal{M}$ a symmetric, positive-definite bilinear form $g_p(\cdot, \cdot)$ on tangent space $T_p\mathcal{M}$ which smoothly varies with $p \in \mathcal{M}$ in the following sense: given a chart $(U, \phi)$ at $p \in \mathcal{U}$ then the $d^2$ functions $g_{ij} : U \to \mathbb{R}$ defined in terms of the coordinate vectors (2.41) by $g_{ij}(q) = g_q(\frac{\partial}{\partial x^i}\big|_q, \frac{\partial}{\partial x^i}\big|_q)$ are smooth on $U$.

A *Riemannian manifold* is a pair $(\mathcal{M}, g)$ where $\mathcal{M}$ is a smooth manifold with specified Riemannian metric $g$. Analogous to the Euclidean geometry, at each $p \in \mathcal{M}$ the associated *Riemannian norm* on $T_p\mathcal{M}$ is denoted by

$$\|v\|_g = \sqrt{g_p(v, v)}, \qquad \text{for all} \qquad v \in T_p\mathcal{M}, \tag{2.65}$$

which in turn defines the *angle* between two tangent vectors $v, u \in T_p\mathcal{M}$ by

$$\cos(\theta) = \frac{g_p(v, u)}{\|v\|_g \|u\|_g}, \qquad \theta \in [0, \pi). \tag{2.66}$$

This is a covariant 2-tensor field because at each $p \in \mathcal{M}$ the Riemannian metric is expressed on $T_p^*\mathcal{M} \otimes T_p^*\mathcal{M}$ in terms of the dual basis according to (2.47)

$$g = g_{ij} dx^i \otimes dx^j, \qquad g_{ij} \in \mathcal{C}^\infty(\mathcal{M}), \tag{2.67}$$

where at each $p \in \mathcal{M}$ the matrix $(g_{ij}(p))$ is symmetric and positive definite with the inverse denoted by $(g^{ij}(p))$. For a chart $(U, \phi)$ at $p \in \mathcal{M}$ the action of (2.67) on $T_p\mathcal{M} \times T_p\mathcal{M}$ is locally expressed in coordinates (2.43)

$$g_p(v, u) = g_{ij}(p) v^i u^j, \qquad v = v^i \left.\frac{\partial}{\partial x^i}\right|_p, u = u^j \left.\frac{\partial}{\partial x^j}\right|_p. \tag{2.68}$$

If at each $p \in \mathcal{M}$ it holds $g_p = \delta_{ij}$ in (2.68) then we call $(\mathcal{M}, g)$ a flat Riemannian manifold.

On $(\mathcal{M}, g)$ there exists a unique connection $\nabla^g$ called the *Levi-Civita* connection that is both torsion-free and compatible with the metric $g$, i.e.:

$$T(X,Y) = 0 \qquad Xg(Y,Z) = g(\nabla^g Y, Z) + g(Y, \nabla^g Z), \qquad \text{for all} \qquad X,Y,Z \in \mathfrak{X}(\mathcal{M}). \tag{2.69}$$

For a given Riemannian manifold $(\mathcal{M}, g)$ let $\gamma\colon [0,1] \to \mathcal{M}$ be a smooth curve connecting two points $p = \gamma(0)$ and $q = \gamma(1)$. The *Riemannian distance* between $p$ and $q$ is then given by

$$d_g(p,q) = \inf_{\gamma\colon \gamma(0)=p, \gamma(1)=q} L(\gamma) \tag{2.70a}$$

with

$$L(\gamma) = \int_0^1 \|\dot\gamma(t)\|_g \,\mathrm{d}t = \int_0^1 \sqrt{g_{\gamma(t)}\big(\dot\gamma(t), \dot\gamma(t)\big)}\,\mathrm{d}t\,. \tag{2.70b}$$

In general the curve at which the minimum in (2.70a) is attained is not unique. For the particular case of Levi-Cevita connection the geodesic (2.64) that satisfies (2.63) is locally length minimizing, i.e. the curve $\overline{\gamma}$ at which the minimum on the right-hand side of (2.70a) is attained is a geodesic. Given a smooth immersion $F : \mathcal{M} \to \mathcal{N}$ a Riemannian structure $h$ on $\mathcal{N}$ induces the *pull back* metric on $\mathcal{M}$ denoted by

$$F^*(h)_p(u,v) = h_p(dF_p(u), dF_p(v)), \qquad u,v \in T_p\mathcal{M}. \tag{2.71}$$

A diffeomorhism $F : \mathcal{M} \to \mathcal{N}$ between Riemannian manifolds $(\mathcal{M}, g)$ and $(\mathcal{N}, h)$ is called an *isometry* if

$$g_p(u,v) = h_{F_p(p)}(dF_p(u), dF_p(v)), \qquad \text{for all} \qquad u,v \in T_p\mathcal{M}, \quad p \in \mathcal{M}. \tag{2.72}$$

If $\mathcal{S} \subseteq \mathcal{M}$ is an embedded submanifold then $(S, i^*g)$ is called a Riemannian submanifold of $(\mathcal{M}, g)$ with the induced pullback metric $i^*g$ through (2.71).

For a function $f$ defined on manifold $(\mathcal{M}, g)$, the *Riemannian gradient* of $f$ is the vector field $\operatorname{grad} f \in \mathcal{X}(\mathcal{M})$ defined by

$$g(\operatorname{grad} f, X) = df(X) = Xf, \qquad \forall X \in \mathcal{X}(\mathcal{M}), \tag{2.73}$$

wheret teh Moreover, the vector field (2.73) is related to the direction of steepest descent with respect to variations on $\mathcal{M}$, that is

$$\frac{\operatorname{grad} f(p)}{\|\operatorname{grad} f(p)\|_g} = \operatorname*{argmax}_{v \in T_p\mathcal{M}, \|v\|_g = 1} df(p)[v], \qquad p \in \mathcal{M}. \tag{2.74}$$

We now focus on the following problem: Given a set of points $\{p_i\}_{i\in[N]} \subset \mathcal{M}$, compute the *weighted Riemannian mean* as minimizer of the objective function

$$\begin{aligned} &\overline{p} = \arg\min_{q\in\mathcal{M}} J(q), \qquad J(q) = \sum_{i\in[N]} \omega_i d_g^2(q, p_i), \\ &\sum_{i\in[N]} \omega_i = 1, \qquad\qquad \omega_i > 0, \ \text{ for all } i. \end{aligned} \tag{2.75}$$

The Riemannian gradient of this objective function is given by [Jos17, Lemma 6.9.4]

$$\operatorname{grad} J(p) = -\sum_{i\in[N]} \omega_i \exp_p^{-1}(p_i). \tag{2.76}$$

Hence the Riemannian mean $\overline{p}$ is determined by the optimality condition

$$\sum_{i\in[N]} \omega_i \exp_{\overline{p}}^{-1}(p_i) = 0. \tag{2.77}$$

A basic numerical method for computing $\overline{p}$ is the fixed point iteration

$$q_{(t+1)} = \exp_{q_{(t)}}\Big(\sum_{i\in[N]} \omega_i \exp^{-1}_{q_{(t)}}(p_i)\Big), \qquad t = 1, 2, \dots \tag{2.78}$$

that may converge for a suitable initialization $q_{(0)}$ to $\overline{p}$.

### Dual Connections

In the following we briefly summarize the main mathematical objects from the field of Information Geometry and refer to [AN00] and [AJLS17] for a more detailed background reading.

For a given affine connection $\nabla$ on a Riemannian manifold $(\mathcal{M}, g)$ the associated *dual connection*, denoted by $\nabla^*$, is uniquely determined in terms of metric $g$ by

$$Zg(X,Y) = g(\nabla_Z X, Y) + g(X, \nabla^*_Z Y) \qquad X, Y, Z \in \mathfrak{X}(\mathcal{M}). \tag{2.79}$$

If (2.79) is satisfied we call the triple $(g, \nabla, \nabla^*)$ a *dual structure* on $\mathcal{M}$. A *statistical manifold* $(\mathcal{M}, g, \nabla, \nabla^*)$ is a manifold $\mathcal{M}$ which is equipped with a dual structure $(g, \nabla, \nabla^*)$. If both $\nabla$ and $\nabla^*$ are flat connections, then we refer to $(\mathcal{M}, g, \nabla, \nabla^*)$ as a *dually flat* manifold.

In the context of identity (2.79) the Levi-Cevita connection is equivalently characterized as the unique self-dual connection, that is $\nabla = \nabla^*$. Moreover, given any two connections $\nabla, \nabla^*$ and a decomposition $\nabla^g = \nabla + \nabla^*$, then $(g, \nabla, \nabla^*)$ is a dual structure on $\mathcal{M}$. Representing (2.79) through coordinates (2.55) the dual connection $\nabla^*$ is uniquely determined through the *Christofel symbols of the first kind*

$$\Gamma_{ij,k} = g(\nabla_{\partial_i}\partial_j, \partial_k), \qquad \Gamma^*_{ij,k} = g(\nabla^*_{\partial_i}\partial_j, \partial_k), \quad \text{with} \quad \partial_i = \frac{\partial}{\partial x^i}. \tag{2.80}$$

There is a direct correspondence between affine coordinates of a dual structure $(g, \nabla, \nabla^*)$ and the Legendre transform of convex function.

**Theorem 2.2.2.** *Let $(M, g, \nabla, \nabla^*)$ be a dual flat manifold with Riemannian metric $g$. Then for $\nabla$-affine coordinates $\theta \in U$ there exist $\nabla^*$-affine coordinates $\nu$ and smooth convex functions $\psi, \phi : U \to \mathbb{R}$ related by a Legendre transform $\psi = \phi^*$ with subgradients satisfying*

$$\nu = \partial\psi(\theta), \quad \theta = \partial\phi(\nu), \qquad \psi(\theta) + \phi(\nu) = \langle\theta, \nu\rangle. \tag{2.81}$$

*Moreover the metric tensor expressed in terms of $\{\frac{\partial}{\partial\theta_i}\}_{i=1}^d$ and $\{\frac{\partial}{\partial\nu_i}\}_{i=1}^d$ is given by the Hessian of $\phi$ and $\psi$ respectively by*

$$g_{ij} = \frac{\partial^2}{\partial\theta^i\partial\theta^j}\psi, \quad g^*_{ij} = \frac{\partial^2}{\partial\nu^i\partial\nu^j}\phi \quad \text{with} \quad g^{ij} = g^*_{ij} \tag{2.82}$$

## 2.3. The Manifold of Symmetric Positive Definite Matrices $\mathcal{P}_d$

For a given positive integer $d \in \mathbb{N}_+$ we next carry over the differential geometric objects from previous chapter to the specific open set of symmetric positive definite $d \times d$ matrices that play an important role in mathematics, physics, numerical analysis and imaging that is given by the linear subspace of $\mathbb{R}^{d\times d}$

$$\mathcal{P}_d = \{S \in \mathbb{R}^{d\times d} \colon S = S^\top,\ S \text{ is positive definite}\}. \tag{2.83}$$

The tangent space at $S \in \mathcal{P}_d$ consists of symmetric matrices

$$T_S\mathcal{P}_d = \{S \in \mathbb{R}^{d\times d} \colon S^\top = S\}. \tag{2.84}$$

As the set $\mathcal{P}_d$ is embedded in the Euclidean space $\mathbb{R}^{c\times c}$ the most simple metric on $T_S\mathcal{P}_d$ is naturally given in terms of the Frobenius norm

$$d_F(U,V) = \|U-V\|_F, \quad \|V\|_F = \operatorname{tr}(V^TV)^{\frac{1}{2}} \quad U,V \in T_S\mathcal{P}_d. \tag{2.85}$$

In this thesis we will use $\mathcal{P}_d$ as a building backbone for prototype extraction (cf. (3.42b)) in Section 4.4.2 in connection with novel labeling approach presented in Chapter 4, (cf. Section 3.1). More specifically, we adopt various geometries on $\mathcal{P}_d$ by utilizing alternative metrics (2.85) and clarify their influence on the resulting mean properties defined by optimization problem (2.75) along with main computational tools for mean approximation. For more background reeding we refer to, e.g., [Bha07; Bha13; PFAE06; MB06].

### 2.3.1. Affine Invariant Riemannian Metric

Geometrically the set of symmetric positive define matrices (2.83) comprises the interior of a convex cone in the Euclidean space $\mathbb{R}^{d\times d}$ with zero curvature. Therefore, one major limitation of metric (2.85) is the finite distance to points on the boundary, i.e. matrices with zero eigenvalues. Instead, equipping the tangent space $T_S\mathcal{P}_d$ with the Riemannian metric [1]

$$g_S(U,V) = \operatorname{tr}(S^{-1}US^{-1}V), \qquad U,V \in T_S\mathcal{P}_d, \tag{2.86}$$

commonly known as the *affine invariant Riemannian metric* alleviates the problem and turns the set $\mathcal{P}_d$ into a negatively curved Riemannian manifold with a natural Riemannian distance (2.70a)

$$d_{\mathcal{P}_d}(S,T) = \Big(\sum_{i\in[d]} \big(\log\lambda_i(S,T)\big)^2\Big)^{1/2}, \tag{2.87}$$

where $\lambda_i(S,T)$ are the *generalized eigenvalues* of the pencil $(S,T)$ that is

$$Tv = \lambda_i(S,T)Sv, \quad \text{for some} \quad v\in\mathbb{R}^d \quad \text{with} \quad \|v\| = 1. \tag{2.88}$$

For this particular case the exponential map (2.64) reads

$$\exp_S(U) = S^{\frac{1}{2}}\operatorname{expm}(S^{-\frac{1}{2}}US^{-\frac{1}{2}})S^{\frac{1}{2}}, \qquad \operatorname{expm}(V) = \sum_{i=0}^{\infty}\frac{V^i}{i!}, \quad V\in\mathbb{R}^{d\times d} \tag{2.89}$$

In (2.89) the map $\operatorname{expm}(\cdot)$ is denoted as the matrix exponential with the inverse given by matrix logarithm $\operatorname{logm} = \operatorname{expm}^{-1}$ [Hig08, Section 11]

$$\operatorname{logm}(S) = \sum_{i=1}^{\infty}\frac{(-1)^{i-1}}{i}(S-I)^i. \tag{2.90}$$

Finally, given a smooth objective function $J\colon \mathcal{P}_d \to \mathbb{R}$, the Riemannian gradient is given by

$$\operatorname{grad} J(S) = S\big(\partial J(S)\big)S \in T_S\mathcal{P}_d, \tag{2.91}$$

where the symmetric matrix $\partial J(S)$ denotes the Euclidean gradient of $J$ at $S$. Since $\mathcal{P}_d$ is a simply connected, complete and nonpositively curved Riemannian manifold [BH99, Section 10], the exponential map (2.89) is globally defined and bijective, and the Riemannian mean always exists and is uniquely defined as minimizer of the objective function (2.75), after substituting the Riemannian distance (2.87).

Given a set of positive definite matrices

$$\mathcal{S}_N = \{(S_1,\omega_1),\dots,(S_N,\omega_N)\} \subset \mathcal{P}_d \tag{2.92}$$

[1] Following [Pet05] the affine invariant Riemannian metric (2.86) possesses an alternative interpretation from the theory of information geometry as the Fisher-Rao metric on the set of multivariate Gaussian distribution with zero mean that is induced by the Hessian of the Boltzmann entropy $\psi(\cdot) = \log(\det(\cdot))$ (cf. Theorem 2.2.2).

together with positive weights $\omega_i$, we next focus on the solution of the problem (2.75) for specific geometry (2.83),

$$\overline{S} = \arg\min_{S \in \mathcal{P}_d} J(S; \mathcal{S}_N), \qquad J(S; \mathcal{S}_N) = \sum_{i \in [N]} \omega_i d^2_{\mathcal{P}_d}(S, S_i), \tag{2.93}$$

with the distance $d_{\mathcal{P}_d}$ given by (2.87). Due to invertibility of (2.89), each tangent vector $U \in T_S\mathcal{P}_d$ is represented at the base point $S$ by

$$U = \exp_S^{-1} \circ \exp_S(U) = S^{\frac{1}{2}} \operatorname{logm}\left(S^{-\frac{1}{2}} \exp_S(U) S^{-\frac{1}{2}}\right) S^{\frac{1}{2}}. \tag{2.94}$$

As a result, optimality condition (2.77) reads

$$\sum_{i \in [N]} \omega_i \overline{S}^{\frac{1}{2}} \operatorname{logm}\left(\overline{S}^{-\frac{1}{2}} S_i \overline{S}^{-\frac{1}{2}}\right) \overline{S}^{\frac{1}{2}} = 0. \tag{2.95}$$

Apart from the specific case $|\mathcal{S}_2| = 2$ in (2.89) where the Riemannian mean is directly given by $\overline{S} = S_1(S_1^{-1}S_2)^{\frac{1}{2}}$, the solution to nonlinear equation (2.95) is not explicitly known. A remedy is the corresponding basic fixed iteration (2.78) initialized at $S_0 \in \mathcal{P}_d$

$$S_{t+1} = S_t \operatorname{expm}(-h_t \sum_{i=[N]} \omega_i \operatorname{logm}(S_i^{-1} S_t)), \tag{2.96}$$

where the step size $h_t > 0$ can be defined heuristically or by following more sophisticated line search strategies, see [AMS09] and [AG09]. However, as pointed out in [CABM15] applying (2.96) is limited in the sense that convergence is not theoretically guaranteed and if the iteration converges, than at a linear rate only. This can be remedied by restricting the set of matrices $\{S_1, \ldots, S_N\}$ in (2.89) to pairwise commute resulting in the following variant of Riemannian mean recovery proposed by [BI13] that comes with guarantees to converge at a *quadratic* rate. Using the parametrization by means corresponding to the Cholesky decomposition

$$S = LL^\top \tag{2.97}$$

along with replacing the map of fixed point iteration (2.78) with its linearization leads to the following fixed point iteration

$$F_\tau(L; \mathcal{S}_N) = LL^\top - \tau \sum_{i \in [N]} \omega_i L^\top \operatorname{logm}(L^{-\top} S_i^{-1} L^{-1}) L, \tag{2.98}$$

with damping parameter $\tau > 0$. Comparing to (2.95) shows that the basic idea is to compute the Riemannian mean $\overline{S}$ as fixed point of the iteration

$$\overline{S} = \lim_{t \to \infty} S_{(t)}, \qquad S_{(t+1)} = F(S_{(t)}; \mathcal{S}_N). \tag{2.99}$$

Algorithm 2.1 provides a refined variant of this iteration including adaptive stepsize selection.

**Algorithm 2.1:** Fixed Point Iteration for Computing the Riemannian Matrix Mean.

**Initialization**
$\epsilon$ (termination threshold)
$t = 0, \quad S_{(0)} = LL^\top$, with $S_{(0)}$ solving (2.102).
$c_0 = \frac{\lambda_{\max}(S_{(0)})}{\lambda_{\min}(S_{(0)}))}$, $\{\alpha_0, \beta_0\} = \left[\frac{\log(c_0)}{c_0 - 1}, c_0 \frac{\log(c_0)}{c_0 - 1}\right]$ (condition number and step size selection parameters)
$\tau_0 = \frac{2}{\alpha_0 + \beta_0}$
$S_{(1)} = F_\tau(L; \mathcal{S}_N)$ (iterative step)
$\epsilon_1 = \left\| \sum_{i \in [N]} \omega_i \operatorname{logm}(S_{(1)}^{\frac{1}{2}} S_i^{-1} S_{(1)}^{\frac{1}{2}}) \right\|_F, \quad t = 1$
**while** $\epsilon_t > \epsilon$ **do**
  $S_{(t)} = LL^\top$
  $c_t = \frac{\lambda_{\max}(S_{(t)})}{\lambda_{\min}(S_{(t)})}$
  **if** $c_t = 1$ **then**
    stop
  $\{\alpha_t, \beta_t\} = \{\sum_{k=0}^{t} \frac{\log(c_k)}{c_k - 1}, c_k \frac{\log(c_k)}{c_k - 1}\}$
  $\tau_t = \frac{2}{\alpha_t + \beta_t}$
  $S_{(t+1)} = F_{\tau_t}(L; \mathcal{S}_N)$
  $\epsilon_{t+1} := \left\| \sum_{i \in [N]} \omega_i \operatorname{logm}(S_{(t+1)}^{\frac{1}{2}} S_i^{-1} S_{(t+1)}^{\frac{1}{2}}) \right\|_F, \quad t \leftarrow t + 1$

See [CABM15] for alternative algorithms that determine the Riemannian mean. We next adopt the geometry of $\mathcal{P}_d$ by instead relying on a more computational efficient Euclidean metric that yield close form expression of the corresponding mean (2.93).

### 2.3.2. Log-Euclidean Metric

Leveraging the specific properties of the mappings (2.89) and (2.90) an alternative metric was proposed by [AFPA07] (among several other ones). More precisely, introducing the operations

$$S_1 \odot S_2 = \operatorname{expm}\big(\operatorname{logm}(S_1) + \operatorname{logm}(S_2)\big), \tag{2.100a}$$

$$\lambda \cdot S = \operatorname{expm}\big(\lambda \operatorname{logm}(S)\big), \tag{2.100b}$$

prescribes on $\mathcal{P}_d$ a Lie group structure where set $(\mathcal{P}_s, \odot, \cdot)$ is isomorphic to the vector space with $\odot$ playing the role of addition. The *Log-Euclidean metric* for two symmetric positive definite matrices $S_1, S_2 \in \mathcal{P}_d$ is then defined by the Euclidean inner product on the flat Riemannian space of zero curvature after applying the mapping $\operatorname{logm} : \mathcal{P}_d \to T_S\mathcal{P}_d$, (cf. (2.90)) and provides a lower bound to the (AIRM) metric (2.86) [Bha07, Theorem 6.1.4] via

$$d_{le}(S_1, S_2) = \| \operatorname{logm}(S_1) - \operatorname{logm}(S_2) \|_F, \qquad S_1, S_2 \in \mathcal{P}_d. \tag{2.101}$$

The corresponding Riemannian mean of the set $\mathcal{S}_N$ (cf. (2.92)) has the closed form expression

$$\overline{S} = \operatorname{expm}\Big( \sum_{i \in [N]} \omega_i \operatorname{logm}(S_i) \Big), \tag{2.102}$$

which has analogous form as the arithmetic mean. While computing the mean is considerably cheaper than integrating the flow (2.91) using approximation Algorithm 2.1, the critical drawback of relying on (2.102) is not taking into account the structure (curvature) of the manifold $\mathcal{P}_d$. Therefore, in the next section, we additionally consider another approximation of the Rie-

mannian mean that better fits the underlying geometry and avoids the expensive computation of generalized eigenvalues (2.88) resulting in a more efficient mean evaluation than the Riemannian mean associated to (2.86) metric.

### 2.3.3. $S$-Divergence

In this section we make use of divergence functions introduced in Section 2.1 and present a general approach of approximating the objective function (2.75) by instead replacing the intractable problem specific squared Riemannian distance (2.86) by a divergence function

$$D(p,q) \approx \frac{1}{2} d_g^2(p,q), \tag{2.103}$$

that satisfies

$$D(p,q) \geq 0 \qquad \text{and} \qquad D(p,q) = 0 \;\Leftrightarrow\; p = q, \tag{2.104a}$$

$$\partial_1^2 D(p,q) \succ 0, \quad \forall p \in \operatorname{dom} D(\cdot, q). \tag{2.104b}$$

Property (2.104b) says that, for any feasible $p$, the Hessian with respect to the first argument is positive definite. In fact, suitable divergence functions $D$ recover in this way locally the metric tensor of the underlying manifold $\mathcal{M}$, in order to qualify as a surrogate for the squared Riemannian distance (2.103).

| **Properties of mean** $\mathcal{G}(S_N)$ | **Riemann.** (2.70a) | **Log-Eucl.** (2.85) | **Stein div.** (2.105) |
|---|---|---|---|
| Invariance by reordering of $S_N$ | ✓ | ✓ | ✓ |
| Congruence invariance $S_N \to A S_N A^T$ for $A \in GL(d)$ | ✓ | ✓, $A \in SO(d)$ | ✓ |
| Self-duality $(\mathcal{G}(S_N))^{-1} = \mathcal{G}((S_N^{-1}))$ | ✓ | ✓ | ✓ |
| Joint homogeneity $\mathcal{G}(\alpha_1 S_1, \ldots, \alpha_N S_N) = (\prod_{i\in[N]} \alpha_i)^{\frac{1}{N}} \mathcal{G}(S_N)$ | ✓ | ✓ | ✗ |
| Determinant identity $\det \mathcal{G}(S_N) = (\prod_{i\in[N]} \det S_i)^{\frac{1}{N}}$ | ✓ | ✓ | ✓ |
| If $S_i \in S_N$ commute pairwise then: $\mathcal{G}(S_N) = (\prod_{i\in[N]} S_i)^{\frac{1}{N}}$ | ✓ | ✓ | ✓ |

**Table 2.1.:** Comparison of key properties satisfied by the mean with respect to metrics presented in Sections 2.3.1,2.100 and 2.3.3

For the present case $\mathcal{M} = \mathcal{P}_d$ of interest, [Sra16] proposed the divergence function, called *Stein divergence*.[2] For $S, S_1, S_2 \in \mathcal{P}_d$ it is defined as

$$D_s(S_1, S_2) = \log\det\left(\frac{S_1 + S_2}{2}\right) - \frac{1}{2}\log\det(S_1 S_2), \tag{2.105}$$

[2] According to definition 2.1.1, the Stein divergence is derived as the symmertized divergence induced by $\log\det$ Bregman function on $\mathcal{P}_d$.

which is not a metric on $\mathcal{P}_d$ due to the lack of triangle inequality. However, as shown by [Sra12] taking the square root in (2.105) yield a metric $d_S(\cdot,\cdot)$ on $\mathcal{P}_d$. Thus replacing the Riemannian distance in the second term of problem (2.93) the Riemannian distance (2.87) by $d_S$ provides an approximate objective

$$\overline{S} = \arg\min_{S\in\mathcal{P}_d} J_s(S;\mathcal{S}_N), \qquad J_s(S;\mathcal{S}_N) = \sum_{i\in[N]} \omega_i D_s(S,S_i), \tag{2.106}$$

which allows mean recovery while avoiding to solve the numerically involved generalized eigenvalue problem as opposed to (2.70a). The resulting Riemannian gradient flow reads

$$\dot{S} = -\operatorname{grad} J_s(S;\mathcal{S}_N) \overset{(2.91)}{=} -S\partial J(S;\mathcal{S}_N)S \tag{2.107a}$$

$$= -\frac{1}{2}\big(SR(S;\mathcal{S}_N)S - S\big), \tag{2.107b}$$

with

$$R(S;\mathcal{S}_N) = \sum_{i\in[N]} \omega_i \Big(\frac{S+S_i}{2}\Big)^{-1}. \tag{2.108}$$

Discretizing the flow using the geometric explicit Euler scheme with step size $h$,

$$S_{(t+1)} = \exp_{S_{(t)}}\big(-h\operatorname{grad} J_s(S_{(t)};\mathcal{S}_N)\big) \tag{2.109a}$$

$$\overset{(2.89)}{=} S_{(t)}^{\frac{1}{2}} \operatorname{expm}\Big(\frac{h}{2}\big(I - S_{(t)}^{\frac{1}{2}} R(S_{(t)};\mathcal{S}_N) S_{(t)}^{\frac{1}{2}}\big)\Big) S_{(t)}^{\frac{1}{2}} \tag{2.109b}$$

and using the log-Euclidean mean (2.102) as initial point $S_{(0)}$, defines Algorithm 2.2 as listed below.

**Algorithm 2.2:** Computing the Geometric Matrix Mean Based on the $S$-divergence.

**Initialization**
$\epsilon$ (termination threshold)
$t = 0, \quad S_{(0)}$ solves (2.102)
$\epsilon_0 > \epsilon$ (any value $\epsilon_0$)
**while** $\epsilon_t > \epsilon$ **do**
  $LL^\top = S_{(t)}$
  $L_i L_i^\top = \frac{S_{(t)}+S_i}{2}$ for $i \in [N]$
  $U = I - S_{(t)}^{\frac{1}{2}}\big(\sum_{i\in[N]} \omega_i (L_i L_i^\top)^{-1}\big) S_{(t)}^{\frac{1}{2}}$
  $S_{(t+1)} = S_{(t)}^{\frac{1}{2}} \operatorname{expm}(\frac{h}{2}U) S_{(t)}^{\frac{1}{2}}$
  $\epsilon_{t+1} := \|U\|_F, \quad t \leftarrow t+1$

The key advantage of Algorithm 2.2 over Algorithm 2.1 is that it respects the geometry of $\mathcal{P}_d$ while remaining numerically efficient. In Section 4.4 we will provide an experimental evaluation and a qualitative comparison of the mean properties with respect to the aforementioned metrics while extracting prototypes (3.42b) for the labeling task. Application details are reported in Chapter 4. We conclude by listing the main properties of the resulting means when relying on the Riemannian, log-Euclidean and Stein divergence summarized in Table 2.1.

## 2.4. Clustering

Given a finite set $\mathcal{X}_n = \{x_1, \dots, x_n\}, x_i \in \mathcal{X}$ of samples from a metric space $(\mathcal{X}, d)$, *clustering* is the task of determining the set of *representatives* or *prototypes* from $\mathcal{X}$

$$C_k = \{c_1, \dots c_k\}, \qquad c_k \in \mathcal{X}. \tag{2.110}$$

Each set of prototypes (2.110) yields a partitioning of $\mathcal{X}$ into *clusters* by assigning each $x \in \mathcal{X}$ to its closest representative via *Voronoi diagrams*

$$\Pi(c_i) = \{x \in X : d(x, c_i) \leq d(x, C_k)\}, \quad i \in C_k, \quad \text{with} \quad d(x, C_k) = \min_{c_j \in C_k} d(x, c_j), \tag{2.111}$$

where the choice of prototypes (2.110) is based upon minimization of expected distance

$$\min_{C_k \subset X} J(C_k), \quad J(C_k) = \sum_{i=1}^{n} v_i d(x_i, C_k), \qquad \sum_{i=1}^{n} v_i = 1, \quad v_i \geq 0. \tag{2.112}$$

In the upcoming section we briefly review some instances of (2.112) along with some established iterative schemes for its optimization.

### Euclidean Clustering

If $(v_i)_{i=1}^n = \frac{1}{n}$ and $d(x, c) = \|x - c\|^2$ for $x, c \in \mathbb{R}^m$ in (2.112) the *k-means* clustering determines the set $C_k$ by minimizing

$$J(C_k) = \frac{1}{n} \sum_{i \in [n]} \min_{j \in [k]} d(x_i, c_j), \quad \mathcal{X}_n \subset \mathbb{R}^m, \quad k \in \mathbb{N}, k \leq n. \tag{2.113}$$

Leveraging the log-exponential function [RW10] as approximation to $\operatorname{vecmin}(v) = \min_{j \in [k]} v_j$ for $v \in \mathbb{R}^k$ and $k \in \mathbb{N}$ , the nonsmooth nonconvex objective (2.113) is smoothly approximated by

$$J_\epsilon(C_k) = -\epsilon \frac{1}{n} \sum_{i \in [n]} \log \Big( \sum_{j \in [k]} \exp(-\frac{\|x_i - c_j\|^2}{\epsilon}) \Big), \qquad \epsilon > 0. \tag{2.114}$$

The necessary optimality conditions (2.114) with respect to prototypes $C_k$

$$\nabla_{c_j} J_\epsilon(C_k) = 0, \qquad j \in [k] \tag{2.115}$$

are solved by a fixed point iteration called the *soft-k*-means clustering

$$p^i_{\epsilon,j}(C_k^{(t)}) = \frac{\exp(\frac{-\|x_i - c_j^{(t)}\|^2}{\epsilon})}{\sum_{l \in [k]} \exp(-\frac{\|x_i - c_l^{(t)}\|^2}{\epsilon})}, \qquad p^i(C_k^{(t)}) \in \Delta_k, \tag{2.116a}$$

$$q^j_{\epsilon,i}(C_k^{(t)}) = \frac{p^i_{\epsilon,j}(C_k^{(t)})}{\sum_{i \in [n]} p^i_{\epsilon,j}(C_k^{(t)})}, \qquad q^j_\epsilon(C_k^{(t)}) \in \Delta_n, \tag{2.116b}$$

$$c_j^{(t+1)} = \sum_{i \in [n]} q^j_{\epsilon,i}(C_k^{(t)}) x_i. \tag{2.116c}$$

The distributions (2.116a) and (2.116b) encode data assignments to class prototype $c_j$ and class label assignments to data point $x_i$ respectively where the *mean shift* iterations (2.116c) determine the set of representatives $C_k$ as a local minimum of (2.114).

### Clustering on Manifolds

If the sample set $\mathcal{X}_n$ is a subset of smooth Riemannian manifold $(\mathcal{M}, g)$ the procedure (2.116) emerges as a particular instance of a more general scenario with (2.114) replaced by

$$J_\epsilon(C_k) = -\epsilon \frac{1}{n} \sum_{i\in[n]} \log\Big(\sum_{j\in[k]} \exp(-\frac{D_f(x_i, c_j)}{\epsilon}\Big), \qquad \epsilon > 0, \tag{2.117}$$

with Bregman divergence (2.31) $D_f : \mathcal{M}\times\mathcal{M} \to \mathbb{R}_+$ on $\mathcal{M}$. The necessary optimality conditions (2.115) are now expressed in terms of the differential $d_j(D_f(x,\cdot))$ with respect to $c_j$ according to (2.46) by Riemannian gradient (2.73)

$$\big(\mathrm{grad} J_\epsilon\big)_j(C_k) = \sum_{i\in[n]} p^i_{\epsilon,j}(C_k) g^{-1}(d_j(D_f(x_i, c_j))) = 0, \qquad j \in [k] \tag{2.118}$$

The corresponding mean shift iterations for determined the set of prototypes $C_k \subset \mathcal{M}$ (2.118) is given by a geometric counterpart of (2.116)

$$p^i_{\epsilon,j}(C^{(t)}_k) = \frac{\exp(\frac{-D_f(x_i,c_j)}{\epsilon})}{\sum_{l\in[k]} \exp(-\frac{D(x_i,c_l)}{\epsilon})}, \qquad p^i(C^{(t)}_k) \in \Delta_k, \tag{2.119a}$$

$$q^j_{\epsilon,i}(C^{(t)}_k) = \frac{p^i_{\epsilon,j}(C^{(t)}_k)}{\sum_{i\in[n]} p^i_{\epsilon,j}(C^{(t)}_k)}, \qquad q^j_\epsilon(C^{(t)}_k) \in \Delta_n, \tag{2.119b}$$

$$c^{(t+1)}_j = \exp_{c^{(t)}_j}\Big(\sum_{i\in[n]} q^j_{\epsilon,i}(C^{(t)}_k) g^{-1}\big(d_j D_f(x_i, c^{(t)}_j)\big)\Big) \tag{2.119c}$$

where $\exp_c$ is the exponential map (2.64) evaluated at $c \in \mathcal{M}$.

### Expectation Maximization (EM)

A widely applied parametric counterpart to soft-k-means clustering for acquiring prototypes on a measurable space $\mathcal{X}$ is based on the assumption of i.i.d. random samples $x_i \in X_n$ and by the following parametric family of mixture distributions

$$p(x, \Gamma) = \sum_{j\in[k]} \pi_j p(x, \theta_j) \qquad \Gamma = (\theta, \pi), \tag{2.120}$$

with unknown parameters

$$\Gamma = (\theta, \pi), \qquad \theta = (\theta_1, \dots, \theta_k) \qquad \pi = (\pi_1, \dots, \pi_k)^T \in \Delta_k. \tag{2.121}$$

Hereby, the a priori different parameters $\theta_j \in \Theta, j \in [k]$ parameterize the mixture distribution on $\mathcal{X}$ that partition the set $\mathcal{X}_n$ into $k$ different clusters with proportions $\pi \in \mathcal{S}$ where each $x_i$ has the density $p(x_i, \theta_j)$.

Starting from this statistical perspective where an approximation $\hat{\Gamma} = (\hat{\theta}, \hat{\Gamma})$ to model parameters $\Gamma$ is given, clustering amounts to fit the mixture distribution (2.120) by estimating true model parameters $\Gamma$ via *maximum log likelihood estimation* of

$$L(\theta) = \sum_{i\in[n]} \log\Big(\sum_{j\in[k]} \pi_j p(x_i, \theta_j)\Big) \tag{2.122}$$

Making a further assumption that each $x_i$ is generated by exactly one component distribution $p(j, \Gamma)$ and augmenting the set

$$(\mathcal{X}_n, \mathcal{Y}_n) = (x_1, \dots, x_n, y_1, \dots y_n), \qquad x_i \in \mathcal{X}_n, y_i \in [k] \tag{2.123}$$

where $y_i$ corresponds to class assignments of points $x_i$ to the associated distribution $p(x_i, \theta_{y_i})$,

optimization is performed by instead maximizing the following lower bound to (2.122)

$$\sum_{j\in[k]}\sum_{i\in[n]} p(j|x_i,\hat{\Gamma})\log(\frac{p(x_i,j,\Gamma)}{p(j|x_i,\hat{\Gamma})}). \tag{2.124}$$

Maximization of (2.124) amounts to perform the so called EM-iterates (*expectation-maximization*), see [Bis07], that result in the updates with initialization $\Gamma^{(0)}=\hat{\Gamma}$ $\Gamma^{(t)}(\theta^{(t)},\pi^{(t)})$

$$p(j|x_i,\Gamma^{(t)}) = \frac{\pi_j^{(t)}p(x_i,\Gamma^{(t)})}{\sum_{l\in[k]}\pi_l^{(t)}p(x_i,\Gamma^{(t)})}, \tag{2.125a}$$

$$\pi_j^{(t+1)} = \frac{1}{n}\sum_{i\in[n]} p(j|x_i,\Gamma^{(t)}), \tag{2.125b}$$

$$\theta^{(t+1)} = \operatorname{argmax}_{\theta_j}\sum_{i\in[n]} p(j|x_i,\Gamma^{(t)})\log p(x_i,\theta_j). \tag{2.125c}$$

The procedure (2.125) is composed in two main steps:$(i)$ expectation over the conditional distributions $p(j|x_i,\hat{\Gamma})$ that yields a current lower bound for objective (2.122) and $(ii)$ successive maximization over parameter $\theta$. For the particular case where the underlying components $p(x,\theta_j)$ belong to an exponential family of distributions that are represented in terms of Bregman divergence via

$$p(x,\Gamma) = \sum_{j\in[k]}\pi_j\exp(-D_f(F(x),\nu_j))b_f(x) \tag{2.126}$$

with parameters expressed in terms of conjugation operation through

$$\Gamma=(\nu,\pi), \qquad \nu=(\nu_1,\dots,\nu_k) \qquad \text{with} \qquad \nu_j=\psi(\theta_j), \quad j\in[k]. \tag{2.127}$$

the updates (2.125) simplify accordingly to

$$p(j|x_i,\Gamma^{(t)}) = \frac{\pi_j^{(t)}\exp(-D_f(F(x_i),\psi(\theta_j^{(t)})))}{\sum_{l\in[k]}\pi_l^{(t)}\exp(-D_f(F(x_i),\psi(\theta_l^{(t)})))}, \tag{2.128a}$$

$$\pi_j^{(t+1)} = \frac{1}{n}\sum_{i\in[n]} p(j|x_i,\Gamma^{(t)}), \tag{2.128b}$$

$$\nu_{ij}^{(t)} = \frac{p(j|x_i,\Gamma^{(t)})}{\sum_{s\in[n]}p(j|x_s,\Gamma^{(t)})} \tag{2.128c}$$

$$\mu_j^{(t+1)} = \operatorname{argmin}_{\mu_j}\sum_{i\in[n]}\nu_{ij}^{(t)}D_f(F(x_i),\mu_j) \tag{2.128d}$$

where the last step admits an closed form solution analogous to mean shift updates (2.116c)

$$\mu_j^{(t)} = \sum_{i\in[n]}\nu_{ij}^{(t)}F(x_i). \tag{2.129}$$

We refer the reader for a detailed treatment of (EM) iterates in connection with Bregman divergences to [BMDG05] and references therein.

## 2.5. Retinal Imaging

This section provides a general overview of anatomical background of the human eye required for the image labeling task introduced in subsequent sections. This includes a summary of different retinal layers, the optic nerve head and the fovea. Finally, we briefly address the basic working principles of (optical coherence tomography) OCT imaging on which the data used for our experimental validation in Section 4.4 is based.

### 2.5.1. Human Eye Anatomy

The human eye is a transparent sensory organ and one of the most complex parts of the human body. Similarly to the working principle of a camera it can automatically adjust to different light intensities by transmitting electromagnetic waves signals to the brain in a parallel-processing like fashion. A schematic illustration of the cross-sectional view of the eye structure with its key anatomic parts is presented in Figure 2.1. Mechanical movement of the eye is controlled by a pair of muscles around the orbital cavity, the medial rectus 12 and the lateral rectus 13. Anatomically, the eye ball is composed of three different layers:
The *external layer* is formed by eye protecting white sclera 2 and by transparent cornea 10, the *intermediate layer* contains the colored iris 8, ciliary body 11 and the choroid 3 and the *inner layer* further subdivided into retinal tissues. After reaching the cornea, light is refracted and transmitted to the anterior chamber through the pupil 7. Here, the contraction and dilation of the pupils regularize the amount of light entering the inner part of the eye caused by movements of the neighboring iris. Passing the pupil the focused light rays enter the fundus (interior area of the eye [CR06]) and travel through a gel like vitreous humour 6 straight to the retinal surface 5. From here, the preprocessed information is relayed via the optic nerve 9, located at the center of the retina, directly to the brain for visual perception.

On top of that it provides an easy optical access to the anterior segment that is organized into distinct processing units interconnected by a hierarchy of anatomical relays with the principal purpose to guarantee protection and efficient functionality for its photosensitive, thin, transparent layer, the retina.

### 2.5.2. The Layers of the Retina

As part of the central nervous system, retina specializes in converting the incoming light in the frequency range of visible light (400-750nm) into electrical impulses. After a short pre-processing, signals are transmitted over the neuronal connections with the optic nerve to the visual cortex for optic perception. The vertebrate retina is a thin, transparent light-sensitive multilayered tissue that lines the intrinsic part of the posterior wall of the eyeball, adjacent to the vitreous humor, towards the choroid layer.

Its structure comprises a range of well-defined ordered layers containing different cell types and nerve fiber tissues interconnected by hundreds of millions of photoreceptor epithelial, glial, and neural cells which are responsible for processing the received light photons into electrical impulses for visual perception.

Near the center of the retina there is a region called macula depicted by the left plot in Figure 2.4 responsible for the eyes visual acuity. The macula is approximately 5.5 mm in diameter and contains the central region called the fovea which is about 1.5 mm in diameter [YAN82]. The

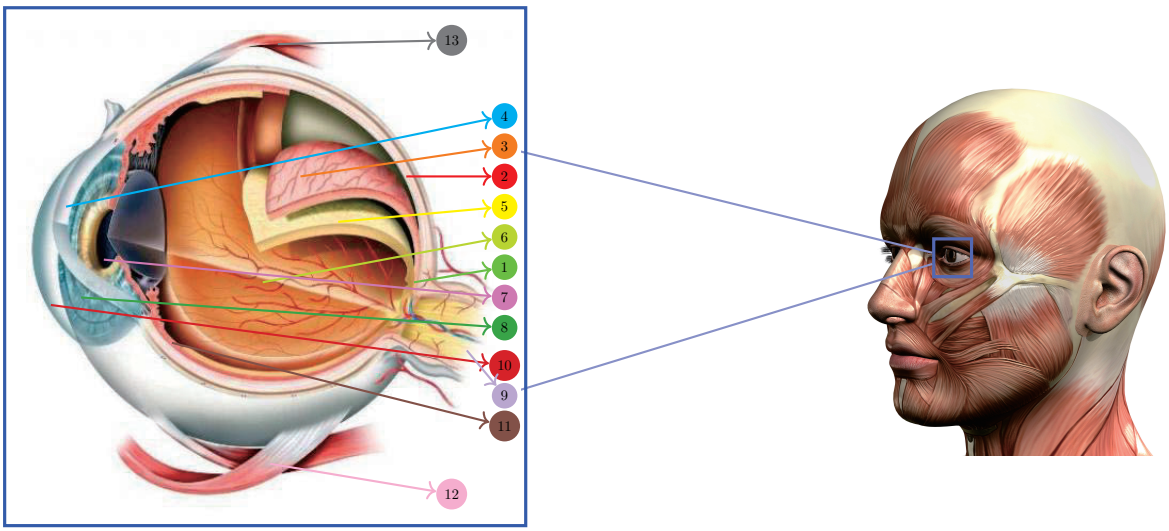


1 Fovea 2 Sclera 3 Chroroid Anterior chamber 5 Retina 6 Vitreous humour 7 Pupil
8 Iris 9 Optic nerve 10 Cornea 11 Ciliary body 12 Medial rectus 13 Lateral rectus

**Figure 2.1.:** Schematic illustration designed by [Kjpnd] of human eye functionality: The light enters the cornea 10 though the vitreous humour 6 towards retina 5 and choroid 3 which are located around the fovea 1.

fovea is characterized by a significant thinning of the retina along with high density of photoreceptor cells which contributes to the high contrast sensitivity.

The photoreceptor cells are classified into two main categories the *cones* and *rodes* named after their specific shape [Mas01]. Rodes are very sensitive cells located at the periphery of the retina detecting contrast changes at low light levels and are responsible for *scotopic* vision but have slow response to light. In contrast, cones are less sensitive but fast densely positioned in the macula area and maximally adaptive to bright color and light changes supporting the *photonic* vision. Figure 2.2 displays a schematic organization of retinal tissues in anatomical order according to [AGS10b]:

- **Optic nerve fiber layer** is densely completed with axons of ganglion cells which transmit the received signals to visual cortex of the brain. Its thickness gradually decreases with age and serves as a measure for detecting eye diseases such as glaucoma. At the edge of the fovea region this layer becomes thickest and completely vanishes directly over the fovea to permit the photons to enter the rods located at inner layers.
- **Retinal Ganglion cell and nerve fiber layer** contain the cell bodies of ganglion cells which are the primary output neurons of the retina that process visual information.
- **Inner plexiform layer** consist of synaptic connections between the information-carrying bipolar cells and ganglion cells supported by a variety of horizontally and vertically aligned amacrine cells. Their interaction contribute to perception and integration of the ganglion cell signal.
- **Inner nuclear layer** is made of horizontal cell bodies and vertically aligned bipolar cells

which receive chemical signal from ganglion cells. Horizontal cells are characterized through a broad receptive field and provide additional information to the photoreceptor cells by modulating the signals from ganglion cell layer.

- **Outer plexiform layer** structure is composed of neuronal junctions between photoreceptor rodes and cones and horizontal and bipolar cells. These interaction facilitates the visual signal processing to detect object transitions between light and dark backgrounds.
- **Outer nuclear layer** contains cell bodies of photoreceptor cones and rodes.
- **Photoreceptor layer** contains photosensitive outer segments of rods and cones.
- **Retinal pigment epithelium** is the last layer of the retina located between the light-sensitive photoreceptor cells and blood supply of the choroid. It consist of heavily pigmented granules for absorbing scattered light and as an isolation of the inner retina from intrinsic influences from the choroidal section.
- **Internal limiting membrane** is the innermost boundary of the retina that defines the transition between the vitreous body and the retina.

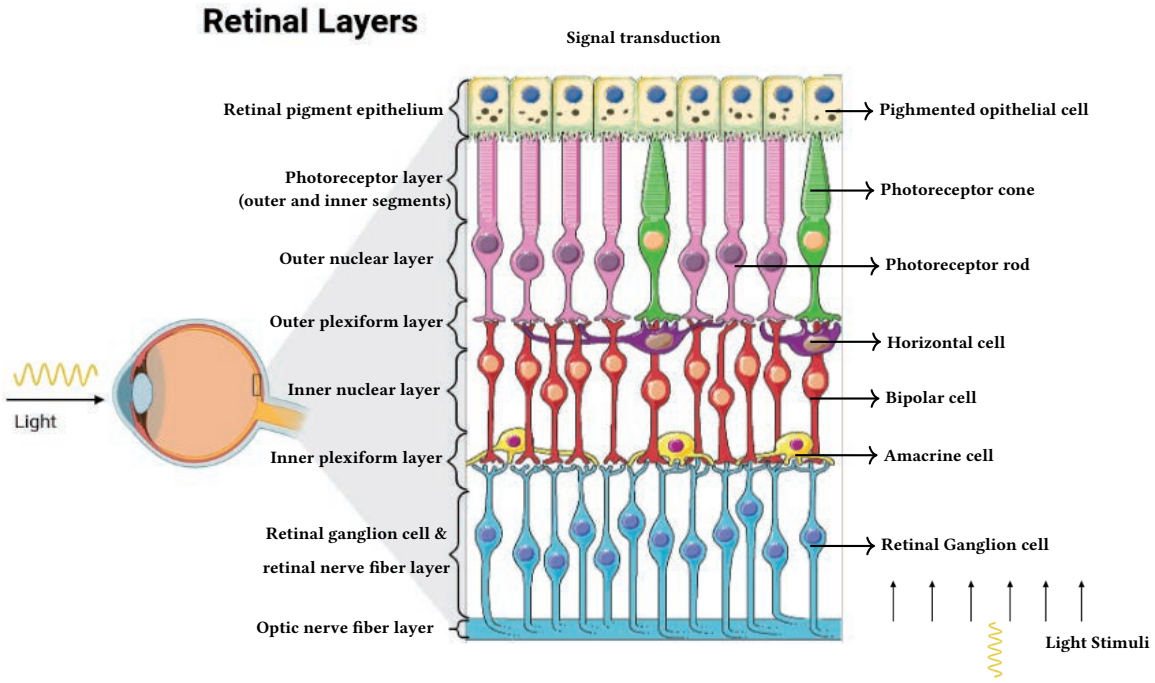


**Figure 2.2.:** Anatomical organization of human retina. Each layer is characterized by a specific occurrence of cell types that preprocess the incoming signal. Starting from the optic nerve fiber layer the light is transmitted up to the brain for ocular perception by passing the photoreceptor layer represented by a dense concentration of cone cells responsible for visual acuity.

At the center of the fovea the blood vessel and all cells except the photoreceptors cones are displaced such that retinal tissues are contracted towards the center of the macula. This region is anatomically known as the foveola, see left plot of Figure 2.4 for an organization of the macula part of human retina.

### 2.5.3. Retinal Eye Diseases

Deteriorations within the retinal area near the macula are responsible for various vision distortions and eye diseases such as glaucoma and age related macula degeneration. Typically, the leading cause of such ocular disorders is directly related to the abnormal structural changes of retinal tissues. Glaucoma has become the second leading cause of blindness [QB06] with 66 millions patients worldwide and characterized by an increased pressure on the optic nerve which influences the retina by damaging the ganglion cells and their axons [Dre11]. This results in thinning of the retinal nerve fiber layer as can be observed from the left scan in figure 2.3. The age related macula degeneration appears when vascular structures within the choroid break through the retinal tissues while leaking fluid, lipids and blood. This leads to persistent filamentary scarring within the retinal tissues.

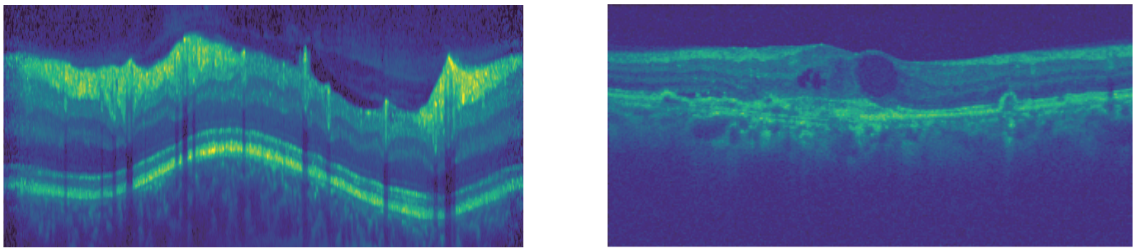

**Figure 2.3.: Left:** B-scan of human retina showing pathological thickness distortion within the retinal nerve fiber layer (RNFL) typical for Glaucoma diseases. **Right:** A B-scan from [PPMV18] database depicting intraretinal exudation near the fovea region representative for patients with age related macular degeneration.

If left untreated, negative effects on the humans eye can occur resulting in an significant damage of vascular and muscular system accompanied by irreversible vision impairment up to blindness. A common indication of disease patterns is the loss of visual perception. Thus, the current progression state and treatment can be examined by performing a visual field test. However, such symptoms only occur on a comparatively late stage with advanced and irreparable destruction of retinal cells. This highlights the necessity to leverage more sophisticated diagnostic methods, which are able to detect diseases at a much earlier stage. For this reason, assessment of quantitative information on retinal shape structure serves as a measure of disease progression or response to therapy. In this context, ophthalmic imaging technologies are crucial to provide an accurate acquisition of human eye scans and detect retinal pathologies from which OCT is among the most successful non-invasive screening techniques.

### 2.5.4. Optical Coherence Tomography (OCT)

Optical Coherence Tomography (OCT) is a non-invasive imaging technique which measures the intensity response of back scattered light from millimeter penetration depth. Here we consider its use in ophthalmology as a means of aquiring high-resolution volume scans of human retina in vivo to understand eye functionalities. Figure 2.1 gives an overview of relevant anatomy. OCT devices record multiple two-dimensional B-scans in rapid succession and combine them to a single volume in a subsequent alignment step. Taking an OCT scan only takes multiple seconds to few minutes and can help detect symptoms of pathological conditions such as glaucoma, diabetes, multiple sclerosis or age-related macular degeneration. The relative ease of data acquisition also

enables to use multiple OCT volume scans of a single patient over time to track the progression of a pathology or quantify the success of therapeutic treatment. As a consequence of the technological progress in OCT imaging which was made over the past few decades since its invention by [HSL+91], more expertise for extraction of manual annotations is required which in the presence of big volumetric datasets is difficult to access.

OCT is a low-coherent light interferometry based on the Michelson interferometer measuring time of flight of the light backscattered from the retina. The procedure is schematically depicted in Figure 2.4. Here a near infrared low intensity light from a broad band source reaches the beamsplitter and is divided into two separate beams. The first vertically oriented beam is reflected by the reference mirror whereas the light that passes the splitter is focused on the sample retinal tissue via an objective lens which is adjusted for particular depths of scan into the tissue. While part of the light is absorbed or scattered from the retina, the other part is reflected back in direction of the beamsplitter. Subsequently the two beams are recombined at the photodetector resulting in an interference pattern. Finally, through a direct comparison of the intensity time delay between reflected light from the retina and from the reference mirror an axial gray-scale plot of the interferometric signal strength commonly denoted as an 1-D **A-scan** is produced. Lateral translation of the optical beam creates multiple A-scans are created which together comprise a 2-D **B-scan**.

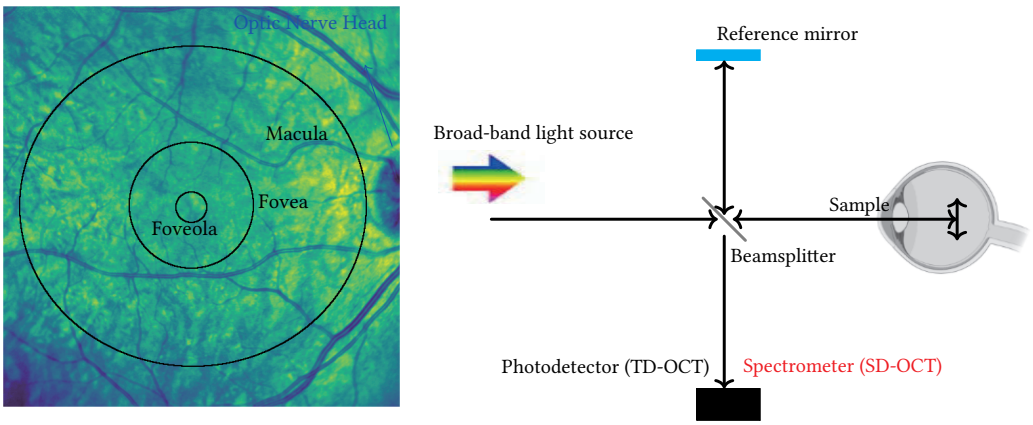


**Figure 2.4.: Right:** The Michelson interferometer configuration with a beamsplitter titled at 45 degrees. The comparison of backreflected signal from the retina and from the reference mirror measured at the Photodetector (TD-OCT) or Spectrometer (SD-OCT) cause the inference pattern inducing an in vivo image of the human retinal layers. **Left:** A top view on the fundus area in which the OCT samples are extracted. The oval shaped dark spot illustrates the location of optic nerve.

In general there are two types of interferometry techniques commonly integrated by OCT scanning devices: **Time-domain OCT** and **Spectral-domain OCT**. The time-domain OCT provides optical perception of the retina from various depths by varying the position of the reference mirror and captures 400 axial scans per second with axial resolution of 10 µm. In contrast, the spectral-domain OCT keeps the location of the reference mirror stationary and instead captures the spectrum of the back scattered light by applying a spectrometer. These measurements are then transformed via Fourier transformation into a sample of spectral variation as a function of depth. As compared to time domain OCT, avoiding the mechanical components by fixing the reference window location during the scanning process allows the spectral domain OCT to generate A-scans at a faster speed. The higher acquisition rate permits a rapid capturing of B-scans and increases the overall scanning accuracy which is advantageous for modeling and visualizing 3D-datasets.

# 3 Image Labeling by Assignments Flows

To provide a clear mathematical access to the ordered assignment flow presented in Chapter 4, in this chapter we recap the main concepts of *assignment flows* [ÅPSS17], which comprises a dynamical formulation of the image labeling problem. As opposed to discrete graphical models [KAH+15], the assignment flow is a *smooth* approach which enables efficient numerical inference [ZSPS20], parameter learning [HSPS21b] and extensions to unsupervised and self-supervised scenarios [ZZPS20a; ZZPS20b]. In particular, we show how this smooth geometric framework can be utilized to encode prior knowledge on the natural ordering of labels for the particular task of segmenting retinal tissue layers of a human eye (cf. Section 2.5.1). Based on a perspective of *information geometry*, we start this chapter by describing details on the geometry of probability distributions in Section 3.1 where the core focus will concentrate on the specific geometry of discrete probability distribution. Following on this geometry, in Section 3.2 we introduce the main mathematical object, the so called *assignment manifold*, which acts as interaction space of a set of probability distributions whose evolution to an integral state is determined by an ordinary differential equation (Section 3.2.2).

## 3.1. Manifolds of Probability Distributions

We first introduce Riemannian manifolds of parametric probability distributions with full support along with the dual structure as specified by Amari [AN00].

Given a measurable space $(\mathcal{X}, \Sigma, \mu)$ with a $\sigma$-algebra $\Sigma$ and measure $\mu : \Sigma \to \mathbb{R}_+$ we denote

$$\mathcal{P}_\mu = \{p \in \mathrm{L}^1(\mathcal{X}, \mu) \colon \mathbb{E}_\mu(p) = 1, p \geq 0\}, \qquad \mathbb{E}_\mu(p) = \int_{\mathcal{X}} p(x)\, \mathrm{d}\, \mu(x), \tag{3.1}$$

as the space of probability density functions $p : \mathcal{X} \to \overline{\mathbb{R}}$ on the *sample space* $\mathcal{X}$. A *statistical model* of dimension $d$ consists of an injective immersion $\iota : \theta \to p_\theta$ [1] into the set of parametric probability density functions

$$\mathcal{P}_\theta = \{p_\theta \in \mathcal{P}_\mu \colon \theta \in \Theta \subset \mathbb{R}^d\} \subset \mathcal{P}_\mu \tag{3.2}$$

that are parametrized on an open subset $\Theta \subset \mathbb{R}^d$ denoted as the *parameter space*. More specifically, the mapping $\iota$ is onto and

$$\frac{\partial p_\theta}{\partial \theta^i}, \qquad i \in [d] \tag{3.3}$$

are linearly independent functions on $\mathcal{X}$. The inverse of the map $\theta \to p_\theta$ provides a local chart

[1] In this thesis we are concerned with the inference task of label decision on a smooth manifold and therefore require a smooth parametrization of probability density functions. However, there exist a more general statistical manifolds with lower regularity assumption on $\iota$.

that turns $\mathcal{P}_\theta$ into a Riemannian manifold of dimension $d$ with *Fisher-Rao metric*

$$g_{ij}(\theta) = g_\theta(\partial_i, \partial_j) \coloneqq \mathbb{E}_\mu\Big(p_\theta \partial_i l(\theta) \partial_j l(\theta)\Big), \qquad l(x) = \log p_\theta, \quad \partial_i l(\theta) = \frac{\partial l(\theta)}{\partial \theta^i}, \tag{3.4}$$

where $l(\theta)$ and $\partial_i l(\theta)$ are denoted as the *log-likelihood* and *score* functions respectively. Up to scaling, the metric (3.4) is unique in the sense that: $(i)$: it is invariant under reparametrizations $\mathcal{X} \to \mathcal{Y} \subset \mathbb{R}^d$ of the sample space $\mathcal{X}$ and $(ii)$: it is covariant under reparametrizations of the parameter space $\Theta$, i.e. the metric tensor transforms as a 2-covariant tensor. For the specific case of the metric (3.4), by virtue of characterization (2.80) there is a one parameter family of symmetric dual connections on $P_\theta$ a.k.a. $\alpha$-connection

$$\Gamma^{(\alpha)}_{ij,k}(\theta) = \mathbb{E}_\nu\Big(\partial_i \partial_j l(\theta) + \frac{1-\alpha}{2} \partial_i l(\theta) \partial_j l(\theta)\Big), \qquad \alpha \in [-1, 1]. \tag{3.5}$$

The corresponding dual parameters are related by the Fenchel conjugate (2.23) through

$$\Gamma^{*(\alpha)}_{ij,k} = \Gamma^{(-\alpha)}_{ij,k}, \tag{3.6}$$

providing a dual structure $(g, \nabla^\alpha, (\nabla^\alpha)^*)$ on $\mathcal{P}_\theta$ for each $\alpha \in [-1, 1]$. In coordinate free notation this means that each connection from the one parameter family (3.6) is recovered by interpolation of $\nabla^{(-1)}$ and $\nabla^{(1)}$ connections via

$$\nabla^{(\alpha)} = \frac{1+\alpha}{2} \nabla^{(1)} + \frac{1-\alpha}{2} \nabla^{(-1)}. \tag{3.7}$$

In addition, the Levi-Cevita-connection (2.69) is represented via

$$\nabla^g = \frac{1}{2}\big(\nabla^\alpha + \nabla^{(-\alpha)}\big) \tag{3.8}$$

and if $\nabla^{(-1)}$ or $\nabla^{(1)}$ are dually flat then (3.7) is flat for each $\alpha \in [-1, 1]$.

### 3.1.1. Geometry of Distributions on Finite Sets

We now concentrate on an important type of statistical models (3.2) used in this thesis for the task of encoding label assignments on graphs. Hereby, we focus on distributions $p : \mathcal{X} \to \mathbb{R}_+$ on finite sample spaces $\mathcal{X} = [c]$ which we identify by vectors $p \in \mathbb{R}^c$. In this setting the counterpart of (3.1) is denoted by

$$\mathcal{S} = \{p \in \Delta_c \colon p > 0\}. \tag{3.9}$$

with the probability simplex

$$\Delta_c = \big\{p \in \mathbb{R}^c_+ \colon \sum_{i=1}^{c} \langle \mathbb{1}_c, p\rangle = 1\big\}, \tag{3.10}$$

Each element of $\mathcal{S}$ is represented on the parameter space by $m$-parameters (mixture)

$$U = \{\mu \in \mathbb{R}^{c-1} \colon \mu^i > 0, \langle \mathbb{1}_{c-1}, \mu\rangle < 1\}, \tag{3.11}$$

by the chart $\phi : \mathcal{S} \to U$:

$$\phi(p) = (p^1, \ldots, p^{c-1})^T, \qquad \phi^{-1}(\mu) = p_\mu = (\mu, 1 - \langle \mathbb{1}_{c-1}, \mu\rangle)^T, \tag{3.12}$$

using a sum of indicator functions $\delta_i : \mathcal{X} \to \{0, 1\}$ for $i \in [c-1]$ via

$$p_\mu = \sum_{i=1}^{c-1} \mu^i \delta_i(x) + (1 - \langle \mathbb{1}, \mu\rangle)(1 - \sum_{i=1}^{c-1} \delta_i(x)), \quad \delta_i(x) = \begin{cases} 1 & , \quad x = i, \\ 0 & , \quad \text{else.} \end{cases} \tag{3.13}$$

An alternative parametrization of $p \in \mathcal{S}$ is given by

$$p_\theta = \exp\big(\sum_{i=1}^{c-1} \theta^i \delta_i(x) - \log(1 + \langle \mathbb{1}, e^\theta\rangle)\big), \tag{3.14}$$

on parameter space $\Theta = \mathbb{R}^c$ with $e$-parameters (exponential) given by

$$\theta^i = \log(\frac{\mu^i}{1 - \langle \mathbb{1}, \mu \rangle}) = \log \frac{p^i}{p^c}, \qquad \xi \in \Theta \qquad i \in [c-1]. \tag{3.15}$$

The coordinate vectors expressed in terms of charts $p \to \mu$ and $p \to \theta$ at $p \in \mathcal{S}$ are

$$\Big(\frac{\partial}{\partial \mu^i}\big|_p\Big) = e_i - e_c, \qquad \Big(\frac{\partial}{\partial \theta^i}\big|_p\Big)_j = \begin{cases} \delta_i(j) - p(j|\theta), & j \in [c-1] \\ -p(j|\theta), & j = c, \end{cases} \tag{3.16}$$

with tangent spaces given respectively by

$$T_0 = \{v \in \mathbb{R}^c \colon \langle \mathbb{1}_c, v \rangle = 0\}, \qquad T_p\mathcal{S} = \{u = \frac{v}{p} \colon v \in T_0\}. \tag{3.17}$$

The Fisher-Rao metric for the two statistical models is expressed through $\mu, \theta$

$$g_{ij}(\theta) = \big(\operatorname{Diag}(\mu) - \mu\mu^T\big), \qquad g_{jk}(\mu) = \Big(\operatorname{Diag}\big(\frac{1}{\mu}\big) + \frac{1}{1 - \langle \mathbb{1}, \mu \rangle} \mathbb{1}_{c-1} \mathbb{1}_{c-1}^T\Big), \tag{3.18}$$

which by Sherman-Morrison-Woodbury formula are inverses of each other. The following theorem shows that leveraging the aforementioned parameters $\mu$ and $\theta$ in (3.5) for the specific case of $m$ and $e$ connections turns $\mathcal{S}$ into a dually flat statistical manifold.

**Theorem 3.1.1 (Dual Structure on $\mathcal{S}$).** *[**Proposition 2.5**; AJLS17] Let $(\mathcal{S}, g, \nabla^{(\alpha)}, \nabla^{(-\alpha)})$ be a family of statistical manifolds with metric $g$ induced by (3.4) with log-likelihood $l : \mathcal{S} \to \mathbb{R}$ . Then, $(\mathcal{S}, g, \nabla^{(-\alpha)}, \nabla^{*(\alpha)})$ is a dually flat manifold and the following holds for $\alpha \in \{-1, 1\}$*

*(i) The $e$-and-$m$ connections define a dually flat structure on $\mathcal{S}$, i.e. $(\nabla^{(m)})^* = \nabla^{(e)}$ and vice versa.*

*(ii) The geodesics $\gamma^{(m)} : (t^-, t^+) \to \mathcal{S}$ and $\gamma^{(e)} : \mathbb{R} \to \mathcal{S}$ starting at $p \in \mathcal{S}$ into direction $v \in T_p\mathcal{S}$ corresponding to $\nabla^{(m)}$-and-$\nabla^{(e)}$ connections respectively are explicitly given by*

$$\gamma_v^{(m)}(t) = p + tv, \qquad \text{and} \qquad \gamma_v^{(e)}(t) = \frac{pe^{t\frac{v}{p}}}{\langle p, e^{t\frac{v}{p}} \rangle}. \tag{3.19}$$

*(iii) The parallel transport map with respect (2.61) reads*

$$\Pi_{p,q} \colon T_p\mathcal{S} \to T_q\mathcal{S}, \qquad \Pi_{p,q}(v) = v - \langle q, v \rangle \mathbb{1}, \qquad u = \frac{v}{p}, \quad v \in T_0, \quad p, q \in \mathcal{S}. \tag{3.20}$$

An important consequence of Theorem 3.1.1 is the closed form of the exponential maps (2.64)

$$\operatorname{Exp}^{(m)} \colon \mathcal{E} \to \mathcal{S} \qquad \operatorname{Exp}_p^{(m)}(v) = p + v, \tag{3.21a}$$

$$\operatorname{Exp}^{(e)} \colon \mathcal{TS} \to \mathcal{S} \qquad \operatorname{Exp}_p^{(e)}(v) = \frac{pe^{\frac{v}{p}}}{\langle p, e^{\frac{v}{p}} \rangle} \tag{3.21b}$$

where $\mathcal{E} = \{(p, v) \in \mathcal{TS} \colon p + v \in \mathcal{S}\}$. An important role in this work will be taken by the $e-$geodesics (3.21b) that are *globally* defined on the tangent bundle $\mathcal{TS}$ which allows numerically convenient computations.

**Remark 3.1.1. (Relation to Legendre Fenchel transform)** The above derivation are in line with Theorem 2.2.2 applied with strictly convex *log-partition* function $\psi(\theta)$

$$\psi(\theta) = \log(1 + \langle \mathbb{1}, e^\theta \rangle), \tag{3.22}$$

that directly relates the coordinate vectors by the Legendre Fenchel transform $\mu \leftrightarrow \theta$ via (2.81) with Fenchel conjugate given by the *negative entropy*

$$\phi(\mu) = \sum_{i=1}^{c-1} \mu^i \log \mu^i + (1 - \langle \mathbb{1}, \mu \rangle) \log(1 - \langle \mathbb{1}, \mu \rangle), \tag{3.23}$$

which serves as measure for how distinct points on $\mathcal{S}$ are from a single label $l \in [c]$, see figure 3.1 and its caption. The Jacobean of $\psi$ and $\psi^*$ recovers the metric tensor $g_{ij}$ and its inverse respectively.

**Remark 3.1.2 (Impact on geodesics).** In general, given a dual structure $(\nabla, \nabla^*)$ on $\mathcal{M}$ the corresponding connections satisfy a weaker version of the metric relation (2.69) given by (2.79). Consequently, the associated geodesics in 3.1.1 are not length minimizing in the sense of (2.70a) but provide a convenient way for evaluating the induced exponential maps with first order approximation accuracy

$$\|\gamma_v(t) - \mathrm{Exp}_p^e(v)\| = \mathcal{O}(t^2) \tag{3.24}$$

of the natural geodesic induced by Levi-Cevita connection and are more convenient for numerical computations. See [ÅPSS17, Proposition 3] and figure 3.1 for an illustrative approximation behavior.

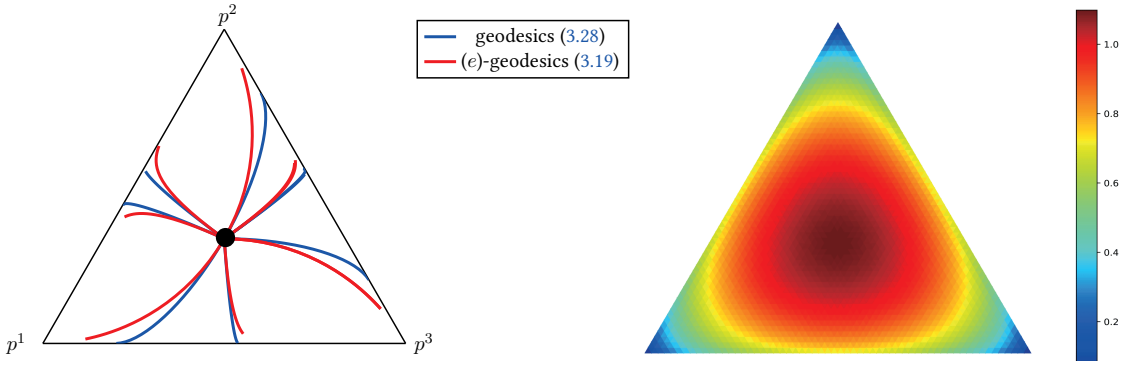


**Figure 3.1.:** Illustration of simplex geometry. **Left:** Red and blue trajectories correspond to $e$-geodesics (3.19) and Riemannian geodesics with respect to Fisher-Rao metric respectively emanating from barycenter for various tangent directions $v \in T_0$. The corners of the simplex represent pixel labelings. As observed from the plots $e$-geodesics provide accurate local approximation of the Riemannian geometry. **Right:** Plot of the negative entropy (3.23). Nodes near the corners of the simplex boundary are characterized by a low entropy state.

**Remark 3.1.3 (Fisher-Rao metric as pullback metric).** An alternative characterization of the Fisher-Rao metric is given by the pullback of Euclidean metric (2.71) through the spherical map

$$\Phi : \mathcal{S} \to 2\mathcal{S}^c_{>0}, \qquad \Phi(p) = 2(\sqrt{p^1}, \dots, \sqrt{p^c})^T, \tag{3.25}$$

where $\mathcal{S}^c_{>0}$ denotes the positive $c-$ sphere, see figure 3.2

$$\mathcal{S}^c_{>0} = \{x \in \mathbb{R}^c \colon x_i > 0, \quad \|x\|^2 = 1\}. \tag{3.26}$$

Because the mapping $\Phi$ is an isometry and as the distance between two points on $S^c$ can be expressed in closed form the corresponding Riemannian distance (2.70a) between two points $p, q \in \mathcal{S}$ is explicitly given by

$$d(p, q) = 2 \arccos(\langle p, q \rangle) \in [0, \pi), \tag{3.27}$$

along with the resulting geodesics and exponential maps

$$\begin{aligned} &\mathrm{Exp}_p \colon V_p \to \mathcal{S}, \qquad \mathrm{Exp}_p(v) = \gamma_v(1), \qquad \text{where} \\ &\gamma_v(t) = \frac{1}{2}\Big(p + \frac{v_p^2}{\|v_p\|^2}\Big) + \frac{1}{2}\Big(p - \frac{v_p^2}{\|v_p\|^2}\Big)\cos(\|v_p\|t) + \frac{v_p}{\|v_p\|}\sqrt{p}\sin(\|v_p\|t), \end{aligned} \tag{3.28}$$

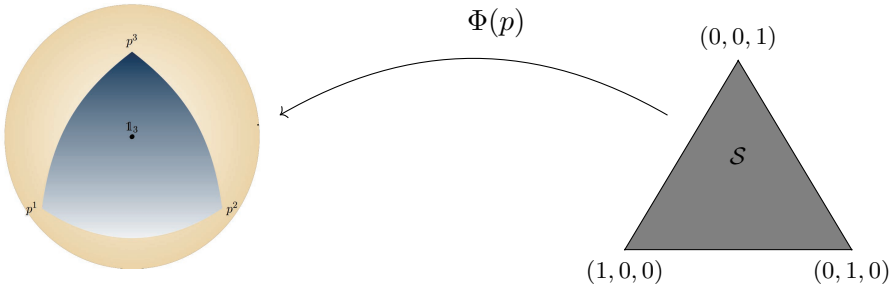


**Figure 3.2.:** The isometric embedding of the simplex geometry into the $2-$ sphere by mapping (3.25) that induces the Fisher-Rau metric as the pull back of Euclidean inner product.

with $v_p = \frac{v}{\sqrt{p}}$, $\gamma_v(0) = p$, $\dot{\gamma}_v(0) = v$ and

$$V_p = \{v \in T_p\mathcal{S} \colon \gamma_v(t) \in \mathcal{S}, t \in [0,1]\}. \tag{3.29}$$

In the following it will be convenient to represent the $e$-geodesics directly on tangent space $T_0$ at the *barycenter*

$$\mathbb{1}_{\mathcal{S}} = \frac{1}{c}\mathbb{1}_c \in \mathcal{S}, \qquad \text{(barycenter)}, \tag{3.30}$$

by leveraging the parametrization of $u = \frac{v}{p} \in T_p\mathcal{S}$ in (3.20). The resulting Fisher-Rao metric expressed at each $p \in \mathcal{S}$ on the ambient space $\mathbb{R}^c$

$$g_p(u,v) = \sum_{j\in J} \frac{u^j v^j}{p^j}, \quad p \in \mathcal{S}, \quad u, v \in T_0. \tag{3.31}$$

The Riemannian gradient that satisfies (2.73) for each $f : \mathcal{S} \to \mathbb{R}$ is

$$\operatorname{grad}_{\mathcal{S}} f(p) = R_p \nabla f(p), \tag{3.32}$$

where $R_p$ is the *replicator map*

$$R_p \colon \mathbb{R}^c \to T_0, \qquad R_p = \operatorname{Diag}(p) - pp^\top, \qquad p \in \mathcal{S}, \tag{3.33}$$

commonly known in the field of population dynamics [HS03]

$$\dot{p}^i = p^i\Big((\nabla f)_i - \langle p, (\nabla f)_i\rangle p^i\Big), \qquad p \in \mathcal{S}, \tag{3.34}$$

with gradient components $(\nabla f)_i$ encoding *payoff functions* for choosing a strategy $j \in [c]$. The replicator map is related to parallel transport by composition

$$R_p = R_p\Pi_0 = \Pi_0 R_p, \qquad R_p = \operatorname{Diag}(q)\Pi_{p,q}, \tag{3.35}$$

with the orthogonal projection $\Pi_0 : \mathbb{R}^c \to T_0$ on the tangent space

$$\Pi_0 \colon \mathbb{R}^c \to T_0, \qquad \Pi_0 = I - \mathbb{1}_{\mathcal{S}}\mathbb{1}_c^\top. \tag{3.36}$$

The following lemma presents key properties of the map $R_p$.

**Lemma 3.1.1.** *For each $p \in \mathcal{S}$ The replicator map $R_p$ in (3.33) satisfies the following properties*

*$(i)$: $(R_p)_{|T_0} : T_0 \to T_0$ is a linear isomorphism for each $p \in \mathcal{S}$ with inverse given by*

$$\big((R_p)_{|T_0}\big)^{-1} = \Pi_0 \operatorname{Diag}\left(\frac{1}{p}\right) \tag{3.37}$$

*$(ii)$: $R_p \in \mathbb{R}^{c\times c}$ is positive semi-definite symmetric matrix with real eigenvalues*

$$0 \le \lambda_1 \le \cdots \le \lambda_c \le \frac{1}{2}. \tag{3.38}$$

*Proof.* Appendix A.1, proof of Lemma 3.1.1. □

With respect to this parametrization the exponential maps and their inverses have shape

$$\mathrm{Exp}\colon \mathcal{S}\times T_0 \to \mathcal{S}, \qquad (p,v)\mapsto \mathrm{Exp}_p(v) = \frac{pe^{\frac{v}{p}}}{\langle p, e^{\frac{v}{p}}\rangle}, \tag{3.39a}$$

$$\mathrm{Exp}_p^{-1}\colon \mathcal{S}\to T_0, \qquad q\mapsto \mathrm{Exp}_p^{-1}(q) = R_p \log\frac{q}{p}, \tag{3.39b}$$

and introduce the following mapping for the reason of convenience [1]

$$\exp_p\colon T_0\to\mathcal{S}, \qquad \exp_p = \mathrm{Exp}_p\circ R_p, \tag{3.39c}$$

$$\exp_p^{-1}\colon \mathcal{S}\to T_0, \qquad \exp_p^{-1}(q) = \Pi_0 \log\frac{q}{p} \tag{3.39d}$$

where multiplication, exponentials and logarithms apply componentwise. Applying the map $\exp_p$ to a vector in $\mathbb{R}^c = T_0\oplus\mathbb{R}\mathbb{1}$ does not depend on the constant component of the argument, due to (3.35). We end this section by summarizing properties of the lifting map $\exp_p : \mathbb{R}^c\to\mathcal{S}$ that will be of particular importance in section 3.2.2.

**Lemma 3.1.2.** ***[Lemma 3.1**; SS21] For each $p\in\mathcal{S}$ the mapping $\exp_p : \mathbb{R}^c\to\mathcal{S}$ satisfies:*

*(i): The restriction $(\exp_p)_{|T_0} : T_0\to\mathcal{S}$ is a diffeomorhism between flat tangent space $T_0$ and $\mathcal{S}$ with the inverse given by (3.39d)*

*(ii): The differential of $\exp_p$ on $\mathbb{R}^c$ is*

$$d\exp_p(v)[u] = R_{\exp_p(v)}[u], \qquad \forall u,v\in\mathbb{R}^c. \tag{3.40}$$

*(iii): The map $\exp_p$ defines a Lie group action on $\mathbb{R}^c$, i.e.*

$$\exp_p(u+v) = \exp_{\exp_p(v)}(u), \qquad \exp_p(0)=p, \qquad \forall u,v\in\mathbb{R}^c, p\in\mathcal{S}. \tag{3.41}$$

## 3.2. The Assignment Flow Framework

Based on simplex geometry presented in section 3.1.1, we now collect key concepts of assignment flows introduced by [ÅPSS17] that comprise a specific type of dynamical systems for the task of labeling metric data on graphs by following a Riemannian gradient flow. In particular, this links a broad field of machine learning problems to the perspective of information theory which allows for a more mathematically sophisticated modeling. We refer to [Sch20] for further details and a review of recent related work.

### 3.2.1. Assignment Manifold

Let $(\mathcal{F}, d_{\mathcal{F}})$ be a metric space and

$$\mathcal{F}_n = \{f_i\in\mathcal{F}\colon i\in\mathcal{V}\}, \qquad |\mathcal{V}| = n \tag{3.42a}$$

[3] In contrast to the *big* map $Exp_p$ which denotes the Riemannian exponential map with respect to Levi-Cevita connection, the the *small* map $\exp_p$ is defined at the whole tangent space $T_0$ and simplifies the involved calculations.

given data. Assume that a predefined set of prototypes

$$\mathcal{F}_* = \{f_j^* \in \mathcal{F} \colon j \in J\}, \qquad |J| = c \tag{3.42b}$$

is given. *Data labeling* denotes the assignments

$$j \to i, \qquad f_j^* \to f_i \tag{3.43}$$

of a single prototype $f_j^* \in \mathcal{F}_*$ to each data point $f_i \in \mathcal{F}_n$. The set $I$ is assumed to form the vertex set of an undirected graph $\mathcal{G} = (I, \mathcal{E})$ which defines a relation $\mathcal{E} \subset I \times I$ and neighborhoods

$$\mathcal{N}_i = \{k \in I \colon ik \in \mathcal{E}\} \cup \{i\}, \tag{3.44}$$

where $ik$ is a shorthand for the unordered pair (edge) $(i,k) = (k,i)$. We require these neighborhoods to satisfy the symmetry relation

$$k \in \mathcal{N}_i \quad \Leftrightarrow \quad i \in \mathcal{N}_k, \qquad \forall i,k \in I. \tag{3.45}$$

The assignments (labeling) (3.43) are represented by matrices in the set

$$\mathcal{W}_* = \{W \in \{0,1\}^{n \times c} \colon W \mathbb{1}_c = \mathbb{1}_n\} \tag{3.46}$$

with unit vectors $W_i$, $i \in I$, called *assignment vectors*, as row vectors. The integrality constraint of (3.46) is relaxed on the Riemannian manifold 3.9 and represented by vectors

$$W_i = (W_{i1}, \ldots, W_{ic})^\top \in \mathcal{S}, \quad i \in I, \tag{3.47}$$

that we still call *assignment vector*,

The *assignment manifold* is defined as

$$(\mathcal{W}, g), \qquad \mathcal{W} = \mathcal{S} \times \cdots \times \mathcal{S}. \qquad (n = |I| \text{ factors}) \tag{3.48}$$

We identify $\mathcal{W}$ with the embedding into $\mathbb{R}^{n \times c}$

$$\mathcal{W} = \Big\{ W \in \mathbb{R}^{n \times c} \colon W \mathbb{1}_c = \mathbb{1}_n \text{ and } W_{ij} > 0, \text{ for all } i \in [n], j \in [c] \Big\}. \tag{3.49}$$

Thus, points $W \in \mathcal{W}$ are row-stochastic matrices $W \in \mathbb{R}^{n \times c}$ with row vectors $W_i \in \mathcal{S}$, $i \in I$ that represent the assignments (3.43) for every $i \in I$. We set

$$\mathcal{T}_0 := T_0 \times \cdots \times T_0 \qquad (n = |I| \text{ factors}). \tag{3.50}$$

The above construction shows that as a product space of probability simplices each element $W \in \mathcal{W}$ is a collection of discrete probability vectors, one for each pixel. As a consequence, the dual structure on $\mathcal{S}$ introduced in Section 3.1 naturally translates to $\mathcal{W}$ via componentwise $e$-and $m$ coordinates

$$\theta = (\theta_1, \ldots, \theta_n)^T, \qquad \mu = (\mu_1, \ldots, \mu_n)^T, \qquad \theta, \mu \in \mathbb{R}^{(c-1)n}. \tag{3.51}$$

Due to (3.49), the tangent space $\mathcal{T}_0$ can be identified with

$$\mathcal{T}_0 = \{V \in \mathbb{R}^{n \times c} \colon V \mathbb{1}_c = 0\}. \tag{3.52}$$

Thus, $V_i \in T_0$ for all row vectors of $V \in \mathbb{R}^{n \times c}$ and $i \in I$. The induced Fisher-Rao metric on $\mathcal{W}$ accordingly reads

$$g_{\mathcal{W}}(V,U) = \sum_{i \in I} g_{\mathcal{W}_i}(V_i, U_i), \qquad \text{for} \qquad U, V \in \mathcal{T}_0. \tag{3.53}$$

The mappings defined in (3.39) on a single $\mathcal{S}$ factorize in a natural way and apply row-wise on the product manifold $\mathcal{W}$, e.g.

$$\operatorname{Exp}_W = (\operatorname{Exp}_{W_1}, \ldots, \operatorname{Exp}_{W_n}), \tag{3.54a}$$

$$R_W = (R_{W_1}, \ldots, R_{W_n}), \tag{3.54b}$$

$$\exp_W^{-1}(\tilde{W}) = \big(\Pi_0 \log \frac{\tilde{W}_1}{W_1}, \ldots, \Pi_0 \log \frac{\tilde{W}_n}{W_n}\big), \tag{3.54c}$$

etc., where with abuse of notation $\Pi_0$ denotes the orthogonal projection into $\mathcal{T}_0$. Moreover, recapitulating Remark 3.1.1 the dually flat structure on $\mathcal{W}$ is composed of $e$-and $m$ affine connections represented for each node $i \in I$ through coordinates $\theta_i, \mu_i$ with Legendre-Fenchel conjugate on $\mathcal{W}$

$$H_{\mathcal{W}}(W) = \sum_{i \in \mathcal{W}} H(W_i) = -\phi(\mu), \tag{3.55}$$

with convex functions

$$\phi(\mu) = \sum_{i \in \mathcal{V}} \mu_i \log(\mu_i) = \psi^*(\mu) = \sum_{\Omega} \max_{i \in \mathcal{V}, \theta_i \in \mathbb{R}^c} \{\langle \theta_i, \mu_i \rangle - \psi_i(\theta_i)\}. \tag{3.56}$$

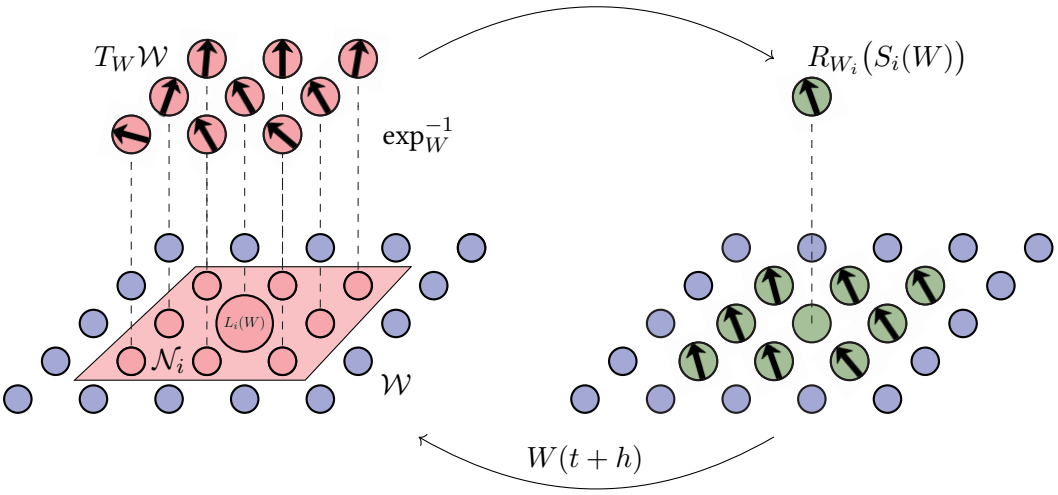


**Figure 3.3.:** Schematic illustration of the evolutionary process (3.63) driving $W(t)$ to a spatially regularized labeling $W^*$. **Left:** Likelihood vectors (3.59) that represent the data (3.58) at the current state $W \in \mathcal{W}$ (blue dots) on a discrete graph $\mathcal{V}$ are lifted to tangent space $T_W\mathcal{W}$ through the inverse map (3.54c). **Right:** The noisy likelihood vectors (black arrows, red points) are regularized at each node $i \in \mathcal{V}$ within a spatial neighborhoods $\mathcal{N}_i$ by means of an averaging matrix $\Omega$ by assembling a spatially coherent denoised vector field (green dots) by the similarity map (3.62).

### 3.2.2. Assignment Flow

Based on (3.42a) and (3.42b), the distance vector field

$$D_{\mathcal{F};i} = \big(d_{\mathcal{F}}(f_i, f_1^*), \ldots, d_{\mathcal{F}}(f_i, f_c^*)\big)^\top, \qquad i \in I \tag{3.57}$$

is well-defined. These vectors are collected as row vectors of the *distance matrix*

$$D_{\mathcal{F}} \in S_+^n, \tag{3.58}$$

where $S_+^n$ denotes the set of symmetric and entrywise nonnegative matrices.
The *likelihood map* and the *likelihood vectors*, respectively, are defined for $i \in I$ as

$$L_i \colon \mathcal{S} \to \mathcal{S},$$

$$L_i(W_i) = \exp_{W_i}\Big(-\frac{1}{\rho} D_{\mathcal{F};i}\Big) = \frac{W_i e^{-\frac{1}{\rho} D_{\mathcal{F};i}}}{\langle W_i, e^{-\frac{1}{\rho} D_{\mathcal{F};i}} \rangle}, \tag{3.59}$$

where the scaling parameter $\rho > 0$ is used for normalizing the a-prior unknown scale of the components of $D_{\mathcal{F};i}$ that depends on the specific application at hand.

**Remark 3.2.1 (rationale of likelihood map $L_i(W_i)$).** For the particular case of $W_i = \mathbb{1}_{\mathcal{S}}$ in (3.59) the likelihood map recovers the commonly used operation from the field of machine learning that admits a characterization by

$$L_i(\mathbb{1}_{\mathcal{S}}) = \operatorname{argmin}_{W_i \in \mathcal{S}} E_{i,\rho}(W_i), \quad \text{with} \quad E_{i,W_i} = \langle \mathcal{D}_{\mathcal{F};i}, W_i \rangle + \rho \langle W_i, \log W_i \rangle, \tag{3.60}$$

i.e., the label assignment to nodes $i \in [n]$ is determined as maximal component of the optimum of a data term $\langle \mathcal{D}_{\mathcal{F},i}, W_i \rangle$ that is regularized by negative entropy. As a consequence, the likelihood map generalizes (3.60) by performing an additional scaling along the labeling space.

A key component of the assignment flow is the interaction of the likelihood vectors through *geometric* averaging within the local neighborhoods (3.44). Specifically, using weights

$$\omega_{ik} > 0 \quad \text{for all } k \in \mathcal{N}_i,\ i \in I \quad \text{with} \quad \sum_{k \in \mathcal{N}_i} w_{ik} = 1, \tag{3.61}$$

the *similarity map* and the *similarity vectors*, respectively, are defined for $i \in I$ as

$$\begin{aligned} &S_i \colon \mathcal{W} \to \mathcal{S}, \\ &S_i(W) = \operatorname{Exp}_{W_i}\Big( \sum_{k \in \mathcal{N}_i} w_{ik} \operatorname{Exp}_{W_i}^{-1}\big(L_k(W_k)\big)\Big). \end{aligned} \tag{3.62}$$

If $\operatorname{Exp}_{W_i}$ were the exponential map of the Riemannian (Levi-Civita) connection, then the argument inside the brackets of the right-hand side would just be the negative Riemannian gradient with respect to $W_i$ of center of mass objective function comprising the points $L_k$, $k \in \mathcal{N}_i$, i.e. the weighted sum of the squared Riemannian distances between $W_i$ and $L_k$ [Jos17, Lemma 6.9.4]. In view of Remark 3.1.2, this interpretation is only approximately true mathematically, but still correct informally: $S_i(W)$ moves $W_i$ towards the geometric mean of the likelihood vectors $L_k$, $k \in \mathcal{N}_i$. Since $\operatorname{Exp}_{W_i}(0) = W_i$, this mean precisely is $W_i$ if the aforementioned gradient vanishes.

The *assignment flow* is induced on the assignment manifold $\mathcal{W}$ by the locally coupled system of nonlinear ODEs

$$\dot{W} = R_W S(W), \qquad W(0) = \mathbb{1}_{\mathcal{W}}, \tag{3.63a}$$

$$\dot{W}_i = R_{W_i} S_i(W), \qquad W_i(0) = \mathbb{1}_{\mathcal{S}}, \quad i \in I, \tag{3.63b}$$

where $\mathbb{1}_{\mathcal{W}} \in \mathcal{W}$ denotes the barycenter of the assignment manifold (3.48). System (3.63) couples replicator equations of type (3.34) through similarity map (3.62) on spatially varying neighborhoods (3.44).

Numerical integration of the assignment flow (3.63) in the geometric setting of assignment manifold evolves the assignment vectors $W(t)$ on $\mathcal{W}$ while simultaneously performing spatial regularization through application of the similarity map (3.62) as commented in Remark 3.2.3.

**Remark 3.2.2 (parameters).** As will be demonstrated in Section 4.4 by various specifications of averaging weights $\Omega$ the role of associated parameter $|\mathcal{N}|$ is to provide regularized (denoised) labelings by increasing the corresponding connectivity $|\mathcal{N}|$. This process is schematically and described by Figure 3.3. On the other hand as pointed out in remark 3.2.1 the selectivity parameter $\rho$ controls the influence of given data vector field $\mathcal{D}_{\mathcal{F}}$ on the labeling along with initial flow velocity of $\dot{W}$, see [ÅPSS17]. In practice, for fixed sizes of $|\mathcal{N}|$ the parameter $\rho$ is selected according to an application task as a trade off between highly regularized labeling and noise-induced oversegmentation at small spatial scales as explained by Figure 3.4.

**Remark 3.2.3 (regularization).** From the viewpoint of variational imaging, *regularization* of the assignment flow has to be understood in a broad sense: The parameters $\Omega$ define by (3.62), at each location $i$ and locally within neighborhoods $\mathcal{N}_i$, what similarity of the collection of likelihood vectors $L_j(W)$, $j \in \mathcal{N}_i$, which represent the input data, really means in terms of a corresponding geometric average (3.62). Unlike traditional variational approaches where regularization affects the primary variables directly, regularization of the assignment flow (3.63) is accomplished more effectivly by affecting *velocities* that *generate* the primary assignment variables: the vector field $S(W)$ drives the assignment flow (3.63). Learning the regularization parameters $\Omega$ from data was studied by [HSPS21a; ZPS22].

Due to the imposed Fisher-Rao geometry (3.31), $W(t)$ converges to an integral solution [ZZS20]: for $t \to \infty$, each $W_i(t)$ approaches an unit vector that encodes the class label $j$ assigned to the data point $f_i$ given at pixel $i \in I$ that is characterized by a state of low normalized negative entropy. Convergence and stability of the assignment flow have been studied by [ZZS20].

### 3.2.3. Geometric Numerical Integration

Due to the geometric nature of system (3.63) this section is devoted to an accurate numerical approximation of the integral curve $W(t)$ that solves system (3.63) by means of geometric integration schemes, see [HLW10] and references therein. Following [ZSPS20] the methods of choice are provided by Lie Group schemes [IMKNZ00],[EFBL18] for integrating flows that admit a representation on a manifold $\mathcal{M}$ through a Lie group action on Lie group $\mathcal{G} \times \mathcal{M} \to \mathcal{M}$:

$$\Lambda(e, x) = x, \quad \Lambda(h \circ g, x) = \Lambda(h, \Lambda(g, x)), h, g \in \mathcal{G}, x \in \mathcal{M}, \tag{3.64}$$

where $e \in \mathcal{G}$ denotes the neutral element of $\mathcal{G}$ and $\mathfrak{g}$ is the corresponding Lie algebra. That is, defining the Lie-Algebra action $\lambda$ in terms of (3.64) by composition with the exponential mapping $\exp_{\mathcal{G}} : \mathfrak{g} \to \mathcal{G}$ via

$$\lambda(v, p) = \Lambda(\exp_{\mathrm{G}}(v), p), \tag{3.65}$$

followed by introducing the associated differential

$$(\lambda_* v)_p = \frac{\mathrm{d}}{\mathrm{d}t} \Lambda(\exp_{\mathrm{G}}(tv), p)\big|_{t=0} \qquad \text{for all } v \in \mathfrak{g},\ p \in \mathcal{M}. \tag{3.66}$$

The flow on $\mathcal{M}$ is equivalently formulated on the tangent bundle $\mathcal{TM}$

$$\dot{v} = (\mathrm{dexp}_{\mathrm{G}}^{-1})_v\big(f(t, \lambda(v, p))\big), \qquad v(0) = 0. \tag{3.67}$$

where $F : \mathbb{R} \times \mathcal{M} \to \mathcal{M}$ is any smooth function satisfying

$$\dot{x}(t) = \big(\lambda_* F(t, x)\big)_x, \qquad x(0) = p. \tag{3.68}$$

An important consequence of representation (3.67) is that the corresponding ODE (3.68) now evolves on the underlying tangent space rather than on manifold $\mathcal{M}$. The linearity of $\mathcal{TM}$ establishes a connection to classical Runge-Kutta methods [HNWxx] of arbitrary order for an accurate numerical approximation of $v(t)$. In this context assignment flows permit a particularly lucrative Lie Group structure on $\mathcal{W}$ in terms of $e$-geodesics

$$\mathcal{G} = T_0, \qquad \Lambda : T_0 \times \mathcal{W} \to \mathcal{W}, \quad \Lambda(v, p) = \exp_p(v), \qquad F(t, W) = S(W)(t) \tag{3.69}$$

where $\Lambda$ is a Lie group action according to lemma 3.1.2 and $S(W)$ is the similarity map (3.9). As shown in [ZSPS20, Proposition 3.1] for this particular case the solution to the flow (3.63) emanating from any $W_0 = W(0)$ is represented globally on $T_0$ by

$$W(t) = \exp_{W_0}\big(V(t)\big) \tag{3.70a}$$

where $V(t) \in \mathcal{T}_0$ is determined by (3.67) satisfying

$$\dot{V} = \Pi_{\mathcal{T}_0} S\big(\exp_{W_0}(V)\big), \qquad V(0) = 0. \tag{3.70b}$$

Overall, the integral curve $W(t), t \in \mathbb{R}_+$ is approximated by a choice of an $s$ stage Runge-Kutta method of order $p$ given by the Butcher tableau notation convention

$$\begin{array}{c|cccc} c_1 & a_{11} & a_{12} & \cdots & a_{1s} \\ c_2 & a_{21} & a_{22} & \cdots & a_{2s} \\ \vdots & \vdots & \vdots & & \vdots \\ c_s & a_{s1} & a_{s2} & \cdots & a_{s(s-1)} \\ \hline & b_1 & b_2 & \cdots & b_s \end{array}$$

and satisfies consistency condition $c_i = \sum_j a_{ij}$. Specifying the integration parameter $h$, the approximated value $W(t+h)$ is then obtained by advancing $W(t)$ in time through the Lie group action $\Lambda$ via

$$k^i = h \sum_{j \in [s]} a_{i,j} \widetilde{k}^j, \qquad i \in [s] \tag{3.71a}$$

$$\widetilde{k}^i = F\big(t + hc_i, \Lambda(k^i, W(t))\big), \qquad i \in [s] \tag{3.71b}$$

$$V = h \sum_{j \in [s]} b_j \widetilde{k}^j \tag{3.71c}$$

$$W(t+h) = \Lambda(V, W(t)). \tag{3.71d}$$

Evaluating after each iteration (3.71) the *averaged negative entropy* of the current assignment $W(hk)$ given in terms of (3.55) by

$$-\frac{1}{n}\mathcal{H}\big(W(kh)\big), \tag{3.72}$$

the geometric integration is stopped at a sufficient large time $T = k^* h$ as soon as (3.72) drops below a prescribed termination threshold parameter $\varepsilon$. According to Remark 3.1.1 the final labeling $W(T)$ is then characterized by state that is $\varepsilon$-close to an integral assignment $W^*$ after trivial rounding operation. In this work we will rely on constant step sizes $h > 0$ and benchmark two basic explicit schemes, explicit Euler and second order Heuns method, that are given by tableaus

$$\begin{array}{c|c} 0 & \\ \hline & 1 \end{array}$$

Euler (**FE**)

$$\begin{array}{c|cc} 0 & & \\ 1 & 1 & \\ \hline & 1/2 & 1/2 \end{array}$$

Heun-2 (**H2**)

More elaborate Runge-Kutta methods for integrating the assignment flow and their coupling with adaptive step size selection rule are evaluated in [ZSPS20].

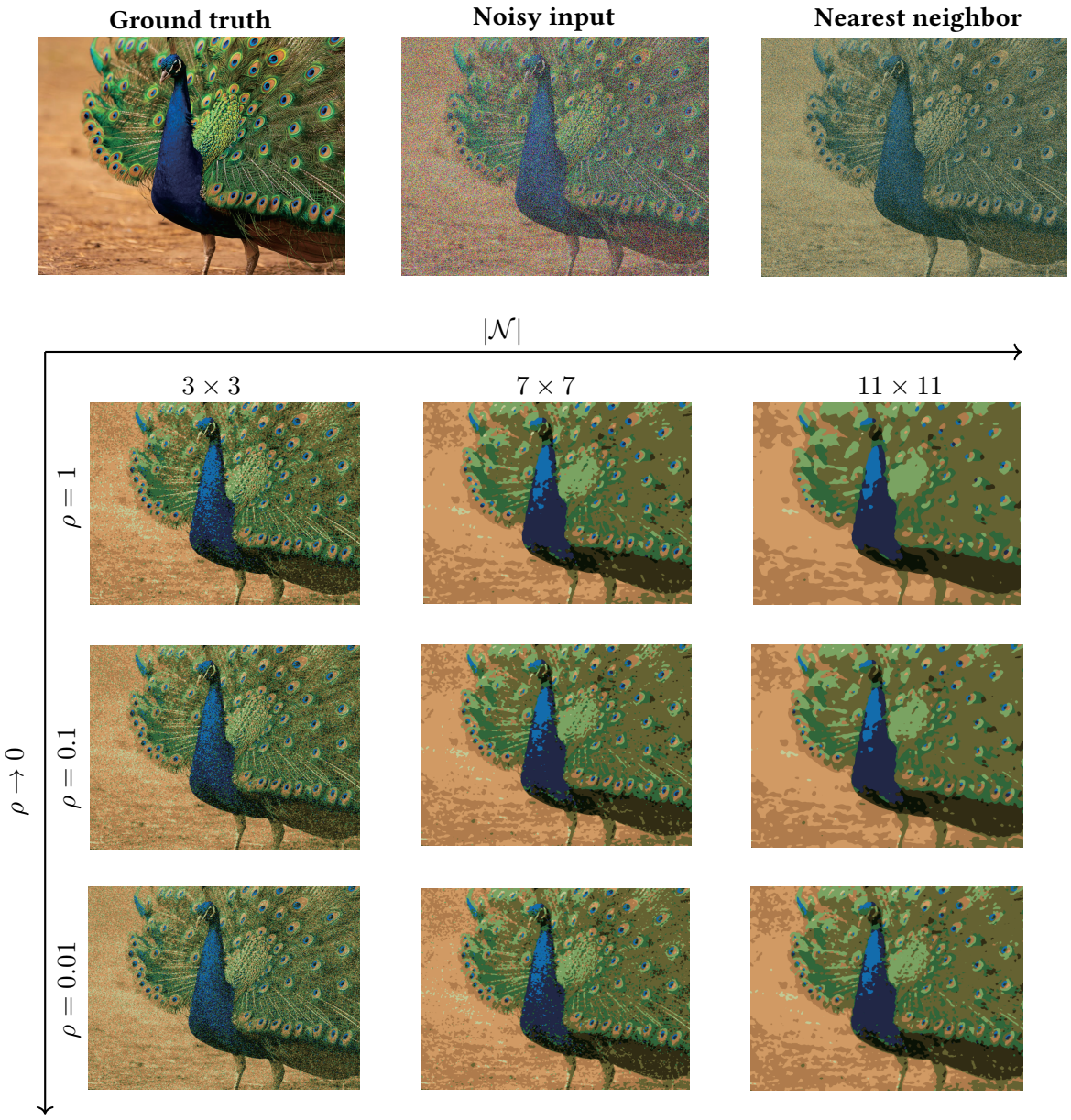


**Figure 3.4.:** Parameter influence on the labeling. **Top:** Ground truth image that is corrupted by adding gaussian noise (middle figure). The corresponding nearest neighbor assignment is depicted on the right using the set $|\mathcal{F}_*| = 10$ of predefined prototypes computed by k-means (2.113) on the RGB space. **Bottom:** Labeling results for various choices of the data selectivity parameter $\rho$ and of the spatial connectivity sizes $\mathcal{N}$ using uniform neighborhoods. Increasing the sizes of neighborhoods from left to right amplifies the regularization effect by removing locally noisy assignments. By contrast, keeping the spatial averaging connectivity fixed and decreasing the parameter $\rho$ (from top to bottom) results in an noisy over-segmentation.

# 4 Assignment Flows for Order-Constrained OCT Segmentation

## 4.1. Introduction and Motivation

Various mathematical concepts for modeling physical processes in real-world scenarios comprise an inference of a random vector $X \in K$ that is distributed according to an unknown density function $p$ on the cone

$$K = \{x \in \mathbb{R}^c \colon x_1 \leq \cdots \leq x_c\}. \tag{4.1}$$

This covers ubiquitous potential application scenarios of inferring boundaries of cell tissues, segmentation of cross-sectional coronary arterial images [EX17] or non-medical task of seismic horizon tracking for landscape analysis [YS20]. In particular, this includes clinical applications such as making diagnosis of several eye disorders, as mentioned in Figure 2.3, by revealing shape changes in the retina.

In this chapter we use the information geometric framework of assignment flows (cf. Chapter 3) as a mathematical interpretable foundation to provide theoretical support for guiding modeling design of automatic shape detection algorithms in various applications. Hereby, building upon spatial interrelation of discrete probability distributions from Section 3.2, we extend the assignment flow approach to produce integral assignments in the feasible set 4.1. This will allow us to devise algorithms for the task of order-preserving labeling by using sophisticated geometric numerical integration routines on an elementary statistical manifold that comes up with a high parallelism as opposed to ordinary graphical model approaches.

To accomplish this we pursue three key strategies:

- First, by constraining the geometry of Section 3.1 we introduce a probabilistic notion of ordered assignments along a specified axis according to the rule
$$W_{il} < W_{ik}, \qquad \text{for all} \qquad 1 \leq l < k \leq c, \quad \forall i \in I \tag{4.2}$$
which comprises a subset of assignment manifold $\mathcal{W}$.

- Secondly, we present a general way to construct regularization functionals on $\mathcal{W}$ of the form
$$E_{\text{tot}}(W) = E_{\text{data}}(W) + \lambda E_{\text{reg}}(W), \qquad W \in \mathcal{W}, \tag{4.3}$$
where $E_{\text{data}}$ incorporates the data term $W_0$ encoding the noisy observations while the second term acts as Dirichlet-like energy that takes over the regularization part by penalizing high norms of the spatial gradient $\nabla W$. The impact of regularization is controlled by the regularization parameter $\lambda > 0$.

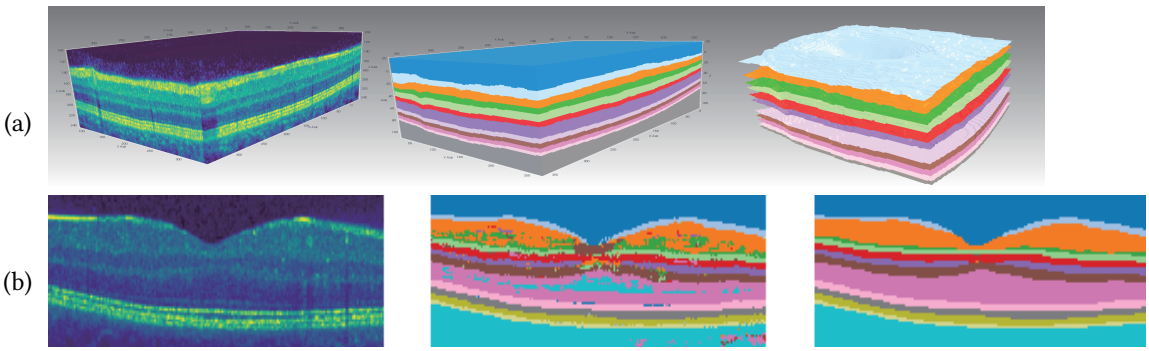


**Figure 4.1.: (a)** *Left*: Normalized view on a 3D OCT volume scan dimension $512 \times 512 \times 256$ of healthy human retina with ambiguous locations of layer boundaries. *Middle:* The resulting segmentation of 11 layers displaying the order preserving labeling of the proposed approach. *Right:* Boundary surfaces between different segmented cell layers are illustrated. **(b)**: Typical result of the proposed segmentation approach for a single B-scan of healthy retina. *Left*: raw OCT input data. *Middle*: segmentation by locally selecting the label with maximum score for each voxel after feature extraction. *Right*: segmentation by the proposed order-constrained assignment flow approach using the same extracted features.

- Finally, with the aid of compositional structure of the vector field (3.63) we show how a choice of geometric integration scheme for approximating the integral curve of
$$\dot{W} = R_W(F(W)), \qquad W(0) = W_0, \qquad F : \mathcal{W} \to T\mathcal{W} \tag{4.4}$$
allows simultaneous minimization of objective (4.3) while evolving the flow (4.4) to ordered critical points of (4.3). This results in an inference task where the regularization is not only performed in the sense of smoothing noisy data, but also includes an implicit smooth ordering of assignments.

In reference to introductory guideline into OCT imaging presented in Section 2.5.4, we apply the novel concept of ordered assignments to the specific task of automatic cell layer segmentation. To do so, we represent the volumetric OCT data 2.5.4 directly on the assignment manifold by lifting the distance matrix (3.58) underlying the feature space (3.43) through adaption of modified likelihood map (4.23). In this context, property (4.2) resembles the global geometric invariant, i.e. the natural order of cell layers along the vertical axis of each B-scan, as shown in the second row of Figure 4.1.

Apart from the ordering constraint, segmentation of layers in OCT volumes encounters the challenges

- Presence of vascular structures in outermost cell layers produces erroneous OCT-scans persisting of shadow regions and blurred appearance of layer boundaries.
- Low signal to noisy ratio of speckle noise that is difficult to handle.
- High shape variability of retinal layer boundaries along the B-scan dimension.

Compared to other methods, a key advantage of our approach lies in the exclusion of smoothness constraints which is common for the most graphical based models. Instead, including the ordering in an probabilistic manner on the assignment manifold opens a perspective for extending the smooth labeling framework from Chapter 3 to detection if pathological retinal tissues. Moreover, as opposed to state of the art approaches that mainly focus on the segmentation of 2D

slices that are taken from volumetric OCT-data sets, our ansatz analyses 3D sets. In addition to respecting the natural order of cell layers, the proposed algorithmic framework has a high amount of built-in parallelism that allows the utilization of modern graphics acceleration hardware.

We show that despite the mentioned difficulties our novel approach shows high effectiveness by selecting input features and prototypes that are capable of recovering the global retinal shape from features that comprises only local information of the voxel-wise OCT data. In this regard we present in Section 4.4.2 two classes of features (3.43) ranging from traditional covariance descriptors to convolutional neural networks. Due to hierarchical structure of the latter to guarantee locality we aim to localize the influence of feature extraction on the segmentation process by limiting the field of view. Consequently, the used features are semantically weaker than the ones computed by competing deep learning methods. However, we still achieve state of the art performance by leveraging domain knowledge.

In our pipeline, ambiguities in local features are resolved by regularization, achieving local regularity as well as physiological cell layer ordering. Figure 4.1 shows a typical volume segmentation computed by the proposed method. It illustrates how local ambiguity is caused by similar signal intensity and visual appearance of some layers which is further exacerbated by speckle noise. This ambiguity in local features is systematically resolved by leveraging the domain knowledge of local smoothness and global physiological layer order.

Finally, in Section 4.4 we demonstrate by a vast experimental study, that incorporating local information in a global measure allows to produce high-quality segmentations of OCT volumes within a range of seconds. This is in contrast to common machine learning approaches which use essentially full B-scans as input. We refer to [ZRS18] for a variant of assignment flows that takes into account global convex constraints using linear filters in the labeling space

## Organization

The remainder of this chapter is organized according to Figure 4.2 as follows:

- Related work on OCT segmentation ranging from graph based approaches probabilistic models and machine learning pipelines is reviewed in Section 4.2.

- In Section 4.3.1, we introduce the notion of *ordered assignment vectors* and provide mathematical results for extending assignments flows to include the layer ordering as a global constraint in Section 4.3.2.

- Based on Differential geometry and machine learning, respectively, we present in Section 4.4.2 two representations of OCT volumes: $(i)$: region covariance descriptor and $(ii)$: neural nets with small field of view.

- The resulting features and reports on overall proposed labeling approach are then numerically evaluated in Section 4.4.5 where a detailed comparison of performance measures is provided for two other state-of-the-art methods with available standalone software.

- Finally, in Section 4.5, we shortly discuss the access to appropriate ground truth data and the impact of feature locality underlying our approach.

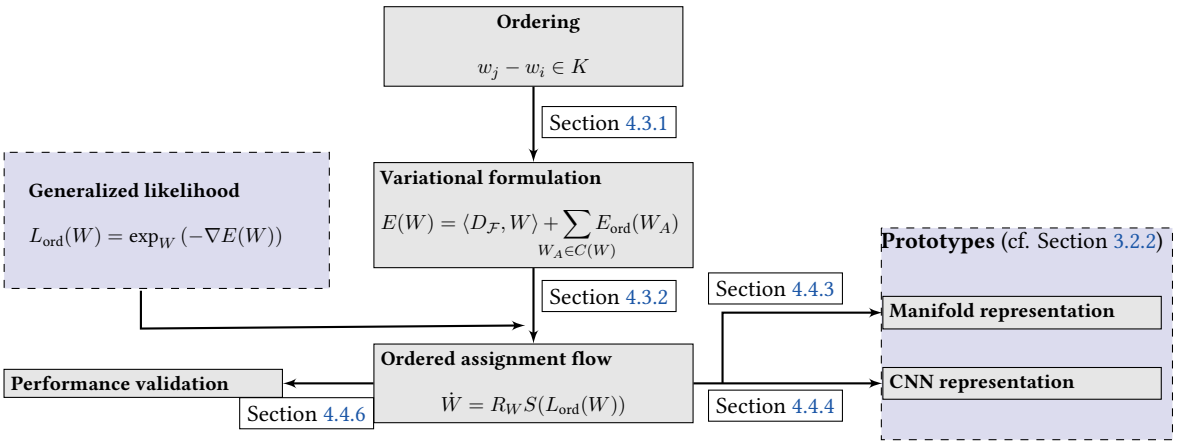


**Figure 4.2.: Organization of ordered segmentation method**: Gray boxes present the main components of proposed approach that are introduced in sections as shown by the arrows. Blue boxes indicate the key adoption of assignment flow approach for extension to ordered segmentation.

## 4.2. Related Work

Since the last two decades image processing of OCT data has become very active area of research. This includes tasks ranging from denoising OCT data by suppressing speckle noise, through classification of retinal tissues up to detection of anatomical abnormalities. Different routes are pursued to model algorithms that can deal with formidable challenges appearing in the OCT-data. On the one hand, graph based approaches and variational methods are pushed by the progress made in development of tailored optimization techniques that take into account the natural layer ordering within the retina (cf. Figure 2.1). On the other hand, recent advances in machine learning of neuronal networks uncovered a new branch of fast computational techniques for effective OCT-processing. Here, we briefly review the current state of the art approaches for classification of human retina originating from the broad research fields of graphical models, variational methods and machine learning.

### 4.2.1. Graphical Models

The first mathematical access to the problem is provided by the theory of graphical models which transforms the segmentation task into an optimization problem of minimizing a predefined cost functional with integrated hard pairwise interaction constraints between nodes of the graph. Starting with [KXCS06] and [HAW+07], simultaneous retina layer detection attempts were made by finding an $s$-$t$ minimum graph cut. [GAW+09] further extended this approach with a shape prior modeling layer boundaries. The methods benefit from low computational complexity, but are lacking of robustness in the presence of speckle and therefore require additional preprocessing steps. Along this line of reasoning, [AAL+10] used a two stage segmentation process by applying anisotropic diffusion in a preprocessing step and consequently segmenting outer retina layers using graphical models. Similarly, [KRAS13] proposed to use specific distances based on diffusion maps which are computed by coarse graining the original graph. However, increased performance for noisy OCT data gained by regularizing in this way comes at the cost of introducing bias in the preprocessing step which in turn inpairs robustness in settings with medical pathologies.

Motivated by [SBG+13], [DCA+13] comes up with a circular shape prior for segmentation of 6 retinal layers by incorporating soft constraints which are more suitable for the robust detection of pathological retina structures. Following this line of research utilizing effective dynamical programming routines from graph theory, the authors in [CLN+10] present an automatic layer boundary segmentation method for detecting up to 8 intraretinal surfaces. An extension of this method to detection of AMD (cf. Section 2.5.1) pathologies is applied in [CIO+12]. [CAM+15] relies on a graphical model approach as a postprocessing step after applying a supervised kernel regression classification with features extracted according to [QLD+10]. However, accuracy of the aforementioned approaches builds upon prior knowledge of healthy retina configuration and upon complex processing procedures making it intractable for direct application on 3D (OCT) volumes. To tackle this problem, [RSS14] reduced the overall complexity by a parallelizable segmentation approach based on probabilistic graphical models with global low-rank shape prior representing interacting retina tissues surfaces. While the *global* shape prior works well for non-pathological OCT data, it cannot be adapted to the broad range of variations caused by *local pathological* structure resulting in a inherent limitation of this approach. Here we refer to [RDS17] for possible adaption of the probabilistic approach [RSS14] to pathological retina detection.

### 4.2.2. Variational Methods

Another category of layer detection methods focus on minimizing an energy functional to express the quantity of interest as the solution to an optimization problem. To this class of methods for retina detection level set approaches have proven to be particularly suitable by encoding each retina layer as the zero level sets of a certain functional. [YHSS11] introduces a level set method for minimizing an active contour functional supported by a multiphase model presented in [CV01] as circular shape prior, to avoid limitations of hard constraints as opposed to graphical model proposed by [GAW+09]. [DTG+15] suggests the approach to model layer boundaries with a mixture of Mumford Shah and Vese and Osher functionals by first preprocessing the data in the Fourier domain. A capable level set approach for joint segmentation of pathological retina tissues was reported in the work of [NVd+17]. However, due to the involved hierarchical optimization, their method is computationally expensive. One common downside of the above algorithms are their inherent limitations to only include local notions of layer ordering, making their extension to cases with pathologically caused retina degeneracy a difficult task.

### 4.2.3. Machine Learning

Besides their good segmentation performance, the effectiveness of variational and graph based approaches is heavily biased towards a proper selection of hand crafted features for defining the underlying cost functional. This makes these methods prone to generalization to unseen outliers such as pathological appearance of the retina along with a manual timeconsuming restruction of the algorithm. In this context, machine learning based approaches serve as a powerful tool to tackle this problems by providing an outstanding performance and broad application field on image classification, speech recognition and medical image analysis tasks. Specifically, for retinal surface detection Zawadski et al. [ZFW+07] proposes an semiautomatic algorithm by incorporating a variant of support vector machine that is shown to be robust against speckle noise. Vidal et al. [VMN+18] elaborated 312 distinct features out from the OCT data in combination with a support vector machine to tackle the classification of retinal boundaries.

To address the task of cell layer segmentation in a purely data driven way much recent work has focused on the use of deep learning methods which have the key property of acquiring the most significant features out from the data. The U-net architecture [RFB15] has proven influential in this domain because of its good predictive performance in settings with limited availability of training data. Multiple modifications of U-net have been proposed to specifically increase its performance in OCT applications [RCK+17; LCF+19]. This includes the recent approach [HZL+22] to detect retinal surfaces by proposing a model that combines graph theory and a U-net structure for parametrization of cost functional for each layer. The inference of retinal layer boundaries is then realized by optimization of a total surface cost functional on a graph with additional linear constants accounting for the surfaces interaction by means of primal-dual-Interior-Point-Method. A comparative study of eight most notable U-net models for retinal boundary detection is performed in [KAR+22]. The common methods largely rely on convolutional neural networks trained on large-scale data sets to predict layer segmentations for individual B-scans which are subsequently combined to full volumes. Hereby, the network weights are trained by optimization of a specified loss function. After training taking raw OCT data as input, output of CNN is a probabilistic map that assign to each node a probability distribution over retinal layers which encode voxel-layer belonging. These methods have also been used as part of a two-stage pipeline where additional prior knowledge such as local regularity and global order of cell layers along a spatial axis is incorporated through graph-based methods [FCW+17] or a second machine learning component [HCL+19]. For the particular task of differentiating between retinal tissues and fluid region caused by pathological vascular edema the authors in [HFTC22] rely on a encoder decoder structure for approaching the corresponding binary classification problem.

To support the high parametrization accuracy of neuronal nets from machine learning based models by effective constraint treatment of graph based methods, [HLC+21] developed Embedded Residual Neural Net retinal tissue segmentation that include a graph search on directed graph as postprocessing to guarantee the layer smoothness. In summery, besides each of the above methods provides good segmentation accuracy on healthy data sets, their potential extension to volumetric 3D OCT data sets persisting of retinal abnormalities remains limited. A further limitation shared by these methods when applied to 3D retina segmentation is the lack of publicity available annotated data sets which comes at the cost of achieved performance. Moreover, in order to learn the global shape of volumetric 3D tissues requires a high amount of hierarchical layer composition that results a vast number of parameters not computable with available GPU hardware. In this thesis we show in the following section how this challenges can be remedied by formulating a *natural* ordering prior directly on the assignment manifold that allow an utilization of low parametrized networks for local feature representation of OCT volumes.

## 4.3. Ordered Layer Segmentation

In this section, we work out an extension of the assignment flow (Section 3.2.2) which is able to respect the order of cell layers as a global constraint while remaining in the same smooth geometric setting. In particular, schemes from Section 3.2.3 for numerical integration still apply to the novel variant.

### 4.3.1. Ordering Constraint

With regard to segmenting OCT data volumes, the order of cell layers is crucial prior knowledge. In this thesis we focus on segmentation of the following 11 retina layers: Retinal Nerve

Fiber Layer (RNFL), Ganglion Cell Layer (GCL), Inner Nuclear Layer (INL), Outer Plexiform Layer (OPL), Outer Nuclear Layer (ONL), two photoreceptor layers (PR1, PR2) separated by the External Limiting Membrane (ELM), Choriocapillaris (CC) and the Retinal Pigment Epithelium (RPE) together with the Choroid Section (CS). Figure 4.3 also contains positions for the Internal Limiting Membrane (ILM) and Bruch's membrane Membrane (BM).

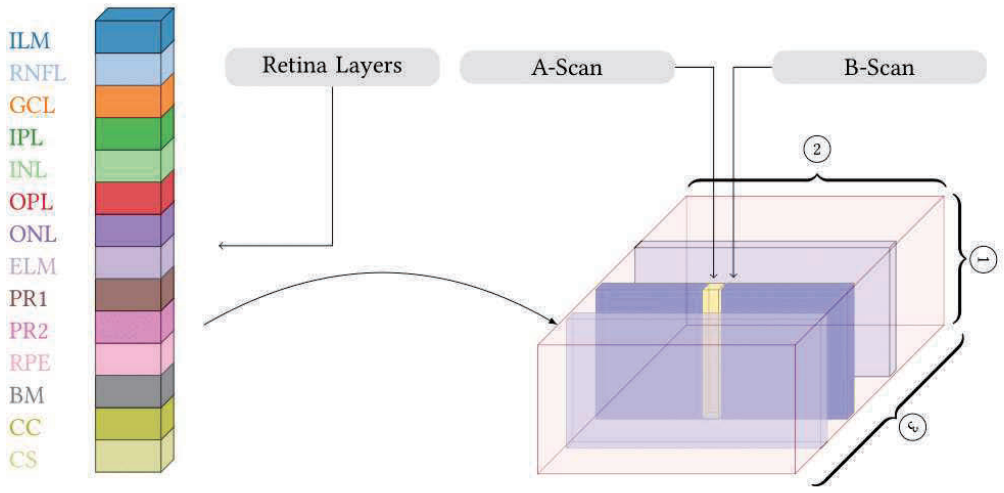


**Figure 4.3.:** OCT volume acquisition: ① is the A-scan axis (single A-scan is marked yellow). Multiple A-scans taken in rapid succession along axis ② form a two-dimensional B-scan (single B-scan is marked blue). The complete OCT volume is formed by repeating this procedure along axis ③. A list of retina layers that we expect to find in every A-scan is shown on the left.

In the following, we assume prototypes $f_j^* \in \mathcal{F}, j \in [n]$ in some feature space $\mathcal{F}$ to be indexed such that ascending label indices reflect the physiological order of cell layers.

## Ordering via Graphical Models

To incorporate this knowledge into the geometric setting of Section 3.2.2, we require a smooth notion of ordering. To do so, we first focus on a discrete instance of (4.3) given by a graphical model on a graph $\mathcal{G} = (\mathcal{V}, \mathcal{E})$

$$E_{\mathcal{G}}(W, M) = \sum_{i \in \mathcal{V}} \langle W_i, \Theta_i \rangle + \theta \sum_{ij \in \mathcal{E}} \langle M_{ij}, \Theta_{ij} \rangle, \tag{4.5}$$

where $\Theta_i, i \in [N]$ are the unary costs defined in terms of the distance matrix $D_i$, encoding the data, and $\Theta_{ij}$ are the costs prescribed by the ordering constraint (4.2) through fixed matrix

$$\widetilde{\Theta} = \begin{pmatrix} 0 & 0 & 0 & \cdots & 0 & 0 \\ 1 & 0 & 0 & \cdots & 0 & 0 \\ 1 & 1 & 0 & \cdots & 0 & 0 \\ \vdots & \vdots & \ddots & \vdots & \vdots & \\ 1 & 1 & 1 & \cdots & 0 & 0 \\ 1 & 1 & 1 & \cdots & 1 & 0 \end{pmatrix} \qquad \forall ij \in \mathcal{E}. \tag{4.6}$$

Determining the labeling $W^*$ with minimal cost amounts to minimize of (4.5) over all possible integral assignments $W \in \{0, 1\}^{|\mathcal{V}| \times c}$ and couplings $M_{ij} \in \mathbb{R}^{c \times c}$ for $i, j \in \mathcal{V}$ subject to ordering

constraint imposed along the $c$-axis

$$\mathcal{A}\mathrm{vec}(M_{ij}) - (W_i, W_j)^T = 0, \quad M_{ij} \geq 0 \qquad \forall ij \in \mathcal{E}, \tag{4.7}$$

with matrix $\mathcal{A}$ defined in accordance with respective row and column sums of a matrix $M \in \mathbb{R}^{c\times c}$

$$\mathcal{A} = \begin{pmatrix} I_c \otimes \mathbb{1}^T \\ \mathbb{1}^T \otimes I_c \end{pmatrix}. \tag{4.8}$$

The corresponding labeling adhering to the ordering constraint (4.7) is then characterized by a node-wise integral state $W^*$ attaining minimum of $E_{\mathcal{G}}$ via

$$l_i^* = \mathrm{argmax}_{j\in[c]} W_{ij}, \qquad \forall j \in \mathcal{V}. \tag{4.9}$$

In addition, taking into account the combinatorial nature of problem (4.5) where each $W_i$ is assumed to be a unit vector referring to assigned label, the ensemble of constraints given by the first equation in (4.7) reveals insights on the form of matrix $M_{ij}$

$$M_{ij}\mathbb{1}, \quad M_{ij}^T\mathbb{1} \in \{e_1, \ldots, e_c\}, \qquad \forall i, j \in \mathcal{V}, \tag{4.10}$$

i.e. $\mathrm{vec}(M_{ij})$ is a discrete probability distribution on $\Delta_{c^2}$.

## Geometric Ordering Constraint

A major limitation of minimizing energy (4.5) is the exponential nature of the optimization task, i.e. the size $c^{|\mathcal{V}|}$ of all possible labeling outcomes scales exponentially with respect to number of nodes in the graph $\mathcal{V}$. This constitutes a NP-hard problem [Coo90] that is intractable in practice. A way out of this computational bottleneck yields a proper construction of an cyclic graph $\mathcal{G}$ which allows application of efficient dynamical programming algorithm that comes with a linear complexity in the problem size. However, this alternative leads to nonsmooth layer boundaries outcomes which require incorporation of additional smoothness constraints and increase the problem complexity. Moreover, when modeling $3D$ problems acyclic graph structure negatively affects the expressive power of the model which comes at the cost of resulting accuracy. To bypass this challenges, in this thesis we follow a different strategy by instead building upon a tight approximation of problem (4.5) that relinquish a novel characterization of ordering through a representation theorem on a pointed convex cone as pioneered in [Bol19]. Dropping the integral assumption on $W$ by allowing simplex valued assignments $W_i \in \Delta_c$ we relax feasible set of NP-hard optimization of graphical model (4.5) followed by tightening the ordering constraint via $\theta \to \infty$ leading to a linear program

$$\min_{W\in\mathcal{Q}} \langle W, D\rangle, \quad \text{subject to} \quad \langle \widetilde{\Theta}, M\rangle = 0 \quad \text{and} \quad (4.7) \tag{4.11}$$

The feasible set $\mathcal{Q}$ in (4.11) is now directly related to the map $M \in \mathbb{R}^{|\mathcal{E}|\times c\times c}$ that for each $ij \in \mathcal{E}$ needs to satisfy a generalized version of (4.10) with respect to a pair of marginals $(w_i, w_j)$, i.e.

$$\Pi(w_i, w_j) = \{A \in \Delta_{c^2} : A\mathbb{1} = w_i, A^T\mathbb{1} = w_j\}. \tag{4.12}$$

In particular, due to $\frac{1}{c}\mathbb{1}_n \otimes \mathbb{1}_c \in \mathcal{Q}$ the linear program (4.11) is well posed and there exists an exhaustive ensemble of algorithms that yields a solution that satisfies the ordering constraints in a polynomial time. Despite the resulting numerical benefits of approaching the ordering problem by optimizing (4.11) finding a solution to linear program (4.11) is only feasible in the full extent of small problem sizes that prohibits real life applications. In addition, the postprocessing rounding of obtained solution $W$ to an integral state $W^*$ poses a challenging problem as it is not clear a-priory if $W^*$ still satisfies the ordering constraint. The following Theorem provides an equivalent representation of the feasible set $\mathcal{Q}$ that is key to subsequent approximation of the graphical model problem by means the assignment flows 3.2.2.

**Theorem 4.3.1.** *For each edge $(ij)$ an a given marginal $w_i \in \Delta_c$ the set of all $w_j \in \Delta_c$ such that $(w_i, w_j) \in \mathcal{Q}$ defines a pointed convex cone*

$$\{\omega_j \colon (w_i, w_j) \in \mathcal{Q}\} = w_i + K, \qquad K = \{By \colon y \in \mathbb{R}^c_+\} \tag{4.13}$$

*with the matrix*

$$B = \begin{pmatrix} -1 & & & & \\ 1 & -1 & & & \\ & 1 & \ddots & & \\ & & \ddots & -1 & \\ & & & 1 & -1 \end{pmatrix} \in \mathbb{R}^{c \times c}. \tag{4.14}$$

*Proof.* See [Bol19]. □

Based on Theorem 4.3.1 we are ready to introduce a smooth notion of ordering.

**Definition 4.3.1** (Ordered Assignment Vectors)**.** A pair of voxel assignments $(w_i, w_j) \in \mathcal{S}^2$, $i < j$ within a single A-scan is called *ordered*, if $w_j - w_i \in K = \{By \colon y \in \mathbb{R}^c_+\}$.

For each $w_i$ the geometric ordering constraint adhering to Definition 4.3.1 restrict the probability simplex to evolve on the specific subset of $\mathcal{S}$. See Figure 4.4 for visualization for the particular case $c = 3$. More importantly, in view of Definition 4.3.1 for a pair $(\omega_i, \omega_j)$ to satisfy the ordering constraint, one needs to check if their difference belongs to the cone $K$. In practice this condition can be verified more conveniently by taking into account the parametrization of the cone by positive vectors $y \in \mathbb{R}^c_+$ and instead checking if the resulting entries of $B^{-1}(\omega_j - \omega_i)$ are positive.

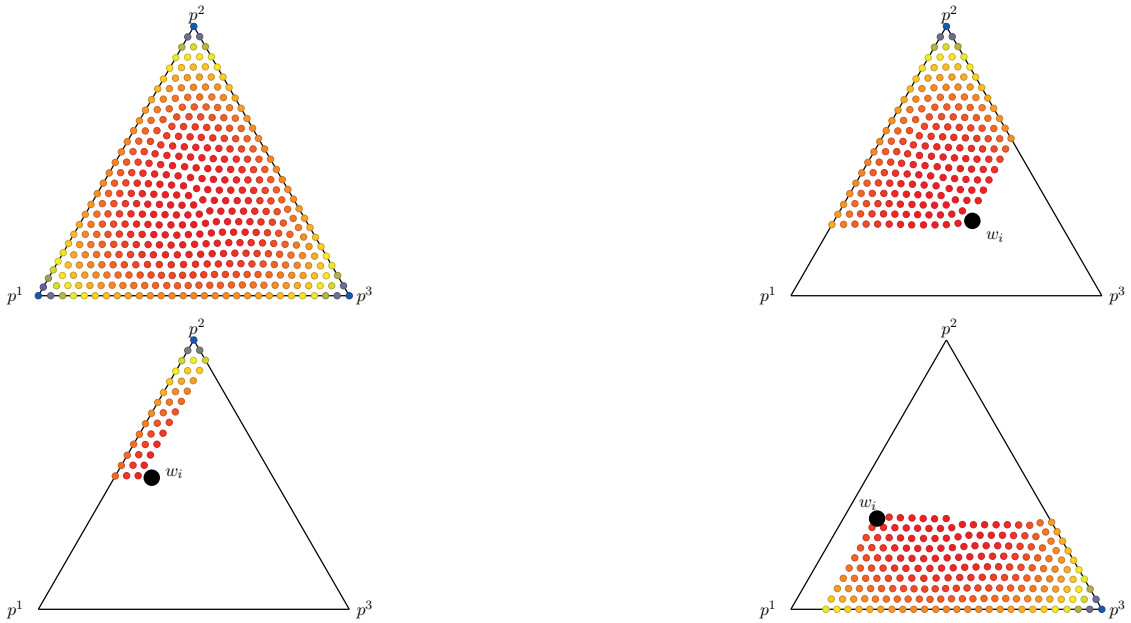


**Figure 4.4.:** Illustration of valid probability vectors relative to a given state $w_i$ according to definition 4.3.1. The color encodes the negative entropy (cf. 3.1). **From top left to right bottom**: Probability simplex for $c = 3$ overlayed by uniformly spaced nodes sampled as in [BDD+21]. Each plot shows remaining domain of the simplex satisfying the geometric ordering constraint given by pairs $(w_j, w_i)$ with respect to fixed reference assignment $w_i$ shown in black.

This new continuous ordering of probability distributions is consistent with discrete ordering of layer indices in the following way.

**Lemma 4.3.1.** *Let $w_i = e_{l_1}$, $w_j = e_{l_2}$, $l_1, l_2 \in [c]$ denote two integral voxel assignments. Then $w_j - w_i \in K$ if and only if $l_1 \leq l_2$.*

*Proof.* Appendix A.2, proof of Lemma 4.3.1. □

Recapitulating the queue of ordering constraints (4.7) at the beginning of this chapter, the continuous notion of order preservation put forward in Definition 4.3.1 is directly related to the discrete graphical model (4.5) consisting of two nodes connected by a single edge. The order constrained image labeling problem on this graph can be written as the integer linear program

$$\min_{W \in \{0,1\}^{2\times c}, M \in \Pi(w_i, w_j)} \langle W, D \rangle + \theta \langle Q - I_c, M \rangle \tag{4.15}$$

where $\Pi(w_i, w_j)$ denotes the set of coupling measures for marginals $w_i$, $w_j$ and $\theta \gg 0$ is a penalty associated with violation of the ordering constraint. By taking the limit $\theta \to \infty$ we find the more tightly constrained problem

$$\min_{W \in \{0,1\}^{2\times c}, M \in \Pi(w_i, w_j)} \langle W, D \rangle \qquad \text{s.t. } \langle Q - I_c, M \rangle = 0 \,. \tag{4.16}$$

Its feasible set has an informative relation to Definition 4.3.1 examined in Proposition 4.3.1.

**Lemma 4.3.2.** *Let $M \in \mathbb{R}^{c\times c}$ be an upper triangular matrix with non-negative entries above the diagonal and non-negative marginals*

$$M \mathbb{1}_c \geq 0, \qquad M^\top \mathbb{1}_c \geq 0 \,. \tag{4.17}$$

*Then there exists a modified matrix $M^1$ with the same properties such that $M^1 \geq 0$.*

*Proof.* Appendix A.2, proof of Lemma 4.3.2. □

In particular, each upper triangular matrix $M$ can be relaxed through performing elementary algebraic operations entailed in proof of Lemma 4.3.2 to satisfy a constraint restrictive form of (4.17) and (4.7) which play a key role in the derivation of the main result of this chapter that is presented next.

**Proposition 4.3.1.** *A pair of voxel assignments $(w_i, w_j) \in \mathcal{S}^2$ within an single A-scan is ordered if and only if the set*

$$\Pi(w_i, w_j) \cap \{M \in \mathbb{R}^{c\times c} \colon \langle Q - I_c, M \rangle = 0\} \tag{4.18}$$

*is not empty.*

*Proof.* Appendix A.2, proof of Proposition 4.3.1. □

Proposition 4.3.1 shows that transportation plans between ordered voxel assignments $w_i$ and $w_j$ exist which do not move mass from $w_{i,l_1}$ to $w_{j,l_2}$ if $l_1 > l_2$. This characterizes order preservation for non-integral assignments as put forward in Definition 4.3.1.

### 4.3.2. Ordered Assignment Flow

Likelihoods as defined in (3.59) emerge by lifting $-\frac{1}{\rho} D_{\mathcal{F}}$ regarded as Euclidean gradient of $-\frac{1}{\rho}\langle D_{\mathcal{F}}, W \rangle$ to the assignment manifold. It is our goal to encode order preservation into a generalized likelihood matrix $L_{\text{ord}}(W)$. To this end, consider the assignment matrix $W \in \mathcal{S}^N$ for a single A-scan

consisting of $N$ voxels. We define the related matrix $Y(W) \in \mathbb{R}^{N(N-1)\times c}$ with rows indexed by pairs $(i,j) \in [N]^2$, $i \neq j$ in fixed but arbitrary order. Using the matrix $Q$ defined by (A.6), let the rows of $Y$ be given by

$$Y_{(i,j)}(W) = \begin{cases} Q(w_j - w_i) & \text{if } i > j \\ Q(w_i - w_j) & \text{if } i < j \end{cases} . \tag{4.19}$$

By construction, an A-scan assignment $W$ is ordered exactly if all entries of the corresponding $Y(W)$ are nonnegative. This enables to express the ordering constraint on a single A-scan in terms of the energy objective

$$E_{\text{ord}}(W) \;=\; \sum_{(i,j)\in[N]^2,\; i\neq j} \phi(Y_{(i,j)}(W)) \,. \tag{4.20}$$

where $\phi\colon \mathbb{R}^c \to \mathbb{R}$ denotes a smooth approximation of $\delta_{\mathbb{R}^c_+}$. In our numerical experiments, we choose

$$\phi(y) = \left\langle \gamma \exp\left(-\frac{1}{\gamma} y\right), \mathbb{1} \right\rangle \tag{4.21}$$

with a constant $\gamma > 0$. Suppose a full OCT volume assignment matrix $W \in \mathcal{W}$ is given and denote the set of submatrices for each A-scan by $C(W)$. Then order preserving assignments consistent with given distance data $D_{\mathcal{F}}$ in the feature space $\mathcal{F}$ are found by minimizing the energy objective

$$E(W) = \langle D_{\mathcal{F}}, W \rangle + \sum_{W_A \in C(W)} E_{\text{ord}}(W_A) \,. \tag{4.22}$$

Specifically, in view of distance vector field $D_{\mathcal{F}}$ in (4.22) we adopt two instances of metric data spaces $(\mathcal{F}, d_{\mathcal{F}})$ underlying (3.42):

- Riemannian manifold $(\mathcal{P}_d, d_g)$ of positive definite matrices of dimension $d \times d$, with Riemannian metric $g$ and Riemannian distance $d_g$ as specified in section 4.4.
- Convolutional neural net with small field of view with distance vector $D_{\mathcal{F}}$ determined by the output score of the last layer as detailed in Section 4.4.4.

We consequently define the generalized likelihood map

$$\begin{aligned} L_{\text{ord}}(W) &= \exp_W\left(-\nabla E(W)\right) \\ &= \exp_W\left(-\frac{1}{\rho} D_{\mathcal{F}} - \sum_{W_A \in C(W)} \nabla E_{\text{ord}}(W_A)\right) \end{aligned} \tag{4.23}$$

and specify a corresponding assignment flow variant.

**Definition 4.3.2** (Ordered Assignment Flow)**.** The dynamical system

$$\dot{W} = R_W S(L_{\text{ord}}(W)), \qquad W(0) = \mathbb{1}_{\mathcal{W}} \tag{4.24}$$

evolving on $\mathcal{W}$ is called the *ordered assignment flow*.

Besides adopting this more general definition, the remaining components of the assignment flow 3.2.2 are kept unchanged so that all geometric integration schemes still apply. As a consequence applying known numerical schemes [ZSPS20] for approximately integrating the flow (4.24), we find a class of discrete-time image labeling algorithms which respect the physiological cell layer ordering in OCT data. In chapter 4.4, we benchmark the simplest instance of this class, emerging from the choice of geometric Euler integration. Moreover, building upon the

assignment flow framework allows to work with input data from any metric space, making our model agnostic to the choice of feature extraction and suitable as plug-in replacement in diverse pipelines.

## 4.4. Experimental Results

To access the effectiveness of our approach for segmenting retinal tissues with ordered assignment flow introduced section 4.3.1, we next perform a range of numerical experiments on volumetric OCT scans and provide exhaustive performance comparison to various state of the art approaches with respect to a queue of evaluation metrics described next.

### 4.4.1. Data, Performance Measures

#### OCT-Data

In the following sections, after introducing key terminology in volumetric OCT data we describe experiments performed on a set of OCT volumes depicting the intensity of light reflection in chorioretinal tissues centered around the fovea. The scans were obtained using a spectral domain OCT device (Heidelberg Engineering, Germany) for multiple patients at a variety of resolutions by averaging various registered B-scans which share the same location in order to reduce speckle noise. This is representative of the fact that different resolutions may be desirable in clinical settings at the preference of medical practitioners. In the following, we always assume an OCT volume in question to consist of $N_B$ B-scans, each comprising $N_A$ A-scans with $N$ voxels and use the term surface to refer to the set of voxels located at the interface of two retina layers. See Fig. 4.3 for a schematic illustration of the data acquisition process.

In the present work, we use a private dataset of 3D OCT volume scans provided by Heidelberg Engineering GmbH which we split into 82 volumes for training and 8 volumes for testing. In particular, the test set contains scans from multiple different patients without any observable pathological retina changes. See Appendix A.4 for a detailed list of volume sizes and resolutions along each axis.

Fig. 4.5 demonstrates the typical organization of a 3D-OCT volume acquired by scanning healthy human retina using an OCT device. B-Scans are indicated as blue lines placed in the Fundus image on the left. The particular B-Scan marked in red is depicted in the middle of Fig. 4.5. This illustrates the typical artifacts and corrupted layer intensities of the OCT volume. The right plot depicts the noisy signal along an A-scan indicated by a yellow vertical line which underpins the difficulty of segmenting the underlying data sets.

#### Reference Methods

To assess the segmentation performance of our proposed approach we compare ourselves to state of the art retina segmentation methods presented in [RSS14] and [KXCS06] which are applicable for both healthy and pathological patient data. In particular, we prefer these reference methods over [DCA+13], [SBG+13] and [GAW+09] because available implementations of the latter are limited to the segmentation of up to 9 retina layers. For both reference methods, we use the software implementation of their authors without any additional tuning or retraining.

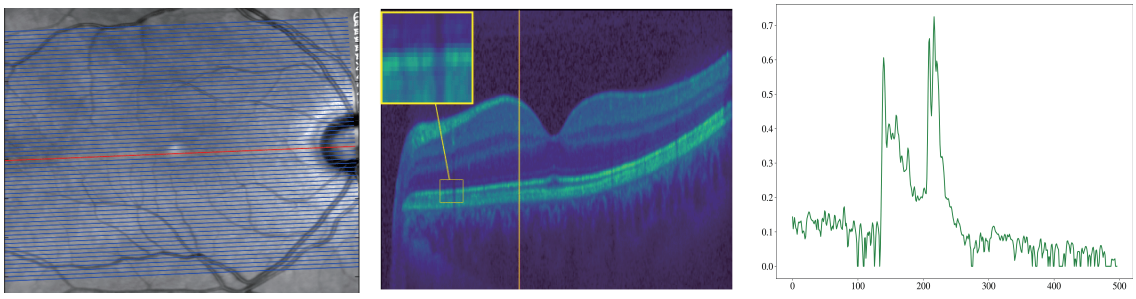


(a) (b) (c)

**Figure 4.5.: Left**: En-face view on the volumetric OCT data superimposed by parallel blue lines which represent the location of 61 B-scans within the volume. The red line indicates the position of a B-scan shown in the center image. **Center**: The enlarged view on a B-scan depicts typical artifacts such as shadow regions and speckle noise. **Right**: The gray value intensity of a single vertical A-scan located near the Fovea region. This A-scan is highlighted by a yellow line in the enlarged B-scan (center image). Noisy intensity variations along the A-scan indicate the difficulty of automatically extracting retinal tissue boundary positions.

***IOWA Reference Algorithm:*** A well-known graph-based approach to segmentation of macular volume data was developed by the Retinal Image Analysis Laboratory at the Iowa Institute for Biomedical Imaging [KXCS06; AGS10a; GAW+09]. The problem of localizing cell layer boundaries in 3D OCT volumes is posed and ultimately transformed into a minimum $st$-cut problem on a non-trivially constructed graph $G$. To this end, a distance tensor $D_k \in \mathbb{R}^{N_B \times N_A \times N}$ is formed in a feature extraction step for each boundary $k \in [c-1]$. This encodes $c-1$ separate binary segmentation problems on a geometric graph $G_k$ spanning the volume. In each instance, voxels are to be classified as either belonging to boundary $k$ or not belonging to boundary $k$. By utilizing a (directed) neighborhood structure on each $G_k$, smoothness constraints are introduced and regulated via user-specified stiffness parameters. To model interactions between different boundaries, the graphs $G_k$ are combined to a global graph $G$, introducing additional edges between them. The latter set up constraints on the distance between consecutive boundaries within each A-scan which can be used to enforce physiological ordering of cell layers. On $G$, the problem of optimal boundary localization takes the form of minimal closed set construction which is in turn transformed into a minimum $st$-cut problem for which standard methods exist. Their standalone software is freely available for research purposes[1].

***Probabilistic Model:*** [RSS14] proposed a graph-based probabilistic approach for segmenting OCT volumes for given data $y$ by leveraging the Bayesian ansatz

$$p(y, s, b) = p(y|s)p(s|b)p(b) \ . \tag{4.25}$$

Here, the tensor $b \in \mathbb{R}^{N_B \times N_A \times (c-1)}$ contains real-valued boundary positions between retina layers and $s$ denotes discrete (voxel-wise) segmentation. The appearance terms $p(y|s)$, $p(s|b)$ and $p(b)$ represent data likelihood, Markov random field regularizer and global shape prior respectively. In order to approximate the desired posterior

$$p(b, s|y) = \frac{p(y|s)p(s|b)p(b)}{p(y)} \ , \tag{4.26}$$

a variational inference strategy is employed. This aims to find a tractable distribution $q$ decoupled

[1] see https://www.iibi.uiowa.edu/oct-reference

into

$$q(b,s) = q_b(b)q_s(s) \tag{4.27}$$

which is close to $p(b,s|y)$ in terms of the relative entropy $\mathrm{KL}(q\,|\,p)$. The shape prior $p(b)$ is learned offline by maximum likelihood estimation in the space of normal distributions using a low-rank approximation of the involved covariance matrix. Ordering constraints

$$1 \leq s_{1,ij} \leq s_{2,ij} \leq \cdots \leq s_{c-1,ij}, \quad ij \in [N_B] \times [N_A] \tag{4.28}$$

are enforced for the discrete segmentation $s$ and are not enforced for the continuous boundaries $b$. This is in contrast to the proposed model which integrates the ordering of retina layers by adding a cost function (4.18) penalizing the overall deviation of soft assignments during numerical integration of (3.63) from the subspace of probability distributions satisfying (4.3.1). The method comes along with a standalone software which is freely available[2].

### Performance Measures

We will evaluate the computed segmentations by their direct comparison with manual annotations regarded as gold standard which were realized by a medical expert. Respective metrics are suitable for segmentation tasks that involve multiple tissue types [CCH06]. Specifically, we report the mean DICE similarity coefficient [Dic45] for each segmented cell layer.

**Definition 4.4.1.** ***(DICE)*** Given two sets $A, B$ the *DICE similarity coefficient* is defined as

$$\mathrm{DSC}(A,B) := \frac{2|A \cap B|}{|A| + |B|} = \frac{2TP}{2TP + FP + FN} \in [0,1], \tag{4.29}$$

where $\{TP, FN, FP\}$ denotes the number of *true positives*, *false negatives* and *false positives* respectively.

The DICE similarity coefficient quantifies the region agreement between computed segmentation results and manually labeled OCT volumes which serve as ground truth. High similarity index $\mathrm{DSC}(A,B) \approx 1$ indicates large relative overlap between the sets $A$ and $B$. This metric is well suited for average performance evaluation and appears frequently in the literature (e.g. [CAM+15], [YHSS11] and [NVd+17]). It is closely related to the positively correlated Jaccard similarity measure [Jac08] which in contrast to (4.29) is more strongly influenced by worst case performance.

In addition, we report the mean absolute error (MAE) of computed layer boundaries used in [RSS14] and [GAW+09] to make our results more directly comparable to these references.

**Definition 4.4.2.** ***(Mean Absolute Error)*** For a single A-scan indexed by $ij \in [N_B] \times [N_A]$, let $e_{ij} := |g_{ij} - p_{ij}|$ denote the absolute difference between a layer boundary position $g_{ij}$ in the gold standard segmentation and a predicted layer boundary $p_{ij}$. The mean absolute error (MAE) is defined as the mean value

$$\mathrm{MAE}(g,p) = \frac{1}{N_B N_A} \sum_{ij \in [N_B] \times [N_A]} e_i \,. \tag{4.30}$$

## 4.4.2. Feature Extraction

In particular regarding the computation of corresponding prototypes (3.42b), an important aspect concerns the trade-off between respecting the Riemannian distance $d_g$ of the matrix manifold

[2] https://github.com/FabianRathke/octSegmentation

$\mathcal{P}_d$ and approximating surrogate distance functions, that enable to compute more efficiently Riemannian means of covariance descriptors while adopting their natural geometry. In addition we present an evaluation study on the prototypes distinguishing characteristics while using various metric choices for mean recovery reviewed in Section 2.3.

### Region Covariance Descriptors

To apply the geometric framework proposed in Section 2.3 we next introduce the *region covariance descriptors* [TPM06] which have been widely applied in computer vision and medical imaging, see e.g. [CS16; TS16; DFVDVM14; SSR15]. We model the raw intensity data for a given OCT volume by a mapping $I : \mathcal{D} \to \mathbb{R}_+$ where $\mathcal{D} \subset \mathbb{R}^3$ is the underlying spatial domain. To each voxel $v \in \mathcal{D}$, we associate the local feature vector $f \colon \mathcal{D} \to \mathbb{R}^{10}$,

$$f : \mathcal{D} \to \mathbb{R}^{10} \tag{4.31}$$

$$v \mapsto (I(v), \nabla_x I(v), \nabla_y I(v), \nabla_z I(v), \sqrt{2}\nabla_{xy} I(v), \dots, \nabla_{zz} I(v))^\top . \tag{4.32}$$

assembled from the intensity $I(v)$ as well as first- and second-order responses of derivative filters capturing information from larger scales following [HS87]. To improve the segmentation accuracy we combine the derivative filter responses from various scales in an computationally efficient way we first normalize the derivatives of the input volume $I(v)$ at every scale $\sigma_s$ by convolution each dimension with a 1D window:

$$\nabla_x \tilde{I}_{\sigma_s}(v) = \sigma_s^2 \frac{\partial}{\partial x} \tilde{G}(v, \sigma_s) \tag{4.33}$$

where $\tilde{G}(v, \sigma_s)$ is an approximation to a Gaussian window $\big(G(v, \sigma_s) * I\big)(v)$ at scale $\sigma_s$ as in detail described in [HS87]. Subsequently we follow the idea presented by [Lin04] by taking local maxima over scales

$$\nabla_x \tilde{I}(v) = \max_{\sigma_s} \nabla_x \tilde{I}_{\sigma_s}(v), \tag{4.34}$$

which are serving for the mapping (4.31).

By introducing a suitable geometric graph spanning $\mathcal{D}$, we can associate a neighborhood $\mathcal{N}_i$ of fixed size with each voxel $i \in [n]$ as in (3.62). For each neighborhood, we define the regularized *region covariance descriptor*

$$S_i := \sum_{j \in \mathcal{N}_i} \theta_{ij} (f_j - \overline{f_i})(f_j - \overline{f_i})^T + \epsilon I, \quad \overline{f_i} = \sum_{k \in \mathcal{N}_i} \theta_{ik} f_k, \tag{4.35}$$

as a weighted empirical covariance matrix with respect to feature vectors $f_j$. The small value $1 \gg \epsilon > 0$ acts as a regularization parameter enforcing positive definiteness of $S_i$. Diagonal entries of each covariance matrix $C_i$ are empirical variances of feature channels in (4.31) while the off-diagonal entries represent empirical correlations within the region $\mathcal{N}_i$.

## 4.4.3. Prototypes on $\mathcal{P}^d$

In view of the assignment flow framework introduced in Section 3.2.2, we interpret region covariance descriptors (4.35) as data points in the metric space $\mathcal{P}^d$ of symmetric positive definite matrices and model each retina tissue indexed by $l \in [c]$ with a random variable $S_l$ taking values in $\mathcal{P}^d$. Suppose we draw $N_l$ samples $\{S_l^k\}_{k=1}^{N_l}$ from the distribution of $S_l$. The most basic way to apply assignment flows to data in $\mathcal{P}^d$ is based on computing a prototypical element of $\mathcal{P}^d$ for each tissue layer, e.g. the Riemannian center of mass of $\{S_l^k\}_{k=1}^{N_l}$. This corresponds to directly choosing $\mathcal{P}^d$ as feature space $\mathcal{F}$ in (3.42a). We find that superior empirical results are

achieved by considering a dictionary of $K_l > 1$ prototypical elements for each layer $l \in [c]$. This entails partitioning the samples $\{S_l^k\}_{k=1}^{N_l}$ into $K_l$ disjoint subsets $\hat{S}_l^j \subseteq \{S_l^k\}_{k=1}^{N_l}$, $j \in [K_l]$ with representatives $\tilde{S}_l^j$ determined offline.

To find a set of representatives which captures the structure of the data, we minimize expected loss measured by the Stein divergence (2.105) leading to the $K$-means like functional

$$\begin{aligned} \mathbb{E}_{p_l}(\tilde{S}_l) &= \sum_{j=1}^{K_l} p(j) \sum_{S_l^i \in \hat{S}_l^j} \frac{p(i|j)}{p(j)} D_S(S_l^i, \tilde{S}_l^j), \\ p(i,j) &= \frac{1}{N_l}, p_l(j) = \frac{N_j}{N_l}\,. \end{aligned} \tag{4.36}$$

A partitioning is achieved by applying Lloyd's algorithm of the form (2.119) with $\epsilon = 1$ in conjunction with algorithm 2.2 for mean retrieval. We additionally employ the more common soft K-means like approach for determining prototypes by employing the mixture exponential family model based on Stein divergence to given data

$$p(S_l^i, \Gamma_l) = \sum_{j=1}^{K} \pi_l^j p(S_l^i, \tilde{S}_l^j)), \tag{4.37}$$

where the parameters

$$\Gamma_l = \{(\pi_l^j\}_{j=1}^K, \{\tilde{S}_l^j\}_{j=1}^K), \quad (\pi_l^1, \cdots, \pi_l^{|J|}) \in S \tag{4.38}$$

have to be adjusted to given data. The prototypes are recovered as mean parameters $S_l^{j,T}$ though the expectation maximization algorithm 2.128 that for our task boils down to the alternation of the following iterations

$$p_l(j|S_l^i, \Gamma_l^t) = \frac{\pi_l^{(j,t)} e^{-D_S(S_l^i, \tilde{S}_l^{(j,t)})}}{\sum_{k=1} \pi_l^{(k,t)} e^{-D_S(S_l^i, \tilde{S}_l^{(k,t)})}}, \tag{4.39}$$

***(Expectation step)***

followed by updating the marginals at each time step up to final time $T$

$$\pi_l^{(j,t+1)} = \sum_{i=1}^{N_j} p_l(j|S_l^i, \Gamma_l^t) \tilde{S}^{j,t} \tag{4.40}$$

$$\tilde{S}_l^{j,t+1} = \operatorname{argmin}_{S \in \mathcal{P}_d} \Big( \sum_{i=1}^{n} p(j|\Gamma_i^t) D_S(S_l^i, S) \Big). \tag{4.41}$$

***(Maximization step)***

The decision to approximate the Riemannian metric on $\mathcal{P}_d$ by the Stein divergence (2.105) can be backed up empirically. To this end, we randomly select descriptors (4.35) representing the nerve fibre layer in real-world OCT data and compute their Riemannian mean as well as their mean w.r.t. the Log-Euclidian metric (2.100) and Stein divergence (2.105). Fig. 4.7 illustrates that Stein divergence approximates the full Riemannian metric more precisely than the Log-Euclidian metric while still achieving a significant reduction in computational effort. Furthermore to evaluate the classification we extracted a dictionary of 200 prototypes for representing each retina tissue for different choice of metric and subsequently evaluated the resulting segmentation accuracy by assigning each voxel to a class containing the prototype with smallest distance using a cropped OCT Volume of size $138 \times 100 \times 40$ taken from the testing set.

Fig. 4.6 visualizes the correct classification matches for retina layers ordered by color accord-

ing to Figure 4.3. In particular, we inspect a notable gain of correct matches while respecting the Riemannian geometry (first column) as opposed to Log-Euclidean setting (third column). Regarding the approximation of (2.87) by (2.105), we are observing more effective detection of outer Photoreceptor Layer (PR1), Inner Nuclear Layer (INL) and Retinal Pigment Epithelium (RPE). Furthermore, taking a closer look at (OPL) and (ONL) we note a typical tradeoff between the number of prototypes and detection performance indicating superior retina to voxel allocation by applying (2.100), whereas the surrogate divergence metric (2.105) has the tendency to improve the accuracy while increasing the size of evaluated prototypes in contrast to flattening curves when relying on (2.102).

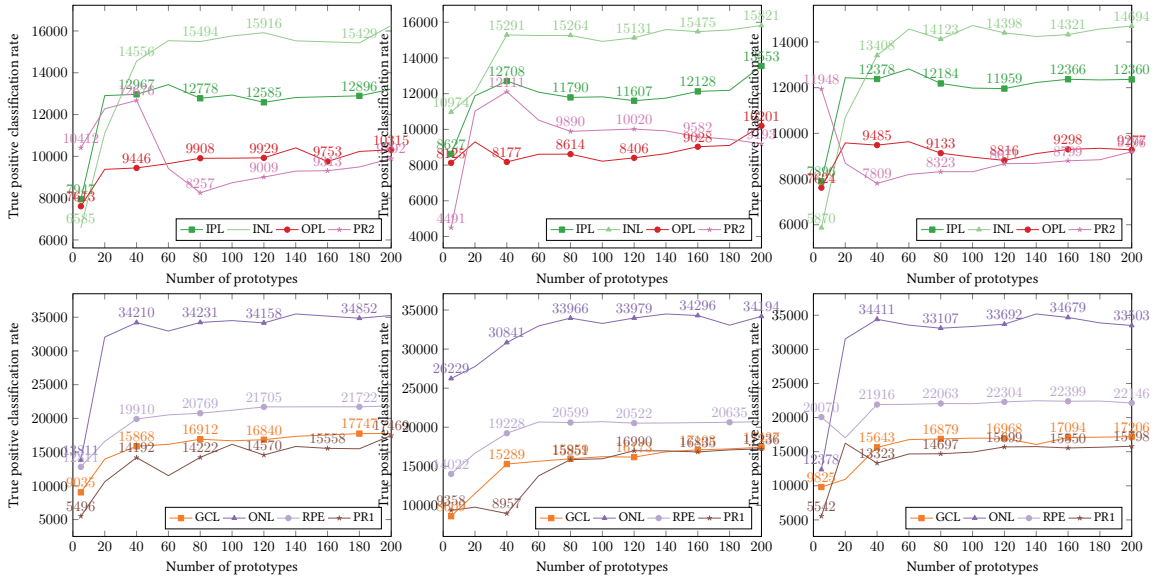


**Figure 4.6.: Top**: Metric classification evaluated on thin layers (IPL,INL,OPL,PR2). **Bottom**: Analogous metric evaluation for (GCL,ONL,PR1,RPE). **From left to right**: The number of true outcomes after direct comparison with ground truth, for the choice of the exact Riemannian geometry of $\mathcal{P}_d$, Stein divergence and Log-Euclidean distance for geometric mean computation. The results of first two columns indicate higher detection performance while respecting the Riemannian geometry of a curved manifold. Enlarging the set of prototypical covariance descriptors leads to increased matching accuracy which is in contrast to the observed flattening of matching curves when using the Log-Euclidean distance.

This illustrates a tradeoff between computational effort and labeling performance, cf. Fig. 4.7. Note that prototypes are computed offline, making runtime performance less relevant to medical practitioners. However, building a distance matrix involves computing $n \sum_{l \in [c]} K_l$ Riemannian distances resp. Stein divergences to prototypes. This still leads to a large difference in (online) runtime since evaluation of the Riemannian distance (2.87) involves generalized eigendecomposition while less costly Cholesky decomposition suffices to evaluate the Stein divergence (2.105).

Summarizing the discussed results concerning the application of Algorithm 2.1 and Algorithm 2.2, we point out that respecting the Riemannian geometry leads to superior labeling results providing more descriptive prototypes.

### 4.4.4. CNN Features

In addition to the covariance features in Section 4.4.2, we compare a second approach to local feature extraction based on a convolutional neural network architecture. For each node $i \in [n]$,

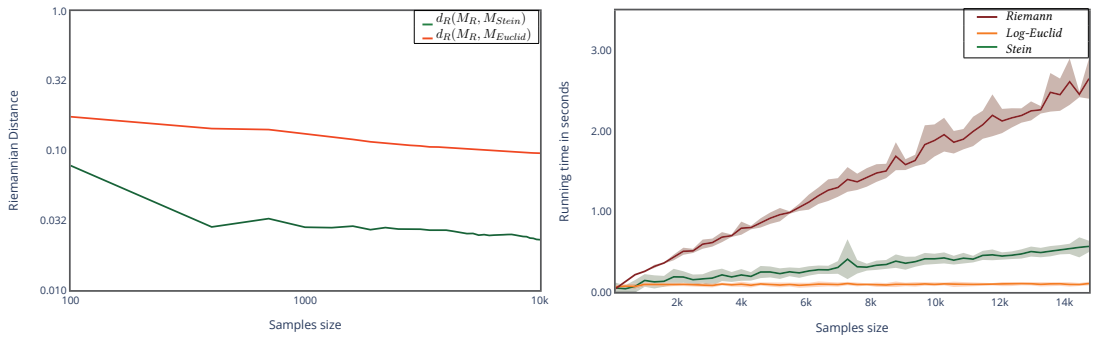


**Figure 4.7.: Left**: Deviation of the geometric means computed using the Log-Euclidian metric and Stein divergence, respectively, from the true Riemannian mean. **Right**: Runtime for geometric mean computation using the different metrics. All evaluations were performed on a randomly chosen subset of covariance descriptors representing the retinal nerve fibre layer in a real-world OCT scan. Both graphics clearly highlight the advantages of using Stein the divergence in terms of approximation accuracy and efficient numerical computation.

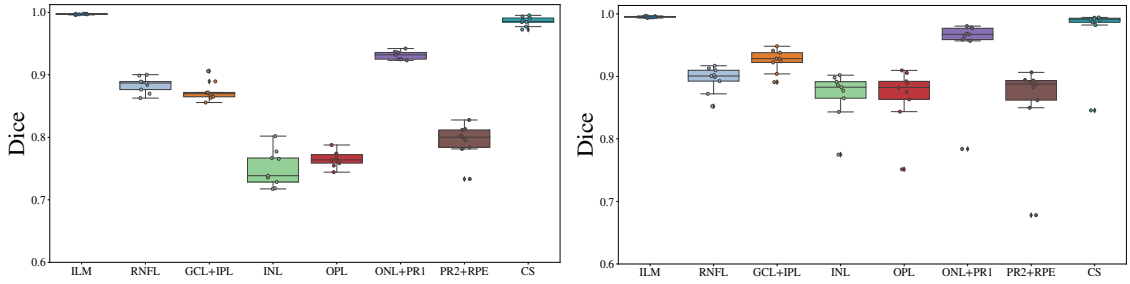


**Figure 4.8.:** Box plots of DICE similarity coefficients between computed segmentation results and manually labeled ground truth. **Left**: Probabilistic approach (4.25) proposed in [RSS14]. **Right**: OAF based on CNN features. See Table 4.1 for mean and standard deviations. Direct comparison shows a notably higher detection performance for segmenting the intraretinal layers using OAF (B).

we trained the network to directly predict the correct class in $[c]$ using raw intensity values in $\mathcal{N}_i$ as input. As output, we find a score for each layer which can directly be transformed into a distance vector suitable as input to the ordered assignment flow (4.24) via (4.23). The specific network used in our experiments has a ResNet architecture comprising four residually connected blocks of 3D convolutions and ReLU activation. Model size was hand-tuned for different sizes of input neighborhoods, adjusting the number of convolutions per block as well as corresponding channel dimensions. Details of the employed architecture are listed in Appendix A.3. In particular, the input is a patch of voxels with size $17 \times 17 \times 5$ which upper-bounds the network field of view. We thus limit the network to extracting localized features as compared to commonly used machine learning approaches which aim to incorporate as much global context into the feature extraction process as possible. For example, the U-Net architecture employed in [LCF+19] works with large ($496 \times 64$) slices of B-scans and comprises three $2 \times 2$ pooling operations. On the coarsest scale (bottom of the $U$), a single convolution with filter size $7 \times 3$ thus translates into a field of view of at least $56 \times 24$ after unpooling. During the training, no continuity constraint on the location of voxel near the retinal surface is imposed which results in generation of discontinuous and unordered of layer segmentation. However as will be shown in Section taking the output of CNN-net as input to ordered assignment flow alleviates this problem leading smooth layer transition while respecting the layer ordering.

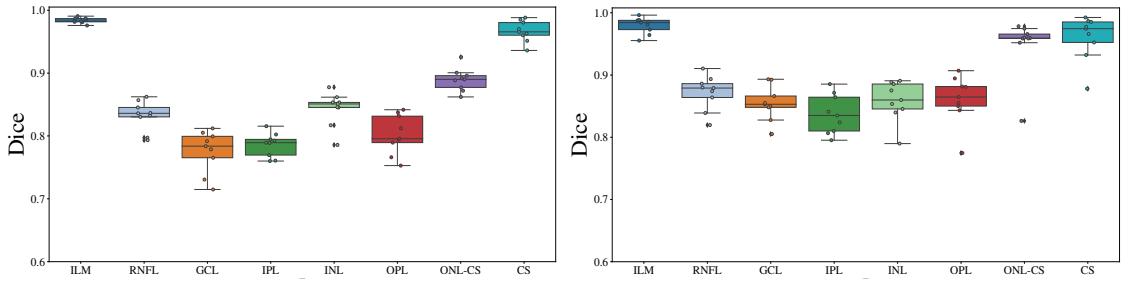


**Figure 4.9.:** Box plots of DICE similarity coefficients between computed segmentation results and manually labeled ground truth. **Left**: IOWA reference algorithm [GASnd]. **Right**: OAF based on CNN features. See Table 4.1 for mean and standard deviations. Exploiting OAF (B) for retina tissue classification results in improved overall layer detection performance, especially for the PR 1-RPE region.

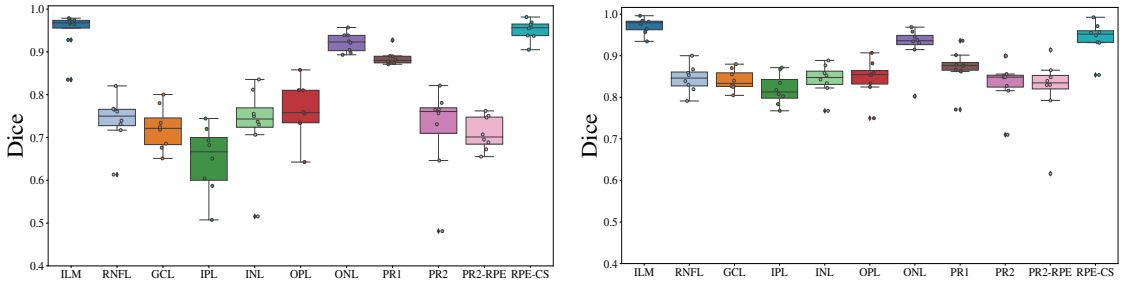


**Figure 4.10.:** Box plots of DICE similarity coefficients between computed segmentation results and manually labeled ground truth. **Left**: OAF (A). **Right**: OAF (B). The OAF based on CNN features yields improved segmentations for all retina layers.

### 4.4.5. Segmentation via Ordered Assignment

By numerically integrating the ordered assignment flow (4.3.2) parametrized by the distance matrix $D$, an assignment state $W$ is evolved on $\mathcal{W}$ until mean entropy of pixel assignments is low. We specifically use geometric Euler integration steps on $T\mathcal{W}$ with a constant step-length of $h = 0.1$ (see [ZSPS20] for details of this process). Geometric averaging with uniform weights leads to local regularization of assignments which smooths regions in which the features do not conclusively point to any label. More global knowledge about the ordering of cell layers is incorporated into $E_{\text{ord}}$ which addresses more severe inconsistencies between local features and global ordering. In all experiments, the neighborhood of each voxel $i \in [n]$ is choosen as the voxel patch of size 5 x 5 x 3 centered at $i$.

### 4.4.6. Evaluation

To benchmark our novel segmentation approach, we first extract local features for each voxel from a raw OCT volume. As described above, either region covariance descriptors (Section 4.4.2) or class scores predicted by a CNN (Section 4.4.4) are computed for segmenting the retina layers with ordered assignment flow which we in the following abbreviate as **OAF (A)** and **OAF (B)** respectively. To facilitate the performance examination between the proposed approach and the reference methods introduced in (Section 4.4.1) we evaluate the obtained results through direct comparison of different metrics from (Section 4.4.1) and by providing side-by-side visualizations of segmented OCT-volumes in each subsection separately. Specifically, we calculate the DICE

similarity coefficient [Dic45] and the mean absolute error for segmented cell layers within the pixel size of 3.87 µm compared to human grader by segmenting 8 OCT volumes consisting of 61 B-scans. Throughout the performed experiments, we fixed the grid connectivity $\mathcal{N}_i$ for each voxel $i \in I$ to $3 \times 5 \times 5$.

### Covariance Descriptor vs. CNN

In order to compare **OAF (A)** and **OAF (B)**, we first specifically evaluate the segmentation performance based on local features given by the covariance descriptor (4.4.2) as well as features extracted by a CNN (4.4.4). For OAF (A), a dictionary of $k = 400$ prototypical cluster centers on the positive definite cone (2.83) has been determined offline for each retina layer using the iterative clustering with (4.37). These are compared to descriptors extracted from the unseen volume by computing pairwise Stein divergence (2.3.3). The minimum value corresponding to the lowest divergence for each pair of voxel $i \in [n]$ and cell layer $j \in [c]$ is noted as entry $d_{ij}$ of the distance matrix $D_{\text{cov}}$, i.e. for every voxel $i$ the divergence to its closest representative of layer $j$ is given by

$$(D_{\text{cov}})_{ij} := \min_{k \in [400]} D_S(S_i, \tilde{S}_j^k). \tag{4.42}$$

For OAF (B), class scores $C \in \mathbb{R}^{n \times c}$ predicted by the neuronal network (4.4.4) are transformed into a distance matrix $D_{\text{cnn}} = -C$ simply by switching their sign followed by adjusting the parameter $\rho$ to adjust data scale in the likelihood matrix (3.59).

A naive way to segment the volume in accordance with the observed data is by choosing $\arg\min_{j \in [c]} D_{ij}$ for each voxel $i$. However, due to the challenging signal-to-noise ratio in real-world OCT data, classes will not usually be well-separated in the feature space at hand. The resulting uncertainty pertaining to the assignment of classes using exclusively local features is encoded into each distance matrix.

The experimental results discussed next illustrate the relative influence of the covariance descriptors (4.35) and regularization properties of the ordered assignment flow, respectively. To overcome the high computational complexity when extracting features given by (4.35) and the subsequent assembly of distance matrix (4.42) during the experiments carried out for **OAF(A)** and **OAF(B)** we segmented OCT volumes consisting of 41 remaining B-scans after cropping 10 B-scans from each volume boundary. Additionally we reduced the size of each B-scan by 148 voxels from each side along the $N_A$ axis to avoid artifacts caused by high varying shape and strong thinning of the retinal layers near volume bounds. Fig. 4.11 illustrates real-world labeling performance based on extracting a dictionary of 400 prototypes per layer by minimizing (4.36) and employing Algorithm 2.2 for mean retrieval. The second row in Fig. 4.11 illustrates a typical result of volume segmentation by nearest neighbor assignment *without* ordering constraint. As expected, the high texture similarity between the choroid and GCL layer yields wrong predictions resulting in violation of physiological cell layer ordering through the whole volume. However, using pairwise correlations captured by covariance matrices leads to accurate detection of the internal limiting membrane (ILM) with its characteristic highly reflective boundary. Similarly, the light rejecting fiber layers RNFL, PR1 and RPE can also be detected by this approach. For the particularly challenging inner layers such as GCL, INL and ONL that are mainly comprised of weakly reflective neuronal cell bodies, regularization by imposing (4.20) is required. In the third row of Fig. 4.11, we plot the *ordered* volume segmentation for two different values of the parameter $\gamma$ defined in (4.21), which controls the ordering regularization by means of the novel generalized likelihood matrix (4.23). Direct comparison with the ground truth shows how ordered labelings

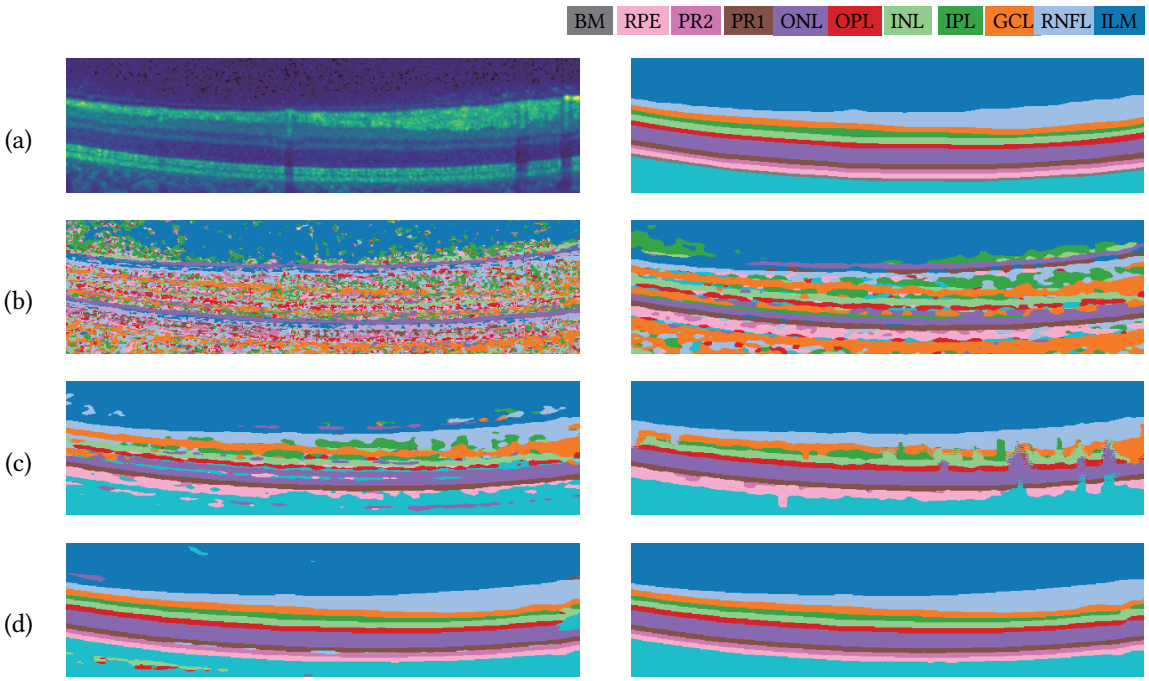


**Figure 4.11.: From top to bottom: Row (a)**: One B-scan from a OCT-volume showing the shadow effect, with ground truth plot on the right. **Row (b)**: Local nearest neighbor assignments based on prototypes by minimizing (4.36) computed with Stein divergence, with the result of the segmentation returned by the basic assignment flow (Section 3.2.2) on the right. **Row (c)**: Proposed *layer-ordered* volume segmentation based on covariance descriptors. From left to right: ordered volume segmentation for different $\gamma = 0.5, \gamma = 0.1$ (cf. Eq. (4.21)). **Row (d)**: Local rounding result extracted from Res-Net on the left and the result of the ordered assignment flow on the right.

evolve on the assignment manifold while simultaneously giving accurate data-driven detection of RNFL, OPL, INL and the ONL layer. For the remaining critical inner layers, the local prototypes extracted by (4.36) fail to represent the retina layers properly and lead to artifacts due to the presence of vertical shadow regions caused by existing blood vessels, which contribute to a loss of the interference signal during the OCT scanning process, as shown in Fig. 4.11.

After segmentation of the test data set, the mean and standard deviation were calculated for better assessment of the retina layer detection accuracy of the proposed segmentation method, according to the performance measures (4.30) and (4.29). The evaluation results for each retina tissue as depicted in Fig. 4.3, are detailed in Table 4.1 and Table 4.2. The first row of Fig. 4.16 clearly shows the superior detection accuracy of utilizing the Ordered Assignment Flow for the first outer retina layers (RNFL, GCL, IPL, INL) and the (PR2-RPE) region in connection with local features extracted by a CNN (4.4.4). Nonetheless, the covariance descriptor achieves comparable results for characterization of the outer plexiform layer (OPL) and exhibits increased retina detection regarding the photoreceptor region (PR1,PR2) and outer nuclear region (ONL). Table 4.1 includes the evaluation based on Dice similarity which is less sensitive to outliers and serves as an appropriate metric for calculating the performance measures across large 3D volumes. To obtain a consistent and clear comparability between the involved features on which we rely to tackle the specific problem of retina layer segmentation, the corresponding results are visualized in Figure 4.10. The graphic illustrates higher Dice similarity and relatively small standard deviation when incorporating features (4.4.4) as input to our model, which characterizes their

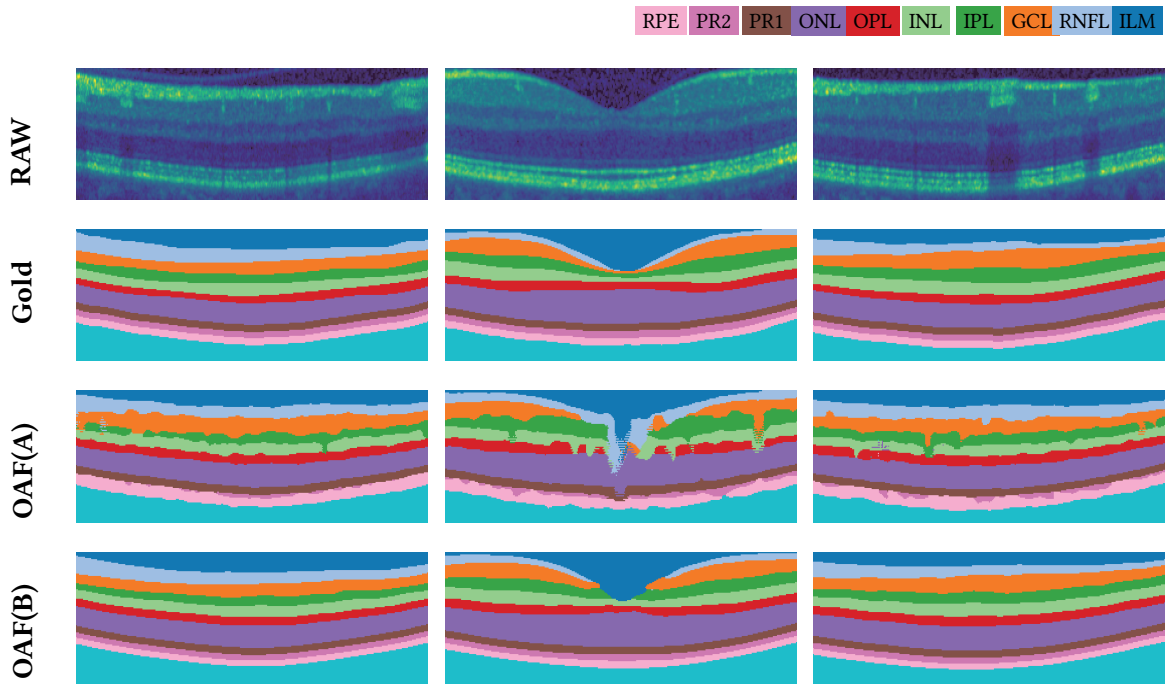


**Figure 4.12.: From top to bottom**: Three sample B-Scans extracted for different locations from a healthy OCT volume with 61 scans, with the fovea centered OCT scan visualized in the middle column. The associated augmented labeling. OAF (A) segmentation using a dictionary of covariance descriptors determined by (4.37). OAF (B) segmentation using features determined the CNN network. In contrast to to results achieved by OAF (A), the above visualization indicates more accurate detection of retina boundaries using OAF (B), in particular near the fovea region (middle column).

superior informative content. According to the left plot, the covariance descriptor performs well for detecting the prototypical textures of the internal limiting membrane (ILM), the (ONL) and (PR1) layers as well as the RPE boundary to the choroid section. Especially this highlights the ability of using gradient based features for accurate detection of retina tissues indicating sharp contrast between the neighboring layers, as is the case for ONL and PR1.

In general, the more robust retina detection features extracted by a CNN can be attributed to the underlying manifold geometry of symmetric positive definite matrices where the data partition is performed linearly by hyperplanes. This further indicates the nonlinear structure of the acquired volumetric OCT data. Fig. 4.12 presents typical labelings of a B-scan for different locations in the segmented healthy OCT volume obtained with the proposed approach. Direct comparison with the ground truth, as depicted in row (b), demonstrates higher accuracy and smoother boundary transitions by using CNN features instead of covariance descriptors. In particular, for the challenging segmentation of the ganglion cell layer (GCL) with a typical thinning near the macular region (middle scan), we report a Dice index of $0.8373 \pm 0.0263$ as opposed to $0.6657 \pm 0.1909$. The remaining numerical experiments are focused on the validation of OAF against the retina segmentation methods summarized in Section 4.4.1 serving as reference.

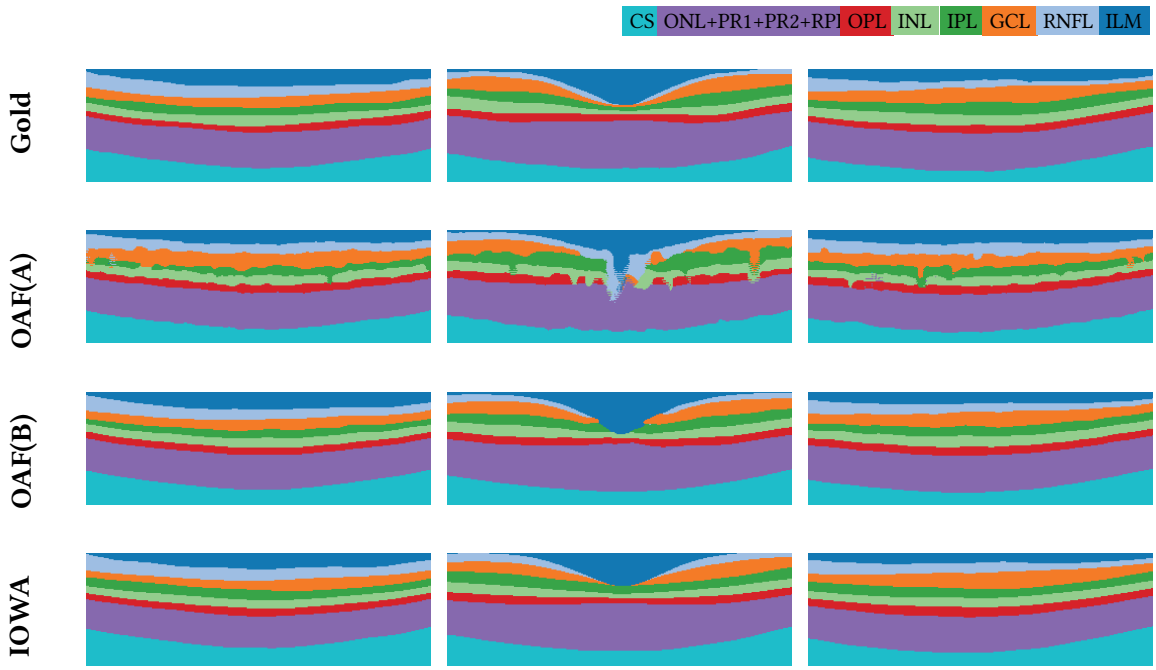


**Figure 4.13.:** Illustration of retina layer segmentation results listed in Table 4.1 and Table 4.2. **From top to bottom:** Ground truth labeling. Labeled retina tissues using the proposed approach based on covariance descriptors and CNN features, respectively. The resulting segmentation obtained using the IOWA reference algorithm.

### IOWA Reference Algorithm

To assess the segmentation performance of our proposed approach, we first compared to the state of the art graph-based retina segmentation method of 10 intra-retinal layers developed by the Retinal Image Analysis Laboratory at the Iowa Institute for Biomedical Imaging [KXCS06; AGS10a; GAW+09], also referred to as the IOWA Reference Algorithm. We quantify the region agreement with manual segmentation regarded as gold standard. Since both the augmented volumes and the compared reference methods determine boundary locations of retina layers intersections, we first transfer the retina surfaces to a layer mask by rounding to the voxel size and assign to voxels within each A-scan the associated layer label, starting from the observed boundary to the location of the next detected intersection surface of two neighboring layers.

To access a quantitative direct comparison with the IOWA reference algorithm, the tested OCT volumes were imported into OCTExplorer 3.8.0 and segmented using the predefined Macular-OCT IOWA software after properly adjusting the resolution parameters. Additionally, we pre-processed each volume by removing 2 B-scans from each side to get rid of boundary artifacts and performed segmentation with the resulting volume size of $498 \times 768 \times 59$ voxels. Quantitative results are summarized in Table 4.1 and Table 4.2. Fig. 4.9 provides a statistical illustration of the Dice index which reveals the high performance accuracy for methods which is in accordance with the mean average error shown in the last row of Fig. 4.16. In particular, we observe a notable increase of performance using the OAF for detection of the ganglion cell layer with overall accuracy of $0.8546 \pm 0.0281\,\mu m$, see Fig. 4.13 for visualized segmentations of 3 B-scans.

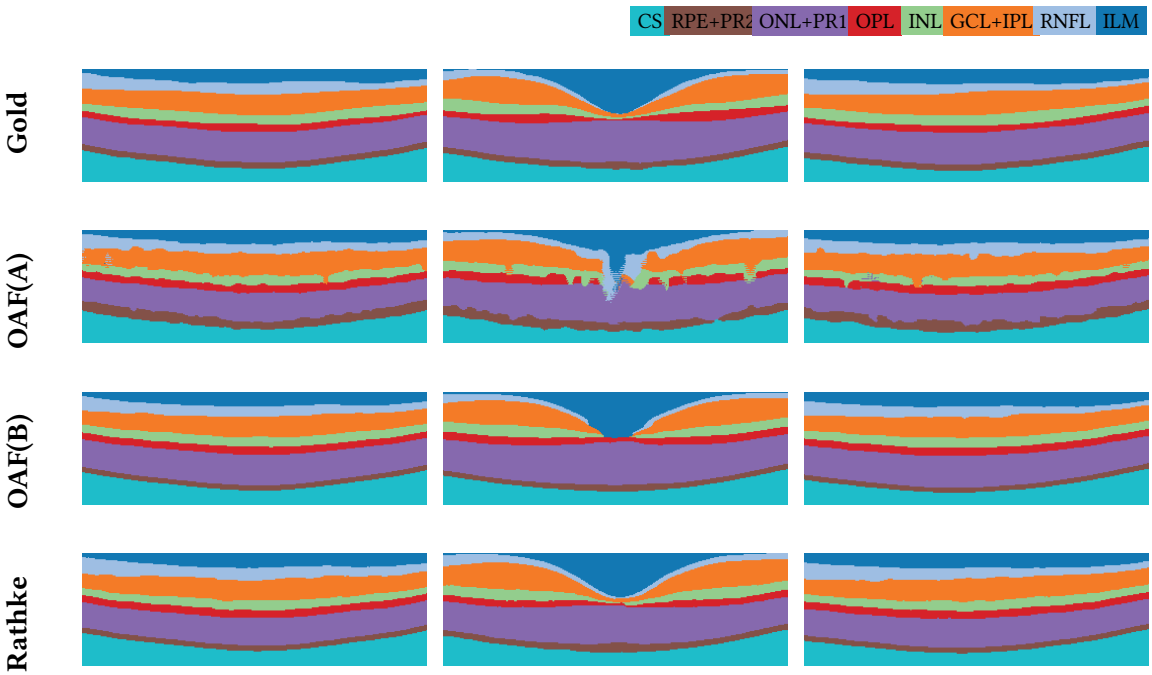


**Figure 4.14.: From top to bottom**: Ground truth for the augmented retina layer corresponding to Table 4.2. Segmentation results of the OAF based on manifold valued features and on CNN features, respectively. Segmentation results achieved by the probabilistic graphical model approach [RSS14].

## Probabilistic model

Next, we provide a visual and statistical comparison of the proposed approach and the probabilistic state of the art retina segmentation approach [RSS14] underlying Eq. (4.25). As before, to achieve a direct comparison with the proposed approach, we first adopted the OCT volumes by performing a cropping of 134 voxel from volume boundary along $N_A$ axis to match the shape and parameters for the trained model given in [RSS14] which supports the detection of retinal layer boundaries on data sets of dimension $496 \times 500 \times 61$. Subsequently, we removed the boundaries between regions GCL and IPL, ONL and PR1, PR2 and RPE to obtain three characteristic layers which have to be detected. Fig. 4.14 displays the labeling accuracy. Both methods perform well by accurately segmenting flat shaped retina tissues, as shown in the first and last columns. However, closer inspection of the second column reveals a more accurate detection of layer thickness for the (PR2+RPE) and (INL) regions below the concave curved fovea region by using OAF(B). This is mainly due to the connectivity constraints imposed on boundary detection in [RSS14]. However, the method in [RSS14] is more accurate by dealing with rapidly decreasing layer thickness near the fovea region, as observed for GCL and IPL layers in the middle column of Fig. 4.14 after visual comparison against the manual delineations (first row). In contrast to the Gaussian shape prior used in [RSS14], the proposed method does not model connectivity constraints. This allows for the observed oversmoothing artifact, but also makes the OAF approach more amenable for extension to pathological volumes with vanishing retina boundaries. For example, in the case of vitreomacular traction or diabetic macular edema, imposing connectivity constraints aggravates the problem of dealing with irregular retina boundaries.

Fig. 4.15 additionally provides a 3D view on detected retina surfaces for each evaluated ref-

erence method used in this publication. The corresponding performance measures (Table 4.1) underpin the notably higher Dice similarity for (PR2+RPE) and for the (INL) layers. The statistical plots for the mean average error and the Dice similarity index are given in Figures 4.8 and 4.16, clearly showing the overall superiority of OAF (B) with respect to both Dice index and mean average error. In particular, following Table 4.2, small error rates are observed among all the segmented layers, except for the (ILM) boundary which is detected by all methods with high accuracy. We point out that in general our method is not limited to any number of segmented layers, if ground truth is available.

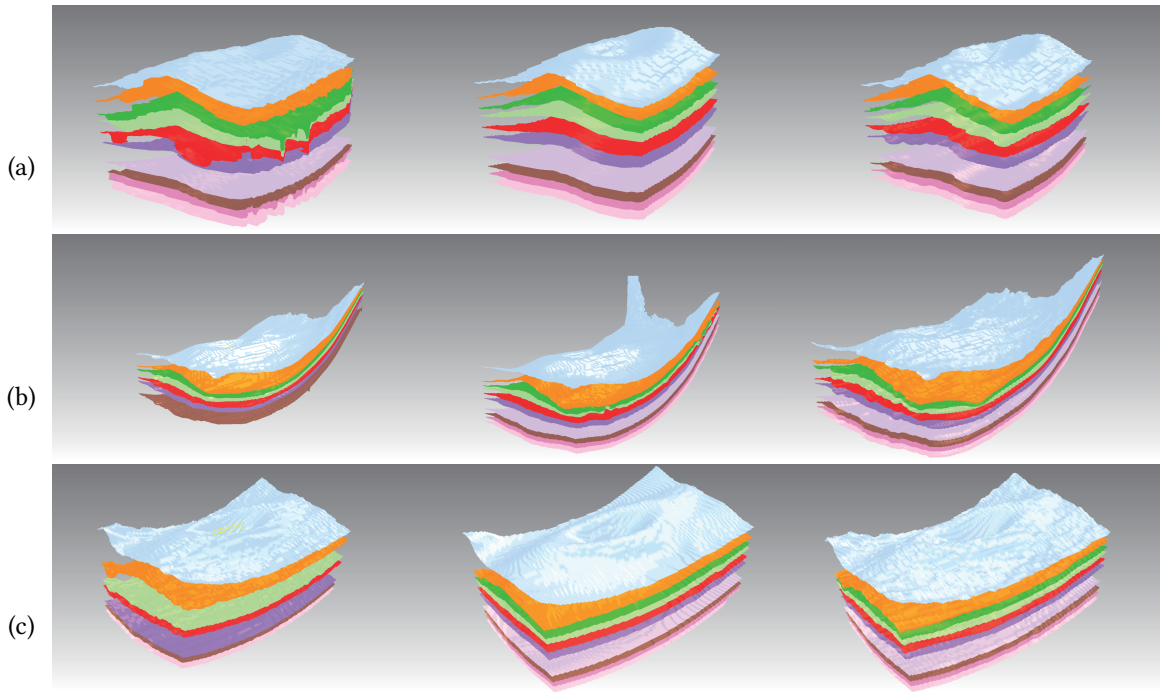


**Figure 4.15.: Row (a)**: **From left to right:** 3D retinal surfaces determined using OAF (A) (left column) and OAF (B) (middle column). The last column depicts ground truth. **Row (b)**: **From left to right:** Segmentation of retinal tissues with the IOWA reference algorithm (left column) with the proposed approach (middle column). **Row (c):** Visual comparison of the probabilistic method [RSS14] (left column) left and the OAF (B) (middle column). Our approach OAF (B) leads to accurate retina layer segmentation with smooth layer boundaries, as observed in the middle column.

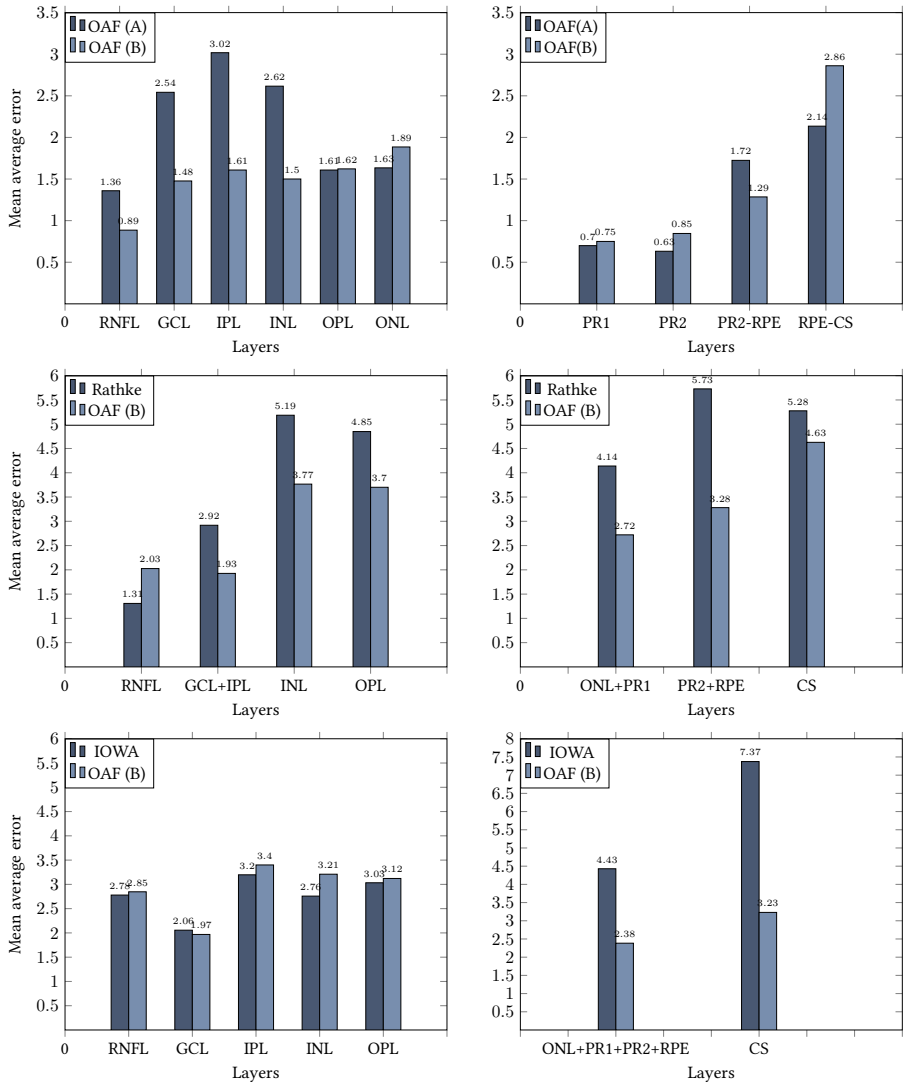


**Figure 4.16.:** Performance measures per layer in terms of the mean average error based on the segmentation of 10 healthy OCT volumes. **Top row**: Error bars for retina layers separated by the external limiting membrane (ELM) corresponding to OAF (A) and OAF (B). **Middle row**: Comparison of the mean errors of OAF (B) and the probabilistic method [RSS14]. **Bottom row**: Comparison of mean average errors of OAF (B) and the the IOWA reference algorithm.

| | OAF (A) | OAF (B) | [RSS14] | IOWA |
|---|---|---|---|---|
| ILM | 0.8837 ± 0.2564 | 0.9739 ± 0.0189 | **0.9972** ± 0.0006 | 0.9837 ± 0.0043 |
| RNFL | 0.6963 ± 0.1998 | **0.8842** ± 0.0313 | 0.8841 ± 0.0125 | 0.8323 ± 0.0236 |
| GCL | 0.6657 ± 0.1909 | 0.8373 ± 0.0263 | **0.8735** ± 0.0152 | 0.7757 ± 0.0334 |
| IPL | 0.5853 ± 0.1773 | 0.8151 ± 0.0367 | | 0.7860 ± 0.0189 |
| INL | 0.6671 ± 0.1773 | 0.8414 ± 0.0035 | 0.7501 ± 0.0292 | **0.8434** ± 0.0269 |
| OPL | 0.7018 ± 0.2013 | **0.8442** ± 0.0437 | 0.7651 ± 0.0124 | 0.8024 ± 0.0311 |
| ONL | 0.8575 ± 0.2523 | 0.9254 ± 0.0486 | **0.9312** ± 0.0068 | 0.8893 ± 0.0182 |
| PR1 | 0.8199 ± 0.2407 | 0.8717 ± 0.0441 | | |
| PR2 | 0.6787 ± 0.1976 | **0.8330** ± 0.0516 | 0.7945 ± 0.0271 | |
| RPE | 0.6313 ± 0.1821 | **0.8213** ± 0.0835 | | |
| CS | 0.8606 ± 0.2469 | 0.9445 ± 0.0488 | **0.9858** ± 0.0073 | 0.9667 ± 0.0167 |

**Table 4.1.:** Dice indices (± standard deviation) per cell layer for each of the compared segmentation approaches. Lowest mean in bold. The reference methods [RSS14] and IOWA distinguish between a smaller number of cell layers as indicated. Evaluation was performed on a test set consisting of eight OCT volumes (see Appendix A.4)

| | OAF (A) | OAF (B) | [RSS14] | IOWA |
|---|---|---|---|---|
| ILM-RNFL | 1.3590 ± 0.4114 | **0.8856** ± 0.3513 | 1.3080 ± 0.6039 | 2.7799 ± 0.9485 |
| RNFL-GCL | 2.5426 ± 0.7819 | **1.4767** ± 0.5589 | 2.9180 ± 1.0303 | 2.0561 ± 0.4978 |
| GCL-IPL | 3.0183 ± 1.0682 | **1.6082** ± 1.5291 | - | 3.1970 ± 1.1408 |
| IPL-INL | 2.6160 ± 1.1294 | **1.5004** ± 0.8652 | 5.1853 ± 1.3642 | 2.7583 ± 1.3776 |
| INL-OPL | **1.6080** ± 0.5120 | 1.6220 ± 1.0786 | 4.8489 ± 1.5898 | 3.0330 ± 1.2837 |
| OPL-ONL | **1.6342** ± 0.7174 | 1.8853 ± 1.3951 | 4.1490 ± 1.2310 | 4.4292 ± 1.5052 |
| ONL-PR1 | **0.6995** ± 0.2467 | 0.7500 ± 0.3216 | - | - |
| PR1-PR2 | **0.6320** ± 0.2442 | 0.8458 ± 0.4914 | 5.7281 ± 1.5411 | - |
| PR2-RPE | 1.7244 ± 0.6038 | **1.2850** ± 1.3660 | - | - |
| RPE-CS | **2.1354** ± 1.0836 | 2.8613 ± 2.5612 | 5.2757 ± 1.6452 | 7.3738 ± 3.2031 |

**Table 4.2.:** Mean absolute errors (± standard deviation) per cell layer interface for each of the compared segmentation approaches in pixels (1 pixel = 3.87 µm). Lowest mean in bold. Evaluation was performed on a test set consisting of eight OCT volumes (see Appendix A.4)

## 4.5. Discussion

We discuss additional aspects pertaining to the data used for training feature extractors as well as the locality of extracted features and limitations of the proposed approach.

### 4.5.1. Ground Truth Generation

The training and evaluation of supervised models for feature extraction requires a sizeable amount of high-quality labeled ground truth data. This presents a commonly encountered challenge in 3D OCT segmentation [DCA+13; KXCS06], because the process of manually labeling every voxel of a 3D volume is extremely laborious. The desire to account for inter-observer variability in manual segmentations further compounds this problem. OCT volumes used for testing purposes in

the present work were initially segmented by an automatic procedure based on hand-crafted features. In a subsequent step, each B-scan segmentation was manually corrected by a medical practitioner. The automatic method used for initial segmentation only explicitly regularizes on each individual B-scan, leading to irregularity between consecutive B-scans (see Figure 4.17).

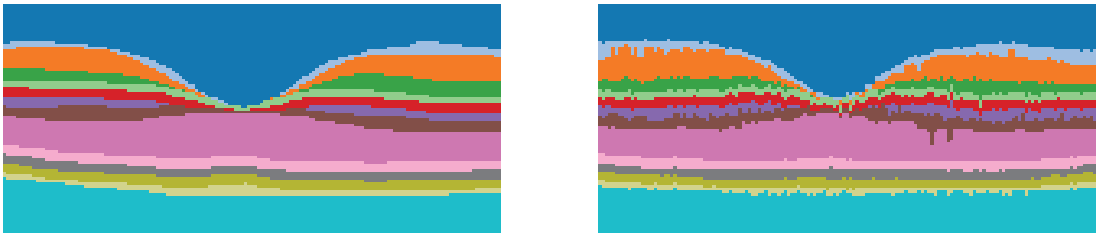

**Figure 4.17.: Left**: Initial automatic segmentation of individual B-scan based on hand-crafted features. **Right**: Section of the same automatically segmented volume orthogonal to each B-scan.

Manual correction of initial automatic segmentations leads to a noticeable reduction of irregularity but does not completely remove it. We therefore cannot rule out that a small bias towards the initial automatic segmentation based on hand-crafted features may still be present in the ground truth segmentations that we used to quantify segmentation performance of novel methods as well as baseline methods in this thesis. During feature extraction, deep learning models may be capable of discovering the specific hand-crafted features used for initial automated segmentation which may in turn lead to exploitation of any bias towards them. In contrast, because the reference methods are not trained on the same data, they can not exploit any such bias, putting them at a possible disadvantage.

Fig. 4.17 also highlights the fact that manual annotations as a gold standard still have non-trivial variance and are partly inconsistent between B-scans. In [RSS14], the variance in manual annotations is further analyzed by comparing between two different human observers. They found that for a similar dataset, the discrepancy between both human observers varies between $1.37 \pm 0.51\,\mu m$ for the most consistent layer boundary and $7.57 \pm 1.06\,\mu m$ for the least consistent. Comparison to the results in Table 4.2 ($1$ pixel $= 3.87\,\mu m$) illustrates that the proposed model is close to the quality of manual annotation in terms of mean average error. It is to be noted, that similar or even higher scores have been reported for deep learning methods such as [LCF+19] which work on individual B-scans. In view of the inconsistency between manual B-scan segmentations displayed in Fig. 4.17, it is to be questioned to what extent further improvement of these scores truly reflects improved detection of retina layers if manual annotation is the most precise method available for reference. Part of the contribution of the present work is notably the introduction of a 3D segmentation framework (Definition 4.3.2) which serves to regularize by leveraging domain knowledge based on *arbitrary* features. In particular, any deep network can be used as a drop-in replacement for the feature extraction methods discussed in Section 4.4.2.

As a final remark we point out that in order to avoid limitations of nonsmooth layer transitions along the B-scan axis which is persistent throughout the most public available data sets and to take the advantage of our segmentation approach we recommend to smooth the ground truth data by applying the assignment flow (3.63) before acquiring prototypes from (4.31) or training the CNN network.

### 4.5.2. Feature Locality

The ordered assignment flow segmentation approach can work with data from any metric space and is hence completely agnostic to the choice of preliminary feature extraction method. In this thesis, we chose to limit the field of view of deep networks such that features with local discriminative information are extracted. This makes empirical results directly comparable between features based on covariance descriptors and features extracted by these networks. In addition, we conjecture that local features may generalize better to unseen pathologies. Specifically, if a pathological change in retinal appearance pertains to the global shape of cell layers, local features are largely uneffected. In this way, we expect segmentation performance to be relatively consistent on real-world data. Conversely, widening the field of view in feature extraction should be accompanied by a well-considered training procedure in order to achieve similar generalization behavior, by employing e.g. extensive data augmentation. While raw OCT volume data has become relatively plentiful in clinical settings, large volume datasets with high-quality gold-standard segmentation are not widely available at the time of writing. Therefore, by representing a given OCT scan *locally* as opposed to incorporating global context at every stage, it is our next hypothesis that superior generalization can be achieved in the face of limited data availability. Similarly, although based on local features, the method proposed by [RSS14] combines local knowledge in accordance with a *global* shape prior. This makes clear why some layer scores achieved by this method are very competitive, but it also limits the methods ability to generalize to unseen data if large deviation from the expected global shape seen in training is present.

### 4.5.3. Limitations, Future Work

While the OAF typically achieves strong improvement over trivial rounding or baseline regularization, it does not come with a guarantee that physiological layer order will be attained. This is because we use the smooth function (4.21) instead of the indicator function $\delta_{\mathbb{R}^c_+}$ to define $E_{\text{ord}}$ in (4.20). The parameter $\gamma$ consequently presents a tradeoff between adherence to physiological layer order and difficulty of numerical integration in the smooth assignment framework (Section 3). In Fig. 4.11 (row (c)), this tradeoff becomes apparent when segmenting based on relatively weak covariance descriptor features. Choosing $\gamma$ smaller leads to improved adherence to the physiological layer order in computed segmentations. However, this also makes numerical integration of the flow (4.24) more difficult such that the choice of constant step-length $h = 0.1$ may lead to artifacts (row (c), right image). In such cases, choosing adaptive step-length for integration or using a higher-order numerical integration scheme should still yield stable algorithms at the cost of longer runtime.
We also note that at the fovea, uniformly weighted $5 \times 5 \times 3$ averaging neighborhoods may lead to oversmoothing (see Fig. 4.14 (c) middle image) which manifests in excessive thinning of e.g. GCL. To combat such artifacts, the choice of averaging weights (3.61) could be made adaptive to each local neighborhood. However, for most regions of the volume the constant choice of averaging weights made in our experiments does not lead to oversmoothing. Thus, weight adaptivity is to be targeted primarily around the fovea which has a distinctive shape. With regard to computational efficiency, another possible future direction is to encode the notion of layer ordering put forward in Definition 4.3.1 within the context of a linear dynamical system for data labeling [ZSPS20].

On the application side, modeling considerations similar to the ones underlying the flow (4.24) most likely also apply in other areas involving ordering constraints such as seismic horizon track-

ing for landscape analysis. We thus expect that much of the present work is also relevant outside of optical coherence tomography.

## 4.6. Conclusion

In this chapter we presented a novel, fully automated and purely data driven approach for retina segmentation in OCT-volumes. Compared to methods [KXCS06] [DCA+13] and [RSS14] that have proven to be particularly effective on tissue classification with a priory known retina shape orientation, our ansatz merely relies on local features and yields ordered labelings which are directly enforced through the underlying geometry of statistical manifold (3.48). To address the task of leveraging 3D-texture information, we proposed two different feature selection processes by means of region covariance descriptors (4.35) and the output obtained by training a CNN network as described in Section 4.4.4, which are both based on the interaction between local feature responses.

As opposed to other machine learning methods developed for segmenting human retina from volumetric OCT data, the proposed method only takes the pairwise distance between voxels and prototypes (3.42b) as input. As a direct consequence our approach can be applied in connection with broader range of features living in any metric space and additionally provides the incorporation of outputs from trained neuronal convolution networks interpreted as image features, where a particular instance of such type was demonstrated in Section 4.4.4. Even in view of the moderate result achieved after segmentation using OAF (A) in connection with covariance descriptors, we observe the importance of our automatic algorithm by its high level of regularization. Compared to the approach presented in [CAM+15] which employs a higher number of input features but still requires postprocessing steps to yield order preserving labeling, our approach provides a way to perform this tasks simultaneously.

Using locally adapted features for handling volumetric OCT data sets from patients with observable pathological retina changes is in particular valuable to suppress wrong layer boundaries predictions caused by prior assumptions on retinal layer thicknesses typically made by graphical model approaches as in [DCA+13] and [SBG+13]. Our method overcomes this limitation by mainly avoiding any bias towards using priors to global retina shape and instead only relies on the natural biological layer ordering, which is accomplished by restricting the assignment manifold to probabilities that satisfy the ordering constraint presented in Section 4.3.1. The experimental results reported in Section 4.4, and the direct comparison to the state of the art segmentation techniques [GASnd] and [RSS14] by using common validation metrics, underpin a notable performance and robustness of the geometric segmentation approach introduced in Section 3.2.2, that we extended to order-preserving labeling in Section 4.3.1. Furthermore, the results indicate that the ordered assignment flow successfully tackles problems in the field of retinal tissue classification on 3D-OCT data which are typically corrupted by speckle noise, with achieved performance comparable to manual gr-aders which makes it to a method of choice for medical image applications and extensions therein. We point out that our approach consequently differs from common deep learning methods which explicitly aim to incorporate global context into the feature extraction process. In particular, throughout the experiments we observed higher regularization resulting in smoother transitions of layer boundaries along the B-scan acquisition axis similar to the effect in [RSS14] where the used smooth global Gaussian prior leads to limitations for pathological applications.

# 5 Assignment Flows and Nonlocal PDEs on Graphs

## 5.1. Overview, Motivation.

Based on the particular example of Optical Coherence Tomography in the previous chapter we presented a concise way of relaxing discrete graphical model inference by geometrically integrating a related gradient descent flow on the assignment manifold. In this part of the thesis, we turn our attention to a different direction and show how geometric integration schemes can be adopted to serve as numerical solvers to specific partial differential equations on graphs (G-PDEs) in the context of image labeling.

Due to their rich ensemble of mathematical properties, for many researchers partial differential equations are the "workinghorse" throughout applied and natural sciences including physical and biological evolution processes such as front propagation and Brownian motion. In this regard, the heat equation is the most basic and well understood evolutionary process describing how initial heat spatially diffuses over time on an open domain $\Omega$

$$\partial_t u(x,t) = \Delta u(x,t), \qquad x \in \Omega. \tag{5.1}$$

Starting with the advent of powerful computers along with progressing development of efficient numerical algorithms, over past decades PDEs have gained a significant attention for approaching problems in computer vision. A few prominent examples include PDEs for image denoising [Wei98], deconvolution [PFS+15], optical flow [WS01], image inpainting [Sch15] and surface smoothing [SACO22]. In fact, models based on PDEs are efficient in the sense that they implement only local computations. However, despite their high descriptive power these methods have not reached their limit in applicability. In particular, this includes scenarios of data deviating from (piecewise) smoothness and contains features which are not purely local. As a consequence, the above mentioned models are prone to irrevocable loss of texture patterns by treating them equally to noise structures.

As for the heat equation (5.1), a simple explanation of this fact is that a solution of (5.1) at each $x \in \Omega$ can be instantaneously inferred upon the knowledge of its time and spatial derivatives, which are assembled by local differential operations. Thus, the study of alternative derivative operators has triggered research in the design of reformulations of PDEs by replacing the classical spatial differential forms by their integro-differential counterparts [AV10] which led to the following generalization of (5.1)

$$\partial_t u(x,t) = -\int_{y \in \mathbb{R}^d} \gamma^\delta(x,y)u(x,t) - \gamma^\delta(y,x)u(y,t)\mathrm{d}y, \qquad x \in \Omega, \tag{5.2}$$

with nonnegative kernel $\gamma^\delta : \mathbb{R}^d \times \mathbb{R}^d \to \mathbb{R}_+$ accounting for long distance interactions with support $\gamma^\delta(x,y) = 0$ if $\|x-y\| > \delta$. The main intuition behind (5.2) is the ability to model processes

that exhibit non-local self-similarities, such as reoccurring localized patterns at distant locations, which serves as an intrinsic property of a large variety of natural images. Presently, there is a vast literature with rigorous mathematical treatment of nonlocal PDEs [AP11; DGLZ12]. This broad array of processes which are governed by dynamics analogous to (5.2) is mainly divided into two main categories:

$(i)$: *fractional* operators [ABK+21; DG13; DGLZ13] which portray anomalous diffusion processes where the interaction of two particles can occur over an infinite distance and

$(ii)$: *nonlocal* operators [PC08; DGLZ12], which are concerned on finite range interactions only.

A key connection between fractional and nonlocal models is given by their convergence behavior to classical local counterparts (5.1) in the limit of vanishing interaction range $\delta \to 0$ as schematically visualized by Figure 5.1. A second connection is established by introducing nonlocal gradient and divergence operators in accordance with [DGLZ13]. We refer to the works [AB17; AV10] for a detailed literature of continuous fractional operators.

In the context of image analysis, the key advantage of nonlocal models $(ii)$ is twofold. Firstly, their ability to facilitate the suppression of noise allows to increase the signal to noisy ratio. Secondly, utilizing nonlocal information from all over the image for each pixel such as changes in intensity patterns over large pixel neighborhoods can recover global image properties like repetitive structures [BCM06]. Similarly to classical PDE-solvers, a solution to (5.2) is approached on discrete domains in various numerical ways by the use of finite elements [TD14], finite volumes and finite difference methods [ZWC18; MT04]. However, the price to pay is the "curse of nonlocality", i.e. the necessity of an appropriate approximation of the occurring integral expressions in (5.2) especially when discontinuous solutions are expected which is inherently present in the field of image processing. Moreover, incorporation of nonlocality results in densely populated matrices which require additional memory.

Recently [ELB08; ETT15], substantial effort has been made to approach nonlocal PDEs by leveraging graph structures with vertices and edges encoding data points and their relationship within the data. This strategy has led to partial difference equations which are successfully applied in irregular and regular domains for image denoising, image inpainting and data processing. Hereby, existing approaches to the specific task of *data labeling* on graphs, that is the assignment of an element of a finite set of labels to data points observed at each vertex, can be categorized by two main aspects: (1): approaches whose mathematical structure is directly dictated by the labeling task, and (2): approaches that combine traditional data processing routines with a subsequent final discretization step.

Examples of (1) are discrete graphical models [WJ08; KAH+15] that encode directly the combinatorial label assignment task, as a basis for the design of various sequential nonlocal processing steps performing approximate inference, like belief propagation. However, the intrinsic nonsmoothness of discrete graphical models constitutes a major obstacle for the design of hierarchical models and for efficient parameter learning. Graphical models, therefore, have been largely superseded by deep networks during the last decade.

Examples of (2) class include the combination of established PDE-based diffusion approaches and threshold operations [MBO94; GGOB14; BF16]. The mathematical formulations inherit the connection between total variation (TV) based variational denoising, mean curvature motion and level set evolution [OS88; ROF92; Gar13; CCN15]. They also exhibit connections to gradient flows in terms of the Allen-Cahn equation with respect to the Ginzburg-Landau functional

[Gar13; GGOB14]. Regarding data labeling, however, a conceptual shortcoming of these approaches is that they do not provide a direct and natural mathematical problem formulation. As a consequence, this renders difficult the assignment of dozens or hundreds of labels to data, and learning parameters in order to tailor regularization properties to the problem and the class of data at hand.

To overcome these shortcomings, in this chapter we build upon the smooth dynamical framework of assignment flows (cf. Chapter 3) and consider spatially nonlocal diffusion processes of the form (5.2) on graphs which are tailored to the data labeling problem. In particular, due to inherent Fisher-Rao geometry no extrinsic thresholding or rounding is required to perform both, nonlocal spatial diffusion for assignment regularization and rounding to an integral solution after performing simple integration steps.

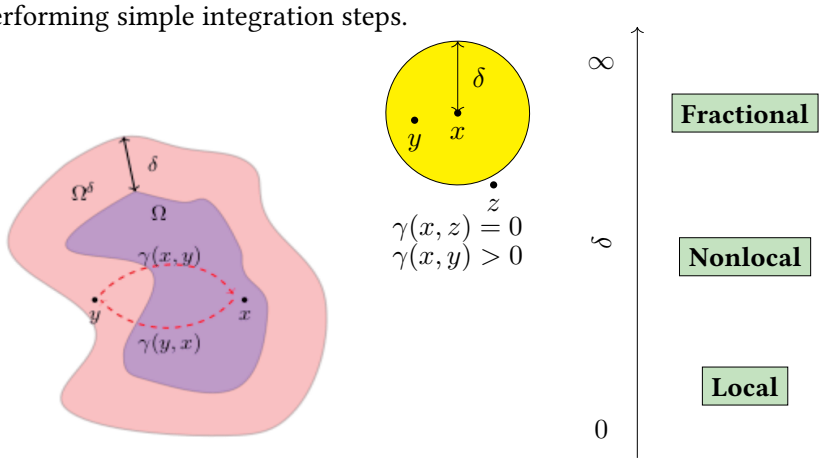


**Figure 5.1.:** Schematic visualization of three different instances of (5.2), presented on the right, with respect to the interaction range of the kernel $\gamma^\delta$. The length scale parameter $\delta$ accounts for nonlocal interactions of points $x \in \Omega$ (blue area) to points outside the underlying domain $y \in \Omega^\delta$ that within the the ball of radius $\delta$ (yellow area) as depicted by the red area. When $\delta$ goes to zero the nonlocal PDE (5.2) recovers its local counterpart (5.1) with vanishing neighboring interactions which forces the process to evolve entirely on $\Omega$.

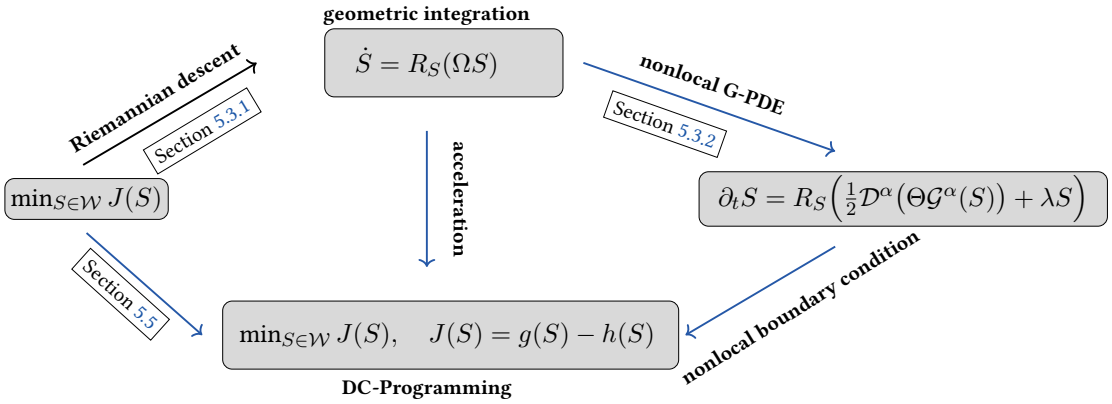


**Figure 5.2.: Summary of results.** Starting point (Section 3.2.2) is a particular formulation of the assignment flow ODE (**top**) that represents the Riemannian gradient descent of a functional $J$ (**left**). The first main contribution of this chapter is an equivalent alternative representation of the assignment flow equation in terms of a partial difference equation on the underlying graph (**right**), with a nonlocal data-driven diffusion term in divergence form and further terms induced by the information-geometric approach to the labeling problem. The second major contribution concerns a DC-decomposition of the nonconvex functional $J$ (**bottom**) and a novel accelerated minimization algorithm using a second-order tangent space parametrization of the assignment flow.

### 5.1.1. Organization

The remainder of this chapter is organized as follows.

- In Section 5.2, we introduce the non-local calculus by adapting differential operators [DGLZ13; DGLZ12] from continuous domains to graphs.
- The necessary notational conventions for interpreting the assignment flows as nonlocal PDEs on graphs are shortly summarized in Section 5.3.1.
- In Section 5.3.1, we present a particular subclass of assignment flows denoted as the $S$-flow, whose dynamics is govern by a nonconvex potential. The equivalence of the $S$-flow and the G-PDE (1.1) is derived in Section 5.3.2, together with a tangent space parametrization as basis for the development of iterative numerical solvers.
- In reference to the novel G-PDE formulation, in Section 5.3.4 we present the balance law that reveals how spatial diffusion interacts with label assignment by solving (1.1).
- Section 5.4 is devoted to explicitly working out common aspects and differences of (1.1) to related work:
  - continuous-domain nonlocal diffusion [AV10],
  - nonlocal variational approaches to image analysis [GO09] and
  - nonlocal G-PDEs on graphs [ELB08; ETT15].

  As summarized by Figure 5.9 and Table 5.1, these approaches can be regarded as special cases from the mathematical viewpoint. They differ however regarding the scope and the class of problems to be solved: the approach (1.1) is only devoted to the data *labeling* problem which explains its mathematical form. Finally, we show how our work extends the result of [SS21].
- Section 5.5 details contribution (b) on DC-programming from the viewpoint of geometric integration.
- In Section 5.6, we provide the corresponding convergence analysis of the numerical algorithm to an integral state.
- Finally, numerical results that illustrate our findings are reported in Section 5.7 and discussed for potential future extensions in Section 5.8.

## 5.2. Nonlocal Calculus

Following [DGLZ12], in this section we collect notions of nonlocal calculus which will be used throughout this chapter. Hereby, we start with formulation of general vector valued operators where the basic scalar valued operators will play a key role in the experimental section. For a detailed exposition and more general formulation we refer to [Du19].

Let $(\mathcal{V}, \mathcal{E}, \Omega)$ be an undirected weighted regular grid graph with nodes

$$\mathcal{V} \subset \mathbb{Z}^d, \qquad n = |\mathcal{V}| \qquad 2 \leq d \in \mathbb{N}, \tag{5.3}$$

with edge set $\mathcal{E} \subset \mathcal{V} \times \mathcal{V}$ that has no self-loops, and with the weighted adjacency matrix $\Omega$ that satisfies

$$0 \leq \Omega(x, y) \leq 1, \qquad \Omega(x, y) = \Omega(y, x), \qquad \forall x, y \in \mathcal{V}. \tag{5.4}$$

$\Omega$ defines the neighborhoods

$$\mathcal{N}(x) := \{y \in \mathcal{V} \colon \Omega(x, y) > 0\}, \qquad x \in \mathcal{V} \tag{5.5}$$

and serves as a function $\Omega \colon \mathcal{V} \times \mathcal{V} \to \mathbb{R}$ measuring the similarity of adjacent nodes.

We define the function spaces

$$\mathcal{F}_{\mathcal{V}} := \{f \colon \mathcal{V} \to \mathbb{R}\}, \qquad \mathcal{F}_{\mathcal{V}\times\mathcal{V}} := \{F \colon \mathcal{V} \times \mathcal{V} \to \mathbb{R}\}, \tag{5.6a}$$

$$\mathcal{F}_{\mathcal{V},E} := \{F \colon \mathcal{V} \to E\}, \qquad \mathcal{F}_{\mathcal{V}\times\mathcal{V},E} := \{F \colon \mathcal{V} \times \mathcal{V} \to E\}, \tag{5.6b}$$

where $E$ denotes a (possibly improper) subset of Euclidean space. The spaces $\mathcal{F}_{\mathcal{V}}$ and $\mathcal{F}_{\mathcal{V}\times\mathcal{V}}$ respectively are equipped with the inner products

$$\langle f, g\rangle_{\mathcal{V}} := \sum_{x\in\mathcal{V}} f(x)g(x), \qquad \langle F, G\rangle_{\mathcal{V}\times\mathcal{V}} := \sum_{(x,y)\in\mathcal{V}\times\mathcal{V}} F(x, y)G(x, y). \tag{5.7}$$

We set

$$\overline{\mathcal{V}} := \mathcal{V} \dot{\cup} \mathcal{V}_{\mathcal{I}}^{\alpha} \qquad \text{(disjoint union)}, \tag{5.8}$$

where the *nonlocal interaction domain* $\mathcal{V}_{\mathcal{I}}^{\alpha}$ *with respect to* an *antisymmetric* mapping

$$\alpha \in \mathcal{F}_{\overline{\mathcal{V}}\times\overline{\mathcal{V}}}, \qquad \alpha(x, y) = -\alpha(y, x), \qquad \forall x, y \in \overline{\mathcal{V}} \tag{5.9}$$

is defined as

$$\mathcal{V}_{\mathcal{I}}^{\alpha} := \{x \in \mathbb{Z}^d \setminus \mathcal{V} : \alpha(x, y) \neq 0 \text{ for some } y \in \mathcal{V}\}. \tag{5.10}$$

$\mathcal{V}_{\mathcal{I}}^{\alpha}$ allows for discrete formulations of conditions on nonlocal boundaries with positive measure in a Euclidean domain. Such conditions are distinct from traditional conditions imposed on boundaries that have measure zero. Figure 5.3 displays a possible nonlocal boundary configuration.

We state the following identity induced by (5.9)

$$\sum_{x,y\in\overline{\mathcal{V}}} \big(F(x, y)\alpha(x, y) - F(y, x)\alpha(y, x)\big) = 0, \qquad \forall F \in \mathcal{F}_{\overline{\mathcal{V}}\times\overline{\mathcal{V}}}. \tag{5.11}$$

The *nonlocal divergence operator* $\mathcal{D}^{\alpha}$ and the *nonlocal interaction operator* $\mathcal{N}^{\alpha}$ are defined by

$$\mathcal{D}^{\alpha} \colon \mathcal{F}_{\overline{\mathcal{V}}\times\overline{\mathcal{V}}} \to \mathcal{F}_{\overline{\mathcal{V}}}, \qquad \mathcal{D}^{\alpha}(F)(x) := \sum_{y\in\overline{\mathcal{V}}} \big(F(x, y)\alpha(x, y) - F(y, x)\alpha(y, x)\big), \qquad x \in \overline{\mathcal{V}}, \tag{5.12a}$$

$$\mathcal{N}^{\alpha} \colon \mathcal{F}_{\overline{\mathcal{V}}\times\overline{\mathcal{V}}} \to \mathcal{F}_{\mathcal{V}_{\mathcal{I}}^{\alpha}}, \qquad \mathcal{N}^{\alpha}(F)(x) := -\sum_{y\in\overline{\mathcal{V}}} \big(F(x, y)\alpha(x, y) - F(y, x)\alpha(y, x)\big), \qquad x \in \mathcal{V}_{\mathcal{I}}^{\alpha}. \tag{5.12b}$$

Based on the mapping $\alpha$ given by (5.9), the operator (5.12b) is nonzero in general and accounts for the density of a *nonlocal flux* from the entire domain $\overline{\mathcal{V}}$ to nodes $x \in \mathcal{V}_{\mathcal{I}}^{\alpha}$ [Du19]. This

generalizes the notion of *local flux* density $\langle q(x), n(x)\rangle$ on continuous domains $\Omega \subset \mathbb{R}^d$ with outer normal vector field $n(x) \in \mathbb{R}^d$ on the boundary $\partial\Omega$, and with a vector-valued function $q(x)$ on $\partial\Omega$ that typically stems from an underlying constitutive physical relation. Due to the identity (5.11), the operators (5.12) satisfy the *nonlocal Gauss theorem*

$$\sum_{x\in\mathcal{V}} \mathcal{D}^\alpha(F)(x) = \sum_{y\in\mathcal{V}_\mathcal{I}^\alpha} \mathcal{N}^\alpha(F)(y). \tag{5.13}$$

The operator $\mathcal{D}^\alpha$ maps two-point functions $F(x,y)$ to $\mathcal{D}^\alpha(F) \in \mathcal{F}_{\overline{\mathcal{V}}}$, whereas $\mathcal{N}^\alpha(F)$ is defined on the domain $\mathcal{V}_\mathcal{I}^\alpha$ given by (5.10) where nonlocal boundary conditions are imposed.

The adjoint mapping $(\mathcal{D}^\alpha)^*$ with respect to the inner product (5.7) is determined by the relation

$$\langle f, \mathcal{D}^\alpha(F)\rangle_{\overline{\mathcal{V}}} = \langle (\mathcal{D}^\alpha)^*(f), F\rangle_{\overline{\mathcal{V}}\times\overline{\mathcal{V}}}, \qquad \forall f \in \mathcal{F}_{\overline{\mathcal{V}}}, \qquad \forall F \in \mathcal{F}_{\overline{\mathcal{V}}\times\overline{\mathcal{V}}}, \tag{5.14}$$

which yields the operator

$$(\mathcal{D}^\alpha)^* \colon \mathcal{F}_{\overline{\mathcal{V}}} \to \mathcal{F}_{\overline{\mathcal{V}}\times\overline{\mathcal{V}}}, \qquad (\mathcal{D}^\alpha)^*(f)(x,y) := -(f(y)-f(x))\alpha(x,y), \qquad \forall f \in \mathcal{F}_{\overline{\mathcal{V}}}. \tag{5.15}$$

The *nonlocal gradient operator* is defined as

$$\mathcal{G}^\alpha \colon \mathcal{F}_{\overline{\mathcal{V}}} \to \mathcal{F}_{\overline{\mathcal{V}}\times\overline{\mathcal{V}}}, \qquad \mathcal{G}^\alpha(f)(x,y) := -(\mathcal{D}^\alpha)^*(f)(x,y), \qquad \forall f \in \mathcal{F}_{\overline{\mathcal{V}}}. \tag{5.16}$$

For *vector-valued* mappings, the operators (5.12) and (5.15) naturally extend to $\mathcal{F}_{\overline{\mathcal{V}}\times\overline{\mathcal{V}},E}$ and $\mathcal{F}_{\overline{\mathcal{V}},E}$, respectively, by acting *componentwise*.

Using the mappings (5.15), (5.16), the nonlocal Gauss theorem (5.13) implies *Greens nonlocal first identity*

$$\sum_{x\in\mathcal{V}} u(x)\mathcal{D}^\alpha(F)(x) - \sum_{x\in\overline{\mathcal{V}}}\sum_{y\in\overline{\mathcal{V}}} \mathcal{G}^\alpha(u)(x,y)F(x,y) = \sum_{x\in\mathcal{V}_\mathcal{I}^\alpha} u(x)\mathcal{N}^\alpha(F)(x), \qquad \begin{matrix} u \in \mathcal{F}_{\overline{\mathcal{V}}}, \\ F \in \mathcal{F}_{\overline{\mathcal{V}}\times\overline{\mathcal{V}}}. \end{matrix} \tag{5.17}$$

Given a function $f \in \mathcal{F}_{\overline{\mathcal{V}}}$ and a symmetric mapping

$$\Theta \in \mathcal{F}_{\overline{\mathcal{V}}\times\overline{\mathcal{V}}} \quad \text{with} \quad \Theta(x,y) = \Theta(y,x), \tag{5.18}$$

we define the *linear nonlocal diffusion operator*

$$\mathcal{D}^\alpha\big(\Theta\mathcal{G}^\alpha(f)\big)(x) = 2\sum_{y\in\overline{\mathcal{V}}} \mathcal{G}^\alpha(f)(x,y)\Theta(x,y)\alpha(x,y), \qquad f \in \mathcal{F}_{\overline{\mathcal{V}}}. \tag{5.19}$$

For the particular case with no interactions, i.e. $\alpha(x,y) = 0$ if $x \in \mathcal{V}$ and $y \in \mathcal{V}_\mathcal{I}^\alpha$, expression (5.19) reduces with $\Theta(x,y) = 1, x, y \in \mathcal{V}$ to

$$\mathcal{L}_\omega f(x) \overset{(5.5)}{=} \sum_{y\in\mathcal{N}(x)} \omega(x,y)\big(f(y)-f(x)\big), \qquad \omega(x,y) = 2\alpha(x,y)^2, \tag{5.20}$$

which coincides with the *combinatorial Laplacian* [CL96; Chu97] after reversing the sign. The next remark provides an intuition for appropriate setup of parameters $\alpha, \Theta \in \mathcal{F}_{\overline{\mathcal{V}}\times\overline{\mathcal{V}}}$.

**Remark 5.2.1. (Role of parameters in modeling nonlocal diffusion processes.)** In our work we differentiate the parameters $\alpha, \Theta$ by their role played in modeling nonlocal diffusion processes of the form (5.19). More precisely, we use the antisymmetric mapping $\alpha \in \mathcal{F}_{\overline{\mathcal{V}}\times\overline{\mathcal{V}}}$ for definition of first order derivative operators $\mathcal{D}^\alpha, \mathcal{G}^\alpha, \mathcal{N}^\alpha$ and the symmetric mapping $\Theta \in \mathcal{F}_{\overline{\mathcal{V}}\times\overline{\mathcal{V}}}$ for specifying the constitutive function at each $x \in \mathcal{V}$ that controls the smoothing properties of operator (5.20). Instances of $\alpha, \Theta$ along with an analytical ablation study will be presented in section 5.4.

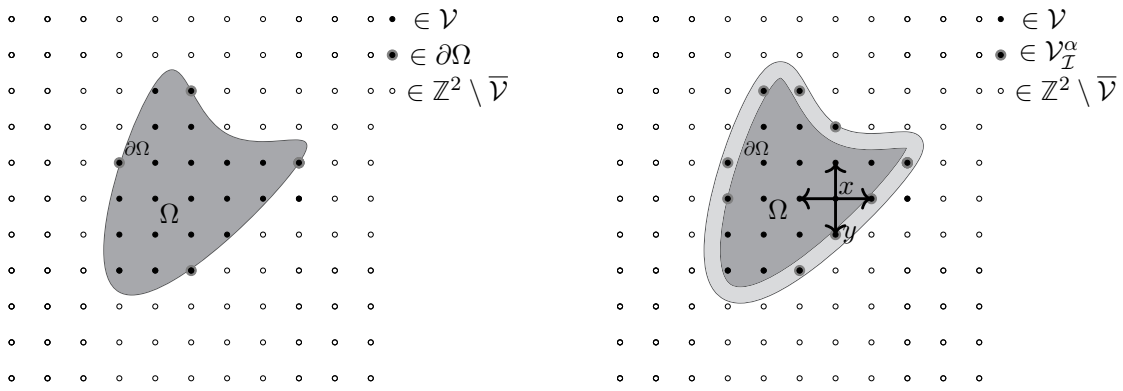


**Figure 5.3.: Schematic visualization of a nonlocal boundary. Left:** A bounded open domain $\Omega \subset \mathbb{R}^2$ with *local* boundary $\partial\Omega$ overlaid by the grid $\mathbb{Z}^2$. **Right:** A bounded open domain $\Omega$ with nonlocal boundary (light gray color). Nodes • and •, respectively, are vertices on the graph $\mathcal{V}$ and on the interaction domain $\mathcal{V}_{\mathcal{I}}^{\alpha}$ given by (5.10).

## 5.3. Relating Assignment Flows and Nonlocal PDEs

Before we proceed with our main result, in this section we briefly adopt conventions from Chapter 3.1 into the common PDE- based notations. To do so, we simply replace the indices $i, j \in I$, denoting the image pixel locations by $x, y \in \mathcal{V}$ referring to nodes on a graph $\mathcal{V}$ and identify vectors $A_i = ((A_i)_1, \dots, (A_i)_c)^T$ by $A(x) = (A_1(x), \dots, A_c(x))^T$ where $c$ denotes the number of prototypes as specified in Section 3. In this setting, after lifting the distance vector field

$$D_{\mathcal{X}}(x) = \big(d_{\mathcal{X}}(X(x), X_1^*), \dots, d_{\mathcal{X}}(X(x), X_c^*)\big)^{\top}, \qquad x \in \mathcal{V}, \tag{5.21}$$

the corresponding likelihood and similarity vectors are now respectively expressed for each $x \in \mathcal{V}$ by

$$L(x) \colon \mathcal{S} \to \mathcal{S}, \qquad L(W)(x) = \frac{W(x) \odot e^{-\frac{1}{\rho} D_{\mathcal{X}}(x)}}{\langle W(x), e^{-\frac{1}{\rho} D_{\mathcal{X}}(x)} \rangle}, \qquad x \in \mathcal{V}, \quad \rho > 0, \tag{5.22}$$

and

$$S(x) \colon \mathcal{W} \to \mathcal{S}, \qquad S(W)(x) = \operatorname{Exp}_{W(x)} \Big( \sum_{y \in \mathcal{N}(x)} \Omega(x, y) \operatorname{Exp}_{W(x)}^{-1} \big(L(W)(y)\big) \Big), \tag{5.23}$$

where the weights $\Omega(x, y)$ determine the regularization properties of the similarity map ( cf. Remark 3.2.3) which satisfy (5.4) and the additional constraint

$$\sum_{y \in \mathcal{N}(x)} \Omega(x, y) = 1, \quad \forall x \in \mathcal{V}. \tag{5.24}$$

By introducing the shorthand for solutions $W(t, x) = W(x)(t)$ we find a new formulation of the *assignment flow* from the perspective of PDEs given by the system of nonlinear ODEs on the assignment manifold $\mathcal{W}$

$$\dot{W}(x) = R_{W(x)} S(W)(x), \qquad W(0, x) = W(x)(0) \in \mathbb{1}_{\mathcal{S}}, \quad x \in \mathcal{V}, \tag{5.25}$$

with the tangent vector field on the right hand side expressed in terms of the replicator map (3.33)

$$\mathcal{V} \ni x \mapsto R_{W(x)} S(W)(x) = \operatorname{Diag}\big(W(x)\big) S(W)(x) - \langle W(x), S(W)(x) \rangle W(x) \ \in \ T_0. \quad (5.26)$$

Integrating system (3.63) numerically [ZSPS20] yields integral assignment vectors $W(t,x),\ x \in \mathcal{V}$ for $t \to \infty$, that uniquely assign a label from the set $\mathcal{X}^*$ to each data point $X(x)$ [ZZS20].

**Remark 5.3.1 (Impact of Nonlocality).** By construction, the vector field that defines the ODE (5.25) instantaneously incorporates local-nonlocal information by prescribing spatial support of neighborhoods $\mathcal{N}(x)$ at each node $x \in \mathcal{V}$, as will be discussed in Sections 5.4 and 5.3.2. In this regard, Figure 5.5 illustrates two scenarios of applying the assignment flow approach which highlight the beneficial impact on labeling accuracy when using data-driven nonlocal regularization.

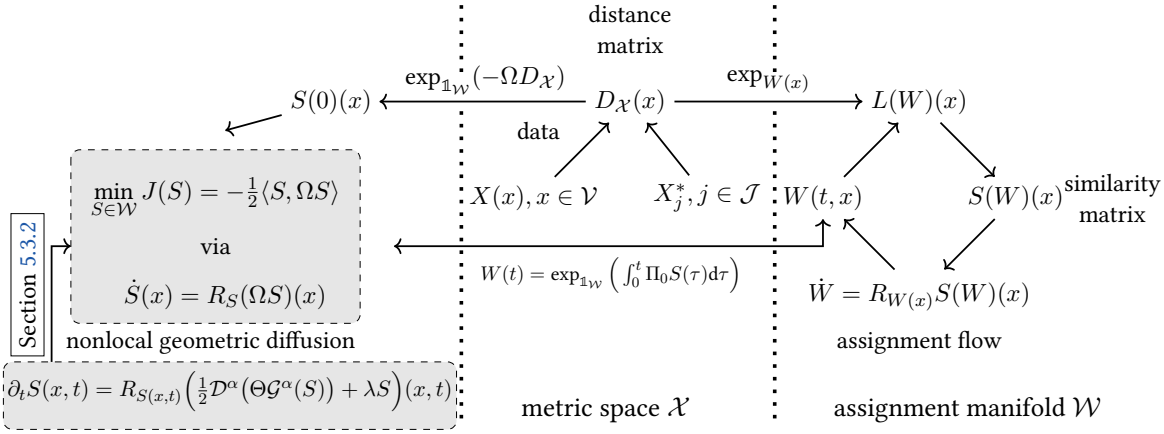


**Figure 5.4.: Inference of label assignments via assignment flows. Center column:** Application task of assigning data to prototypes in a metric space. **Right column:** Overview of the geometric approach [ÅPSS17]. The data are represented by the distance matrix $D_\mathcal{X}$ and by the likelihood vector field $L(W)$ on the assignment manifold $\mathcal{W}$. The similarity vectors $S(W)(x)$, determined through geometric averaging of the likelihood vectors, drive the assignment flow whose numerical geometric integration result in spatially coherent and unique label assignment to the data. **Left column:** Alternative equivalent reformulation of the assignment flow [SS21] which separates (i) the influence of the data that only determine the initial point of the flow (cf. (5.27a)), and (ii) the influence of the parameters $\Omega$ that parametrize the vector field which drives the assignment flow. This enables to derive the novel nonlocal geometric diffusion equation in Section 5.3.2.

### 5.3.1. S-Flow Parametrization.

Under assumptions (5.24) and (5.4) on the weights we next adopt the *S-parametrization* of the assignment flow system (3.63) from [SS21, Prop. 3.6]

$$\dot S = R_S(\Omega S), \qquad S(0) = \exp_{\mathbb{1}_\mathcal{W}}(-\Omega D_\mathcal{X}), \quad (5.27a)$$

$$\dot W = R_W(S), \qquad W(0) = \mathbb{1}_\mathcal{W}, \quad \mathbb{1}_\mathcal{W}(x) = \mathbb{1}_\mathcal{S}, \quad x \in \mathcal{V}, \quad (5.27b)$$

where both $S$ and $W$ are points on $\mathcal{W}$ and hence have the format (3.47) and

$$R_S(\Omega S)(x) = R_{S(x)}\big((\Omega S)(x)\big), \quad (\Omega S)(x) = \sum_{y \in \mathcal{N}(x)} \Omega(x,y) S(y), \quad (5.28)$$

$$\exp_{\mathbb{1}_\mathcal{W}}(-\Omega D_\mathcal{X}) := \big(\dots, \operatorname{Exp}_{\mathbb{1}_\mathcal{S}} \circ R_{\mathbb{1}_\mathcal{S}}(-(\Omega D_\mathcal{X})(x)), \dots\big)^\top \in \mathcal{W}, \quad x \in \mathcal{V}, \quad (5.29)$$

with the mappings $\mathrm{Exp}_p$, $R_p$, $p \in \mathcal{S}$ defined by (3.39) and (3.33), respectively. In addition, one has (cf. (3.50), (3.36))

$$\exp_p(d) = \exp_p(\Pi_0 d), \quad \forall d \in \mathbb{R}^c. \tag{5.30}$$

Analogous to (3.54), the lifting map (3.54) evaluated at $S \in \mathcal{W}$ and parametrized on the tangent space $\mathcal{T}_0$ reads

$$\exp_S \colon \mathcal{T}_0 \to \mathcal{W}, \qquad \exp_S(V) = \big(\dots, \exp_{S(x)}\big(V(x)\big), \dots\big) \tag{5.31a}$$

and the relations (3.41) extend to

$$\exp_{\exp_S(V)}(V') = \exp_S(V + V'), \qquad S \in \mathcal{W}, \quad V, V' \in \mathcal{T}_0, \tag{5.32a}$$

$$\exp_S(D) = \exp_S(\Pi_0 D), \qquad \forall D \in \mathbb{R}^{n \times c}. \tag{5.32b}$$

Parametrization (5.27) has the advantage that $W(t)$ depends on $S(t)$, but not vice versa. As a consequence, it suffices to focus on (5.27a) since its solution $S(t)$ determines the solution to (5.27b) by [ZZS20, Prop. 2.1.3]

$$W(t) = \exp_{\mathbb{1}_\mathcal{W}}\Big(\int_0^t \Pi_0 S(\tau) \mathrm{d}\tau\Big). \tag{5.33}$$

In addition, (5.27a) was shown in [SS21] to be the *Riemannian gradient descent flow* with respect to the potential

$$J \colon \mathcal{W} \to \mathbb{R}, \qquad J(S) = -\frac{1}{2}\langle S, \Omega S\rangle = \frac{1}{4}\sum_{x \in \mathcal{V}} \sum_{y \in \mathcal{N}(x)} \Omega(x,y) \|S(x) - S(y)\|^2 - \frac{1}{2}\|S\|_F^2, \tag{5.34}$$

where $\|\cdot\|_F$ denotes the Frobenius (matrix) norm and the vector field $\mathcal{V} \ni x \mapsto S(x) \in \mathcal{S}$ is identified with the matrix

$$S = (S_j(x))_{x \in \mathcal{V},\, j \in [c]} \in \mathbb{R}^{n \times c}_{++} \tag{5.35}$$

such that (5.28) can be written as

$$\big((\Omega S)(x)\big)_j = \sum_{y \in \mathcal{N}(x)} \big(\Omega(x,y) S(y)\big)_j = \sum_{y \in \mathcal{N}(x)} \Omega(x,y) S(y,j) = (\Omega S)_{x,j}. \tag{5.36}$$

Convergence and stability results for the gradient flow (5.27a) have been established by [ZZS20].

We proceed with the first main result of this chapter and show how the assignment flow (5.27a) emerges as a particular nonlocal diffusion process of the form (5.2). This results in an equivalent formulation of the Riemannian gradient flow (5.27a) in terms of a suitable *nonlinear* extension of the nonlocal *linear* diffusion operator (5.19).

### 5.3.2. $S$-Flow: Non-Local PDE Formulation

We start with specifying a general class of parameter matrices $\Omega$ satisfying (5.4) and (5.24) in terms of an anti-symmetric and a symmetric mapping $\alpha \in \mathcal{F}_{\overline{\mathcal{V}} \times \overline{\mathcal{V}}}$ and $\Theta \in \mathcal{F}_{\overline{\mathcal{V}} \times \overline{\mathcal{V}}}$ respectively.

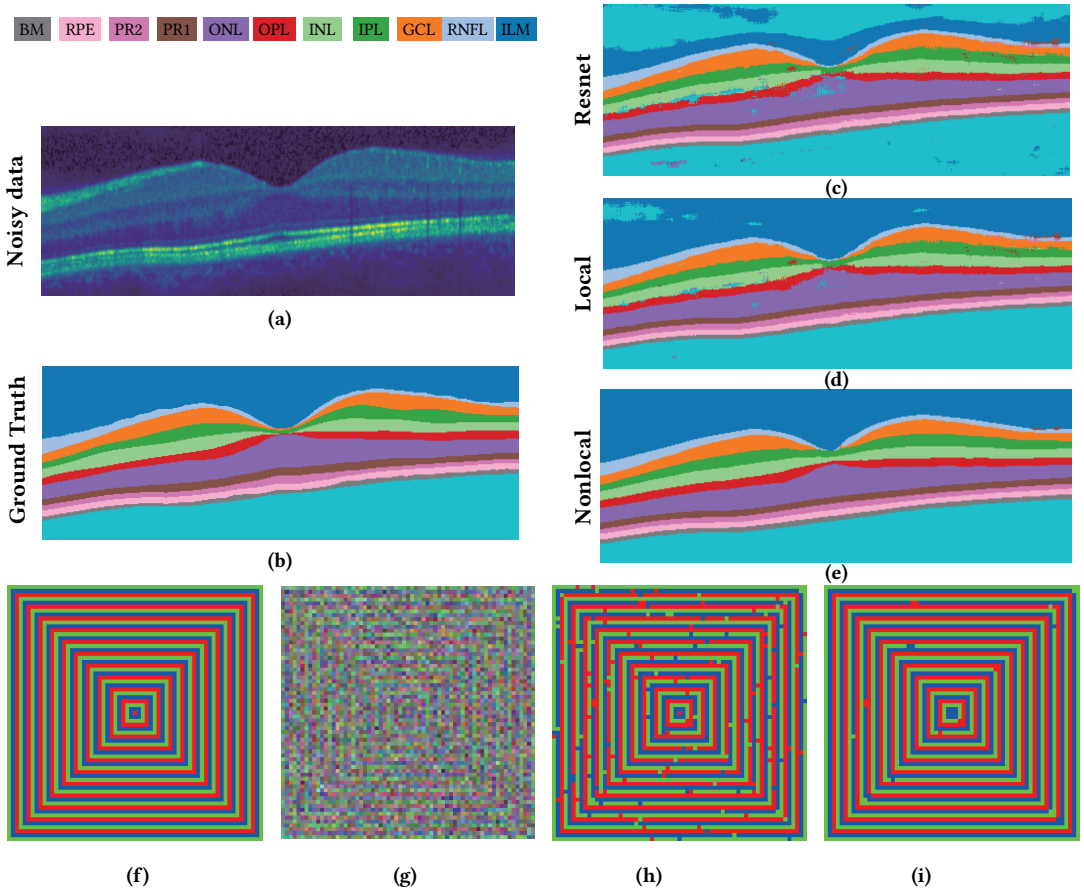


**Figure 5.5.:** Two image labeling scenarios demonstrating the **influence of nonlocal regularization**. **Top**: Application of ordered assignment flow for segmenting the human retina from Chapter 4. **(a)**: A B-scan from a 3D OCT-volume showing a section of the human retina that is corrupted by speckle noise. **(b)**: The corresponding ground truth labeling with ordered retina layers. **(c)**: Output from a Resnet that serves as the distance matrix (5.21). **(d)**: Result of applying assignment flow with local neighborhoods given by a 3D seven point stencil. **(e)**: Labeling obtained with *nonlocal* uniform neighborhoods of size $|\mathcal{N}| = 11 \times 11 \times 11$. Increasing the connectivity leads to more accurate labeling that satisfy the ordering constraint depicted in (b). **Bottom**: Labeling of noisy data by assignment flows with data-driven parameters $\Omega$ determined by nonlocal means [BCM10] using patches of size $7 \times 7$ pixels. **(f)**: Synthetic image with thin repetitive structure. **(g)**: Severly corrupted input image to be labeled with $\mathcal{X}^* = \{$ 9, 10, 11 $\}$. **(h)**,**(i)**: Labeling by the assignment flow that was regularized with neighborhood sizes $|\mathcal{N}| = 3 \times 3$ and $|\mathcal{N}| = 11 \times 11$, respectively. Enlarging the neighborhood size $|\mathcal{N}|$ increases labeling accuracy.

**Lemma 5.3.1.** *Let*

$$\begin{aligned} &\alpha \in \mathcal{F}_{\overline{\mathcal{V}}\times\overline{\mathcal{V}}}, && \alpha(y,x) = -\alpha(x,y), && \forall x,y \in \mathcal{F}_{\overline{\mathcal{V}}\times\overline{\mathcal{V}}}, \\ &\Theta \in \mathcal{F}_{\overline{\mathcal{V}}\times\overline{\mathcal{V}}}, && \Theta(x,y) = \Theta(y,x) \geq 0, && \forall x,y \in \mathcal{F}_{\overline{\mathcal{V}}\times\overline{\mathcal{V}}}, \end{aligned} \tag{5.37}$$

*be anti-symmetric and nonnegative symmetric mappings, respectively. Assume further that $\alpha$ satisfies*

$$\alpha(x,y) = 0, \qquad \forall x,y \in \mathcal{V}_{\mathcal{I}}^{\alpha}. \tag{5.38}$$

*Then, for neighborhoods $\mathcal{N}(x)$ defined by (5.5) and with parameter matrix*

$$\Omega(x,y) = \begin{cases} \Theta(x,y)\alpha^2(x,y), & \text{if } x \neq y, \\ \Theta(x,x), & \text{if } x = y, \end{cases} \qquad x,y \in \mathcal{V}, \tag{5.39}$$

*for each function $f \in \mathcal{F}_{\overline{\mathcal{V}}}$ with $f|_{\mathcal{V}_{\mathcal{I}}^{\alpha}} = 0$, the identity*

$$\sum_{y\in\mathcal{V}} \Omega(x,y)f(y) = \frac{1}{2}\mathcal{D}^{\alpha}\big(\Theta\mathcal{G}^{\alpha}(f)\big)(x) + \lambda(x)f(x), \qquad \forall x \in \mathcal{V}, \quad \forall f \in \mathcal{F}_{\overline{\mathcal{V}}}\colon f\big|_{\mathcal{V}_{\mathcal{I}}^{\alpha}} = 0 \tag{5.40}$$

*holds with $\mathcal{D}^{\alpha}, \mathcal{G}^{\alpha}$ given by (5.12),(5.16) and*

$$\lambda(x) = \sum_{y\in\overline{\mathcal{V}}} \Theta(x,y)\alpha^2(x,y) + \Theta(x,x), \quad x \in \mathcal{V}. \tag{5.41}$$

*In addition, if $\lambda(x) \leq 1$ in (5.41) for all $x \in \mathcal{V}$, then $\Omega$ given by (5.39) satisfies (5.4), and equality $\lambda(x) = 1, \forall x \in \mathcal{V}$ is achieved if property (5.24) holds.*

*Proof.* Appendix A.5.

**Remark 5.3.2 (Comments).** Lemma 5.3.1 characterizes a class of parameter matrices $\Omega$ whose action (5.40) admits an representation using the nonlocal operators from Section 5.2.

Some comments follow on parameter matrices *not* covered by Lemma 5.3.1, due to the imposed constraints.

(i) By ignoring the *nonnegativity constraint* of (5.37) imposed on $\Omega$ through the mapping $\Theta$, Lemma 5.3.1 additionally covers a class of nonlocal graph Laplacians proposed in [ETT15] and [GO09] for the aim of image inpainting. We refer to Section 5.4 for a more detailed discussion.

(ii) Due to assuming *symmetry* of the mapping $\Theta$, formulation (5.39) does *not* cover nonlocal diffusion processes on *directed* graphs $(\mathcal{V}, \mathcal{E}, \Omega)$.

(iii) Imposing *zero nonlocal Dirichlet boundary conditions* is essential for relating assignment flows to the specific class of nonlocal PDEs related to (5.40), see Proposition 5.3.1 below.

As argued in [ZZS20] by a range of counterexamples, using nonsymmetric parameter matrices $\Omega$ compromises convergence of the assignment flow (5.27a) to integral solutions (labelings) and is therefore not considered. The study of more general parameter matrices is left for future work, see Section 5.8 and Section 5.4.1 for modifying the identity (5.40) in view of nonsymmetric parameter matrices $\Omega$.

Next, we generalize the common *local* boundary conditions for PDEs to nonlocal *volume constraints* for *nonlocal* PDEs on discrete domains. Following [DGLZ12], given an antisymmetric mapping $\alpha$ as in (5.10) and Lemma 5.3.1, the natural domains $\mathcal{V}_{\mathcal{I}_N}^{\alpha}, \mathcal{V}_{\mathcal{I}_D}^{\alpha}$ for imposing nonlocal *Neumann* and *Dirichlet* constraints are given by a disjoint decomposition of the interaction domain (5.10)

$$\mathcal{V}_{\mathcal{I}}^{\alpha} = \mathcal{V}_{\mathcal{I}_N}^{\alpha} \dot{\cup} \mathcal{V}_{\mathcal{I}_D}^{\alpha}. \tag{5.42}$$

The following proposition reveals how the flow (5.27a), with $\Omega$ satisfying the assumptions of Lemma 5.3.1, can be reformulated as a nonlocal partial difference equation with zero nonlocal Dirichlet boundary condition imposed on the entire interaction domain, i.e. $\mathcal{V}_{\mathcal{I}}^{\alpha} = \mathcal{V}_{\mathcal{I}_D}^{\alpha}$. Recall the definition of the manifold $\mathcal{S}$ of discrete probability vectors with full support in connection with Eq. (3.47).

**Proposition 5.3.1.** ***(S-flow as nonlocal G-PDE)*** *Let $\alpha, \Theta \in \mathcal{F}_{\overline{\mathcal{V}}\times\overline{\mathcal{V}}}$ be as in (5.38). Then the flow (5.27a) with $\Omega$ given through (5.39) admits the representation*

$$\partial_t S(x,t) = R_{S(x,t)}\Big(\frac{1}{2}\mathcal{D}^{\alpha}\big(\Theta \mathcal{G}^{\alpha}(S)\big) + \lambda S\Big)(x,t), \qquad \text{on } \mathcal{V}\times\mathbb{R}_+, \tag{5.43a}$$

$$\overline{S}(x,t) = 0, \qquad \text{on } \mathcal{V}_{\mathcal{I}}^{\alpha}\times\mathbb{R}_+, \tag{5.43b}$$

$$S(x,0) = \overline{S}(x)(0), \qquad \text{on } \overline{\mathcal{V}}\times\mathbb{R}_+, \tag{5.43c}$$

*where $\lambda = \lambda(x)$ is given by (5.38) and $\overline{S} \in \mathcal{F}_{\overline{\mathcal{V}},\mathbb{R}_+^c}$ denotes the zero extension of the $\mathcal{S}$-valued vector field $S \in \mathcal{F}_{\mathcal{V},\mathcal{S}}$ to the interaction domain $\mathcal{V}_{\mathcal{I}}^{\alpha}$.*

*Proof.* Appendix A.5.

Proposition 5.3.1 states the equivalence of the potential flow (5.27a), with $\Omega$ defined by (5.39), and the nonlocal diffusion process (5.43) with zero nonlocal Dirichlet boundary condition. We now explain that the system (5.43a) can represent *any* descent flow of the form (5.27a) defined in terms of an *arbitrary* nonnegative symmetric mapping $\Omega \in \mathcal{F}_{\mathcal{V}\times\mathcal{V}}$. Specifically, given such a mapping $\Omega$, let the mappings $\widetilde{\alpha}, \widetilde{\Theta} \in \mathcal{F}_{\mathcal{V}\times\mathcal{V}}$ be defined by

$$\widetilde{\Theta}(x,y) = \begin{cases} \Omega(x,y) & \text{if } y \in \mathcal{N}(x), \\ 0 & \text{else} \end{cases}, \qquad \widetilde{\alpha}^2(x,y) = 1, \qquad x,y \in \mathcal{V}. \tag{5.44}$$

Further, denote by $\Theta, \alpha \in \mathcal{F}_{\overline{\mathcal{V}}\times\overline{\mathcal{V}}}$ the extensions of $\widetilde{\alpha}, \widetilde{\Theta}$ to $\overline{\mathcal{V}}\times\overline{\mathcal{V}}$ by 0, that is

$$\Theta(x,y) = \big(\delta_{\mathcal{V}\times\mathcal{V}}(\widetilde{\Theta})\big)(x,y), \quad \alpha(x,y) := \big(\delta_{\mathcal{V}\times\mathcal{V}}(\widetilde{\alpha})\big)(x,y) \quad x,y \in \overline{\mathcal{V}}, \tag{5.45}$$

where $\delta_{\mathcal{V}\times\mathcal{V}} \colon \mathbb{Z}^d \times \mathbb{Z}^d \to \{0,1\}$ is the indicator function of the set $\mathcal{V}\times\mathcal{V} \subset \mathbb{Z}^d \times \mathbb{Z}^d$. Then the potential flow (5.27a) with $\Omega$ satisfying $\Omega(x,y) = \Omega(y,x)$ is equivalently represented by the system (5.43) with an empty interaction domain (5.10). This shows how Proposition 5.3.1 generalizes the assignment flow introduced in Section 3.2.2 by ignoring the constraint (5.24) imposed on $\Omega$, and thus enables to use a broader class of parameter matrices $\Omega$ controlling the labeling process; see also Remark 5.3.2.

### 5.3.3. Tangent-Space Parametrization of the $S$-Flow G-PDE

Because $S(x,t)$ solving (5.43) evolves on the non-Euclidean space $\mathcal{S}$, applying some standard discretization in order to evaluate (5.43) numerically will not work. Therefore, motivated by the

work [ZSPS20] on the geometric numerical integration of the original assignment flow system (3.63), we devise a parametrization of (5.43) on the *flat* tangent space (3.50) by means of the equation

$$S(t) = \exp_{S^0}(V(t)) \in \mathcal{W}, \qquad V(t) \in \mathcal{T}_0, \qquad S^0 = S(0) \in \mathcal{W}, \tag{5.46}$$

where analogous to (5.29)

$$\exp_{S^0}(V(t)) = \big(\dots, \exp_{S^0(x)}(-V(x,t)), \dots\big)^\top \in \mathcal{W} \tag{5.47}$$

with $\exp_{S^0(x)}$ given by (3.54). Applying $\frac{d}{dt}$ to both sides and using the expression of the differential of the mapping $\exp_{S^0}$ due to [SS21, Lemma 3.1], we get

$$\dot{S}(t) = R_{\exp_{S^0}(V(t))}\dot{V}(t) \overset{(5.46)}{=} R_{S(t)}\dot{V}(t). \tag{5.48}$$

Comparing this equation and (5.27a), and taking into account $R_S = R_S\Pi_0$, shows that $V(t)$ solving the nonlinear ODE

$$\dot{V}(t) = \Pi_0 \Omega \exp_{S^0}(V(t)), \qquad V(0) = 0 \tag{5.49}$$

determines $S(t)$ by (5.46) solving (5.27a). Hence it suffices to focus on (5.49) which evolves on the flat space $\mathcal{T}_0$. Repeating the derivation above that resulted in the G-PDE representation (5.43) of the $S$-flow (5.27a), yields the nonlinear PDE representation of (5.49)

$$\partial_t V(x,t) = \Big(\frac{1}{2}\mathcal{D}^\alpha\big(\Theta\mathcal{G}^\alpha(\exp_{S^0}(V))\big) + \lambda \exp_{S^0}(V)\Big)(x,t) \qquad \text{on } \mathcal{V}\times\mathbb{R}_+, \tag{5.50a}$$

$$\overline{V}(x,t) = 0 \qquad \text{on } \mathcal{V}_\mathcal{I}^\alpha \times \mathbb{R}_+, \tag{5.50b}$$

$$V(x,0) = \overline{V}(x)(0) \qquad \text{on } \overline{\mathcal{V}}\times\mathbb{R}_+, \tag{5.50c}$$

where $\overline{V} \in \mathcal{F}_{\overline{\mathcal{V}},\mathcal{T}_0}$ denotes the zero extension of the $\mathcal{T}_0$-valued vector field to the interaction domain $\mathcal{V}_\mathcal{I}^\alpha$. From the numerical point of view, this new formulation (5.46), (5.50) has the following expedient properties. Firstly, using a parameter matrix as specified by (5.39) and (5.45) enables to define the entire system (5.50) on $\mathcal{V}$. Secondly, since $V(x,t)$ evolves on the flat space $T_0$, numerical techniques of geometric integration as studied by [ZSPS20] can here be applied as well. We utilize this fact in Section 5.3.5 and in Section 5.5.

### 5.3.4. Nonlocal Balance Law

A key property of PDE-based models are balance laws implied by the model; see [DGLZ13, Section 7] for a discussion of various scenarios. The following proposition reveals a *nonlocal* balance law of the assignment flow based on the novel G-PDE-based parametrization (5.50), that we express for this purpose in the form

$$\partial_t V(x,t) + \mathcal{D}^\alpha(F(V))(x,t) = b(x,t), \qquad b(x,t) = \lambda(x)S(x,t), \qquad x \in \mathcal{V}, \tag{5.51a}$$

$$F(V(t))(x,y) = -\frac{1}{2}\Big(\Theta\mathcal{G}^\alpha\big(\exp_{S^0}(V(t))\big)\Big)(x,y), \tag{5.51b}$$

where $S(x,t) = \exp_{S^0}(V(x,t))$ is given by (5.46) and $\lambda(x)$ is given by (5.41).

**Proposition 5.3.2 (nonlocal balance law of assignment flows).** *Under the assumptions of Lemma 5.3.1, let $V(t)$ solve (5.50). Then, for each component $S_j(t) = \{S_j(x,t) \colon x \in \mathcal{V}\}$, $j \in [c]$, of $S(t) = \exp_{S^0}(V(t))$, the identity*

$$\begin{aligned} \frac{1}{2}\frac{d}{dt}\langle S_j, \mathbb{1}\rangle_{\mathcal{V}} + \frac{1}{2}\langle \mathcal{G}^\alpha(S_j), \Theta\mathcal{G}^\alpha(S_j)\rangle_{\overline{\mathcal{V}}\times\overline{\mathcal{V}}} + \langle S_j, \phi_S - \lambda S_j\rangle_{\mathcal{V}} \\ + \langle S_j, \mathcal{N}^\alpha(\Theta\mathcal{G}^\alpha(S_j))\rangle_{\mathcal{V}_{\mathcal{I}^\alpha}} = 0 \end{aligned} \tag{5.52}$$

*holds, where the inner products are given by (5.7) and (5.8), and $\phi_S(\cdot) \in \mathcal{F}_{\mathcal{V}}$ is defined in terms of $S(t) \in \mathcal{W}$ by*

$$\phi_S : \mathcal{V} \to \mathbb{R}, \qquad x \mapsto \big\langle S(x), \Pi_0\big(\Omega S\big)(x)\big\rangle. \tag{5.53}$$

*Proof.* Appendix A.5.1.

The nonlocal balance law (5.52) comprises four terms. Since $\sum_{j\in[c]} S_j(x) = 1$ at each vertex $x \in \mathcal{V}$, the first term of (5.52) measures the *rate of 'mass'* assigned to label $j$ over the entire image. This rate is governed by two interacting processes corresponding to the three remaining terms:

(i) *spatial propagation of assignment mass* through the nonlocal diffusion process including nonlocal boundary conditions (second and fourth term);

(ii) *exchange of assignment mass* with the remaining labels $\{l \in [c] \colon l \neq j\}$ (third term comprising the function $\phi_S$ (5.53)).

We point out that other approaches to image labeling, including Markov random fields and deep networks, do *not* reveal the flow of information during inference in such an explicit manner.

### 5.3.5. Illustration: Parametrization and Nonlocal Boundary Conditions

In this section, we illustrate two aspects of the mathematical results presented above by numerical results:

(1) The use of *geometric integration* for numerically solving the nonlocal G-PDE (5.43). Here we exploit a basic numerical scheme established for the assignment flow (5.27a) and the one-to-one correspondence to the nonlocal G-PDE (5.43), due to Proposition 5.3.1.

(2) The effect of zero vs. non-zero nonlocal Dirichlet boundary conditions and uniform vs. non-uniform parametrizations (5.39). Using non-zero boundary conditions refers to the observation stated above in connection with Equations (5.44), (5.45): the nonlocal G-PDE (5.43) generalizes the assignment flow when constraints are dropped. Here specifically: the homogeneous Dirichlet boundary condition may be non-homogeneous, and the constraint (5.24) is ignored; see also Remark 5.3.2.

Topic (1) is addressed here to explain how the results illustrating topic (2) were computed, and to set the stage for Section 5.5 that presents an advanced numerical scheme. Item (2) merely illustrates basic choices of the parametrization and boundary conditions. More advanced generalizations of the assignment flow are conceivable, but beyond the scope of this thesis; see Section 5.8.

### Numerically Solving the Nonlocal G-PDE By Geometric Integration

According to Section 5.3.3, imposing the homogeneous Dirichlet condition via the interaction domain (5.10) makes the right-hand side of (5.50a) equivalent to (5.49). Applying to (5.50a) a simple explicit time discretization with stepsize $h$ results in the iterative update formula

$$V(x,t+h) \approx V(x,t) + h\Pi_0 \exp_{S^0(x)}(\Omega V(x,t)), \qquad h > 0. \tag{5.54}$$

By virtue of the parametrization (5.46), one recovers with any nonnegative symmetric mapping $\Omega$ as in Lemma 5.3.1 the *explicit geometric Euler* scheme on $\mathcal{W}$

$$S(t+h) \approx \exp_{S^0}\left(V(t) + h\dot{V}(t)\right) \overset{(5.46)}{=} \exp_{S(t)}\left(h\dot{V}(t)\right) \tag{5.55a}$$

$$\overset{\substack{(5.30)\\(5.49)}}{=} \exp_{S(t)}\left(h\Omega S(t)\right). \tag{5.55b}$$

Higher order geometric integration methods [ZSPS20] generalizing (5.55) can be applied in a similar way. This provides new perspective on solving a certain class of nonlocal G-PDEs numerically, conforming to the underlying geometry, as we demonstrate in Section 5.5.2.

### Basic Parametrizations, Effect of Nonlocal Dirichlet Boundary Conditions

We consider two different parametrizations as well as zero and non-zero nonlocal Dirichlet boundary conditions.

**Uniform parametrization** Mappings $\Theta, \alpha \in \mathcal{F}_{\overline{\mathcal{V}}\times\overline{\mathcal{V}}}$ are given by

$$|\mathcal{N}(x)| = \mathcal{N},\ \forall x, \qquad |\mathcal{N}| = (2k+1)\times(2k+1),\ k \in \mathbb{N} \tag{5.56a}$$

$$\alpha^2(x,y) = \begin{cases} \frac{1}{(2k+1)^2} & \text{if } y \in \mathcal{N}(x) \\ 0 & \text{otherwise} \end{cases}, \qquad \Theta(x,y) = \begin{cases} \frac{1}{(2k+1)^2} & \text{if } x = y \\ 1 & \text{otherwise} \end{cases}. \tag{5.56b}$$

**Nonuniform parametrization** Uniform neighborhoods as in (5.56a) and mappings $\Theta, \alpha \in \mathcal{F}_{\overline{\mathcal{V}}\times\overline{\mathcal{V}}}$ by

$$\begin{aligned} \alpha^2(x,y) &= \begin{cases} e^{-\frac{\|x-y\|^2}{2\sigma_s^2}} & \text{if } y \in \mathcal{N}(x) \\ 0 & \text{otherwise} \end{cases}, && \sigma_s > 0, \\ \Theta(x,y) &= \begin{cases} e^{-G_{\sigma_p} * \|s(x)-s(y)\|^2} & \text{if } y \in \mathcal{N}(x) \\ 0 & \text{otherwise} \end{cases}, && \sigma_p > 0, \end{aligned} \tag{5.57}$$

where the nonlocal function $\Theta$ is designed using a patchwise similarity measure analogous to the basic nonlocal means approach [BCM10]: $s(x) = \{s(x,z) \colon z \in \overline{\mathcal{V}}, s(x,z) = \overline{X}(z)\}$ with $\overline{X} \in \mathcal{F}_{\overline{\mathcal{V}},\mathbb{R}^c}$ denoting the zero extension of data $X \in \mathcal{F}_{\mathcal{V},\mathbb{R}^c}$ to $\mathcal{V}_{\mathcal{I}}^{\alpha}$. $G_{\sigma_p}$ is the Gaussian kernel at scale $\sigma_p$ and $*$ denotes spatial convolution.

We iterated (5.55) with step size $h = 1$ until assignment states (5.27b) of low average entropy $10^{-3}$ were reached. To ensure a fair comparison and to assess solely the effects of the boundary conditions through nonlocal regularization, we initialized (5.43) in the same way as (5.27a) and adopted an uniform encoding of the 31 labels as described by [ÅPSS17, Figure 6].

Figure 5.6 depicts labelings computed using the uniform parametrization with zero and non-zero nonlocal Dirichlet boundary conditions, respectively. Inspecting panels (c) (zero boundary condition) and (d) (non-zero boundary condition) shows that using the latter may improve labeling near the boundary (cf. close-up views), whereas the labelings almost agree in the interior of the domain.

Figure 5.7 shows how the average entropy values of label assignments decrease as the iteration proceeds (left panel) and the number of iterations required to converge (right panel), for different neighborhood sizes. Moreover, a closer look on the right panel of Figure 5.7 reveals besides a slightly slower convergence of the scheme (5.54) applied to the nonlocal G-PDE (5.50) (red curve), the dependence of number of iterations required until convergence is comparable to the $S$-flow (green curve). Consequently, generalizing the $S$-flow by the nonlocal model (5.43) does not have a detrimental effect on the overall numerical behavior. We observe, in particular, that integral label assignments corresponding to zero entropy are achieved no matter which boundary condition is used, at comparable computational costs.

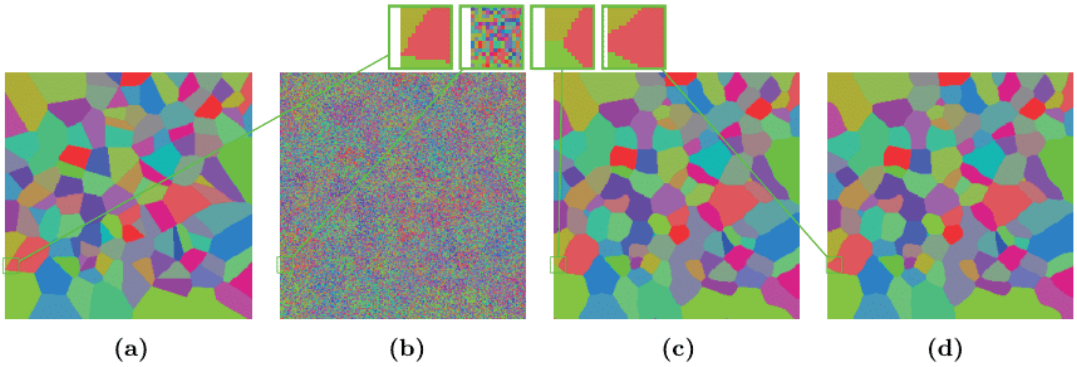


**Figure 5.6.:** Labeling through the nonlocal geometric assignment flow with uniform parametrization (5.56b) and neighborhood size $|\mathcal{N}| = 7$. **(a)** Ground truth with 31 labels. **(b)** Noisy input data used to evaluate (5.27a) and (5.43), respectively. **(c)** Labeling returned when using the zero nonlocal Dirichlet boundary condition. **(d)** Labeling returned when using the non-zero nonlocal Dirichlet boundary condition (uniform extension to the interaction domain). The close-up views show differences close to the boundary, whereas the results in the interior domain are almost equal.

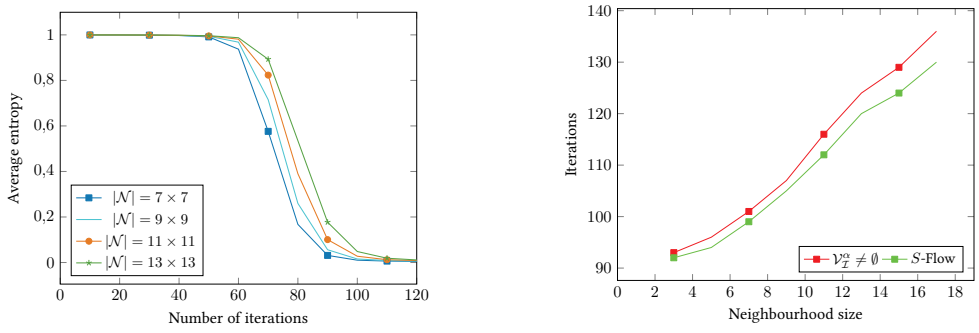


**Figure 5.7.: Left:** Convergence rates of the scheme (5.55) solving (5.43) with nonzero nonlocal Dirichlet boundary condition. The convergence behavior is rather insensitive with respect to the neighborhood size $|\mathcal{N}|$. **Right:** Number of iterations until convergence for (5.43) (2) and (5.27a) (1), with zero nonlocal boundary condition in the latter case. The result shows that different nonlocal boundary conditions have only a minor influence on the required number of geometric integration steps.

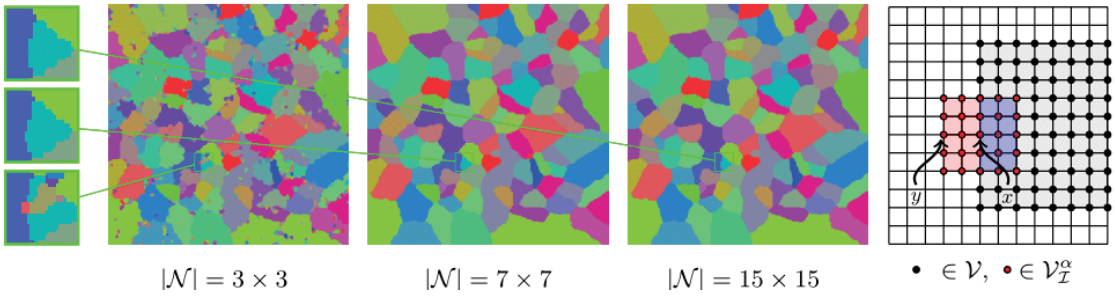


**Figure 5.8.: From left to right:** Labeling results using (5.43) with the non-uniform parametrization (5.57), zero non-local Dirichlet boundary conditions and neighborhood sizes $|\mathcal{N}| \in \{3 \times 3, 7 \times 7, 15 \times 15\}$. Schematic illustration of the nonlocal interaction domain $y \in \mathcal{V}_{\mathcal{I}}^{\alpha}$ (red area) induced by nodes (blue area) in $\mathcal{N}(x)$ with $|\mathcal{N}| = 5 \times 5$. Using nonuniform weights (5.57) improves labeling accuracy.

Iterating (5.55) with step size $h = 0.1$ and $\sigma_s = 1, \sigma_p = 5$ in (5.57) yields labeling results for different patch sizes as depicted by Figure 5.8. As opposed to segmentation results obtained with uniform parametrization (5.56b) for $\mathcal{N} = 7$ depicted in Figure 5.6(d), a direct comparison with Figure 5.8 (close up views) indicates more accurate labelings when using regularization as given by the nonuniform parametrization (5.57).

## 5.4. Related Work

In this section, we discuss how the system (5.43) relates to approaches based on PDEs and variational models in the literature. Specifically, we conduct an *analytical ablation* study of the nonlocal model (5.43) in order to clarify the impact of omitting operators of the nonlocal model and the connection to existing methods. We exhibit both structural similarities from the viewpoint of diffusion processes and differences that account for the *different scope* of our approach: *labeling* metric data on graphs.

### 5.4.1. General Nonlocal Processes on Graphs

We consider again the identity (5.40) that defines the nonlocal G-PDE (5.43) in terms of *symmetric* parameter mapping (5.39) and show next how (5.40) is generalized when a *nonsymmetric* parameter matrix $\Omega \in \mathcal{F}_{\mathbb{Z}^d \times \mathbb{Z}^d}$ is used. Specifically, suppose a kernel $k \in \mathcal{F}_{\mathbb{Z}^d \times \mathbb{Z}^d}$ is given and the induced nonlocal functional

$$\mathcal{L}_k f(x) = \sum_{y \in \mathbb{Z}^d} \big( f(y)k(y,x) - f(x)k(x,y) \big). \tag{5.58}$$

Then, for a mapping $\alpha$ that satisfies $\alpha^2(x,y) = 1$ whenever $k(x,y) \neq 0$, the decomposition

$$k = k^s + k^a \quad \text{with} \quad k^s = \frac{k + k'}{2}, \quad k^a = \frac{k - k'}{2}, \qquad k'(x,y) := k(y,x), \quad x, y \in \mathbb{Z}^d, \tag{5.59}$$

results in the representation

$$k(x,y) = \begin{cases} 2\Theta(x,y)\alpha^2(x,y) + \alpha(x,y)\nu(x,y) & x \neq y, \\ 2\Theta(x,x) & x = y \end{cases} \tag{5.60}$$

of the kernel $k$ in terms of $\alpha, \Theta \in \mathcal{F}_{\mathbb{Z}^d \times \mathbb{Z}^d}$ and $\nu \in \mathcal{F}_{\mathbb{Z}^d \times \mathbb{Z}^d}$ given by

$$\Theta(x,y) := \frac{1}{2} k^s(x,y), \qquad \nu(x,y) := k^a(x,y)\alpha(x,y), \tag{5.61}$$

where the mapping $\nu$ is a symmetric due to the antisymmetry of $\alpha$. Inserting (5.60) into (5.58) yields

$$\mathcal{L}_k f(x) = 2 \sum_{y \in \mathbb{Z}^d} \Theta(x,y)\alpha^2(x,y)\big(f(y) - f(x)\big) - \sum_{y \in \mathbb{Z}^d} \alpha(x,y)\nu(x,y)\big(f(y) - f(x)\big). \tag{5.62}$$

and applying nonlocal calculus of Section 5.2 along with Lemma (5.3.1), we arrive at an equivalent representation of $\mathcal{L}_k$ through nonlocal divergence and gradient operators

$$\mathcal{L}_k f(x) \overset{(5.60)}{=} \underbrace{\mathcal{D}^\alpha\big(\Theta \mathcal{G}^\alpha(f)\big)(x)}_{\text{diffusion}} - \underbrace{\mathcal{D}^\alpha(\nu f)(x)}_{\text{convection}} + \underbrace{\lambda(x) f(x)}_{\text{fidelity}}, \tag{5.63}$$

where $\nu$ plays the role of the convection parameter. Consequently, on a grid graph $\mathcal{G}$ with $\mathcal{V} \subset \mathbb{Z}^d$ and setting $\Omega$ by (5.60), we get

$$\partial_t S(x,t) = R_{S(x,t)}\Big(\mathcal{D}^\alpha\big(\Theta \mathcal{G}^\alpha(S)\big) - \mathcal{D}^\alpha(\nu S)\Big)(x,t) + \lambda(x) S(x,t) \qquad \text{on} \quad \mathcal{V} \times \mathbb{R}_+, \tag{5.64a}$$

$$\overline{S}(x,t) = 0 \qquad \text{on} \quad \mathcal{V}_{\mathcal{I}}^\alpha \times \mathbb{R}_+, \tag{5.64b}$$

$$\overline{S}(x,0) = S(x)(0) \qquad \text{on} \quad \overline{\mathcal{V}} \times \mathbb{R}_+, \tag{5.64c}$$

with the interaction domain (5.10) directly expressed through the connectivity of kernel $k$ by

$$\mathcal{V}_{\mathcal{I}}^\alpha = \{x \in \mathbb{Z}^d \setminus \mathcal{V} \colon k(x,y) \neq 0 \text{ for some } y \in \mathcal{V}\}. \tag{5.65}$$

In view of (5.64), we therefore recognize the system (5.43) as *specific* nonlocal process that is induced by a *nonnegative symmetric* kernels $k$ with nonzero fidelity parameter $\lambda$, that account for nontrivial steady state solutions and zero convection ($\nu(x,y) = 0$).

| | **Labeling** | | **Denoising and Inpainting** | |
|---|---|---|---|---|
| **Parameters** | **G-PDE** (5.43) | **Local PDE** [SS21] | **Nonl. Laplacian** [ETT15] | **Descent Flow** [GO09] |
| $\Theta \geq 0$ | ✓ | ✗ | ✗ | ✗ |
| $\lambda$ | $\lambda > 0$ | $\lambda = 1$ | $\lambda = 0$ | $\lambda = 0$ |
| $R_S$ | ✓ | ✓ | ✗ | ✗ |
| $\nu$ | ✗ | ✗ | ✗ | ✗ |
| $\mathcal{V}_{\mathcal{I}}^\alpha$ | $\subseteq \mathbb{Z}^d \setminus \mathcal{V}$ | $\partial \mathcal{V}^h$ | $\partial \mathcal{A} \subset \mathcal{V}$ | $\emptyset$ |
| $S^*(t \to \infty)$ | ✓ | ✓ | ✗ | ✗ |

**Table 5.1.: Summary of the analytical ablation study.** Key differences of our approach to existing nonlocal diffusion models are inclusion of the replicator operator $R_S$ and a nonzero fidelity term $\lambda S$ that results in nontrivial solution at the steady state $S^* = S(t = \infty)$.

In the following sections, we relate different established nonlocal models to the proposed G-PDE (5.43) by adapting the parameter mappings $\Theta, \alpha \in \mathcal{F}_{\overline{\mathcal{V}} \times \overline{\mathcal{V}}}$ that parametrize the G-PDE and determine the interaction domain (5.10). Figure 5.9 provides an overview of the analytical ablation study by specifying the model and the corresponding section where it is derived from the generalized G-PDE (5.64). Table 5.1 lists the involved parameters for each model.

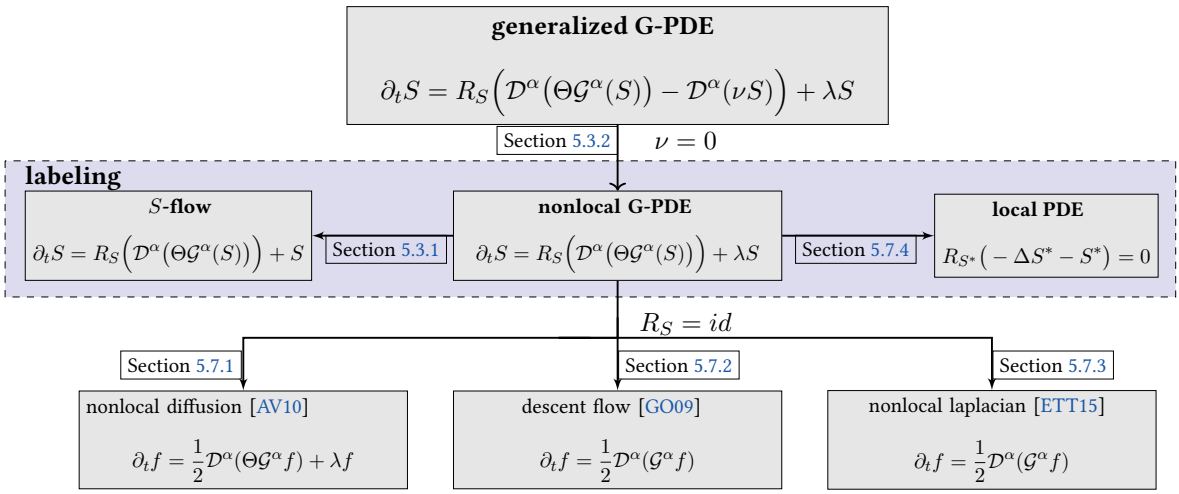


**Figure 5.9.: Overview of nonlocal diffusion processes** proposed in related work [ETT15; GO09; AV10] and their interrelations to the nonlocal G-PDE (5.64). The approaches highlighted by the blue region only model the image labeling problem. Edge labels refer to the corresponding sections of the analytical ablation study.

## 5.4.2. Relation to a Local PDE that Characterizes Labelings

We focus on the connection of the system (5.43) and the *continuous-domain local* formulation of (5.27a) on an open simply connected bounded domain $\mathcal{D} \subset \mathbb{R}^2$, as introduced by [SS21]. The *variational* formulation has been rigorously derived in [SS21] along with a PDE that formally characterizes solutions $S^* = \lim_{t\to\infty} S(t) \in \overline{\mathcal{W}}$ only under strong regularity assumptions. This nonlinear PDE reads

$$R_{S^*(x)}\big(-\Delta S^*(x) - S^*(x)\big) = 0, \quad x \in \mathcal{D}. \tag{5.66}$$

We next show that our novel approach (5.43) includes, as a special case, a natural discretization of (5.66) on the spatial discrete grid $\mathcal{V}^h = h\mathbb{Z}^d \cap \mathcal{D}$ with boundary $\partial\mathcal{V}^h$ specified by a small spatial scale parameter $h > 0$. (5.66) is complemented by *local zero Dirichlet* boundary conditions imposed on $S^*$ on $\partial\mathcal{V}^h$. Adopting the sign convention $L^h_\vartheta = -\Delta^h_\vartheta$ for different discretizations of the *continuous negative Laplacian* on $\mathcal{V}^h$, by a nine-point stencil [WW20] parametrized by $\vartheta \in [0,1]$, lead to strictly positive entries $L^h_\vartheta(x,x) > 0$ on the diagonal.

We introduce the weighted undirected graph $(\mathcal{V}^h, \Omega^h)$ and identify nodes $x = (k,l) \in \mathcal{V}^h$ with interior grid points $(hk, hl) \in \mathcal{V}^h$ (grid graph). Let the parameter matrix $\Omega^h$ be given by (5.39) and the mappings $\alpha, \Theta \in \mathcal{F}_{\overline{\mathcal{V}}\times\overline{\mathcal{V}}}$ defined by

$$\alpha^2(x,y) = \begin{cases} 1, & y \in \widetilde{\mathcal{N}}(x), \\ 0, & \text{else}, \end{cases}, \qquad \Theta(x,y) = \begin{cases} -L^h_\vartheta(x,y), & y \in \widetilde{\mathcal{N}}(x), \\ 1 - L^h_\vartheta(x,x), & x = y, \\ 0 & \text{else}, \end{cases} \tag{5.67}$$

where the neighborhoods $\widetilde{\mathcal{N}}(x) = \mathcal{N}(x) \setminus \{x\}$ represent the connectivity of the stencil of the discrete Laplacian $L^h_\vartheta$ on the mesh $\mathcal{V}^h \dot\cup \partial\mathcal{V}^h$. Recalling the definitions from Section 5.2 with respect to undirected graphs and setting $\alpha$ by (5.67), the interaction domain (5.10) agrees for parameter choices $\vartheta \neq 0$ with the discrete local boundary, i.e. $\mathcal{V}^\alpha_{\mathcal{I}} = \partial\mathcal{V}^h$; see Figure 5.10 and

the caption for further explanation. Then, for each $x \in \mathcal{V}^h$, the action of $\Omega^h$ on $S$ reads

$$(\Omega^h S)(x) = \sum_{y \in \widetilde{\mathcal{N}}(x)} -L^h_\vartheta(x,y)S(y) + \big(1 - L^h_\vartheta(x,x)\big)S(x) = -\big(-\Delta^h_\vartheta(S) - S\big)(x), \tag{5.68}$$

which is the discretization of (5.66) by $L^h_\vartheta$ multiplied by the minus sign. In particular, due to the

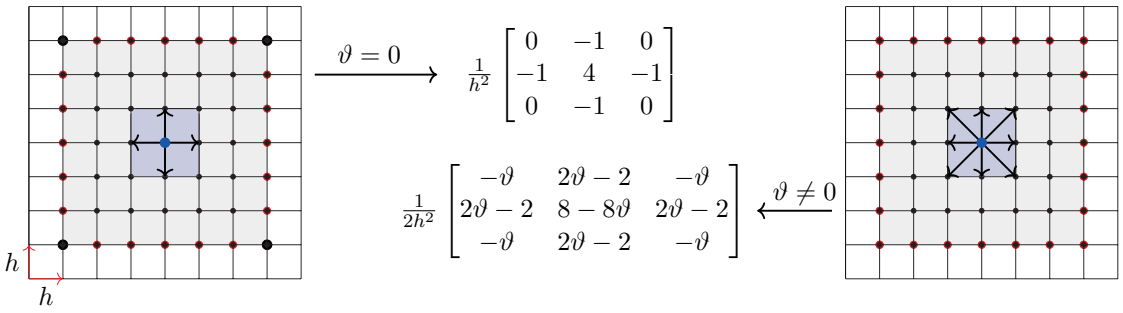


**Figure 5.10.:** Illustration of the rectangular grid $\mathcal{V}^h$ and the interaction domain $\mathcal{V}^\alpha_I$ represented by (•) and (●), respectively, with $\alpha \in \mathcal{F}_{\overline{\mathcal{V}} \times \overline{\mathcal{V}}}$ given by (5.67) for a family of discrete Laplacians $-\Delta^h_\vartheta$ proposed in [WW20]. **Left**: Neighborhood $\widetilde{\mathcal{N}}(x)$ specified in terms of the connectivity of the standard 5−point stencil ($\vartheta = 0$). The corresponding interaction domain is part of the local boundary $\mathcal{V}^\alpha_I \subset \partial\mathcal{V}^h$. **Right**: Analogous construction with the 9-point stencil ($\vartheta \neq 0$). The interaction domain coincides with the discrete local boundary configuration, i.e. $\mathcal{V}^\alpha_I = \partial\mathcal{V}^h$.

relation $R_S(-W) = -R_S(W)$ for $W \in \mathcal{W}$, we conclude that the novel approach (5.43) includes the *local* PDE (5.66) as special case and hence provides a *natural nonlocal extension.*

### 5.4.3. Continuous-Domain Nonlocal Diffusion Processes

We follow [AV10]. Consider a bounded domain $\mathcal{D} \subset \mathbb{R}^d$ and let $J : \mathbb{R}^d \to \mathbb{R}_+$ be a radial continuous function satisfying

$$\int_{\mathbb{R}^d} J(x-y)\mathrm{d}y = 1, \quad J(0) > 0 \qquad \forall x \in \mathbb{R}^d. \tag{5.69}$$

The term $J(x-y)$ in (5.69) may be interpreted as a probability density governing jumps from position $y \in \mathbb{R}^d$ to $x \in \mathbb{R}^d$. The authors of [AV10] introduced the integral operator

$$\mathcal{L}f(x) = \int_{\mathbb{R}^d} J(x-y)f(y,t)\mathrm{d}y - f(x,t), \quad x \in \mathbb{R}^d \tag{5.70}$$

acting on $f \in C(\mathbb{R}^d, \mathbb{R}_+)$ and studied *nonlocal linear* diffusion processes of the form

$$\partial_t f(x,t) = \mathcal{L}f(x,t) \qquad \text{on} \quad \mathcal{D} \times \mathbb{R}_+ \tag{5.71a}$$
$$f(x,t) = g(x) \qquad \text{on} \quad \mathbb{R}^d \setminus \mathcal{D} \times \mathbb{R}_+, \tag{5.71b}$$
$$f(x,0) = f_0 \qquad \text{on} \quad \mathbb{R}^d \times \mathbb{R}_+, \tag{5.71c}$$

where $f_0 \in C(\mathcal{D}, \mathbb{R}_+)$ and $g \in C(\mathbb{R}^d \setminus \mathcal{D}, \mathbb{R}_+)$ specify the initial state and the nonlocal boundary condition of the system (5.71), respectively. We compare this system with our model (5.43) and

introduce, as in Section 5.4.3, the weighted undirected graph $(\mathcal{V}^h, \Omega^h)$ with a Cartesian mesh $\mathcal{V}^h$, with boundary $\partial\mathcal{V}^h$ and neighborhoods (5.5), and with $\Omega^h$ defined by (5.44) through

$$\Theta(x,y) = \begin{cases} 0, & \text{for } x,y \notin \mathcal{V}^h, \\ J(0) - 1, & \text{for } x = y, \\ 1, & \text{else}, \end{cases} \qquad \alpha^2(x,y) = J(x-y). \tag{5.72}$$

Then, for the particular case $g = 0$ in (5.71b) and using Equation (5.40) with $\lambda(x)$ defined by (5.41), the spatially discrete counterpart of (5.71) is the *linear nonlocal scalar-valued* diffusion process

$$\partial_t f(x,t) = \frac{1}{2}\mathcal{D}^\alpha(\Theta\mathcal{G}^\alpha f)(x,t) + \lambda(x) f(x,t) \qquad \text{on} \quad \mathcal{V} \times \mathbb{R}_+, \tag{5.73a}$$

$$f(x,t) = 0 \qquad \text{on} \quad \mathcal{V}_{\mathcal{I}}^\alpha \times \mathbb{R}_+, \tag{5.73b}$$

$$f(x,0) = \overline{f}_0 \qquad \text{on} \quad \overline{\mathcal{V}} \times \mathbb{R}_+. \tag{5.73c}$$

System (5.73) possess a structure which resembles the structure of nonlinear system (5.43) after dropping the replicator mapping $R_S$ and assuming $S(x) \in \mathbb{R}$ to be a scalar-valued rather than simplex-valued $S(x) \in \mathcal{S}$, as in our approach.

This comparison shows by virtue of the structural similarity that assignment flows may be characterized as genuine nonlocal diffusion processes. Essential differences, i.e. simplex-valued variables and the underlying geometry, reflect the entirely different scope of this process, however: labeling metric data on graphs.

### 5.4.4. Nonlocal Variational Models in Image Analysis

We relate the system (5.73) to variational approaches presented in [GO09] and to graph-based nonlocal PDEs proposed by [ELB08; ETT15].

Based on a scalar-valued positive function $\phi(t)$ which is convex in $\sqrt{t}$ with $\phi(0) = 0$, Gilboa et al. [GO09] studied *isotropic* and *anisotropic nonlocal regularization functionals* on a continuous spatial domain $\mathcal{D} \subset \mathbb{R}^d$ defined in terms of a nonnegative symmetric mapping $\omega : \mathcal{D} \times \mathcal{D} \to \mathbb{R}_+$:

$$J_i^\phi(f) = \int_{\mathcal{D}} \phi(|\nabla_\omega(f)(x)|^2)\mathrm{d}x, \qquad \textbf{(isotropic)} \tag{5.74a}$$

$$J_a^\phi(f) = \int_{\mathcal{D}}\int_{\mathcal{D}} \phi(f(y) - f(x))^2 \omega(x,y)\mathrm{d}y\mathrm{d}x. \qquad \textbf{(anisotropic)} \tag{5.74b}$$

(5.74a) involves the nonlocal graph-based gradient operator which for given neighborhoods $\mathcal{N}(x)$ reads

$$\nabla_\omega f(x) = \big(\ldots, (f(y) - f(x))\sqrt{\omega(x,y)}, \ldots\big)^T, \qquad y \in \mathcal{N}(x). \tag{5.75}$$

Given an initial real valued function $f_0(x)$ on $\Omega$, the variational models of (5.74) define dynamics in terms of the steepest descent flows

$$\partial_t f(x,t) = -\partial_f J_i^\phi(f)(x,t), \qquad \partial_t f(x,t) = -\partial_f J_a^\phi(f)(x,t), \qquad f(x,0) = f_0(x), \tag{5.76}$$

where the variation with respect to $f$ on right hand side of (5.76) is expressed in terms of (5.75) via

$$\partial_f J_i^\phi(f)(x,t) = -2\int_{\mathcal{D}} (f(y,t)-f(x,t))\omega(x,y)\Big(\phi'(|\nabla_\omega f(y,t)|^2)(y) + \phi'(|\nabla_\omega f(x,t)|^2)(x)\Big)\mathrm{d}y, \tag{5.77}$$

$$\partial_f J_a^\phi(f)(x,t) = -4\int_{\mathcal{D}} \big(f(y,t)-f(x,t)\big)\omega(x,y)\phi'\big((f(y,t)-f(x,t))^2\omega(x,y)\big)\mathrm{d}y. \tag{5.78}$$

Then, given a graph $(\mathcal{V},\mathcal{E},\omega)$ with neighborhoods as in Section 5.2, the discrete counterparts of the dynamical systems (5.76) on $\mathcal{V}$ read

$$\dot f(x,t) = \sum_{y\in\mathcal{N}(x)} A^\phi_{\omega,f}(x,y)f(y), \qquad \dot f(x,t) = \sum_{y\in\mathcal{N}(x)} B^\phi_{\omega,f}(x,y)f(y), \tag{5.79}$$

where the mappings $A^\phi_{\omega,f}, B^\phi_{\omega,f} \in \mathcal{F}_{\mathcal{V}\times\mathcal{V}}$ represent explicit expressions of the right-hand sides of (5.76) on $\mathcal{V}$

$$A^\phi_{\omega,f}(x,y) = \begin{cases} 2\omega(x,y)\Big(\phi'(|\nabla_\omega f(y,t)|^2)(y) + \phi'(|\nabla_\omega f(x,t)|^2)(x)\Big) & x\neq y, \\ -2\sum\limits_{\substack{z\in\mathcal{N}(x)\\ z\neq x}} \omega(x,z)\Big(\phi'(|\nabla_\omega f(z,t)|^2)(z) + \phi'(|\nabla_\omega f(x,t)|^2)(x)\Big) & x=y, \end{cases} \tag{5.80a}$$

$$B^\phi_{\omega,f}(x,y) = \begin{cases} 4\omega(x,y)\phi'\big((f(z,t)-f(x,t))^2\omega(x,y)\big) & x\neq y, \\ -4\sum\limits_{\substack{z\in\mathcal{N}(x)\\ z\neq x}} \omega(x,z)\phi'\big((f(z,t)-f(x,t))^2\omega(x,y)\big), & x=y. \end{cases} \tag{5.80b}$$

Depending on the specification of $\phi(t)$, the dynamics governed by the systems (5.79) define nonlinear nonlocal diffusion processes with various smoothing properties according to the mappings (5.80). Specifically, for $\phi(t)=t$, the functionals (5.74) coincide as do the systems (5.79), since the mappings (5.80) do not depend on $f(x,t)$, but only on $\omega$ which is symmetric and nonnegative, and hence agree. Invoking Lemma 5.3.1 with $\Omega\in\mathcal{F}_{\mathcal{V}\times\mathcal{V}}$ defined through (5.80), setting $\Theta,\alpha\in\mathcal{F}_{\mathcal{V}\times\mathcal{V}}$ by $\Theta(x,y)=1, \alpha^2(x,y)=4\omega(x,y), x\neq y$ and $\Theta(x,x)=-4\sum_{y\in\mathcal{N}(x)}\omega(x,y), x\in\mathcal{V}$ yields the decomposition (5.39) which characterizes (5.75) in terms of the nonlocal operators from Section 5.2 if $f_{|\mathcal{V}_{\mathcal{I}}^\alpha}=0$ holds, by means of relation (5.40). Consequently, (5.79) admits the representation by (5.73) for the particular case of zero nonlocal Dirichlet conditions.

While the above approaches are well suited for image denoising and inpainting, our *geometric* approach performs *labeling* of arbitrary metric data on arbitrary graphs.

### 5.4.5. Nonlocal Graph Laplacians

Elmoataz et. al [ETT15] studied discrete nonlocal differential operators on weighted graphs $(\mathcal{V},\mathcal{E},\omega)$. Specifically, based on the nonlocal gradient operator (5.75), a class of Laplacian operators acting on functions $f\in\mathcal{F}_{\mathcal{V}}$ was defined by

$$\mathcal{L}_{\omega,p}f(x) = \begin{cases} \beta^+(x)\sum\limits_{y\in\mathcal{N}^+(x)}\big(\nabla_\omega f(x,y)\big)^{p-1} + \beta^-(x)\sum\limits_{y\in\mathcal{N}^-(x)}(-1)^p\big(\nabla_\omega f(x,y)\big)^{p-1}, & p\in[2,\infty) \\ \beta^+(x)\max\limits_{y\in\mathcal{N}^+(x)}\big(\nabla_\omega f(x,y)\big) + \beta^-(x)\max\limits_{y\in\mathcal{N}^-(x)}(-1)^p\big(\nabla_\omega f(x,y)\big), & p=\infty, \end{cases} \tag{5.81a}$$

where

$$\mathcal{N}^+(x) = \{y \in \mathcal{N}(x) : f(y) - f(x) > 0\}, \qquad \mathcal{N}^-(x) = \{y \in \mathcal{N}(x) : f(y) - f(x) < 0\}. \tag{5.81b}$$

As detailed in [ETT15, Section 4] depending on the weighting function $\omega \in \mathcal{F}_{\mathcal{V}\times\mathcal{V}}$ and on the positive functions $\beta^+, \beta^- \in \mathcal{F}_{\mathcal{V}}$ satisfying $\beta^+(x) + \beta^-(x) = 1, x \in \mathcal{V}$, the Laplacians (5.81) enable to generalize a broad class of variational approaches including [ELB08] whose Euler Lagrange equations involve graph Laplacians.

In the following, we focus on undirected graphs $(\mathcal{V}, \mathcal{E}, \omega)$ with $\omega(x, y) = \omega(y, x)$. Then, for the purpose of data inpainting and following [ETT15], given a vertex set $\mathcal{A} \subset \mathcal{V}$ together with a function $g \in \mathcal{F}_{\partial\mathcal{A},\mathbb{R}^c}$ specifying the boundary condition imposed on

$$\partial\mathcal{A} = \{x \in \mathcal{V} \setminus \mathcal{A} : \exists y \in \mathcal{A} \text{ with } y \in \mathcal{N}(x)\}, \tag{5.82}$$

the nonlocal Laplacian (5.81) generates a family of nonlocal discrete diffusion processes of the form

$$\begin{aligned} \partial_t f(x,t) &= \mathcal{L}_{\omega,p} f(x,t) && \text{on } \mathcal{A}\times\mathbb{R}_+, && \text{(5.83a)}\\ f(x,t) &= g(x,t) && \text{on } \partial\mathcal{A}\times\mathbb{R}_+, && \text{(5.83b)}\\ f(x,0) &= f_0(x) && \text{on } \mathcal{A}. && \text{(5.83c)} \end{aligned}$$

To establish a comparison with the proposed nonlocal formulation (5.43), we represent the model (5.83) with $g = 0$ on $\partial\mathcal{A}$ in terms of the operators introduced in Section 5.2. Following [ETT15, Section 5] and setting the weighting function

$$\alpha^f(x,y) = \begin{cases} \beta^+(x)\sqrt{\omega(x,y)}^{p-1}\big(\nabla_\omega f(x,y)\big)^{p-2}, & \text{if } f(y) > f(x),\\ \beta^-(x)\sqrt{\omega(x,y)}^{p-1}\big(\nabla_\omega f(y,x)\big)^{p-2}, & \text{if } f(y) < f(x), \end{cases} \tag{5.84}$$

the particular case $p = 2$ simplifies to a linear diffusion process (5.20) with (5.84) directly given in terms of weights $\omega(x, y)$ prescribed by the adjacency relation of the graph $\mathcal{V}$. Moreover, if at each vertex $x \in \mathcal{V}$ the equation $\beta^+(x) = \beta^-(x) = \frac{1}{2}$ holds, then for any $p \in [2, \infty)$ the mapping (5.84) is nonnegative and symmetric. As a consequence, $\alpha^f$ from (5.84) can substitute $\omega(x, y)$ in (5.20) and hence specifies a representation of the form (5.19) when choosing the antisymmetric mapping $\alpha \in \mathcal{F}_{\mathcal{V}\times\mathcal{V}}$ to satisfy $2\alpha^2(x, y) = \alpha^f(x, y)$. Finally, specifying the symmetric mapping $\Theta \in \mathcal{F}_{\mathcal{V}\times\mathcal{V}}$ as $\Theta(x, y) = 1$ if $x \neq y$ and $\Theta(x, x) = -\sum_{y\in\mathcal{N}(x)} \alpha^2(x, y)$, expresses the system (5.83) through (5.73) with $\mathcal{V}$ and $\mathcal{V}_{\mathcal{I}}^{\alpha}$ given by $\mathcal{A}$ and $\partial\mathcal{A}$, respectively.

We conclude with a comment similar to the previous sections. While the similarity of the above mathematical structures to our approach is evident from the viewpoint of diffusion processes, the scope of our approach, data labeling, differs and is not directly addressed by established diffusion-based approaches. We further point out the different role of interaction domain (5.10). While for model (5.83) we set $\alpha$ through (5.84) to satisfy $\mathcal{V}_{\mathcal{I}}^{\alpha} = \partial\mathcal{A}$ which is subset of given set of vertices $\mathcal{V}$, i.e. $\overline{\mathcal{V}} = \mathcal{V}$ as illustrated by the right panel of 5.11), we focus in our work on mappings $\alpha$ that lead to an *extension* of $\mathcal{V}$ by vertices in $\mathbb{Z}^d \setminus \mathcal{V}$, as presented by the left panel of Figure 5.11.

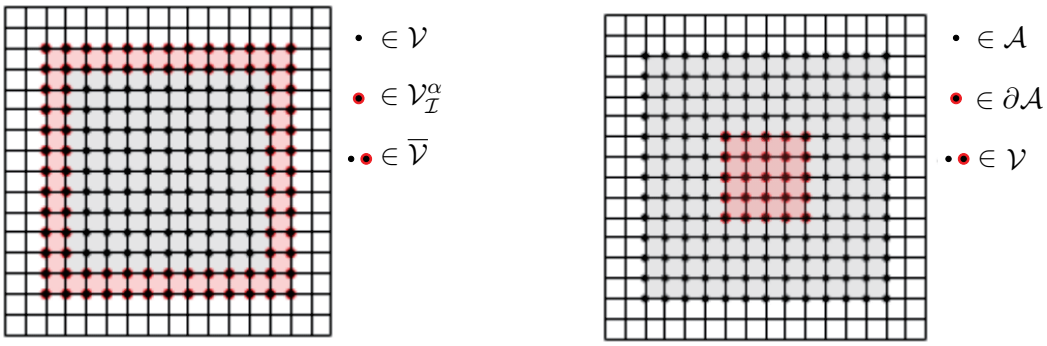


**nonlocal G-PDE** (5.43) **nonlocal approach** [ETT15]

**Figure 5.11.:** Schematic illustration of two different instances of $\mathcal{V}_{\mathcal{I}}^{\alpha}$. Nodes ($\bullet$) and ($\bullet$) represent points of the interaction domain $\mathcal{V}_{\mathcal{I}}^{\alpha}$ and the vertex set $\mathcal{V}$, respectively, in terms of the mapping $\alpha \in \mathcal{F}_{\overline{\mathcal{V}}\times\overline{\mathcal{V}}}$. **Left**: Boundary configuration for the nonlocal G-PDE (5.43) introduced in this thesis. Nonzero interaction of nodes in $\mathcal{V}$ with nodes outside the graph $\mathbb{Z}^d \setminus \mathcal{V}$ results in an extended domain $\overline{\mathcal{V}}$ according to (5.8). **Right**: Boundary configuration for the task of inpainting as proposed in [ETT15]. The parameter $\alpha$ is specified entirely on $\mathcal{V}$ resulting in a disjoint decomposition $\mathcal{V} = \mathcal{A}\dot{\cup}\partial\mathcal{A}$ where now $\mathcal{V}_{\mathcal{I}}^{\alpha}$ satisfies $\mathcal{V}_{\mathcal{I}}^{\alpha} = \partial\mathcal{A}$ to represent the set of all nodes with missing information $\mathcal{V} \setminus \mathcal{A}$.

## 5.5. Nonconvex Optimization by Geometric Integration

We show in Section 5.5.1 how geometric integration provides a numerical scheme for solving the nonlocal partial difference equation (5.43) on a regular discrete grid $\mathcal{V}$ by generating a sequence of states on $\mathcal{W}$ that monotonically decrease the energy objective (5.34). In particular, we show that the geometric Euler scheme is equivalent to the basic two-step iterative approach provided by [HAPD05] for solving nonconvex optimization problems in *DC (difference of convex functions)* format.

In Section 5.5.2, we prove the monotonic decrease property for a *novel* class of geometric *multistage* integration schemes that speed up convergence and show the relation of this class to the nonconvex optimization framework presented in [FM81; AFV18]

Figure 5.12 provides a schematic overview over key components of the two proposed algorithms, including references to the corresponding subsections. Proofs are provided in Appendix A.5.3 to enable efficient reading.

### 5.5.1. First-Order Geometric Integration and DC-Programming

We focus on an one-stage iterative numerical scheme derived by discretizing the explicit geometric Euler integration (5.55) in time with a fixed time-step size $h > 0$. In this specific case, (5.55) generates the sequence of iterates for approximately solving (5.27a) given by

$$(S^k)_{k\geq 1} \subset \mathcal{F}_{\mathcal{V},\mathcal{W}}, \quad S^{k+1}(x) = \exp_{S^k(x)}\big(h(\Omega S)(x)\big), \quad S^0(x) = \exp_{\mathbb{1}_c}\Big(-\frac{D_{\mathcal{X}}(x)}{\rho}\Big), \quad x \in \mathcal{V}, \tag{5.85}$$

where the index $k$ represents the point in time $kh$. We next show that the sequence (5.85) locally minimizes the potential (5.34) and hence, based on the formulation derived in Proposition 5.3.1, how geometric integration provides a finite difference scheme for numerically solving the nonlocal G-PDE (5.43) for the particular case of zero nonlocal boundary conditions.

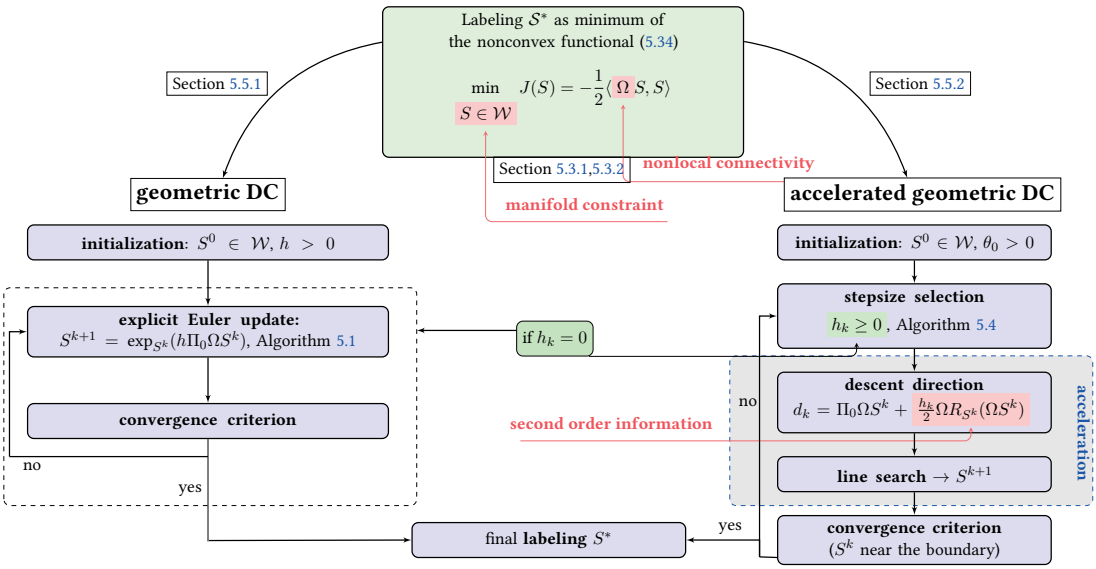


**Figure 5.12.:** Sketch of the two algorithmic schemes, Algorithm 5.1 and Algorithm 5.4, developed in Section 5.5. Common basic components as well as essential differences are highlighted. The major difference corresponds to the acceleration of the basic numerical scheme by geometric integration for solving the nonconvex DC program displayed in the top box.

**Proposition 5.5.1.** *Let $\alpha, \Theta \in \mathcal{F}_{\overline{\mathcal{V}}\times\overline{\mathcal{V}}}$, $\lambda \in \mathcal{F}_{\mathcal{V}}$ and $\Omega \in \mathcal{F}_{\mathcal{V}\times\mathcal{V}}$ be given as in Lemma 5.3.1. Then the sequence (5.85) satisfies*

$$S^{k+1}(x) = \exp_{S^k(x)}\left(h\Big(\frac{1}{2}\mathcal{D}^\alpha\big(\Theta\mathcal{G}^\alpha(h\overline{S}^k)\big) + \lambda\overline{S}^k\Big)(x)\right), \qquad x \in \mathcal{V}, \tag{5.86}$$

*where the zero extension $\overline{S}^k$ of $S^k$ to $\overline{\mathcal{V}}$ is a discrete approximation $S(hk)$ of the continuous time solution to the system (5.43), initialized by $S^0(x)$ (5.85) with imposed zero nonlocal boundary conditions. In addition, if*

$$h \leq \frac{1}{|\lambda_{\min}(\Omega)|}, \tag{5.87}$$

*where $\lambda_{\min}(\Omega)$ denotes the smallest eigenvalue of $\Omega$, then the sequence $(S^k)$ achieves the monotone decrease property*

$$J(S^{k+1}) \leq J(S^k), \qquad k \in \mathbb{N} \tag{5.88}$$

*for the potential function (5.34).*

*Proof.* Appendix A.5.2.

Recent work [ZZS20] on the convergence of (5.27a) showed that, up to negligible situations that cannot occur when working with real data, limit points $S^* = \lim_{t\to\infty} S(t)$ of (5.27a) are *integral* assignments $S^* \in \overline{\mathcal{W}}$. Proposition 5.5.1 says that for stepsizes $h < 1$ the geometric integration step (5.85) yields a *descent* direction for moving $S(t) \in \mathcal{W}$ to $S(t+h) \in \mathcal{W}$ and therefore sufficiently approximates the integral curve corresponding to (5.27a) at time $t + h$. We conclude that the fixed point determined by Algorithm 5.1 listed below solves the nonlocal G-PDE (5.43).

**Algorithm 5.1:** Geometric DC-Programming Scheme.

**Initialization**: $\gamma > |\lambda_{\min}(\Omega)|$ (DC-decomposition parameter, see proof Proposition 5.5.1)
$S^0 = S(0) \in \mathcal{W}$ (initial point by (5.27a))
$\epsilon > 0$ (termination threshold)
$\epsilon_0 = \| \operatorname{grad}_g J(S^0) \| \quad (\operatorname{grad}_g J(S) = R_S(\partial_S J(S)))$
$k = 0$
**while** $\epsilon_k > \epsilon$ **do**
  $\widetilde{S}^k = \Omega S^k + \gamma \log S^k$
  compute: $S^{k+1} = \operatorname{argmin}_{S \in \overline{\mathcal{W}}} \{\gamma S \log S - \langle \widetilde{S}^k, S \rangle\}$ given by (5.85) resp. (5.86) with $h = \frac{1}{\gamma}$
  $\epsilon_k = \| \operatorname{grad}_g J(S^{k+1}) \|$
  $k \leftarrow k + 1$

### 5.5.2. Higher-Order Geometric Integration

In this section we show how higher-order geometric integration schemes can be used and enhance the first-order method of the previous section.

We continue the discussion of the numerical integration of the assignment flow (5.27a) by employing the tangent space parameterization (5.46). For a discussion of relations to the geometry of $\mathcal{W}$, we refer to [ZSPS20]. In what follows, we drop the argument $x \in \mathcal{V}$ and just work with matrix products – cf. (5.36) – besides the lifting map $\exp_S$ that acts row-wise as defined by (5.29).

Our starting point is the explicit geometric Euler scheme (5.55) and (5.85), respectively,

$$S(t+h) \approx \exp_{S^0}\big(V(t) + h\dot{V}(t)\big) = \exp_{S(t)}\big(h(\Omega S)(t)\big). \tag{5.89}$$

Now compute the second-order derivative of all component functions on $\mathcal{T}_0$

$$\ddot{V}(t) \overset{(5.49)}{=} \Pi_0 \Omega \frac{\mathrm{d}}{\mathrm{d}t} \exp_{S^0}\big(V(t)\big) \overset{(5.48)}{\overset{(5.46)}{=}} \Pi_0 \Omega R_{\exp_{S^0}(V(t))} \dot{V}(t) \overset{(5.46)}{=} \Pi_0 \Omega R_{S(t)}\big(\Omega S(t)\big). \tag{5.90}$$

Then the second-order expansion $V(t+h) = V(t) + h\dot{V}(t) + \frac{h^2}{2}\ddot{V}(t) + \mathcal{O}(h^3)$ in $\mathcal{T}_0$ leads to the second-order geometric integration scheme

$$S(t+h) \approx \exp_{S(t)}\Big(h\dot{V}(t) + \frac{h^2}{2}\ddot{V}(t)\Big) \tag{5.91a}$$

$$= \exp_{S(t)}\Big(h\Omega S(t) + \frac{h^2}{2}\Omega R_{S(t)}(\Omega S(t))\Big), \tag{5.91b}$$

which may be read due to (5.32a) as the *two-stage iterative algorithm*

$$\widetilde{S}(t) = \exp_{S(t)}\big(h\Omega S(t)\big), \tag{5.92a}$$

$$S(t+h) = \exp_{\widetilde{S}(t)}\Big(\frac{h^2}{2}\Omega R_{S(t)}(\Omega S(t))\Big). \tag{5.92b}$$

Below, we set in view of (5.46)

$$J(V) := J(S)|_{S=\exp_{S^0}(V)} = J\big(\exp_{S^0}(V)\big) \tag{5.93}$$

to simplify the notation. The following lemma prepares our main result.

**Lemma 5.5.1.** *Based on the parametrization (5.46), the Euclidean gradient of the function $V \mapsto J(V)$ is given by*

$$\partial J(V) = -R_{\exp_{S^0}(V)}\big(\Omega \exp_{S^0}(V)\big) = \operatorname{grad}_g J(S), \tag{5.94}$$

*that is by the Riemannian gradient of the potential (5.34).*

*Proof.* Appendix A.5.3.

The next proposition asserts that applying the second-order geometric integration scheme (5.92) leads to a sufficient decrease of the sequence of values $(J(S^k))_{k\in\mathbb{N}}$, if at each iteration the step sizes are chosen according to a *Wolfe rule* like line search procedure [DY99; NW06]. Specifically, the step sizes $h$ and $h^2$ in (5.92a) and (5.92b), respectively, are replaced by step size sequences $(\theta_k)_{k\geq 0}$ and $(h_k\theta_k)_{k\geq 0}$. In addition, the proposition reveals that, under mild assumptions on the sequence $(h_k)_{k\geq 0}$, the norm of the Riemannian gradient (5.94) becomes arbitrarily small. The proposition is proved in Appendix A.5.3.

**Proposition 5.5.2.** *Let $\Omega(x,y)$ be as in Lemma 5.3.1 and let $d : \mathcal{W} \times \mathbb{R}_+ \to \mathcal{T}_0$ be a mapping given by*

$$d(S,h) = \Pi_0\Big(\Omega S + \frac{h}{2}\Omega R_S(\Omega S)\Big), \qquad S \in \mathcal{W}, \quad h \in \mathbb{R}_+. \tag{5.95}$$

*Then the following holds:*

*(i) There exist sequences $(h_k)_{k\geq 0}, (\theta_k)_{k\geq 0}$ and constants $0 < c_1 < c_2 < 1$ such that setting*

$$S^{k+\frac{1}{2}} = \exp_{S^k}(\theta_k \Omega S^k), \tag{5.96a}$$

$$S^{k+1} = \exp_{S^{k+\frac{1}{2}}}\Big(\frac{h_k\theta_k}{2}\Omega R_{S^k}(\Omega S^k)\Big), \tag{5.96b}$$

*and*

$$d^k := d(S^k, h_k) \in \mathcal{T}_0 \tag{5.97}$$

*yields iterates*

$$S^{k+1} = \exp_{S^k}(\theta_k d^k), \qquad k \in \mathbb{N} \tag{5.98}$$

*satisfying*

$$J(S^{k+1}) - J(S^k) \leq c_1\theta_k \langle \operatorname{grad}_g J(S^k), R_{S^k}(d^k)\rangle_{S^k}, \quad \text{(Armijo condition)} \tag{5.99a}$$

$$|\langle \operatorname{grad}_g J(S^{k+1}), R_{S^k}(d^k)\rangle_{S^k}| \leq c_2 |\langle \operatorname{grad}_g J(S^k), R_{S^k}(d^k)\rangle_{S^k}|, \quad \text{(curvature condition)} \tag{5.99b}$$

*and (recall (3.31))*

$$\langle U, V\rangle_S = \sum_{x\in\mathcal{V}} g_{S(x)}\big(U(x), V(x)\big), \qquad U, V \in \mathcal{T}_0, \quad S \in \mathcal{W}. \tag{5.100}$$

*(ii) Suppose the limit point $\gamma_*$ of $(\theta_k)_{k\geq 0}$ is bounded away from zero, i.e. $\gamma_* = \lim_{k\to\infty} \theta_k > 0$. Then any limit point $S^* \in \overline{\mathcal{W}}$ of the sequence (5.96) is an equilibrium of the flow (5.27a).*

*(iii)* *If $S^*$ is a limit point of (5.96) which locally minimizes $J(S)$, with sequences $(\theta_k)_{k\geq 0}, (h_k)_{k\geq 0}$ as in* (ii)*, then $S^* \in \overline{\mathcal{W}} \setminus \mathcal{W}$.*

*(iv)* *If additionally $\sum_{k\geq 0} h_k = 0$ holds in $(ii)$, then the sequence $(\epsilon_k)_{k\geq 0}$ with $\epsilon_k := \|\mathrm{grad}_g J(S^k)\|$ is a zero sequence.*

*Proof.* Appendix A.5.3.

Given a state $S^k \in \mathcal{W}$, Proposition 5.5.2 asserts the existence of step sizes $(h_k)_{k\geq 0}, (\theta_k)_{k\geq 0} \subset \mathbb{R}_+$ that guarantee a sufficient decrease of the objective (5.34) through (5.98) while still remaining numerically efficient by avoiding too small step sizes through (5.99). A corresponding proper stepsize selection procedure is summarized as Algorithm 5.3 that calls Algorithm 5.2 as a subroutine. Based on Algorithm 5.3, the two-stage geometric integration scheme (5.92) that *accelerates* Algorithm 5.1 is listed as Algorithm 5.4. Acceleration is accomplished by utilizing at each $S^k$ descent directions $d_k$ given by (5.97), based on second-order information provided by the vector field (5.90).

**Algorithm 5.2:** Search $(S^k, \theta_k, d_k, c_1, c_2, a, b)$.

**Input:** current iterate: $S^k \in \mathcal{W}$, initial step size $\theta_k > 0$,
descent direction $d_k$ with $\langle \mathrm{grad}_g J(S^k), R_{S^k} d_k \rangle_{S^k} < 0$,
$k = 1$.
**repeat**
  $S^{k+1} = \exp_{S^k}(\theta_k d^k)$
  **if** $J(S^{k+1}) - J(S^k) > \theta_k c_1 \langle \mathrm{grad}_g J(S^k), R_{S^k} d_k \rangle_{S^k}$ **then**
    $a = a, b = \theta_k$
  **else**
    **if** $|\langle \mathrm{grad}_g J(S^{k+1}), R_{S^k} d_k \rangle_{S^k}| \leq |c_2 \langle \mathrm{grad}_g J(S^k), R_{S^k} d_k \rangle_{S^k}|$ **then**
      **stop**
    $a = \theta_k, b = b, \theta_{k+1} = \frac{a+b}{2}$.
  $k \leftarrow k + 1$.
**until** $\theta_k$ *satisfies* (5.99);
**Return:** $S^k, \theta_k$

In Section 5.6, we show that Algorithm 5.4 converges. This implies, in particular, that Algorithm 5.1 and Algorithm 5.4 terminate after a finite number of steps for any termination parameter $\varepsilon$ with respect to the entropy of the assignment vectors, which measures closeness to an integral solution. Theorem 5.6.2 asserts the existence of basins of attraction around integral solutions from which the sequence $(S^k)$ can never escape once it has reached such a region.

We elaborate in terms of Theorem 5.6.1 a theoretical guideline for choosing a sequence $(h_k)_{k\geq 0}$ which meets the condition of Proposition 5.5.2 (iv). In practice, to achieve an acceleration by Algorithm 5.4 in comparison with Algorithm 5.1, we choose a large value of the step size parameter $h_k$ in the beginning and monotonically decrease $h_k$ to zero after a fixed number of iterations. One particular step size selection strategy that we used for the numerical experiments will be highlighted in Section 5.7.

The following remark clarifies how the line search procedure formulated as Algorithm 5.3,

**Algorithm 5.3:** Step $(S^k, \theta_k, d_k, c_1, c_2, \lambda_{\min}(\Omega))$.

**Input:** current iterate: $S^k \in \mathcal{W}$, initial step size $\theta_k > 0$,
descent direction $d_k$ with $\langle \operatorname{grad}_g J(S^k), R_{S^k} d_k \rangle_{S^k} < 0$,
smallest eigenvalue of $\Omega$, $\lambda_{\min}(\Omega)$ $c_1, c_2 \in (0,1)$ with $c_2 \in (c_1, 1)$,
initial search interval: $a_1 = \theta_k, b_1 = \frac{1}{|\lambda_{\min}(\Omega)|}$ with $a_1 < b_1$,
$k = 1$.
**repeat**
  $\theta_k = \frac{a_k + b_k}{2}$, $S^{k+1} = \exp_{S^k}(\theta_k d_k)$,
  **if** $J(S^{k+1}) - J(S^k) > \theta_k c_1 \langle \operatorname{grad}_g J(S^k), R_{S^k} d_k \rangle_{S^k}$ **then**
    $S^{k+1}, \theta_{k+1} \leftarrow \text{Search}(S^k, \theta_k, c_1, c_2, a_k, b_k)$ (Algorithm 5.2), **stop**
  **else**
    **if** $|\langle \operatorname{grad}_g J(S^{k+1}), R_{S^k} d_k \rangle_{S^k}| \leq |c_2 \langle \operatorname{grad}_g J(S^k), R_{S^k} d_k \rangle_{S^k}|$ **then**
      **stop**
    **else**
      $a_{k+1} = \theta_{k+1}, b_{k+1} = b_k$.
  $k \leftarrow k + 1$.
**until** $\theta_k$ *satisfies* (5.99a);
**Return:** $S^k$

that is used in Algorithm 5.4, differs from the common line search accelerated DC-programming schemes proposed by [FM81] and [AFV18].

**Remark 5.5.1 (directly related work).** Using the notation of Proposition 5.5.1 and its proof, the step iterated by Algorithm 5.1 at $S^k \in \mathcal{W}$ reads

$$\widetilde{S}^k = \operatorname{argmin}_{S \in \mathbb{R}^n} \left\{ h^*(S) - \langle S^k, S \rangle \right\}, \qquad \text{with} \qquad h(S) = \langle S, \Omega S \rangle + \gamma S \log S, \tag{5.101a}$$

$$S^{k+1} = \operatorname{argmin}_{S \in \mathbb{R}^n} \left\{ g(S) - \langle S, \widetilde{S}^k \rangle \right\}, \qquad \text{with} \qquad g(S) = \delta_{\overline{\mathcal{W}}}(S) + \gamma S \log S, \tag{5.101b}$$

where $h^*$ is the conjugate of the convex function $h$. Motivated by the work [FM81], Aragón et al. [AFV18] proposed an accelerated version of the above scheme by performing an additional line search step along the descent direction

$$\widetilde{d}^k = S^{k+1} - S^k \tag{5.102}$$

in (5.101b) for scenarios, where the primary variable $S$ to be determined is not manifold-valued.

The direct comparison with Algorithm 5.1 reveals that for the specific choice $h_k = 0, k \in \mathbb{N}$ in (5.97), (5.95), line search is performed along the descent direction

$$d^k = \Pi_0 \Omega S^k = V^{k+1} - V^k \in \mathcal{T}_0, \tag{5.103}$$

where the last equation follows from applying the parametrization (5.46) to (5.96) while taking into account (3.54) and $R_S = R_S \Pi_0$ for $S \in \mathcal{W}$.

**Algorithm 5.4:** Accelerated Geometric DC Optimization

**Initialization**: (DC-decomposition parameter, see the proof of Prop. 5.5.1),
$S^0 = S(0) \in \mathcal{W}$, (initial iterate (5.27a)),
$\epsilon > 0$, (termination threshold),
$\lambda_{\min}(\Omega)$, (smallest eigenvalue of $\Omega$),
$c_1, c_2 \in (0,1)$, (cf. Prop. 5.5.2),
$\epsilon_0 = \|\mathrm{grad}_g J(S^0)\|$, $\theta_0 = \frac{1}{\gamma}$ (cf. (A.39))
$k = 0$.
**while** $\epsilon_k > \epsilon$ **do**
  Choose: $h_k \in \left(0, \frac{\|R_{S^k}(\Omega S^k)\|^2_{S^k}}{|\langle R_{S^k}(\Omega S^k), \Omega R_{S^k}(\Omega S^k)\rangle|}\right)$
  $d_k = \Pi_0 \Omega S^k + \frac{h_k}{2} \Omega R_{S^k}(\Omega S^k)$ (descent direction by (5.97),(5.95))
  **if** $\theta_k$ *satisfies* (5.99) **then**
    Set: $\widetilde{S}^k = \frac{1}{\theta_k} \log(\frac{S^k}{\mathbb{1}_c}) + d_k$
    Compute: $S^{k+1} = \mathrm{argmin}_{S \in \overline{\mathcal{W}}} \{\frac{1}{\theta_k} S \log S - \langle \widetilde{S}^k, S\rangle\}$, by
    $S^{k+1} = \exp_{S^k}(\theta_k d^k)$
  **else**
    $S^{k+1} \leftarrow \mathrm{Step}\big(S^k, \theta_k, d_k, c_1, c_2, \lambda_{\min}(\Omega)\big)$ by Algorithm 5.3.
  $\epsilon_{k+1} = \|\mathrm{grad}_g J(S^{k+1})\|$,
  $k \leftarrow k+1$.
**Returns:** $S^k \approx S^*$

Comparing $\widetilde{d}^k$ and $d^k$ shows the geometric nature of our algorithm in order to handle properly the manifold-valued variable $S$ and the more general descent directions $d^k$ with step sizes $h_k > 0$ in Algorithm 5.4.

### 5.5.3. Influence of Nonlocal Boundary Conditions

We conclude this section by explaining in more detail the effect of imposing in (5.43) the zero nonlocal boundary condition on the nonempty interaction domain, on the stepsize selection procedure presented as Algorithm 5.3. This explanation is formulated as Remark 5.5.2 below after the following proposition, that states a result analogous to [AV10, Proposition 2.3]. The proposition is proved in Appendix A.5.4.

**Proposition 5.5.3.** *For mappings $\Theta, \alpha \in \mathcal{F}_{\overline{\mathcal{V}}\times\overline{\mathcal{V}}}$, let $\Omega \in \mathcal{F}_{\mathcal{V}\times\mathcal{V}}$ and $\lambda \in \mathcal{F}_{\mathcal{V}}$ be given as in Lemma 5.3.1 such that property (5.24) holds and $\lambda = 1, x \in \mathcal{V}$ in (5.41) is achieved. Assume further that the weighted graph $(\mathcal{V}, \mathcal{E}, \Omega)$ in (5.3) is connected. Then the following holds:*

*(i) The smallest Dirichlet eigenvalue of the nonlocal operator (5.19)*

$$\lambda_1^D = \inf_{f \neq 0} -\frac{\frac{1}{2}\langle f, \mathcal{D}^\alpha(\Theta \mathcal{G}^\alpha f)\rangle_{\overline{\mathcal{V}}}}{\langle f, f\rangle_{\overline{\mathcal{V}}}}, \qquad f \in \mathcal{F}_{\overline{\mathcal{V}}}, \quad f_{|\mathcal{V}_{\mathcal{I}}^\alpha} = 0, \tag{5.104}$$

*is bounded away from zero and admits the equivalent expression*

$$0 < \lambda_1^D = \inf_{f \neq 0} \frac{\langle f, (\Lambda - \Omega) f\rangle_{\mathcal{V}}}{\langle f, f\rangle_{\mathcal{V}}}, \tag{5.105}$$

*where*

$$\Lambda = \mathrm{Diag}(\lambda), \qquad \lambda = (\dots, \lambda(x), \dots)^\top \tag{5.106}$$

*with $\lambda(x)$ given by (5.41).*

*(ii) One has $\lambda_{\min}(\Omega) > -1$.*

*Proof.* Appendix A.5.4.

We are now in the position to characterize the effect of imposing the zero nonlocal boundary condition on the step size selection procedure (Algorithm 5.3).

**Remark 5.5.2 (parameter selection).** Recalling the proof of Proposition 5.5.1, the update (5.86) amounts to perform at each step $k \in \mathbb{N}$ one iteration of a basic DC programming scheme [HAPD05] with respect to the suitable DC decomposition (A.39) of (5.34), with $\Omega$ satisfying (5.4), (5.24) by choosing parameter $\gamma > 0$ such that $\lambda_{\min}\big(\Omega + \gamma\,\mathrm{Diag}(\frac{\mathbb{1}}{S})\big) > 0$. In the case of a *nonzero* interaction domain (5.10) with $\Omega, \alpha, \Theta$ as in Lemma 5.5.3, Proposition 5.5.3(ii) and estimate (A.42) yield for $S \in \mathcal{W}$

$$\lambda_{\min}\Big(\Omega + \gamma\,\mathrm{Diag}\,\big(\frac{\mathbb{1}}{S}\big)\Big) > -1 + \beta + \gamma > 0 \qquad \text{for} \qquad \gamma > 1 - \beta, \tag{5.107a}$$

$$\beta = \sum_{x \in \mathcal{V}_b} \sum_{y \in \mathcal{V}_{\mathcal{I}}^{\alpha}} \Theta(x,y)\alpha^2(x,y)f^2(x). \tag{5.107b}$$

In particular, following the steps in proof of Lemma 5.5.1, relation $h = \frac{1}{\gamma}$ in connection with (5.107) accounts for bigger step sizes in Algorithm 5.1 for integrating (5.43) with nonzero interaction domain (5.10). This will be numerically validated in Section 5.7 (see Figure 5.13).

We conclude this section with a final comment on the lower bound of the objective (5.34).

**Remark 5.5.3. (global minimizer of (5.34))** Recalling the terms involved in the objective (5.34), the lower bound is attained precisely when the first term $\sum_{x\in\mathcal{V}} \sum_{y\in\mathcal{N}(x)} \Omega(x,y)\|S(x) - S(y)\|^2$ is minimal and the last term $-\frac{1}{2}\|S\|_F^2$ is maximal. Therefore the global minimizers of $J(S)$ are given by the set of spatially constant assignments, where to each node in graph $\mathcal{V}$ the same prototype $X_j^* \in \mathcal{X}$ is assigned.

## 5.6. Convergence Analysis

This section is devoted to the convergence analysis of Algorithm 5.4 that performs accelerated geometric integration of the Riemannian descent flow (5.27a). The main results are stated as Theorem 5.6.1 and Theorem 5.6.2 in Section 5.6.2. The lenghty proofs have been relegated to Appendix A.5.5.

### 5.6.1. Preparatory Lemmata

**Lemma 5.6.1.** *For a nonnegative, symmetric mapping $\Omega \in \mathcal{F}_{\mathcal{V}\times\mathcal{V}}$, let the sequences $(S^k)_{k\geq 0}$, $(\theta_k)_{k\geq 0}$ and $(h_k)_{k\geq 0}$ be recursively defined by Algorithm 5.4 and let $\Lambda$ denote the set of all limit points of the sequence $(S^k)_{k\geq 0}$,*

$$\Lambda = \{S \in \overline{\mathcal{W}} : \exists (S^{k_l})_{l\geq 0} \text{ with } S^{k_l} \to S \text{ for } l \to \infty\}. \tag{5.108}$$

*Then there exists $J^* \in \mathbb{R}$ with $\lim_{k\to\infty} J(S^k) = J^*$, i.e. $J(S)$ is constant on $\Lambda$.*

*Proof.* Appendix A.5.5.

Next, we inspect the behavior of the iterates generated by Algorithm 5.4 near a limit point $S^* \in \overline{W}$. To this end, the following index sets are considered at each node $x \in \mathcal{V}$:

$$J_+(S^*(x)) = \{j \in [c] \colon (\Omega S^*)_j(x) - \langle S^*(x), (\Omega S^*)(x)\rangle < 0\}, \tag{5.109a}$$
$$J_-(S^*(x)) = \{j \in [c] \colon (\Omega S^*)_j(x) - \langle S^*(x), (\Omega S^*)(x)\rangle > 0\}, \tag{5.109b}$$
$$J_0(S^*(x)) = \{j \in [c] \colon (\Omega S^*)_j(x) - \langle S^*(x), (\Omega S^*)(x)\rangle = 0\}. \tag{5.109c}$$

**Lemma 5.6.2.** *Let $\Omega \in \mathcal{F}_{\mathcal{V}\times\mathcal{V}}$ and $(S^k)_{k\geq 0}, (\theta_k)_{k\geq 0}, (h_k)_{k\geq 0}$ be as in Proposition 5.5.2 (iv) with a sequence $(\theta_k)_{k\geq 0}$ bounded by $\theta_k \in [\theta_{min}, \theta_{max}]$. Let $S^* \in \overline{\mathcal{W}}$ be a limit point of $(S^k)_{k\geq 0}$. Then, for the positive function $Q(S) = \sum_{x\in\mathcal{V}} \sum_{j\in J_+(S^*(x))} S_j(x)$, there are constants $\varepsilon > 0$, $M^* > 1$ and an index $k_0$ such that for all $k \geq k_0$ with $\|S^* - S^k\| < \varepsilon$ the inequality*

$$Q(S^{k+1}) - Q(S^k) < \frac{\theta_k}{M^*} \sum_{x\in\mathcal{V}} \sum_{j\in J_+(S^*(x))} S_j^k(x)((\Omega S^*)_j(x) - \langle \Omega S^*(x), S^*(x)\rangle) < 0 \tag{5.110}$$

*is satisfied.*

*Proof.* Appendix A.5.5.

### 5.6.2. Main Results

This section provides the main results of our convergence analysis: convergence of the accelerated Algorithm 5.4 (Theorem 5.6.1) and an estimate of the basins of attraction around equilibria that enable early stopping of Algorithm 5.4 (Theorem 5.6.2).

In the following, we well rely on the *Kullback-Leibler (KL) divergence* (2.37) induced by the negative discrete entropy function (cf. Definition 2.1.1) and define with abuse of notation

$$D_{\mathrm{KL}} \colon \overline{\mathcal{W}} \times \mathcal{W} \to \mathbb{R}_+, \qquad D_{\mathrm{KL}}(S, P) = \sum_{x\in\mathcal{V}} D_{\mathrm{KL}}\big(S(x), P(x)\big). \tag{5.111}$$

**Theorem 5.6.1 (convergence of Algorithm 5.4).** *Let $(S^k)_{k\geq 0}$ be a sequence generated by Algorithm 5.4, where the sequences of step sizes $(\theta_k)_{k\geq 0}, (h_k)_{k\geq 0}$ additionally satisfy the assumptions of Lemma 5.6.2 and Proposition 5.5.2, respectively. If there exists an index $K \in \mathbb{N}$ such that the sequence $(h_k)_{k\geq K}$ satisfies*

$$h_k \leq C(\Omega) \frac{\|\mathrm{grad}_g J(S^k)\|_{S^k}^2}{n} \tag{5.112a}$$
$$\text{with} \qquad C(\Omega) := 2\frac{\theta_{\min} c_1}{\lambda^2(\Omega)}, \qquad \lambda(\Omega) = \max\{|\lambda_{\min}(\Omega)|, |\lambda_{\max}|(\Omega)\}, \tag{5.112b}$$

*then the set $\Lambda = \{S^*\}$ defined by (5.108) is a singleton and $\lim_{k\to\infty} D_{\mathrm{KL}}(S^*, S^k) = 0$ holds, i.e. the sequence $(S^k)_{k\geq 0}$ converges to a unique $S^* \in \overline{\mathcal{W}}$ which is an equilibrium of (5.27a).*

*Proof.* Appendix A.5.6.

According to Proposition 5.5.2 (iii),(iv) the sequence $(S^k)_{k\geq 0}$ converges to a critical point $S^* \in \overline{\mathcal{W}} \setminus \mathcal{W}$ on the boundary of convex set $\overline{\mathcal{W}}$. Since both functions $g, h$ of the DC-decomposition

(A.39) have been regularized by the negative entropy, global Lipschitz continuity of the derivatives does *not* hold and hence does not allow to study the convergence rate of Algorithm 5.4 along the lines pursued in [AFV18], [BSTV18], [PLT18]. Therefore, we confine ourselves to establish a *local linear* rate of convergence $S^k \to S^*$ within a suitably define basin of attraction in $\mathcal{W}$ around $S^*$. To this end, we adopt the following basic

**Assumption:** Any stationary point $S^* \in \overline{\mathcal{W}}$ of the sequence $(S^k)$ generated by Algorithm 5.4 is a stable equilibrium of the flow (5.27a):

$$(\Omega S^*)_j(x) - (\Omega S^*)_{j^*(x)}(x) < 0, \qquad j \in [c] \setminus j^*(x) = \operatorname{argmax}_{l \in [c]} S^*_l(x), \qquad \forall x \in \mathcal{V}. \tag{5.113}$$

**Remark 5.6.1.** As worked out in [ZZS20, Section 2.3.2], the set of initial points $S(0)$ of the flow (5.27a) for which Assumption (5.113) is not satisfied has measure zero. Hence Assumption (5.113) holds in all practically relevant cases.

Based on Assumption 5.113, we adopt the results reported in [ZZS20, Section 2.3.3] by defining the open convex polytope for each integral equilibrium $S^* \in \mathcal{W}^*$ as

$$A(S^*) \coloneqq \bigcap_{x \in \mathcal{V}} \bigcap_{j \neq j^*(x)} \{S \in \mathcal{F}_{\mathbb{R}^{n \times c}} \colon (\Omega S)_j(x) < (\Omega S)_{j^*(x)}(x)\}, \tag{5.114}$$

and by introducing the *basins of attraction*

$$B_\varepsilon(S^*) \coloneqq \{S \in \overline{W} \colon \max_{x \in \mathcal{V}} \|S(x) - S^*(x)\|_1 < \varepsilon\} \subset A(S^*) \cap \overline{W}, \tag{5.115}$$

where $\varepsilon > 0$ is small enough such that the inclusion in (5.115) holds. Due to [ZZS20, Proposition 2.3.13] a sufficient upper bound $\varepsilon \leq \varepsilon^*$ for the inclusion (5.115) to hold is

$$\varepsilon^* = \min_{x \in \mathcal{V}} \min_{j \in [c] \setminus j^*(x)} \frac{2\big((\Omega S^*)_{j^*(x)} - (\Omega S^*)_j\big)(x)}{\sum\limits_{y \in \mathcal{N}(x)} \Omega(x,y) + \big((\Omega S^*)_{j^*(x)} - (\Omega S^*)_j\big)(x)} > 0. \tag{5.116}$$

The following theorem asserts that a modified criterium applies to the sequence generated by Algorithm 5.4, together with a linear convergence rate $S^k \to S^*$, whenever the sequence $(S^k)$ enters a basin on attraction $B_\varepsilon(S^*)$.

**Theorem 5.6.2 (basins of attraction).** *For $\Omega \in \mathcal{F}_{\mathcal{V} \times \mathcal{V}}$ as in Lemma 5.3.1, let $(S^k)_{k \geq 0}$ be a sequence generated by Algorithm 5.4. Let $S^* \in \overline{\mathcal{W}}$ be a limiting point $(S^k)_{k \geq 0}$ that fulfills Assumption 5.113 and let $\varepsilon^* > 0$ be as in (5.116). Then, introducing the positive constants*

$$\overline{h} = \max_{k \in \mathbb{N}} h_k, \quad \rho^* = \max_{S \in \overline{\mathcal{W}}} \Big( \max_{\substack{x \in \mathcal{V}, \\ j \in [c] \setminus j^*(x)}} \big((\Omega S)_{j^*(x)} - (\Omega S)_j\big)(x) \Big), \quad N = \max_{y \in \mathcal{V}} |\mathcal{N}(y)|, \tag{5.117}$$

*for all $\varepsilon > 0$ small enough such that*

$$\varepsilon \leq \min_{x \in \mathcal{V}} \min_{j \in [c] \setminus j^*(x)} \frac{2 \cdot \big((\Omega S^*)_{j^*(x)} - (\Omega S^*)_j\big)(x)}{1 + C \cdot \rho^* + \big((\Omega S^*)_{j^*(x)} - (\Omega S^*)_j\big)(x)}, \quad C = \overline{h} \cdot c \cdot N, \tag{5.118}$$

*the following applies: If for some index $k_0 \in \mathbb{N}$ it holds that $S^{k_0} \in B_\varepsilon(S^*) \subset B_{\varepsilon^*}(S^*)$, then for all $k \geq k_0$ there exists a mapping $\xi \in \mathcal{F}_{\mathcal{V}}$ with $\xi(x) \in (0,1)$, $\forall x \in \mathcal{V}$, such that*

$$\|S^k(x) - S^*(x)\|_1 < \xi^{k-k_0}(x) \|S^{k_0}(x) - S^*(x)\|_1, \qquad \forall x \in \mathcal{V}. \tag{5.119}$$

*Proof.* See Appendix A.5.6.

## 5.7. Experiments and Discussion

In this section, we report numerical results obtained with the algorithms introduced in Section 5.5. Details of the implementation and parameters settings are provided in Section 5.7.1. Section 5.7.2 deals with the impact of the nonlocal boundary conditions of system (5.50) on properties of averaging matrices $\Omega$ (see Section 5.3.2), and how this effects the selection of the step size parameter $h > 0$ in Algorithm 5.1. Section 5.7.3 reports results obtained by computing the assignment flow with Algorithm 5.1 and different constant step sizes $h > 0$ using the nonlocal G-PDE parametrization (5.50). In addition, we studied numerical consequences of nonlocal boundary conditions (5.43b), (5.43c) using the maximal allowable step size (5.87) according to Proposition 5.5.1. Finally, in Section 5.7.4, we compare Algorithm 5.1 and the accelerated Algorithm 5.4 by evaluating their respective convergence rates to an integral solution of the assignment flow corresponding to a stationary point of the potential (5.34), for various nonlocal connectivities.

### 5.7.1. Implementation Details

All evaluations were performed using the noisy image data depicted by Figure 5.6 (b). System (5.43) was initialized by $S^0 = L(\mathbb{1}_{\mathcal{W}}) \in \mathcal{W}$ with $\rho = 1$, as specified by (3.59). Since the iterates $(S^k)$ converge in all cases to integral solutions which are located at vertices on the boundary $\partial\mathcal{W}$ of $\mathcal{W}$, whereas the numerics is designed for evolutions *on* $\mathcal{W}$, we applied the renormalization routine adopted in [ÅPSS17, Section 3.3.1] with $\varepsilon = 10^{-10}$ whenever the sequence $(S^k)_{k\geq 0}$ came that close to $\partial\mathcal{W}$ on its path to the vertex.

The averaging matrix $\Omega$ was assembled in two ways as specified in Section 5.3.5 as items (i) and (ii), called *uniform* and *nonuniform* averaging in this section. In the latter case, the parameter values $\sigma_s = 1, \sigma_p = 5$ in were chosen (5.57), as for the experiments reported in Section 5.3.5. The iterative algorithms were terminated at step $k$ when the averaged gradient norm

$$\epsilon_k = \frac{1}{n} \sum_{x \in \mathcal{V}} \| R_{S^k(x)}(\Omega S^k(x)) \| \leq \epsilon \tag{5.120}$$

reached a threshold $\epsilon$ which when chosen sufficiently small to satisfy bound (5.118) that guarantees a linear convergence rate as specified in Theorem 5.6.2.

We point out that during the evaluation and discussion of realized experiments our focus was *not* on assessing a comparison of computational speed in term of absolute runtimes, but on the numerical behavior of the proposed schemes with regard to number of iterations required to solve system (5.50) and in terms of the labeling performance. Thus, we did not confine ourselves to impose any restriction on the minimum time step size and the maximum number of iterations and instead appropriately adjusted the parameter (5.120) to stop the algorithm when a stationary point at the boundary of $\mathcal{W}$ was reached.

Since $S^*$ is unknown, we can not directly access the exact bound in (5.118) beforehand and therefore it is not evident how to set $\epsilon$ in practice. However, based on experimental evidence, setting the termination threshold by $\epsilon = 10^{-7}$ in (5.120) serves as good estimate, see Figures 5.17 and 5.19. Algorithm 5.3 requires to specify two parameters $c_1, c_2$ (see line 3). We empirically found that using $c_1 = 0.4, c_2 = 0.95$ is a good choice that we used in all experiments.

### 5.7.2. Step Size Selection

This section reports results of several experiments that highlight aspects of imposing nonlocal boundary conditions (5.43b), (5.43c) and their influence on the selection of step sizes in Algo-

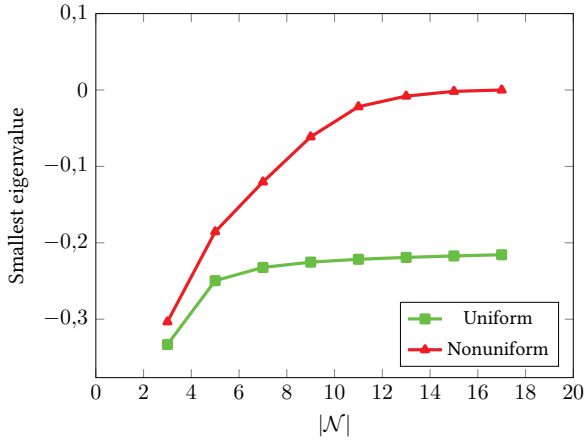


**Figure 5.13.:** Effect of imposing nonlocal boundary conditions. The green (1) and the red (2) curves plot the smallest eigenvalues $\lambda_{\min}(\Omega)$ of the parameter matrix (5.39) for uniform and nonuniform averaging, respectively, and for different neighborhood sizes $|\mathcal{N}|$. Choosing larger neighborhoods (5.5) increases the smallest eigenvalue and consequently, by (5.87), enables to choose bigger step sizes in Algorithm 5.1 that achieve the monotone decrease property (5.88).

rithms 5.1 and 5.4.

To demonstrate these effects we used two different parameter matrices $\Omega$ defined in accordance with Lemma 5.3.1, with $\Theta, \alpha$ given as in Section 5.3.5, called *uniform* and *nonuniform* averaging, respectively. To access the maximal bound (5.87) for the step size $h > 0$, as derived in Proposition 5.5.1 in order to achieve the monotone decrease property (5.88), we directly approximated the exact smallest eigenvalue $\lambda_{\min}(\Omega)$ using available software [LCC98].

Figure 5.13 displays values of the smallest eigenvalue for uniform and nonuniform averaging, respectively, and different sizes of the nonlocal neighborhoods (5.5): Increasing the size $|\mathcal{N}|$ decreases the value of $\lambda_{\min}(\Omega)$ and consequently, by virtue of relation $h \geq \frac{1}{|\lambda_{\min}(\Omega)|}$ in Proposition 5.5.1, to a larger upper bound for setting the step size $h$ in Algorithm 5.1. This confirms our observation and statement formulated as Remark 5.5.2.

In practice, however, it is too expensive to compute $\lambda_{\min}$ numerically for choosing the step size $h$. Figure 5.14 shows for three sizes of neighborhoods $|\mathcal{N}|$ and for step sizes $h$ *smaller and larger* than the upper bound (5.87) indicated by dashed vertical lines,

(i) the number of iterations required to reach the termination criterion (5.120) (Figure 5.14, left panel);

(ii) the labeling accuracy compared to ground truth (Figure 5.14, right panel).

The results show that the bound (5.87) should be considered as a hard constraint indeed: Increasing the step size $h$ up to this bound (cf. Fig. 5.14, left panel) decreases the required number of iterations, as to be expected. But exceeding the bound yields unreliable computation, possibly caused by a too small DC decomposition parameter $\gamma < |\lambda_{\min}(\Omega)|$ which compromises the convexity and hence convergence of the auxiliary optimization problems in Algorithm 5.1, line (8)). Likewise, Fig. 5.14, right panel, shows that labelings quickly become inaccurate once the step size exceeds the upper bound. Figure 5.15 visualizes examples.

Overall, these results show that a wide range of save choices of the step size parameter $h$ exists, and that choosing the "best" value depends on how accurate $\lambda_{\min}(\Omega)$ is known beforehand.

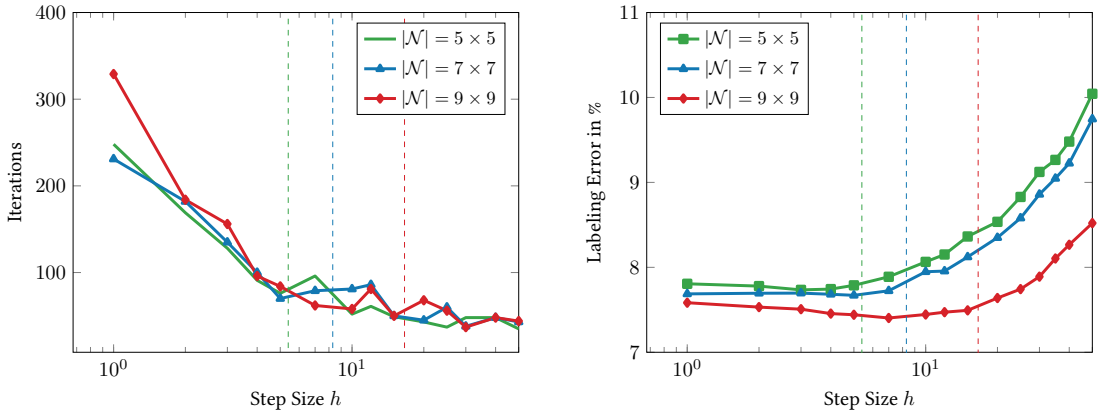


**Figure 5.14.:** Effects of selecting the step size $h$ in Algorithm 5.1 for various neighborhood sizes $|\mathcal{N}|$. Dashed vertical lines indicate the step size upper bound $\frac{1}{|\lambda_{\min}(\Omega)|}$ that guarantees the monotone decrease property (Proposition 5.5.1). **Left:** Number of iterations required to satisfy the termination criterion (5.120). Larger step sizes decrease the number of iterations but yield unreliable numerical computation when $h$ exceeds the upper bound (see text). **Right:** Pixel-wise labeling error compared to ground truth. Labeling accuracy quickly deteriorates when $h$ exceeds the upper bound.

.

### 5.7.3. First-Order Optimization

This section is devoted to the evaluation of Algorithm 5.1. We examine how effectively this algorithm converges to an integral solution (labeling) for both uniform and nonuniform averaging, for different sizes of nonlocal neighborhoods $|\mathcal{N}|$, and for different admissible step sizes $h$ based on the insights gained in Section 5.7.2: the largest admissible step size increases with the neighborhood size $|\mathcal{N}|$ and when using nonuniform, rather than uniform, averaging.

Figure 5.16 displays the corresponding values of the objective function (5.34) as a function of the iteration counter. We observe that this first-order algorithm minimizes quite effectively the non-convex objective function during the first few dozens of iterations.

Figure 5.17 displays the same information, this time in term of the function $k \mapsto \frac{1}{n}\|S^k - S^*\|_1$, however. We observe two basic facts: (i) Due to using admissible step sizes, the sequences $(S^k)_{k\geq 0}$ always converge to the integral solution $S^*$. (ii) In agreement with Theorem 5.6.2, the order of convergence increases whenever the sequence $(S^k)_{k\geq 0}$ reaches the basin of attraction.

### 5.7.4. Accelerated Geometric Optimization

In this section, we report the evaluation of Algorithm 5.4 using Algorithm 5.1 as baseline. The main ingredients of Algorithm 5.4 are:

(i) The descent direction $d^k$ given by (5.95) exploits the second-order term $\frac{1}{2}\Omega R_{S_k}(\Omega S_k)$ weighted by parameter $h_k$ which, according to line 9 of Algorithm 5.4, is determined with negligible

[1]The plotted curves in the figure illustrate progressing objective values of $J(S)$ stagnating near a *local minimizer* $S^*$. In particular, the depicted stagnating value is *not* the lower bound of $J(S)$ on $\mathcal{W}$ that is given by $J(S^*) = -\frac{|\mathcal{V}|}{2}$ and attained at the *global* minimizer $S^*$, that is always a constant labeling and therefore of no interest, see Remark 5.5.3

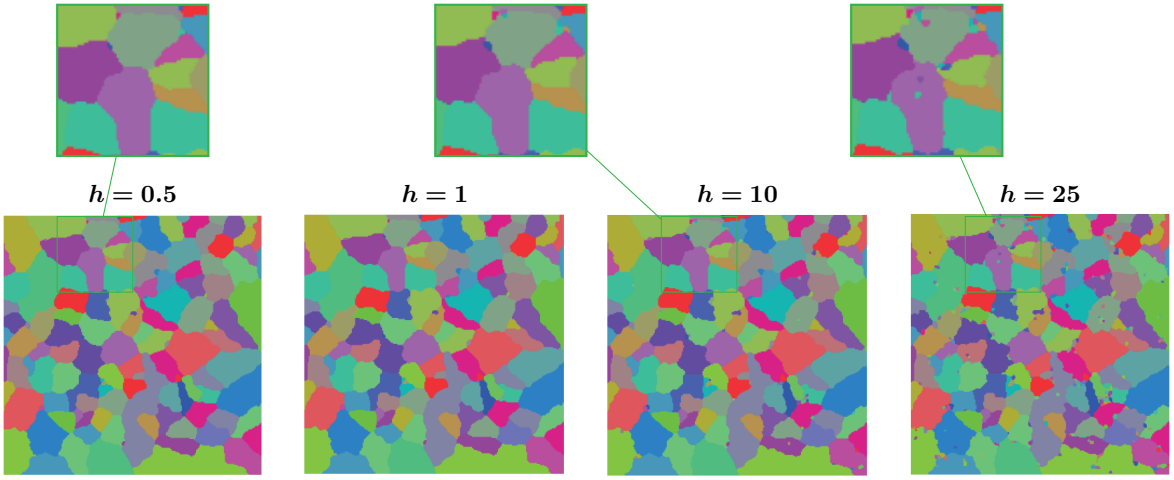


**Figure 5.15.:** Visualization of regularization impacts when increasing the step size $h$ corresponding to the results in Figure 5.14. Labeling results for various step sizes and the neighborhood size $|\mathcal{N}| = 9 \times 9$. Conforming to Figure 5.14, right panel, labeling accuracy quickly deteriorates once $h$ exceeds the upper bound (5.87) (rightmost panel).

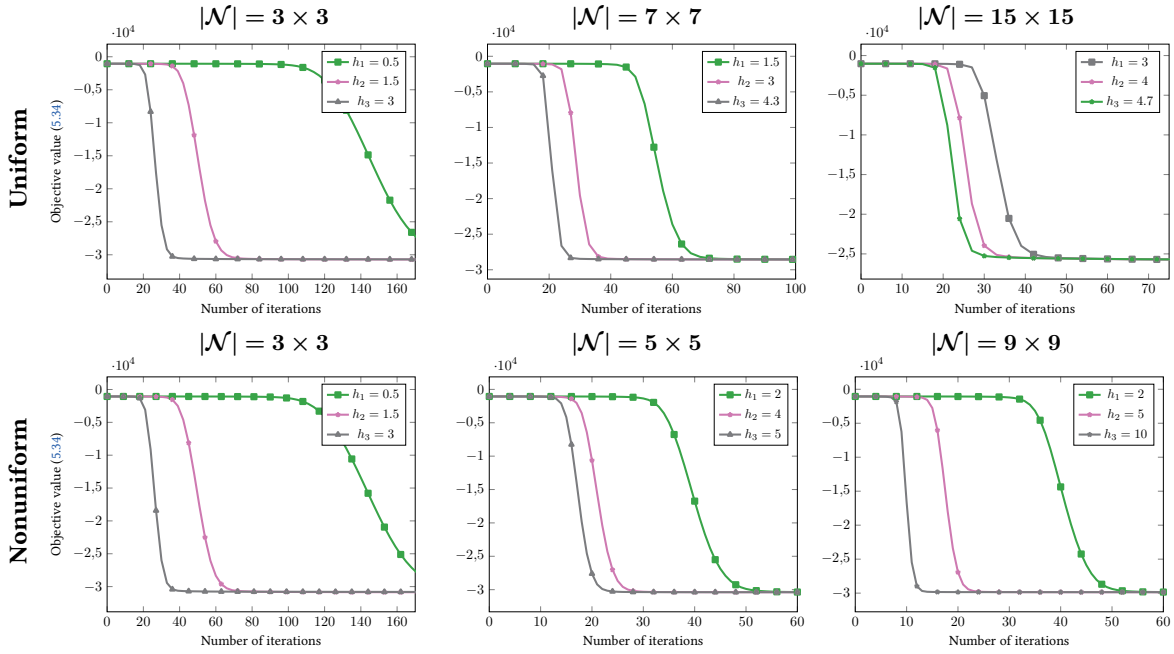


**Figure 5.16.:** Minimization of the nonconvex potential (5.34) by Algorithm 5.1 for various neigborhood sizes $|\mathcal{N}|$, for uniform averaging (top row) and nonuniform averaging (bottom row), and for three constant step sizes $0 < h_1 < h_2 < h_3$, where in each experiment $h_3$ was chosen smaller than the upper bound discussed in Section 5.7.2 that guarantees a monotonously decreasing sequence of potential values (Proposition 5.5.1). All experiments illustrate this property and that the largest admissible step size $h_3$ is most effective. [1]

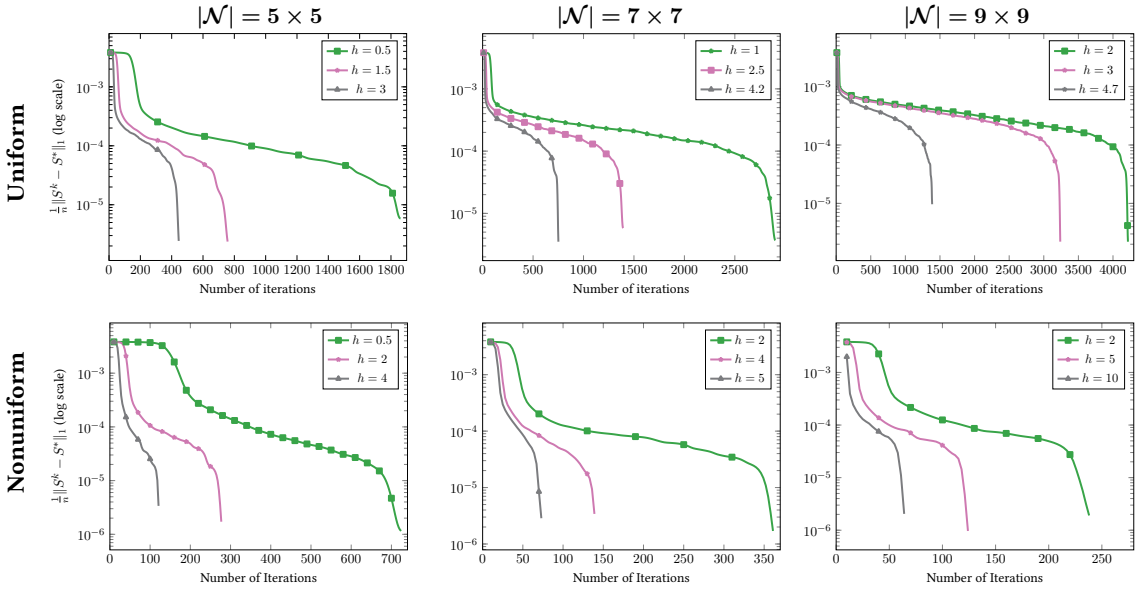


**Figure 5.17.:** Norm convergence of the sequence generated by Algorithm 5.1 towards an integral solution (labeling). Once the basin of attraction of the integral solution has been reached (Theorem 5.6.2), the convergence rate increases considerably.

additional computational cost by

$$h_k = \tau \cdot \Big( \frac{\|R_{S^k}(\Omega S^k)\|_{S^k}^2}{|\langle R_{S^k}(\Omega S^k), \Omega R_{S^k}(\Omega S^k) \rangle|} \Big), \qquad \tau \in (0,1). \tag{5.121}$$

Choosing the parameter $\tau$ is a compromise between making larger steps (large value of $\tau$) and accuracy of labeling (small value of $\tau$). According to our experience, $\tau = 0.1$ is a reasonable choice that did never compromise labeling accuracy. This value was chosen for all experiments discussed in this section.

(ii) Algorithm 5.4 calls Algorithm 5.3 which in turn calls Algorithm 5.2 in order to satisfy both conditions (5.99) for sufficient decrease. In order to reduce the computational costs of the inner loop started in line 16 of Algorithm 5.4, we only checked the conditions (5.99a) and (5.99b) at each iteration up to $K_{\max} = 100$ iterations. Figure 5.18 illustrates that, while condition (5.99a) is satisfied throughout all outer loop iterations, condition (5.99b) is satisfied too except for a tiny fraction of inner loops, and therefore the validity of (5.99) is still guaranteed up to a negligible part of iteration steps.

Parameter $\theta_k$ of Algorithm 5.4 corresponds to the step size parameter $h_k$ of Algorithm 5.4. According to the discussion of proper choices of $h_k$ in Section 5.7.2, parameters $\theta_k$ was initialized by values $\theta_0 \in \{\frac{1}{2}, 2\}$ and the adaptive search of $\theta_k$ was not allowed to exceed the upper bound $\theta_{\max} = 10$.

Like Algorithm 5.1, Algorithm 5.4 terminated when condition (5.120) was satisfied with $\epsilon = 10^{-7}$.

Figure 5.19 illustrates the convergence of Algorithms 5.1 and 5.4 towards labelings for the two initial step sizes $\theta_0 \in \{\frac{1}{2}, 2\}$ corresponding to the fixed step size $h \in \{\frac{1}{2}, 2\}$ of Algorithm 5.1), and for different sizes $|\mathcal{N}|$ of neighborhoods with nonuniform averaging. Throughout all experiments, we observed that due to using adaptive step sizes $\theta_k$ and second-order information for

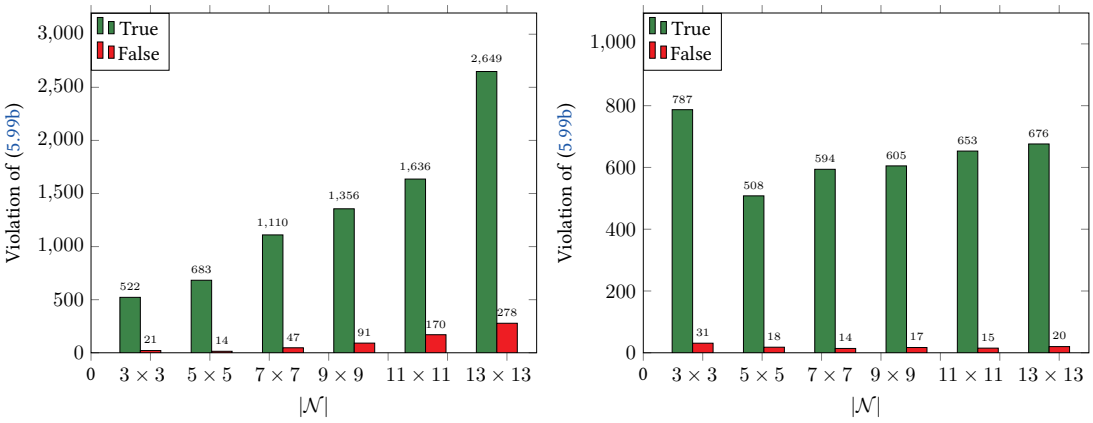


**Figure 5.18.:** Fraction of inner loops of Algorithm 5.4 based on condition (5.99a) that also satisfied condition (5.99b) ({●} = True) or not ({●} = False), with initialization $\theta_0 = 0.5$ and uniform averaging (left panel) or nonuniform averaging (right panel). Up to a tiny fraction, condition (5.99b) is satisfied which justifies to reduce the computational costs of the inner loop by only checking condition (5.99a) and dispensing with condition (5.99b) after $K_{\max}$ iterations.

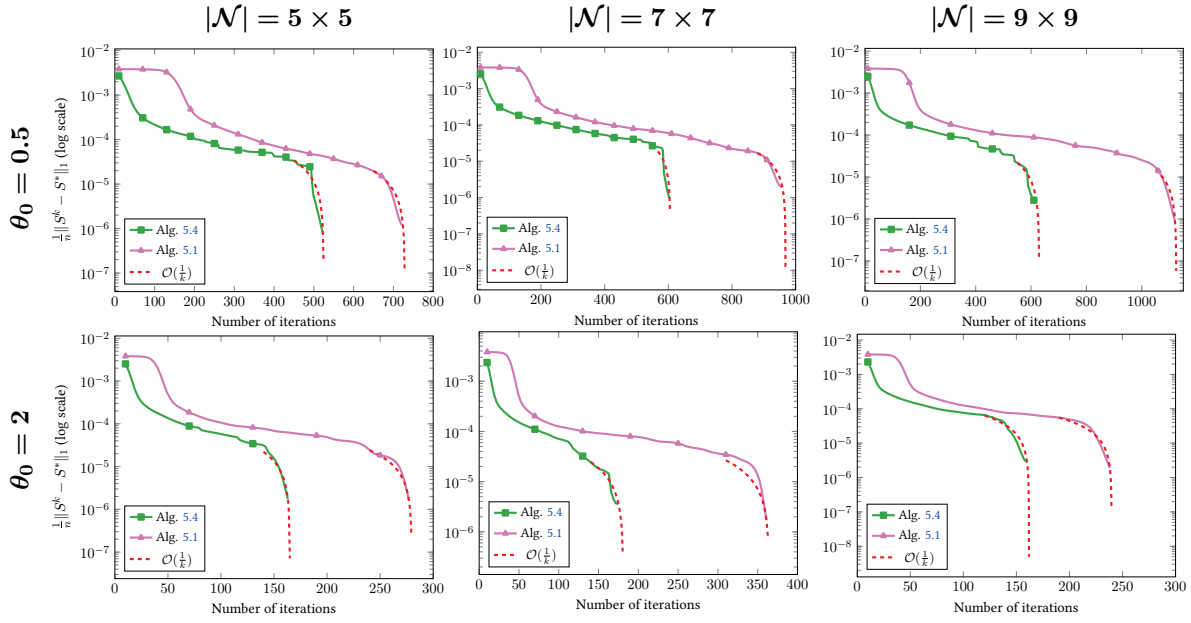


**Figure 5.19.:** Comparison of the convergence of Algorithm 5.1 (●) and Algorithm 5.4 (●) towards integral solutions (labelings) for various sizes $|\mathcal{N}|$ of neighborhoods and nonuniform averaging. For all parameter settings Algorithm 5.4 terminates after a smaller number of iterations.

determining the search direction, Algorithm 5.4 terminates after a smaller number of iterations. In particular, the fast convergence of Algorithm 5.1 within the basins of attraction is preserved.

Table 5.2 compares Algorithms 5.1 and 5.4 in terms of factors of additional iterations required by Algorithm 5.1 to terminate. We observe that the efficiency of Algorithm 5.4 is more pronounced when larger neighborhood sizes $|\mathcal{N}|$ or uniform averaging are used.

| | **Uniform** | | | **Nonuniform** | | |
|---|---|---|---|---|---|---|
| $\lvert\mathcal{N}\rvert$ | Alg. 5.1 | Alg. 5.4 | Acc. | Alg. 5.1 | Alg. 5.4 | Acc. |
| $3 \times 3$ | 828 | **543** | 1.52 | 760 | **557** | 1.36 |
| $5 \times 5$ | 1860 | **697** | 2.66 | 726 | **526** | 1.38 |
| $7 \times 7$ | 3465 | **1158** | 3 | 961 | **608** | 1.58 |
| $9 \times 9$ | 4707 | **1447** | 3.25 | 1123 | **622** | 1.81 |
| $11 \times 11$ | 9216 | **1806** | 5.10 | 1402 | **668** | 2.1 |
| $13 \times 13$ | 9957 | **2927** | 3.40 | 1510 | **696** | 2.17 |

**Table 5.2.:** Number of iterations required by Algorithms 5.1 and 5.4 until convergence to a solution of the nonlocal PDE (5.43), for *uniform* and *nonuniform* averaging and various neighborhood sizes $|\mathcal{N}|$. Columns Acc. list the additional factor of iterations required by Algorithm 5.1 relative to Algorithm 5.4.

## 5.8. Conclusion

**Conclusion.** Using established nonlocal calculus, in this chapter we devised a novel nonlocal PDE with nonlocal boundary conditions on weighted graphs. We provided rigorous discrete mathematical framework that bridges common regularization techniques from image denoising [BCM10] and image inpainting [GO07; GO09] with the data labeling task. An in-depth discussion (Section 5.4) clarified common aspects and differences to related nonlocal approaches from the mathematical viewpoint. Our work has been motivated by the assignment flow approach [ÅPSS17; Sch20] to metric data labeling which was shown to constitute a special instance of our general approach introduced in this paper. In particular, our PDE contains the local PDE derived in [SS21] as special case and thus provides a natural nonlocal generalization.

Furthermore in this chapter we established two relations to numerical schemes [ZSPS20] for the geometric integration of the assignment flow: (i) Geometric integration can be applied to solve the novel nonlocal PDE. (ii) We showed that the basic geometric Euler integration scheme corresponds to the basic DC-algorithm of DC programming [LT18]. Moreover, the geometric viewpoint reveals how second-order information can be used in connection with line-search in order to accelerate the basic DC-algorithm for nonconvex optimization. On top of that, in Section 5.5.3 we have unveiled an interesting fundamental concept linking the two parts of the paper, namely the imposition of nonlocal boundary conditions and their positive influence on the step size selection.

A range of numerical results were reported in order to illustrate properties of the approach and the theoretical convergence results. This includes, in particular a linear convergence rate whenever a basin of attraction corresponding to an integral labeling solution is reached, whose existence was estabilised in [ZZS20].

# 6 Conclusion and Outlook

## Summary

Based on the concept of assignment flows [ÅPSS17], in the first part of the thesis we demonstrated how the underlying geometric framework can be adopted to smoothly integrate constraints adhering to application specific problems in medical imaging. This resulting in a novel, fully automated and purely data driven segmentation pipeline of retinal tissues in OCT-volumes. We applied the novel approach to the challenging task of tissue classification on volumetric optical coherence tomography data which typically comprises artifacts ranging from presence of speckle noise up to the lack of information near regions of vascular structures. An introduction to the required medical terms and concepts was given, together with the description of data acquisition process that was used throughout the experimental sections. We alleviated the aforementioned intricacies by leveraging 3D-texture information comprising two different feature selection processes by means of region covariance descriptors [TPM06] and the output obtained by training a CNN network. Hereby, we proved the effectiveness of our method by providing detailed performance evaluation against state of the art approaches [GASnd] and [RSS14] and have shown how voxel wise probabilistic characterization of ordering can be included in a statistical manifold as a global constraint. In particular, we achieved performance comparable to manual graders which makes our approach a method of choice for medical image applications. A key advantage of our method is its high range of flexibility in the choice of features living in any metric space which additionally provides the incorporation of outputs from trained neuronal convolution networks interpreted as image features. In addition, presented ideas can be easily transferred to other imaging domains such as seismographic horizon detection [YS20]

In the second part of our work, we focused on the theoretical perspective of the labeling approach by adopting the ideas from [DGLZ12; Du19] and added a novel approach to the literature on PDE-based image analysis that extends the scope from denoising and inpainting to image labeling. This resulted in a novel class of *nonlocal* partial *difference* equations for contextual data classification on weighted graphs from which the assignment flow emerges as a particular instance. To support our findings, we carried out an in-depth discussion of their connection to continuous PDE established in [SS21] and to models introduced in [AV10; ETT15]. We then considered class of such systems given by descent flows of a specific nonconvex potential (5.34) endowed with zero Dirichlet boundary conditions. Hereby, to fully manifest key regularization properties of the proposed G-PDE we provided two representatives of nonlocal boundaries in terms of *uniform* and *nonuniform* domain extensions respectively. We demonstrated how exploiting higher order information of the vector field (5.90) offers a new class of descent directions which are accompanied by *Wolfe*-like conditions that are of practical importance from the viewpoint of nonconvex optimization [NW06]. To our knowledge, convergence and acceleration of geometric DC-algorithms variants to critical points located at the manifold boundary have not been studied much in the literature which makes our work attractive to open new trends on

nonconvex programming.

## Future Work

Overall, our work presented a number of theoretical guidelines and practical implications of extending the geometric framework [Sch20] towards robust state of the art segmentation approach that has proved to be effective in medical applications. Hence, there are various potential ways that can be pursued for further examination. Regarding the classification of retinal tissues this includes the possible directions:

- Taking into account the recent extension of the assignment flows to unsupervised data segmentation in the context of [ZZPS20b] in connection with the results achieved in Chapter 4 can reduce the reliance of manually segmented ground truth for extracting dictionaries of prototypes which is a desirable property in clinical scenarios.
- To deal with highly variable layer boundaries another attractive line of research is to incorporate the weights of geometric averaging (3.61) in an optimal control theoretic way, to cope with the linearized dynamics of the assignment flow [ZSPS20].
- By building on the feasible concept of spatially regularized assignments [Sch20], the ordered flow (4.3.2) possesses the potential to be adopted to the detection of pathological retina changes and vascular vessel structure.
- Further future research objective is to incorporate the joint interaction of retina tissues and blood vessels during the segmentation process which will lead to a more effective layer detection and improved diagnosis of eye diseases.
- Finally, attractive research direction is given by the coherent structure of our approach, i.e. segmentation driven by spatial regularized decisions with initial data represented by (3.57), that can be used to support the vessel tracking on OCTA volumes by simultaneous layer segmentation. In particular this will lead to a more accurate extraction of 3D vascular networks by avoiding artifact caused by shadow effects.

In order to facilitate the proposed approach by building upon new mathematical insights derived in Chapter 5, possible future objectives can concern the following tasks

(i) Theoretical justification of a more generous class of nonlocal models formulated in terms of parameter matrices $\Omega$ not covered by Lemma 5.3.1. This will include the generalization of scalar valued mapping mappings $\Theta, \alpha$ to *tensor-valued* mappings resulting in diffusion processes that additionally capture the interrelation across labels $i, j, \in [c]$.

(ii) Potential applicability of nonlocal balance laws (5.52) in connection with recent works on parameter learning [ZPS22], uncertainty estimation [GAZS21] and image structure recognition

(iii) Having identified the interrelation of dynamical systems [Sch20] and nonlocal PDEs our next goal is to clarify such connection to a more general class of dynamical systems [SAS21b; SAS21a].

Pertaining to the line of research (i) and (ii) puts our work in a close relation to the mainstream research on deep neuronal network models for PDE parameter estimation and serves as a natural way to broaden their applicability to image labeling task which is still largely unexplored. In addition based on positive results prospective studies will include identification of further accelerated optimization schemes by exploiting higher order vector field derivatives and presenting it in a unified mathematical framework.

# A Supplementing Proofs

## A.1. Proofs of Chapter 2

*Proof of Lemma 3.1.1.* $(i)$: Let $p \in \mathcal{S}$ be arbitrary but fixed. For $v \in \mathbb{R}^c$ let $v_0 = \Pi_0 v = v - \frac{1}{c}\langle v, \mathbb{1}\rangle \mathbb{1}$ , be the orthogonal projection of $v$ onto $T_0$. It holds $\ker R_p = \mathbb{1}$ and $R_p$ is invertible on $T_0$. Using decomposition $v = v_0 + (v - v_0)$ along with $v - v_0 \in \mathbb{R}\mathbb{1}$, $\langle p, v_0\rangle = 0$ it follows

$$\big((R_p)_{T_0}\big)^{-1} R_p(v) = (R_p)^{-1} R_p(v_0) + R_p(v - v_0) = \Pi_0 \frac{R_p v_0}{p} \overset{(3.33)}{=} \Pi_0(v_0) = v_0. \tag{A.1}$$

$(ii)$ : By the symmetry of $R_p$, $R_p$ has real eigenvalues $\lambda_1 \leq \ldots, \leq \lambda_{\max}$. We show that $\lambda_1 \geq 0$. For $v \in \mathbb{R}^c$ we have

$$\langle v, R_p v\rangle = \langle v, pv\rangle - \langle p, v\rangle^2 = \sum_{i=1}^{c} p_i v_i^2 - (\sum_{i=1}^{c} v_i p_i)^2 = \mathbb{E}_p(v^2) - \big(\mathbb{E}_p(v)\big)^2 = \mathrm{Var}_p(v) \geq 0, \tag{A.2}$$

from which the positive semi-definiteness follows. Let $v \in \mathbb{R}^c$ be the eigenvector to the largest eigenvalue $\lambda_{\max} > 0$. It follows

$$0 < \lambda_{\max}\langle v, v\rangle = \langle v, R_p v\rangle \leq \|R_p v\|\|v\| \leq \|R_p\|_\infty \|v\|^2, \tag{A.3}$$

where $\|R_p\|_\infty = \max_{i\in[c]}\{\sum_{j\in[c]} |(R_p)_{ij}|\}$ is the infinity norm of $R_p$. Recalling definition (3.33) the following inequality holds for each $i \in [c]$

$$\begin{aligned}
\sum_{j\in[c]} |(R_p)_{ij}| &\leq |p_i(1-p_i)| + |p_i \sum_{j\neq i} p_j| = 2p_i(1-p_i) \\
&= \frac{1}{2} - 2\big(\frac{1}{4} - 2\frac{1}{2}p_i + p_i^2\big) \\
&= \frac{1}{2} - (\frac{1}{2} - p_i)^2 \\
&\leq \frac{1}{2}.
\end{aligned} \tag{A.4}$$

As $i \in [c]$ was arbitrary, plugging (A.4) into (A.1) yields

$$\lambda_{\max}\|v\|^2 \leq \frac{1}{2}\|v\|^2 \tag{A.5}$$

which completes the proof after dividing by $\|v\|^2$. □

## A.2. Proofs of Chapter 4

*Proof of Lemma 4.3.1.* Matrix $B$ is regular with inverse

$$B^{-1} = -Q, \qquad Q_{i,j} = \begin{cases} 1 & \text{if } i \geq j \\ 0 & \text{else} \end{cases} \tag{A.6}$$

and $w_j - w_i \in K \Leftrightarrow B^{-1}(w_j - w_i) \in \mathbb{R}^c_+$. It holds

$$B^{-1}(w_j - w_i) = Qe_{l_1} - Qe_{l_2} = \sum_{k=l_1}^{c} e_k - \sum_{k=l_2}^{c} e_k \tag{A.7}$$

such that $B^{-1}(w_j - w_i)$ has nonnegative entries exactly if $l_1 \leq l_2$. □

*Proof of Lemma 4.3.2.* Equation (4.17) directly implies $M_{11} \geq 0$ and $M_{cc} \geq 0$ because $M$ is upper triangular. For row indices $l \neq m$ and column indices $q \neq r$, define the matrix $O^{lm,qr}$ with

$$O^{lm,qr}_{ij} = \begin{cases} -1 & \text{if } (i,j) = (l,q) \vee (i,j) = (m,r) \\ 1 & \text{if } (i,j) = (l,r) \vee (i,j) = (m,q) \\ 0 & \text{else} \end{cases} . \tag{A.8}$$

Then $O^{lm,qr}\mathbb{1} = (O^{lm,qr})^\top \mathbb{1} = 0$. Adding a matrix $O^{lm,qr}$ to $M$ does therefore not change its marginals, but it redistributes mass from the positions $(l,q)$ and $(m,r)$ to the positions $(l,r)$ and $(m,q)$. Due to (4.17), it is possible to choose scalars $\alpha^k_{lr} \geq 0$ such that

$$M + \sum_{2 \leq k \leq c-1} \sum_{\substack{l<k \\ r>k}} \alpha^k_{lr} O^{lk,kr} \geq 0 . \tag{A.9}$$

□

*Proof of Proposition 4.3.1.* "⇐" Suppose there exists a measure $M \in \mathbb{R}^{c \times c}$ with marginals $w_i$, $w_j$ and $\langle Q - I_c, M \rangle = 0$. Then

$$w_j - w_i = By \;\Leftrightarrow\; Q(M - M^\top)\mathbb{1} = y . \tag{A.10}$$

It suffices to show that no entry of $y$ is negative. Define the shorthand $\zeta = (M - M^\top)\mathbb{1}$. Further, let $M_{\cdot,k}$ denote the $k$-th column of $M$ and let $M_{k,\cdot}$ denote the $k$-th row of $M$. For $l \in [c]$ the components of $\zeta$ are given by

$$\zeta_l = (M - M^\top)\mathbb{1}|_l = \langle M_{l,\cdot} - M_{\cdot,l}, \mathbb{1} \rangle = \sum_{k=l}^{c} M_{l,k} - \sum_{k=1}^{l} M_{k,l}. \tag{A.11}$$

By (A.10), the entries of $y$ read

$$y_r = \sum_{q=1}^{r} \zeta_q . \tag{A.12}$$

We can now inductively show that $y_r \geq 0$ for all $r \in [c]$. The cases $r = 1$ and $r = c$ are immediate:

$$y_1 = \zeta_1 = \sum_{k=1}^{c} M_{1,k} - M_{1,1} = \sum_{k=2}^{c} M_{1,k} \geq 0 \tag{A.13}$$

$$y_c = \langle \zeta, \mathbb{1} \rangle = \langle M - M^\top, \mathbb{1}\mathbb{1}^\top \rangle = \sum_{i,j \in [c]} M_{i,j} - \sum_{i,j \in [c]} M_{i,j}^\top = 0\,. \tag{A.14}$$

For $r \in \{2, \ldots, c-1\}$ we make the hypothesis that

$$y_r = \sum_{q=1}^{r} \zeta_q = \sum_{k=r+1}^{c} (M_{1,k} + \ldots + M_{r,k}) \geq 0 \tag{A.15}$$

which is consistent with the result for $r = 1$ in (A.13). It follows

$$y_{r+1} = \sum_{q=1}^{r+1} \zeta_q \tag{A.16}$$

$$= \zeta_{r+1} + \sum_{k=r+1}^{c} (M_{1,k} + \ldots + M_{r,k}) \tag{A.17}$$

$$= \sum_{k=r+1}^{c} M_{r+1,k} - \sum_{k=1}^{r+1} M_{k,r+1} + \sum_{k=r+1}^{c} (M_{1,k} + \ldots + M_{r,k}) \tag{A.18}$$

$$= \sum_{k=r+2}^{c} M_{r+1,k} + \sum_{k=r+2}^{c} (M_{1,k} + \ldots + M_{r,k}) \tag{A.19}$$

$$= \sum_{k=r+2}^{c} (M_{1,k} + \ldots + M_{r,k} + M_{r+1,k}) \tag{A.20}$$

where we used (A.15) in (A.17). This completes the inductive step and thus shows $y \geq 0$.

"⇒" Let $(w_i, w_j)$ be ordered. Following Definition (4.3.1), it holds

$$B^{-1}(w_j - w_i) = Q(w_i - w_j) \in \mathbb{R}^c_+. \tag{A.21}$$

We show the existence of a transport plan $M \geq 0$ satisfying

$$M\mathbb{1} = w_i, \quad M^\top \mathbb{1} = w_j \tag{A.22}$$

as well as the ordering constraint $\langle Q - I_c, M \rangle = 0$ by direct construction. For $c = 2$,

$$M = \begin{pmatrix} (w_j)_1 & (w_i)_1 - (w_j)_1 \\ 0 & 1 - (w_i)_1 \end{pmatrix} \tag{A.23}$$

satisfies these requirements. Now, let $c > 2$ and define the mapping

$$C_1^{c-1} : \Delta_c \to \Delta_{c-1} \tag{A.24}$$

$$w \mapsto \tilde{w} = (w_2, \ldots, w_c) + \frac{w_1}{c-1} \mathbb{1}_{c-1}. \tag{A.25}$$

If $(w_i, w_j) \in \Delta_c^2$ is ordered, then the two assignments

$$(\tilde{w}_i, \tilde{w}_j) := (C_1^{c-1}(w_i), C_1^{c-1}(w_j)) \in \Delta_{c-1}^2 \tag{A.26}$$

are ordered as well because

$$Q(\tilde{w}_i - \tilde{w}_j) = Q(\bar{w}_i - \bar{w}_j) + \frac{(w_i)_1 - (w_j)_1}{c-1} Q\mathbb{1} \geq 0 \tag{A.27}$$

where $\bar{w}_i$ denotes the vector $((w_i)_2, \ldots, (w_i)_c)$. Suppose a transport plan $\tilde{M} \in \mathbb{R}^{(c-1)\times(c-1)}$ exists such that

$$\tilde{M}\mathbb{1}_{c-1} = \tilde{w}_i \quad \tilde{M}^\top \mathbb{1}_{c-1} = \tilde{w}_j, \quad \tilde{M} \geq 0. \tag{A.28}$$

To complete the inductive step, we consider the matrix

$$M^0 := \begin{pmatrix} (w_j)_1 & s^\top \\ 0 & \tilde{M} - \frac{(w_i)_1}{c-1} I \end{pmatrix}, \quad s = \frac{(w_i)_1 - (w_j)_1}{c-1} \mathbb{1}_{c-1} \tag{A.29}$$

which satisfies (A.22) as well as $\langle Q - I_c, M^0 \rangle = 0$. By Lemma 4.3.2, $M^0$ can be modified to yield a transport plan with the desired properties. □

## A.3. Details of employed CNN architecture

As described in Section 4.4.4, we employed a CNN architecture for feature extraction which comprises four residually connected blocks. Fig. A.1 shows a detailed account of how network components are connected. The network produces a sequence of hidden states with channel dimensions 8, 16, 32, 64. Each block contains 3D convolution with filter size $3 \times 3 \times 3$ and rectified linear unit (ReLU) is used as activation function. We trained the network until training loss stopped decreasing after around 4.45M iterations of the stochastic gradient descent optimizer in pytorch with step-length $0.001$, momentum $0.9$ and batch size $512$. Image patches were drawn in random order from the volumes in the training set. During training, we also used dropout with probability $0.3$ prior to the single linear layer which decodes class scores.

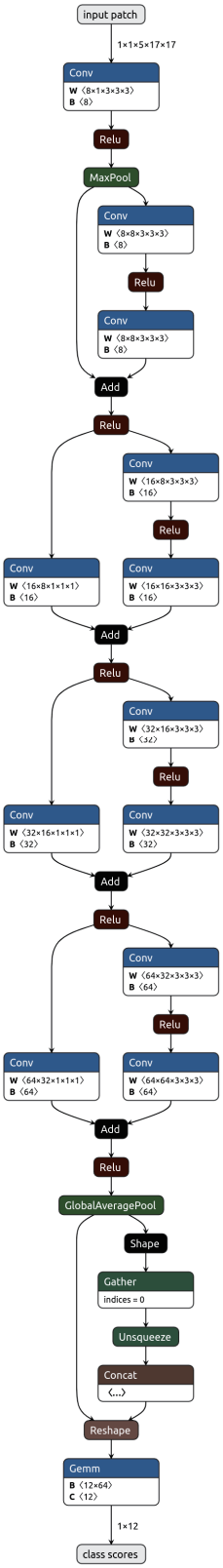


**Figure A.1.:** Convolutional neural network architecture employed for feature extraction.

## A.4. Details of used OCT Data

**Table A.1.:** Metadata of OCT volume scans used for training.

| # B-Scans | # A-Scans | Height (px) | B-Scan Distance (µm) | A-Scan Distance (µm) | H-Scale (µm / px) |
|---|---|---|---|---|---|
| 19 | 1536 | 496 | 232.68 | 5.50 | 3.87 |
| 19 | 1536 | 496 | 249.88 | 5.51 | 3.87 |
| 19 | 1536 | 496 | 230.57 | 5.59 | 3.87 |
| 19 | 1536 | 496 | 23.55 | 5.40 | 3.87 |
| 19 | 1536 | 496 | 241.00 | 0.58 | 3.87 |
| 19 | 1536 | 496 | 249.07 | 5.79 | 3.87 |
| 19 | 1536 | 496 | 231.81 | 5.48 | 3.87 |
| 19 | 1536 | 496 | 255.27 | 5.78 | 3.87 |
| 19 | 1536 | 496 | 249.04 | 5.70 | 3.87 |
| 19 | 1536 | 496 | 261.67 | 5.97 | 3.87 |
| 19 | 1536 | 496 | 244.90 | 5.58 | 3.87 |
| 19 | 1536 | 496 | 233.74 | 5.44 | 3.87 |
| 19 | 1536 | 496 | 240.63 | 5.59 | 3.87 |
| 19 | 1536 | 496 | 236.18 | 5.45 | 3.87 |
| 19 | 1536 | 496 | 233.71 | 5.36 | 3.87 |
| 19 | 1536 | 496 | 244.55 | 0.57 | 3.87 |
| 19 | 1536 | 496 | 252.80 | 5.93 | 3.87 |
| 19 | 1536 | 496 | 239.38 | 5.61 | 3.87 |
| 19 | 1536 | 496 | 254.07 | 0.60 | 3.87 |
| 19 | 1536 | 496 | 247.47 | 5.83 | 3.87 |
| 19 | 1536 | 496 | 238.06 | 5.52 | 3.87 |
| 19 | 1536 | 496 | 259.48 | 6.05 | 3.87 |
| 19 | 1536 | 496 | 26.13 | 5.88 | 3.87 |
| 19 | 1536 | 496 | 243.29 | 5.60 | 3.87 |
| 19 | 1536 | 496 | 241.77 | 5.76 | 3.87 |
| 61 | 768 | 496 | 118.57 | 11.31 | 3.87 |
| 61 | 768 | 496 | 1.17 | 11.29 | 3.87 |
| 61 | 768 | 496 | 117.17 | 11.08 | 3.87 |
| 61 | 768 | 496 | 122.79 | 11.37 | 3.87 |
| 61 | 768 | 496 | 121.09 | 11.52 | 3.87 |
| 61 | 768 | 496 | 123.31 | 11.38 | 3.87 |
| 61 | 768 | 496 | 123.50 | 11.72 | 3.87 |
| 61 | 768 | 496 | 115.40 | 10.92 | 3.87 |
| 61 | 768 | 496 | 114.32 | 10.79 | 3.87 |
| 61 | 768 | 496 | 116.34 | 10.96 | 3.87 |
| 61 | 768 | 496 | 119.15 | 11.30 | 3.87 |
| 61 | 768 | 496 | 127.25 | 11.81 | 3.87 |
| 61 | 768 | 496 | 126.43 | 12.19 | 3.87 |
| 61 | 768 | 496 | 121.90 | 11.45 | 3.87 |
| 61 | 768 | 496 | 12.30 | 11.64 | 3.87 |
| 61 | 768 | 496 | 124.78 | 11.86 | 3.87 |
| 61 | 768 | 496 | 123.42 | 11.40 | 3.87 |
| 61 | 768 | 496 | 120.17 | 11.40 | 3.87 |
| 61 | 768 | 496 | 126.53 | 12.04 | 3.87 |
| 61 | 768 | 496 | 115.97 | 10.96 | 3.87 |
| 61 | 768 | 496 | 128.34 | 12.19 | 3.87 |
| 61 | 768 | 496 | 124.72 | 11.74 | 3.87 |
| 61 | 768 | 496 | 119.16 | 11.10 | 3.87 |
| 61 | 768 | 496 | 119.46 | 11.23 | 3.87 |

Continued on next page

**Table A.1.:** Metadata of OCT volume scans used for training.

| # B-Scans | # A-Scans | Height (px) | B-Scan Distance (µm) | A-Scan Distance (µm) | H-Scale (µm / px) |
|---|---|---|---|---|---|
| 61 | 768 | 496 | 123.59 | 11.80 | 3.87 |
| 61 | 768 | 496 | 118.64 | 11.07 | 3.87 |
| 61 | 768 | 496 | 125.97 | 1.21 | 3.87 |
| 61 | 768 | 496 | 119.12 | 11.47 | 3.87 |
| 61 | 768 | 496 | 122.94 | 11.65 | 3.87 |
| 61 | 768 | 496 | 129.43 | 12.07 | 3.87 |
| 61 | 768 | 496 | 116.85 | 11.26 | 3.87 |
| 61 | 768 | 496 | 122.56 | 11.64 | 3.87 |
| 61 | 768 | 496 | 128.97 | 12.09 | 3.87 |
| 512 | 512 | 496 | 0.58 | 0.58 | 3.87 |
| 512 | 512 | 496 | 0.58 | 0.58 | 3.87 |
| 256 | 384 | 496 | 11.57 | 1.15 | 3.87 |
| 256 | 384 | 496 | 11.57 | 1.15 | 3.87 |
| 512 | 512 | 496 | 0.58 | 0.58 | 3.87 |
| 256 | 384 | 496 | 11.57 | 1.15 | 3.87 |
| 512 | 512 | 496 | 5.86 | 5.85 | 3.87 |
| 256 | 384 | 496 | 11.57 | 1.15 | 3.87 |
| 512 | 512 | 496 | 5.77 | 0.58 | 3.87 |
| 256 | 384 | 496 | 11.57 | 1.15 | 3.87 |
| 512 | 512 | 496 | 0.58 | 0.58 | 3.87 |
| 512 | 512 | 496 | 0.58 | 0.58 | 3.87 |
| 256 | 384 | 496 | 12.10 | 12.05 | 3.87 |
| 512 | 512 | 496 | 6.04 | 6.03 | 3.87 |
| 512 | 512 | 496 | 6.04 | 6.03 | 3.87 |
| 512 | 512 | 496 | 6.04 | 6.03 | 3.87 |
| 512 | 512 | 496 | 5.70 | 5.69 | 3.87 |
| 19 | 512 | 496 | 242.72 | 11.38 | 3.87 |
| 19 | 512 | 496 | 241.81 | 11.33 | 3.87 |
| 19 | 512 | 496 | 242.72 | 11.38 | 3.87 |
| 19 | 512 | 496 | 242.72 | 11.38 | 3.87 |
| 19 | 512 | 496 | 241.81 | 11.33 | 3.87 |
| 19 | 512 | 496 | 245.15 | 1.15 | 3.87 |
| 19 | 512 | 496 | 242.72 | 11.38 | 3.87 |

**Table A.2.:** Metadata of OCT volume scans used for testing.

| # B-Scans | # A-Scans | Height (px) | B-Scan Distance (µm) | A-Scan Distance (µm) | H-Scale (µm / px) |
|---|---|---|---|---|---|
| 61 | 768 | 496 | 116.89 | 11.08 | 3.87 |
| 61 | 768 | 496 | 120.11 | 11.33 | 3.87 |
| 61 | 768 | 496 | 123.18 | 11.72 | 3.87 |
| 61 | 768 | 496 | 127.47 | 11.94 | 3.87 |
| 61 | 768 | 496 | 127.31 | 1.23 | 3.87 |
| 61 | 768 | 496 | 122.97 | 11.52 | 3.87 |
| 61 | 768 | 496 | 113.69 | 1.10 | 3.87 |
| 61 | 768 | 496 | 124.13 | 11.80 | 3.87 |

## A.5. Proofs of Section 5.3.2

*Proof of Lemma 5.3.1.* In order to show (5.40), we directly compute using assumption (5.38) and the parametrization (5.39), for any $x \in \mathcal{V}$,

$$\sum_{y\in\mathcal{V}} \Omega(x,y)f(y) \overset{(5.39)}{=} \sum_{y\in\mathcal{N}(x)} \Theta(x,y)\alpha^2(x,y)f(y) + \Theta(x,x)f(x) \tag{A.30a}$$

$$= \sum_{y\in\mathcal{N}(x)} \Theta(x,y)\alpha^2(x,y)f(y) + \Theta(x,x)f(x) + \big(\lambda(x)-\lambda(x)\big)f(x) \tag{A.30b}$$

$$\overset{(5.41)}{=} \sum_{y\in\mathcal{N}(x)} \Theta(x,y)\alpha^2(x,y)\big(f(y)-f(x)\big) + \lambda(x)f(x) \tag{A.30c}$$

$$\overset{f|_{\mathcal{V}_\mathcal{I}^\alpha}=0}{=} -\sum_{y\in\overline{\mathcal{V}}} \Theta(x,y)\alpha^2(x,y)\Big(-\big(f(y)-f(x)\big)\Big) + \lambda(x)f(x) \tag{A.30d}$$

$$\overset{(5.15)}{=} -\sum_{y\in\overline{\mathcal{V}}} \Theta(x,y)\big((\mathcal{D}^\alpha)^*(f)(x,y)\big)\alpha(x,y) + \lambda(x)f(x) \tag{A.30e}$$

$$= \sum_{y\in\overline{\mathcal{V}}} \frac{1}{2}\Theta(x,y)\big(-2(\mathcal{D}^\alpha)^*(f)(x,y)\alpha(x,y)\big) + \lambda(x)f(x) \tag{A.30f}$$

$$\overset{(5.16)}{=} \sum_{y\in\overline{\mathcal{V}}} \frac{1}{2}\Theta(x,y)\big(2\mathcal{G}^\alpha(f)(x,y)\alpha(x,y)\big) + \lambda(x)f(x) \tag{A.30g}$$

$$\overset{(5.19)}{=} \frac{1}{2}\mathcal{D}^\alpha\big(\Theta\mathcal{G}^\alpha(f)\big)(x) + \lambda(x)f(x) \tag{A.30h}$$

which proves (5.40).

Assume that $\lambda(x) \leq 1$ for all $x \in \mathcal{V}$. Then, properties (5.4) easily follows from the nonnegativity of $\Theta \in \mathcal{F}_{\overline{\mathcal{V}}\times\overline{\mathcal{V}}}$ and definition (5.41). In addition, if $\Omega$ is given by (5.39) and also satisfies (5.24), then equality in (5.41) is achieved:

$$1 = \sum_{y\in\mathcal{V}} \Omega(x,y) = \sum_{y\in\mathcal{V}} \Theta(x,y)\alpha^2(x,y) + \Theta(x,x) = \lambda(x) \underbrace{-\sum_{y\in\mathcal{V}_\mathcal{I}^\alpha} \Theta(x,y)\alpha^2(x,y)}_{\geq 0} \leq \lambda(x) \overset{(5.41)}{\leq} 1. \tag{A.31}$$

□

*Proof of Proposition 5.3.1.* Recalling definition (5.28), we directly compute

$$R_{S(x,t)}\big((\Omega S)(x,t)\big) = R_{S(x,t)}\Big(\sum_{y\in\mathcal{V}} \Omega(x,y)S(y,t)\Big) \tag{A.32a}$$

$$\overset{(5.40)}{=} R_{S(x,t)}\Big(\frac{1}{2}\mathcal{D}^\alpha\big(\Theta\mathcal{G}^\alpha(S)\big)(x) + \lambda(x)S(x)\Big). \tag{A.32b}$$

□

### A.5.1. Proofs of Section 5.3.4

*Proof of Proposition 5.3.2.* For brevity, we omit the argument $t$ and simply write $S = S(t), V = V(t)$. With the componentwise operation $\odot$ given as $(S \odot V)_j(x) = S_j(x)V_j(x)$ for $j \in [c]$, and $S^2(x) = (S \odot S)(x)$.

Multiplying both sides of (5.51a) with $S(x) = \exp_{S^0}(V(x))$ and summing over $x \in \mathcal{V}$ yields

$$\sum_{x\in\mathcal{V}} \big(S \odot \dot{V}\big)_j(x) - \sum_{x\in\mathcal{V}} \frac{1}{2}\Big(S \odot \mathcal{D}^\alpha\big(\Theta\mathcal{G}^\alpha(S)\big)\Big)_j(x) = \sum_{x\in\mathcal{V}} \big(\lambda S^2\big)_j(x). \tag{A.33}$$

Applying Greens nonlocal first identity (5.17) with $u(x) = S_j(x)$ to the second term on the left-hand side yields with (5.8)

$$\sum_{x\in\mathcal{V}} \big(S \odot \dot{V}\big)_j(x) + \frac{1}{2}\sum_{x\in\overline{\mathcal{V}}}\sum_{y\in\overline{\mathcal{V}}} \big(\mathcal{G}^\alpha(S) \odot (\Theta\mathcal{G}^\alpha(S))\big)_j(x,y) \tag{A.34a}$$

$$+ \sum_{y\in\mathcal{V}_I^\alpha} S_j(y)\mathcal{N}^\alpha\big(\Theta\mathcal{G}^\alpha(S_j)\big)(y) = \sum_{x\in\mathcal{V}} \big(\lambda S^2\big)_j(x). \tag{A.34b}$$

Now, using the parametrization (5.46) of $S$, we compute at each $x \in \mathcal{V}$:

$$\dot{S}(x) = \frac{d}{dt}\exp_{S^0(x)}\big(V(x)\big) \tag{A.35a}$$

$$\overset{(5.47)}{=} \frac{\big(\frac{d}{dt}\big(S^0(x)\odot e^{V(x)}\big)\big)\langle S^0(x), e^{V(x)}\rangle - \big(\frac{d}{dt}\langle S^0(x), e^{V(x)}\rangle\big)S^0(x)\odot e^{V(x)}}{\langle S^0(x), e^{V(x)}\rangle^2} \tag{A.35b}$$

$$= \frac{\langle S^0(x), e^{V(x)}\rangle(S^0 \odot e^V)(x)\odot \dot{V}(x) - \langle S^0(x)\odot e^{V(x)}, \dot{V}(x)\rangle(S^0\odot e^V)(x)}{\langle S^0(x), e^{V(x)}\rangle^2} \tag{A.35c}$$

$$= (S\odot\dot{V})(x) - \langle S(x), \dot{V}(x)\rangle S(x) \tag{A.35d}$$

$$\overset{(5.49)}{=} (S\odot\dot{V})(x) - \langle S(x), (\Pi_0\Omega\exp_{S^0}(V))(x)\rangle S(x) \tag{A.35e}$$

$$\overset{(5.53)}{=} (S\odot\dot{V})(x) - \phi_S(x)S(x). \tag{A.35f}$$

Solving the last equation for $(S\odot\dot{V})(x)$ and substitution into (A.34) yields after taking the sum over $x \in \mathcal{V}$, for each $S_j = \{S_j(x) \colon x \in \mathcal{V}\}$, $j \in [c]$

$$\frac{1}{2}\frac{d}{dt}\Big(\sum_{x\in\mathcal{V}} S_j(x)\Big) + \frac{1}{2}\langle\mathcal{G}^\alpha(S_j), \Theta\mathcal{G}^\alpha(S_j)\rangle_{\overline{\mathcal{V}}\times\overline{\mathcal{V}}} + \sum_{x\in\mathcal{V}}\phi_S(x)S_j(x) \tag{A.36a}$$

$$+ \sum_{y\in\mathcal{V}_{\mathcal{I}^\alpha}} S_j\mathcal{N}^\alpha\big(\Theta\mathcal{G}^\alpha(S_j)\big)(y) = \sum_{x\in\mathcal{V}}\big(\lambda S_j^2\big)(x), \tag{A.36b}$$

which after rearranging the terms is equal to (5.52). □

### A.5.2. Proofs of Section 5.5.1

*Proof of Proposition 5.5.1.* Equation (5.86) directly follows from Proposition 5.3.1, from the specification (3.62) of the similarity mapping and from the relation $\exp_p = \mathrm{Exp}_p \circ R_p$ for $p \in \mathcal{S}$

(cf. (5.29), (3.54)). Leveraging the parametrization (5.50) of system (5.43), discretization of (5.50) by forward finite differences with step size parameter $h > 0$ yields for $x \in \mathcal{V}$

$$\frac{V^{k+1}(x) - V^k(x)}{h} = \Big(\frac{1}{2}\mathcal{D}^\alpha\big(\Theta\mathcal{G}^\alpha(\exp_{S^0}(V^k))\big) + \lambda \exp_{S^0}(V^k)\Big)(x) \tag{A.37}$$

which is (5.86) after applying the lifting map (3.54) to $V^{k+1}$. Consequently, in view of zero nonlocal boundary conditions, the zero extension of (5.86) to $\overline{\mathcal{V}}$ verifies that $\overline{S}^k$ is indeed a first order approximation of solution $S(kh)$ to (5.43).

It remains to show that (5.85) implies (5.88). Adding and subtracting a convex negative entropy term

$$\langle S, \log S\rangle = \sum_{x\in\mathcal{V}} \langle S(x), \log S(x)\rangle, \qquad \log S(x) = \big(\log S_1(x), \dots, \log S_c(x)\big)^\top \tag{A.38}$$

to the potential (5.34), we write with the convex constraint $S \in \overline{\mathcal{W}}$ represented by the delta-function $\delta_{\overline{\mathcal{W}}}$,

$$J(S) = \underbrace{\gamma\langle S, \log S\rangle + \delta_{\overline{\mathcal{W}}}(S)}_{g(S)} - \Big(\underbrace{\frac{1}{2}\langle S, \Omega S\rangle + \gamma\langle S, \log S\rangle}_{h(S)}\Big), \quad \gamma > |\lambda_{\min}(\Omega)|, \tag{A.39}$$

which is a DC-function [Har59] if $\gamma > |\lambda_{\min}(\Omega)|$, i.e. both $g(S)$ and $h(S)$ are convex. Indeed, while the convexity of $g$ is obvious, the convexity of $h$ becomes apparent when inspecting its Hessian. Writing

$$s = \mathrm{vec}_r(S) \tag{A.40}$$

with the row-stacking mapping $\mathrm{vec}_r$, we have ($\otimes$ denotes the Kronecker matrix product)

$$\langle S, \Omega S\rangle = \langle s, (\Omega \otimes I_c)s\rangle \tag{A.41a}$$

$$\langle S, \log S\rangle = \langle s, \log s\rangle, \qquad \log s = (\dots, \log s_i, \dots)^\top \tag{A.41b}$$

and hence for any $v \in \mathbb{R}^{nc}$ with $\|v\| = 1$

$$d^2h(S)(v,v) = \Big\langle v, \Big((\Omega \otimes I_c) + \gamma\,\mathrm{Diag}\Big(\frac{\mathbb{1}}{s}\Big)\Big)v\Big\rangle > \lambda_{\min}(\Omega) + \gamma, \tag{A.42}$$

where the last inequality follows from $\lambda \geq \lambda_{\min}(\Omega)$ for any eigenvalue $\lambda$ of the symmetric matrix $\Omega$ (recall (5.4), (5.24)), $\lambda(A \otimes B) = \lambda_i(A)\lambda_j(B)$ for some $i, j$ [Gra81], and $\lambda_{\min}(\mathrm{Diag}(\frac{\mathbb{1}}{s})) > 1$ if $S \in \overline{\mathcal{W}}$.

Thus, if $\gamma > |\lambda_{\min}(\Omega)|$ then $h$ is convex and minimizing (A.39) is a DC-programming problem [HT99; HAPD05]. Using Fenchel's inequality $-h(S^k) \leq h^*(\widetilde{S}) - \langle S^k, \widetilde{S}\rangle$, $\forall \widetilde{S}$, let $\widetilde{S}^k$ minimize at the current iterate $S^k$ the upper bound

$$J(S^k) = g(S^k) - h(S^k) \leq g(S^k) + h^*(\widetilde{S}) - \langle S^k, \widetilde{S}\rangle, \qquad \forall \widetilde{S} \tag{A.43a}$$

with respect to $\widetilde{S}$, i.e.

$$0 = \partial h^*(\widetilde{S}^k) - S^k \qquad \Leftrightarrow \qquad \widetilde{S}^k \in \partial h(S^k) = \nabla h(S^k). \tag{A.43b}$$

In particular, $-h(S^k) = h^*(\widetilde{S}^k) - \langle S^k, \widetilde{S}^k\rangle$ and hence

$$J(S^k) = g(S^k) + h^*(\widetilde{S}^k) - \langle S^k, \widetilde{S}^k\rangle. \tag{A.44}$$

Minimizing in turn the right-hand side with respect to $S^k$ guarantees (5.88) and defines the update $S^{k+1}$ by

$$S^{k+1} = \arg\min_S\{g(S) - \langle S, \widetilde{S}^k\rangle\} \qquad \Leftrightarrow \qquad 0 = \partial g(S^{k+1}) - \widetilde{S}^k \tag{A.45a}$$

$$\Leftrightarrow \quad \gamma(\log S^{k+1}(x) + \mathbb{1}) + \partial\delta_{\overline{S}}\big(S^{k+1}(x)\big) \overset{(A.43b)}{=} \nabla h(S^k)(x) \tag{A.45b}$$

$$= (\Omega S^k)(x) + \gamma(\log S^k(x) + \mathbb{1}). \tag{A.45c}$$

Solving for $S^{k+1}(x)$ yields (5.85) resp. (5.86) with stepsize $h = \frac{1}{\gamma} < 1$ due to $\gamma > |\lambda_{\min}(\Omega)|$. □

## A.5.3. Proofs of Section 5.5.2

*Proof of Lemma 5.5.1.* Taking into account the parametrization (5.46), we compute the partial derivative of (5.34)

$$\partial_i J(V) = -\big\langle \Omega \exp_{S^0}(V), \partial_i \exp_{S^0}(V)\big\rangle \tag{A.46a}$$

$$= -\big\langle \Omega \exp_{S^0}(V), \exp_{S^0}(V) \odot e_i + \exp_{S^0}(V)_i \exp_{S^0}(V)\big\rangle \tag{A.46b}$$

$$= -\big(\Omega \exp_{S^0}(V) \odot \exp_{S^0}(V)\big)_i + \big\langle \Omega \exp_S(V), \exp_{S^0}(V)\big\rangle \exp_{S^0}(V)_i \tag{A.46c}$$

$$= -\big(R_{\exp_{S^0}(V)}(\Omega \exp_{S^0}(V))\big)_i \tag{A.46d}$$

and consequently $\partial J(V) = \partial_V J(V) = -R_{\exp_{S^0}(V)}(\Omega \exp_{S^0}(V)) = R_S \partial_S J(S) = \operatorname{grad}_g J(S)$. □

*Proof of Proposition 5.5.2.*

(i) Using $S^k = \exp_{S^0}(V^k)$ and

$$\partial J(V^k) = -R_{S^k}(\Omega S^k) = \operatorname{grad}_g J(S^k) \tag{A.47}$$

by Lemma 5.5.1 along with the identities (recall that both $R_S$ and the orthogonal projection $\Pi_0$ act row-wise)

$$R_S = \Pi_0 R_S = R_S \Pi_0 = \Pi_0 R_S \Pi_0 = R_S|_{\mathcal{T}_0}, \quad S \in \mathcal{W}, \qquad \Pi_0^2 = \Pi_0 \tag{A.48}$$

and

$$\big(R_{S^k}|_{\mathcal{T}_0}\big)^{-1} V = \Big(\dots, \Pi_0 \frac{V(x)}{S^k(x)}, \dots\Big)^\top, \quad x \in V, \quad V \in \mathcal{T}_0, \quad S^k \in \mathcal{W} \tag{A.49}$$

by [SS21, Lemma 3.1], we have

$$\langle \partial J(V^k), d^k\rangle \overset{(5.97)}{=} \langle \partial J(V^k), d(S^k, h_k)\rangle \tag{A.50a}$$

$$= -\langle R_{S^k}(\Omega S^k), \Pi_0 \Omega S^k\rangle - \frac{h_k}{2}\langle \partial J(V^k), \Pi_0 \Omega \partial J(V^k)\rangle \tag{A.50b}$$

$$= -\langle R_{S^k}(\Omega S^k), \big((R_{S^k}|_{\mathcal{T}_0})^{-1} R_{S^k}|_{\mathcal{T}_0}\big)\Pi_0 \Omega S^k\rangle - \frac{h_k}{2}\langle \partial J(V^k), \Pi_0 \Omega \partial J(V^k)\rangle \tag{A.50c}$$

$$\overset{(5.100),(A.48),(A.49)}{=} -\langle R_{S^k}(\Omega S^k), R_{S^k}(\Omega S^k)\rangle_{S^k} - \frac{h_k}{2}\langle \partial J(V^k), \Pi_0 \Omega \partial J(V^k)\rangle. \tag{A.50d}$$

Since the first term on the right-hand side of (A.50d) is negative on $\mathcal{T}_0$, setting

$$h_k \in \left(0, \frac{\|R_{S^k}(\Omega S^k)\|_{S^k}^2}{|\langle \partial J(V^k), \Pi_0 \Omega \partial J(V^k)\rangle|}\right) \tag{A.51}$$

yields a sequence $(d^k)_{k\geq 1}$ satisfying

$$\langle \partial J(V^k), d^k\rangle < 0, \qquad k \geq 1. \tag{A.52}$$

Consider $c_1, c_2 \in (0,1)$ with $c_1 < c_2$ and set

$$G(\gamma) = J(V^k + \gamma d^k), \tag{A.53a}$$
$$L(\gamma) = J(V^k) + c_1 \gamma \langle \partial J(V^k), d^k\rangle \quad \text{for} \quad \gamma \geq 0. \tag{A.53b}$$

Due to $c_1 < 1$ and (A.52), the inequality

$$G'(0) = \langle \partial J(V^k), d^k\rangle < c_1 \langle \partial J(V^k), d^k\rangle = L'(0) < 0 \tag{A.54}$$

holds. Hence there is a constant $t_k > 0$ such that

$$G(\gamma) < L(\gamma), \quad \gamma \in (0, t_k), \tag{A.55a}$$
$$G(t_k) = L(t_k). \tag{A.55b}$$

Substituting the first-order Taylor expansion

$$G(t_k) = J(V^k + t_k d^k) = G(0) + t_k G'(\widetilde{\gamma}_k) \tag{A.56a}$$
$$= J(V^k) + t_k \langle \partial J(V^k + \widetilde{\gamma}_k d^k), d^k\rangle, \qquad \widetilde{\gamma}_k \in (0, t_k) \tag{A.56b}$$

into (A.55b) yields with (A.53b), (A.52) and $0 < c_1 < c_2 < 1$

$$\langle \partial J(V^k + \widetilde{\gamma}_k d^k), d^k\rangle = c_1 \langle \partial J(V^k), d^k\rangle \geq c_2 \langle \partial J(V^k), d^k\rangle. \tag{A.57a}$$

Therefore, with $\partial J(V^k), d^k \in \mathcal{T}_0$ and using that the restriction $R_{S^k}|_{\mathcal{T}_0}$ of the map $R_{S^k}$ to $\mathcal{T}_0$ is invertible with the inverse $(R_{S^k})^{-1}_{|\mathcal{T}_0}$ acting row-wise as specified by (A.49), the right-hand side of (A.57) becomes

$$c_2 \langle \partial J(V^k), d^k\rangle = c_2 \big\langle \partial J(V^k), (R_{S^k}|_{\mathcal{T}_0})^{-1}(R_{S^k}(d^k))\big\rangle \tag{A.57b}$$
$$\overset{(5.100),(A.49)}{=} c_2 \big\langle \Pi_0 \partial J(V^k), R_{S^k}(d^k)\big\rangle_{S^k}. \tag{A.57c}$$

By virtue of (A.47) and $\Pi_0 \partial J(V^k) = \partial J(V^k)$, both sides of (A.57) correspond to the expressions of (5.99b) between the bars $|\cdots|$. Since the above derivation shows that both sides of (A.57) are negative, taking the magnitude on both sides proves (5.99b).

Recalling the shorthand (5.93), inequality (A.56) and setting $\theta_k$ small enough with $\theta_k \leq \widetilde{\gamma}_k$, the iterates $S^{k+1} = \exp_{S^0}(V^k + \theta_k d_k)$ satisfy

$$J(S^{k+1}) - J(S^k) \overset{(A.56)}{=} t_k \langle \partial J(V^k + \widetilde{\gamma}_k d^k), d^k \rangle \tag{A.58a}$$

$$\leq \theta_k \langle \partial J(V^k + \widetilde{\gamma}_k d^k), d^k \rangle \tag{A.58b}$$

$$\overset{(A.57)}{\leq} \theta_k c_2 \langle \partial J(V^k), d^k \rangle \tag{A.58c}$$

$$\overset{(A.47)}{\overset{(A.57)}{=}} \theta_k c_2 \langle \operatorname{grad}_g J(S^k), R_{S^k}(d^k) \rangle_{S^k} \tag{A.58d}$$

which proves inequality (5.99a) since both sides are non-positive and $c_1 < c_2$.

(ii) We prove by contradiction: Assume, on the contrary, that there exists a sequence $(S^k)_{k\geq 0} \subset \overline{\mathcal{W}}$ in the compact set $\overline{\mathcal{W}}$ and a convergent subsequence $(S^{k_l})_{l\geq 0}$ with limit point $\lim_{l\to\infty} S^{k_l} = S^*$ which is *not* an equilibrium of (5.27a). Then, since the functional (5.34) is bounded from below on $\overline{\mathcal{W}}$, taking the sum in (5.99a) yields

$$\sum_{l=0}^{\infty} c_1 \gamma_{k_l} \langle \operatorname{grad}_g J(S^{k_l}), R_{S^{k_l}}(d^{k_l}) \rangle_{S^{k_l}} > \sum_{l=0}^{\infty} \big( J(S^{k_{l+1}}) - J(S^{k_l}) \big) = \underbrace{J(S^*) - J(S^0)}_{>-\infty}, \tag{A.59}$$

and consequently

$$c_1 \gamma_* \langle \operatorname{grad}_g J(S^*), R_{S^*}(d^*) \rangle_{S^*} = 0. \tag{A.60}$$

Using $d^* = d(S^*, h_*)$ given by (5.95) along with $c_1 > 0$ and the assumption $\gamma_* > 0$, we evaluate this equation similarly to (A.50)

$$0 = \langle \operatorname{grad}_g J(S^*), R_{S^*}(d^*) \rangle_{S^*} \tag{A.61a}$$

$$\overset{(A.48)}{=} \Big\langle -R_{S^*}(\Omega S^*), R_{S^*}\Big( \Omega S^* + \frac{h_*}{2} \Omega R_{S^*}(\Omega S^*) \Big) \Big\rangle_{S^*} \tag{A.61b}$$

$$\overset{(5.100),(A.48)}{=} -\sum_{x\in\mathcal{V}} \Big\langle \Pi_0 R_{S^*(x)}(\Omega S^*)(x), \frac{R_{S^*(x)}\big(\Omega S^* + \frac{h_*}{2}\Omega R_{S^*}(\Omega S^*)\big)(x)}{S^*(x)} \Big\rangle \tag{A.61c}$$

$$\overset{(A.49)}{=} -\sum_{x\in\mathcal{V}} \Big\langle R_{S^*(x)}(\Omega S^*)(x), (R_{S^*(x)}|_{T_0})^{-1} R_{S^*(x)}\Big( \Omega S^* + \frac{h_*}{2} \Omega R_{S^*}(\Omega S^*) \Big)(x) \Big\rangle \tag{A.61d}$$

$$\overset{(A.48)}{=} -\langle \Omega S^*, R_{S^*}(\Omega S^*) \rangle - \frac{h_*}{2} \big\langle \Omega S^*, R_{S^*}\big( \Omega R_{S^*}(\Omega S^*) \big) \big\rangle. \tag{A.61e}$$

Hence

$$\frac{h_*}{2} \big\langle \Omega S^*, R_{S^*}\big( \Omega R_{S^*}(\Omega S^*) \big) \big\rangle = -\langle \Omega S^*, R_{S^*}(\Omega S^*) \rangle \tag{A.62a}$$

$$= -\sum_{x\in\mathcal{V}} \big\langle (\Omega S^*)(x), R_{S^*(x)}(\Omega S^*)(x) \big\rangle \tag{A.62b}$$

using $R_p \mathbb{1}_c = 0,\ p \in \mathcal{S}$

$$= -\sum_{x\in\mathcal{V}} \Big\langle (\Omega S^*)(x) - \big\langle (\Omega S^*)(x), S^*(x) \big\rangle \mathbb{1}_c, R_{S^*(x)}(\Omega S^*)(x) \Big\rangle \tag{A.62c}$$

$$\overset{(3.33)}{=} -\sum_{x\in\mathcal{V}} \Big\langle (\Omega S^*)(x) - \big\langle (\Omega S^*)(x), S^*(x)\big\rangle \mathbb{1}_c, \tag{A.62d}$$

$$S^*(x) \odot \Big( (\Omega S^*)(x) - \big\langle S^*(x), (\Omega S^*)(x)\big\rangle \mathbb{1}_c \Big) \Big\rangle \tag{A.62e}$$

$$= -\sum_{x\in\mathcal{V}} \sum_{j\in[c]} S_j^*(x) \Big( (\Omega S^*)_j(x) - \big\langle (\Omega S^*)(x), S^*(x)\big\rangle \Big)^2. \tag{A.62f}$$

By [ZZS20, Proposition 5], $S^*$ is an equilibrium of the flow (5.27a) if and only if

$$(\Omega S^*)_j(x) = \langle (\Omega S)^*(x), S^*(x)\rangle, \qquad \forall x \in \mathcal{V}, \qquad \forall j \in \operatorname{supp}(S^*(x)). \tag{A.62g}$$

Therefore, by assumption, there exists $\widetilde{x} \in \mathcal{V}$ and $l \in \operatorname{supp}\big(S^*(\widetilde{x})\big)$ with $(\Omega S^*)_l(\widetilde{x}) \neq \langle \Omega S^*(\widetilde{x}), S^*(\widetilde{x})\rangle$ and consequently

$$\frac{h_*}{2}\big\langle \Omega S^*, R_{S^*}\big(\Omega R_{S^*}(\Omega S^*)\big)\big\rangle = -\langle \Omega S^*, R_{S^*}(\Omega S^*)\rangle \tag{A.62h}$$

$$\leq -S_l^*(\widetilde{x}) \Big( (\Omega S^*)_l(\widetilde{x}) - \big\langle (\Omega S^*)(\widetilde{x}), S^*(\widetilde{x})\big\rangle \Big)^2 \tag{A.62i}$$

$$< 0. \tag{A.62j}$$

Since the first two expressions are strictly negative, this yields the contradiction

$$-\frac{1}{2}\langle \Omega S^*, R_{S^*}(\Omega S^*)\rangle = -\frac{1}{2}\frac{\langle \Omega S^*, R_{S^*}(\Omega S^*)\rangle}{|\langle \Omega S^*, R_{S^*}(\Omega R_{S^*}(\Omega S^*))\rangle|} |\langle \Omega S^*, R_{S^*}(\Omega R_{S^*}(\Omega S^*))\rangle| \tag{A.63a}$$

$$\overset{(A.48),(5.93)}{=} -\frac{1}{2}\frac{\langle \Omega S^*, R_{S^*}(\Omega S^*)\rangle}{|\langle \operatorname{grad}_g J(S^*), \Pi_0 \Omega \operatorname{grad}_g J(S^*)\rangle|} |\langle \Omega S^*, R_{S^*}(\Omega R_{S^*}(\Omega S^*))\rangle| \tag{A.63b}$$

$$\overset{(A.51),(5.93)}{\leq} -\frac{h_*}{2}|\langle \Omega S^*, R_{S^*}(\Omega R_{S^*}(\Omega S^*))\rangle| \tag{A.63c}$$

$$\overset{(A.62h)}{=} -\langle \Omega S^*, R_{S^*}(\Omega S^*)\rangle \tag{A.63d}$$

which proves (ii).

(iii) We prove by contraposition and show that a limit point $S^* \in \mathcal{W}$ cannot locally minimize $J(S)$. Let $\overline{S}_{(l)} \in \overline{\mathcal{W}}$ be a constant vector field given for each $x \in \mathcal{V}$ by

$$\overline{S}_{(l)}(x) = e_l = (0, \dots, 0, 1, 0 \dots, 0)^\top \in \mathbb{R}^c, \tag{A.64}$$

for arbitrary $l \in [c]$. Then, for any $S \in \overline{\mathcal{W}}$ with $S(x) \in \Delta_c$ for each $x \in \mathcal{V}$, and with $\Omega(x,y) \geq 0$,

$$\langle S, \Omega S\rangle = \sum_{x\in\mathcal{V}} \sum_{j\in[c]} \sum_{y\in\mathcal{N}(x)} \Omega(x,y) S_j(x) S_j(y) \leq \sum_{x\in\mathcal{V}} \Big( \sum_{y\in\mathcal{N}(x)} \Omega(x,y) \Big) \underbrace{\sum_{j\in[c]} S_j(x)}_{=1} \tag{A.65a}$$

$$= \sum_{x\in\mathcal{V}} \sum_{j\in[c]} \sum_{y\in\mathcal{N}(x)} \Omega(x,y) \overline{S}_{(l)j}(x) \overline{S}_{(l)j}(y) \tag{A.65b}$$

$$= \langle \overline{S}_{(l)}, \Omega \overline{S}_{(l)}\rangle, \tag{A.65c}$$

where the inequality is strict if $S \in \mathcal{W}$. Consequently, the constant vector $\overline{S}_{(l)}$ is a global minimizer of the objective function $J(S)$ (5.34) with minimal value $J(\overline{S}_{(l)}) = -\frac{1}{2}\sum_{x\in\mathcal{V}}\sum_{y\in\mathcal{N}(x)}\Omega(x,y)$.

Let $B_\delta(S^*) \subset \mathcal{W}$ be the open ball with radius $\delta > 0$ containing $S^*$. By assumption, $S_j^*(x) > 0$, $\forall x \in \mathcal{V}$, $\forall j \in [c]$ and there exists an $\epsilon > 0$ small enough such that

$$S_\epsilon^* \coloneqq S^* + \epsilon(\overline{S}_{(l)} - S^*) \in B_\delta(S^*) \subset \mathcal{W}. \tag{A.66}$$

Evaluating $J(S)$ at $S_\epsilon^*$ yields

$$\begin{aligned}
J(S_\epsilon^*) &\overset{(A.66)}{=} -\frac{1}{2}\big\langle S^* + \epsilon(\overline{S}_{(l)} - S^*), \Omega(S^* + \epsilon(\overline{S}_{(l)} - S^*))\big\rangle && \text{(A.67a)}\\
&= J(S^*) - \epsilon\langle S^*, \Omega(\overline{S}_{(l)} - S^*)\rangle - \frac{\epsilon^2}{2}\langle \overline{S}_{(l)} - S^*, \Omega(\overline{S}_{(l)} - S^*)\rangle && \text{(A.67b)}\\
&\overset{\text{(ii)},(5.4)}{=} J(S^*) - \epsilon\Big\langle \langle S^*, \Omega S^*\rangle \mathbb{1}, \overline{S}_l - S^*\Big\rangle + \frac{\epsilon^2}{2}\Big\langle \langle S^*, \Omega S^*\rangle \mathbb{1}, \overline{S}_{(l)} - S^*\Big\rangle && \text{(A.67c)}\\
&\qquad + \epsilon^2\big(J(\overline{S}_{(l)}) + \frac{1}{2}\langle \overline{S}_{(l)}, \Omega S^*\rangle\big), && \text{(A.67d)}
\end{aligned}$$

and since $\langle \mathbb{1}, \overline{S}_{(l)} - S^*\rangle = \sum_{x\in\mathcal{V}}\sum_{j\in[c]}(\overline{S}_{(l)j}(x) - S_j^*(x)) \overset{(A.64)}{=} \sum_{x\in\mathcal{V}}(1 - \sum_{j\in[c]} S_j^*(x)) = 0$,

$$= J(S^*) + \epsilon^2\big(J(\overline{S}_{(l)}) + \frac{1}{2}\langle \overline{S}_{(l)}, \Omega S^*\rangle\big). \tag{A.67e}$$

It follows from (ii) that $S^*$ is an equilibrium point. Hence we can invoke condition (A.62g) to obtain the identity

$$\begin{aligned}
\frac{1}{2}\langle \overline{S}_{(l)}, \Omega S^*\rangle &= \frac{1}{2}\sum_{x\in\mathcal{V}}\sum_{j\in[c]}(\Omega S^*)_j(x)\overline{S}_{(l)j}(x) = \frac{1}{2}\sum_{x\in\mathcal{V}}(\Omega S^*)_l(x) && \text{(A.67f)}\\
&\overset{(A.62g)}{=} \frac{1}{2}\sum_{x\in\mathcal{V}}\langle S^*(x), \Omega S^*(x)\rangle = -J(S^*) && \text{(A.67g)}
\end{aligned}$$

and consequently, since $\overline{S}_{(l)}$ was shown above to be a global minimizer of $J$,

$$J(S_\epsilon^*) = J(S^*) + \epsilon^2\big(J(\overline{S}_{(l)}) - J(S^*)\big) < J(S^*). \tag{A.67h}$$

By assumption we have $S^* \in \mathcal{W}$ and using (A.65) it holds $J(S_\epsilon^*) < J(S^*)$. As $\delta > 0$ was chosen arbitrarily subject to the constraint (A.66), this shows that $S^*$ cannot be a local minimizer which proves (iii).

(iv) Analogous to (A.62) we compute

$$\begin{aligned}
&-\frac{h_k}{2}\big\langle \Omega S^k, R_{S^k}\big(\Omega R_{S^k}(\Omega S^k)\big)\big\rangle - \langle \Omega S^k, R_{S^k}(\Omega S^k)\rangle\\
&= -\frac{h_k}{2}\big\langle \Omega S^k, R_{S^k}\big(\Omega R_{S^k}(\Omega S^k)\big)\big\rangle - \sum_{x\in\mathcal{V}}\sum_{j\in[c]} S_j^k(x)\Big((\Omega S^k)_j(x) - \big\langle (\Omega S^k)(x), S^k(x)\big\rangle\Big)^2\\
&= -\frac{h_k}{2}\big\langle \Omega S^k, R_{S^k}\big(\Omega R_{S^k}(\Omega S^k)\big)\big\rangle - \sum_{x\in\mathcal{V}}\sum_{j\in[c]} \frac{1}{S_j^k(x)}\Big(S_j^k(x)\big((\Omega S^k)_j(x) - \big\langle (\Omega S^k)(x), S^k(x)\big\rangle\big)\Big)^2\\
&= -\frac{h_k}{2}\big\langle \Omega S^k, R_{S^k}\big(\Omega R_{S^k}(\Omega S^k)\big)\big\rangle - \sum_{x\in\mathcal{V}}\Big\langle \frac{\mathbb{1}}{S^k(x)}, \operatorname{grad}_g(J(S^k))(x) \odot \operatorname{grad}_g(J(S^k))(x)\Big\rangle.
\end{aligned} \tag{A.68}$$

Since this expression converges to 0 for $k \to \infty$, the additional assumption $\sum_{k=0}^{\infty} h_k < \infty$ implies that the second term on the right hand side is a zero sequence which shows (iv). □

### A.5.4. Proofs of Section 5.5.3

*Proof of Proposition 5.5.3.*

(i) Let $D$ be the diagonal degree matrix

$$D(x,x) = \sum_{y \in \mathcal{V}} \Omega(x,y), \tag{A.69}$$

and let $f \in \mathcal{F}_{\mathcal{V}}$. Then, using $\sum_{x,y \in \mathcal{V}} f^2(x) = \sum_{x,y \in \mathcal{V}} f^2(y)$, one has

$$\begin{aligned}
\langle f, (D-\Omega)f \rangle_{\mathcal{V}} &= \sum_{x \in \mathcal{V}} \sum_{y \in \mathcal{V}} \Omega(x,y)\big((f^2(x) - f(x)f(y)\big) && \text{(A.70a)} \\
&\overset{\Omega(x,y)=\Omega(y,x)}{=} \sum_{x \in \mathcal{V}} \sum_{y \in \mathcal{V}} \Omega(x,y)\big((\frac{1}{2}f^2(x) - f(x)f(y) + \frac{1}{2}f^2(y)\big) && \text{(A.70b)} \\
&= \frac{1}{2} \sum_{x \in \mathcal{V}} \sum_{y \in \mathcal{V}} \Omega(x,y)(f(x) - f(y))^2. && \text{(A.70c)}
\end{aligned}$$

Now we directly derive the right-hand side of (5.105) from (5.104).

$$-\frac{\langle f, \mathcal{D}^{\alpha}(\Theta \mathcal{G}^{\alpha} f)\rangle_{\overline{\mathcal{V}}}}{\langle f, f\rangle_{\overline{\mathcal{V}}}} \overset{(5.19),(5.16)}{=} \frac{\sum_{x \in \overline{\mathcal{V}}} f(x) 2\big(\sum_{y \in \overline{\mathcal{V}}} \Theta(x,y)\alpha^2(x,y)(f(x) - f(y))\big)}{\sum_{x \in \overline{\mathcal{V}}} f^2(x)} \tag{A.71a}$$

$$\overset{(5.8),\ f|_{\mathcal{V}_{\mathcal{I}}^{\alpha}}=0}{=} \frac{\sum_{x \in \mathcal{V}} f(x) 2\big(\sum_{y \in \mathcal{V} \dot{\cup} \mathcal{V}_{\mathcal{I}}^{\alpha}} \Theta(x,y)\alpha^2(x,y)(f(x) - f(y))\big)}{\sum_{x \in \mathcal{V}} f^2(x)} \tag{A.71b}$$

$$= \frac{\sum_{x \in \mathcal{V}} \sum_{y \in \mathcal{V}} \big(\Theta(x,y)\alpha^2(x,y)(f^2(x) - 2f(x)f(y) + f^2(x))\big)}{\sum_{x \in \mathcal{V}} f^2(x)} \tag{A.71c}$$

$$+ \frac{2\sum_{x \in \mathcal{V}} \big(\sum_{y \in \mathcal{V}_{\mathcal{I}}^{\alpha}} \Theta(x,y)\alpha^2(x,y)\big) f^2(x)}{\sum_{x \in \mathcal{V}} f^2(x)} \tag{A.71d}$$

and analogous to (A.70)

$$= \frac{\sum_{x \in \mathcal{V}} \sum_{y \in \mathcal{V}} \Theta(x,y)\alpha^2(x,y)(f(x) - f(y))^2 + 2\sum_{x \in \mathcal{V}} \big(\sum_{y \in \mathcal{V}_{\mathcal{I}}^{\alpha}} \Theta(x,y)\alpha^2(x,y)\big) f^2(x)}{\sum_{x \in \mathcal{V}} f^2(x)} \tag{A.71e}$$

$$\overset{\substack{(5.8)\\(5.41)\\(5.39)}}{=} \frac{\sum_{x\in\mathcal{V}}\sum_{y\in\mathcal{V}}\Omega(x,y)(f(x)-f(y))^2 + 2\sum_{x\in\mathcal{V}}\big(\lambda(x)-\sum_{y\in\mathcal{V}}\Omega(x,y)\big)f^2(x)}{\sum_{x\in\mathcal{V}} f^2(x)} \tag{A.71f}$$

$$\overset{(A.70)}{=} 2\frac{\langle f,(D-\Omega)f\rangle_{\mathcal{V}} + \langle f,(\Lambda-D)f\rangle_{\mathcal{V}}}{\langle f,f\rangle_{\mathcal{V}}} \tag{A.71g}$$

$$= 2\frac{\langle f,(\Lambda-\Omega)f\rangle_{\mathcal{V}}}{\langle f,f\rangle_{\mathcal{V}}} \tag{A.71h}$$

which proves that the right-hand sides of (5.104) and (5.105) are equal.

By virtue of (5.41) which is an *equation* by assumption, the matrix $\Lambda-\Omega$ defined by (5.106) and (5.39) is diagonal dominant, i.e.

$$\big|\big(\Lambda(x,x)-\Omega(x,x)\big) - \sum_{\substack{y\in\mathcal{V}\\ y\neq x}}\Omega(x,y)\big| = \sum_{y\in\mathcal{V}_{\mathcal{I}}^{\alpha}}\Theta(x,y)\alpha^2(x,y) \geq 0, \qquad x\in\mathcal{V}, \tag{A.72}$$

and therefore positive semidefinite, which shows $\lambda_1^D \geq 0$. In order to show that in fact the strict inequality $\lambda_1^D > 0$ holds, let $f\in\mathcal{F}_{\mathcal{V}}$ be such that equality is achieved in (5.104). We distinguish constant and non-constant functions $f$. For constant $f = c\,\mathbb{1},\ c\in\mathbb{R}$, since the set $\mathcal{V}_{\mathcal{I}}^{\alpha}$ given by (5.10) is nonempty, there exists an $\widetilde{x}\in\mathcal{V}$ with $\sum_{y\in\mathcal{V}_{\mathcal{I}^\alpha}}\Theta(\widetilde{x},y)\alpha^2(\widetilde{x},y) > 0$. Hence by (A.71e), (A.71h),

$$\lambda_1^D = \frac{\langle f,(\Lambda-\Omega)f\rangle_{\mathcal{V}}}{\langle f,f\rangle_{\mathcal{V}}} > \frac{\sum_{y\in\mathcal{V}_{\mathcal{I}^\alpha}}\Theta(\widetilde{x},y)\alpha^2(\widetilde{x},y)}{2n} > 0. \tag{A.73}$$

If $f$ is non-constant, then there exist $\widetilde{x},\widetilde{y}\in\mathcal{V}$ with $f(\widetilde{y})\neq f(\widetilde{x})$. Hence, since $\mathcal{V}$ is connected, (A.71e), (A.71h) yield

$$\lambda_1^D = \frac{\langle f,(\Lambda-\Omega)f\rangle_{\mathcal{V}}}{\langle f,f\rangle_{\mathcal{V}}} > \frac{\Omega(\widetilde{x},\widetilde{y})(f(\widetilde{x})-f(\widetilde{y}))^2}{2\max\limits_{x\in\mathcal{V}} f^2(x)} > 0. \tag{A.74}$$

(ii) We perform similarly to (5.10) a disjoint decomposition of the vertex set $\mathcal{V}$ and introduce the sets

$$\mathcal{V}_i = \{x\in\mathcal{V}\colon \alpha(x,y)=0 \text{ for } y\in\mathcal{V}_{\mathcal{I}}^{\alpha}\}, \qquad \mathcal{V}_b = \mathcal{V}\setminus\mathcal{V}_i. \tag{A.75}$$

Hence $\mathcal{V}_b\neq\emptyset$ if and only if $\mathcal{V}_{\mathcal{I}}^{\alpha}\neq\emptyset$ and (5.38), (5.39) yield

$$\forall x\in\mathcal{V}_i, \qquad \lambda(x) - \sum_{y\in\mathcal{V}}\Omega(x,y) = 0. \tag{A.76}$$

Let $f$ be a *normalized* eigenvector to the smallest eigenvalue $\lambda_{\min}(\Omega)$ of $\Omega$. Then, using (A.76) and the inequality

$$(f(x)-f(y))^2 \leq 2(f^2(x)+f^2(y)), \qquad x,y\in\mathcal{V}, f\in\mathcal{F}_{\mathcal{V}} \tag{A.77}$$

further yields

$$-\lambda_{\min}(\Omega) = -\langle f,\Omega f\rangle_{\mathcal{V}} = \langle f,(D-\Omega)f\rangle_{\mathcal{V}} - \langle f,Df\rangle_{\mathcal{V}} \tag{A.78a}$$

$$\overset{(A.69),(A.70)}{=} \frac{1}{2}\sum_{x\in\mathcal{V}}\sum_{y\in\mathcal{V}}\Omega(x,y)(f(x)-f(y))^2-\sum_{x\in\mathcal{V}}\sum_{y\in\mathcal{V}}\Omega(x,y)f^2(x) \tag{A.78b}$$

$$\overset{(A.77)}{\leq} \sum_{x\in\mathcal{V}}\sum_{y\in\mathcal{V}}\Omega(x,y)f^2(x) \tag{A.78c}$$

$$\overset{(A.75)}{=} \sum_{x\in\mathcal{V}_i}\sum_{y\in\mathcal{V}}\Omega(x,y)f^2(x)+\sum_{x\in\mathcal{V}_b}\sum_{y\in\mathcal{V}}\Omega(x,y)f^2(x) \tag{A.78d}$$

$$\overset{(5.24),(5.39)}{\leq} \sum_{x\in\mathcal{V}_i}f^2(x)+\sum_{x\in\mathcal{V}_b}\big(1-\sum_{y\in\mathcal{V}_{\mathcal{I}}^{\alpha}}\Theta(x,y)\alpha^2(x,y)\big)f^2(x) \tag{A.78e}$$

$$= \sum_{x\in\mathcal{V}}f^2(x)-\sum_{x\in\mathcal{V}_b}\sum_{y\in\mathcal{V}_{\mathcal{I}}^{\alpha}}\Theta(x,y)\alpha^2(x,y)f^2(x) \tag{A.78f}$$

$$\overset{(5.8)}{=} 1-\sum_{x\in\mathcal{V}_b}\Big(1-\Theta(x,x)-\sum_{y\in\mathcal{V}}\Theta(x,y)\alpha^2(x,y)\Big)f^2(x) \tag{A.78g}$$

$$\overset{(5.41)}{<} 1. \tag{A.78h}$$

□

### A.5.5. Proofs of Section 5.6.1

*Proof of Lemma 5.6.1.* Since $\overline{\mathcal{W}} \subset \mathbb{R}^{nc}$ is compact, $(S^k)_{k\geq 0} \subset \overline{\mathcal{W}}$ is bounded and there exists a convergent subsequence $(S^{k_l})_{l\geq 0}$ with $\lim_{l\to\infty} S^{k_l} = S^*$ and $\Lambda$ nonempty and compact. Due to Proposition 5.5.2, the sequence $(J(S^k))_{k\geq 0}$ is nonincreasing and bounded from below with $\lim_{k\to\infty} J(S^k) = J^*$ for some $J^* > -\infty$.

In view of the definition (5.28) of the mapping $S \mapsto R_S(\Omega S)$, the right-hand side of (5.95) is bounded for any $S \in \mathcal{S}$. Hence the subsequence $(d^{k_l})_{l\geq 0}$ induced by $(S^{k_l})_{l\geq 0}$ through (5.95), (5.97) is convergent as well. Consequently, for any limit point $S^* \in \Lambda$, there exists a subsequence $(S^{k_l})_{l\geq 0}$ with

$$S^{k_l} \to S^* \quad \text{and} \quad d^{k_l} \to d^* \quad \text{as} \quad l \to \infty. \tag{A.79}$$

It remains to show that $\lim_{l\to\infty} J(S^{k_l}) = J(S^*) = J^*$.

Analogous to the proof of Proposition 5.5.1, we adopt the decomposition (A.39) of $J(S)$ by

$$J(S) = g(S) - h(S) \quad \text{with} \quad g(S) = \delta_{\overline{\mathcal{W}}}(S) + \gamma\langle S, \log S\rangle, \tag{A.80a}$$

$$h(S) = \frac{1}{2}\langle S, \Omega S\rangle + \gamma\langle S, \log S\rangle, \tag{A.80b}$$

with appropriately chosen initial decomposition parameter $\gamma$ in Algorithm 5.4 such that $g, h$ are strictly convex on $\mathcal{W}$. By the lower semicontinuity of $J(S)$, we have

$$\liminf_{l\to\infty} J(S^{k_l}) \geq J(S^*). \tag{A.81}$$

In addition, by invoking line 13 of Algorithm 5.4 defining the iterate $S^{k_l}$ by the inclusion $\gamma\theta_{k_l-1}\widetilde{S}^{k_l-1} \in \partial g(S^{k_l})$ if $\theta_k$ satisfy the Wolfe conditions, and by line (16) otherwise, we have

$$g(S^{k_l}) - \gamma\theta_{k_l-1}\langle\widetilde{S}^{k_l-1}, S^{k_l} - S^{k_l-1}\rangle \leq g(S^*) - \gamma\theta_{k_l-1}\langle\widetilde{S}^{k_l-1}, S^* - S^{k_l-1}\rangle, \tag{A.82}$$

which after rearranging reads

$$g(S^{k_l}) \leq g(S^*) - \gamma\theta_{k_l-1}\langle d^{k_l-1}, S^* - S^{k_l}\rangle - \gamma\Big\langle \log\Big(\frac{S^{k_l-1}}{\mathbb{1}_c}\Big), S^* - S^{k_l}\Big\rangle. \tag{A.83}$$

Setting

$$\delta = \sum_{x\in\mathcal{V}} \sum_{j\in\operatorname{supp}(S^*(x))} \log(S_j^*(x)) \cdot S_j^*(x) \tag{A.84}$$

and using (A.79), we obtain for the last term

$$\begin{aligned}
\lim_{l\to\infty}\Big\langle \log\Big(\frac{S^{k_l-1}}{\mathbb{1}_c}\Big), S^* - S^{k_l}\Big\rangle &= \lim_{l\to\infty}\langle \log(S^{k_l-1}), S^* - S^{k_l}\rangle && \text{(A.85a)}\\
&= \lim_{l\to\infty}\Big(\langle \log(S^{k_l-1}) + \log(e^{\theta_{k_l-1}d^{k_l-1}}), S^* - S^{k_l}\rangle - \theta_{k_l-1}\langle d^{k_l-1}, S^* - S^{k_l}\rangle\Big) && \text{(A.85b)}\\
&= \lim_{l\to\infty}\Big(\Big\langle \log\big(\exp_{S^{k_l-1}}(\theta_{k_l-1}d^{k_l-1})\big) + \log\langle S^{k_l-1}, e^{\theta_{k_l-1}d^{k_l-1}}\rangle\mathbb{1}_c, S^* - S^{k_l}\Big\rangle && \text{(A.85c)}\\
&\qquad - \theta_{k_l-1}\langle d^{k_l-1}, S^* - S^{k_l}\rangle\Big) && \text{(A.85d)}
\end{aligned}$$

using $\langle \mathbb{1}_c, S^* - S^{k_l}\rangle = 1 - 1 = 0$

$$\begin{aligned}
&\overset{(A.84)}{=} \underbrace{\lim_{l\to\infty}\langle \log(S^{k_l}), S^* - S^{k_l}\rangle}_{\to\delta-\delta=0} - \underbrace{\lim_{l\to\infty}\langle \theta_{k_l-1}d^{k_l-1}, S^* - S^{k_l}\rangle}_{\to 0} && \text{(A.85e)}\\
&= 0. && \text{(A.85f)}
\end{aligned}$$

Hence by noticing $\theta_k \in [\theta_0, \frac{1}{|\lambda_{\min}(\Omega)|}]$, the sequence $(\theta_{k_l})$ is bounded and taking the limit in (A.83) yields

$$\limsup_{l\to\infty} g(S^{k_l}) \leq g^*(S^*). \tag{A.86}$$

Now, turning to the function $h$ of (A.80), lower semicontinuity yields $\liminf_{l\to\infty} h(S^{k_l}) \geq h(S^*)$ and hence

$$\begin{aligned}
\limsup_{l\to\infty} J(S^{k_l}) &= \limsup_{l\to\infty}\big(g(S^{k_l}) - h(S^{k_l})\big) \leq \limsup_{l\to\infty} g(S^{k_l}) - \liminf_{l\to\infty} h(S^{k_l}) && \text{(A.87a)}\\
&\overset{(A.86)}{\leq} g(S^*) - h(S^*). && \text{(A.87b)}
\end{aligned}$$

Finally, combining this with (A.81) and by uniqueness of the limit $J^*$, we have $J(S^*) = J^*$ for any $S^* \in \Lambda$, which completes the proof. □

*Proof of Lemma 5.6.2.* Throughout the proof we skip the action of projection operator $\Pi_0$ in $d^k(x)$ given by (5.95) and (5.98), due to the invariance of lifting map (3.54) by property (5.30). By definition (5.98) of $S^{k+1}$, it follows for $x \in \mathcal{V}$ and $j \in J_+(S^*(x))$ that

$$\begin{aligned}
\big(S^{k+1}(x) - S^k(x)\big)_j &= S_j^k(x)\Big(\frac{e^{\theta_k d^k(x)}}{\langle S^k(x), e^{\theta_k d^k(x)}\rangle} - \mathbb{1}\Big)_j\\
&= \frac{S_j^k(x)}{\langle S^k(x), e^{\theta_k d^k(x)}\rangle}\Big(e^{\theta_k d_j^k(x)} - \langle S^k(x), e^{\theta_k d^k(x)}\rangle\Big) && \text{(A.88)}\\
&= \frac{S_j^k(x)}{\langle S^k(x), e^{\theta_k d^k(x)}\rangle}\Big(\sum_{l=0}^{\infty}\beta_{l,j}^k(x)\Big), \qquad \forall J_+(S^*(x)),
\end{aligned}$$

where we employed the power series of the exponential function and the shorthand $(\beta_{l,j}^k(x))_{l\geq 0}$

$$\beta_{l,j}^k(x) = \frac{\theta_k^l}{l!}\Big((d_j^k(x))^l - \langle S^k(x), (d^k(x))^l\rangle\Big) \tag{A.89a}$$

$$\overset{(5.95)}{=} \frac{\theta_k^l}{l!}\Big((\Omega S^k)_j^l(x) - \langle S^k(x), (\Omega S^k)^l(x)\rangle\Big) + \mathcal{O}(h_k). \tag{A.89b}$$

Let $M : \overline{\mathcal{W}} \times \mathbb{R}_+ \to \mathbb{R}_+$ denote the function

$$M(S,\gamma) = \max_{x\in\mathcal{V}} \max_{h\in[0,h_{\max}]} \langle S(x), e^{\gamma d(S,h)(x)}\rangle^2 \leq M^*, \qquad S \in \mathcal{W}, \tag{A.90}$$

with $h_{\max} = \max_{k\geq 0} h_k$ and $d(S,h)$ as in (5.95). Since $M(S,\gamma)$ is a continuous mapping on a compact set $\mathcal{W} \times [\theta_{\min}, \theta_{\max}]$, it attains its maximum $M^* > 1$. Due to the equilibrium condition (A.62g) there exists an $\varepsilon_1 > 0$ such that, for all $S \in \mathcal{W}$ with $\|S^* - S\| < \varepsilon_1$, the inequality

$$-\Big((\Omega S)_j(x) - \langle \Omega S(x), S(x)\rangle\Big) > -\frac{1}{\sqrt{M^*}}\Big((\Omega S^*)_j(x) - \langle \Omega S^*(x), S^*(x)\rangle\Big) > 0. \tag{A.91}$$

is satisfied for all indices $j \in J_+(S^*(x))$ given by (5.109) (i.e. the terms inside the brackets on either side are negative) and $x \in \mathcal{V}$. In particular, since $S^* \in \overline{\mathcal{W}}$ is a limit point of $(S^k)_{k\geq 0}$, there is a convergent subsequence $(S^{k_s})_{s\geq 0}$ with $S^{k_s} \to S^*$ and consequently $\|S^{k_{s_0}} - S^*\| < \varepsilon_1$ for some $k_{s_0} \in \mathbb{N}$. Now, using the componentwise inequality $p^l \leq p$ for $l \in \mathbb{N}$ and $p \in \mathcal{S}$, we have

$$0 \leq \big\langle \mathbb{1}, \big(S^k(x) \odot \Omega S^k(x)\big)^l\big\rangle \leq \big\langle S^k(x), (\Omega S^k(x))^l\big\rangle. \tag{A.92}$$

Employing (A.92) in (A.89) and using $h^{k_s} \to 0$ shows that there exists a smallest index $k_0 \geq k_{s_0}$ such that

$$\beta_{l,j}(x) \leq \frac{\theta_k^l}{l!}\Big((\Omega S^{k_{s_0}})_j^l(x) - \langle S^{k_{s_0}}(x), (\Omega S^{k_{s_0}}(x))\rangle^l\Big) + O(h^{k_{s_0}}) < 0, \quad \forall j \in J_+(S^*(x)),\ l \in \mathbb{N}. \tag{A.93}$$

Therefore, setting $\varepsilon_1 := \|S^* - S^{k_0}\|$ for all $S^k$ satisfying $\|S^k - S^*\| < \varepsilon$ and $k \geq k_0$ with $\varepsilon := \min\{\varepsilon_0, \varepsilon_1\}$, the inequalities (A.91) and (A.93) are simultaneously satisfied and using

$$(\Omega S^{k_{s_0}})_j^l(x) \overset{(5.109)}{<} \langle (\Omega S^{k_{s_0}})(x), S^{k_{s_0}}(x)\rangle^l, \quad \forall j \in J_+(S^*(x)), \quad l \in \mathbb{N} \tag{A.94}$$

enables to estimate (A.88) by

$$\big(S^{k+1}(x) - S^k(x)\big)_j = \frac{S_j^k(x)}{\langle S^k(x), e^{\theta_k d^k(x)}\rangle}\Big(\sum_{l=1}^{\infty} \beta_{l,j}^k(x)\Big) \tag{A.95a}$$

$$\overset{(A.93)}{\leq} \frac{S_j^k(x)}{\langle S^k(x), e^{\theta_k d^k(x)}\rangle}\Big(\theta_k\big((\Omega S^k)_j(x) - \langle S^k(x), \Omega S^k(x)\rangle\big) \tag{A.95b}$$

$$+ \sum_{l=2}^{\infty} \frac{\theta_k^l}{l!}\big((\Omega S^k)_j^l(x) - \langle S^k(x), \Omega S^k(x)\rangle^l\big) + \mathcal{O}(h^k)\Big) \tag{A.95c}$$

$$\overset{(A.91)}{\leq} \frac{-S_j^k(x)}{\langle S^k(x), e^{\theta_k d^k(x)}\rangle \cdot \sqrt{M^*}}\Big(\theta_k\big(\langle \Omega S^*(x), S^*(x)\rangle - (\Omega S^*)_j(x)\big)\Big) \tag{A.95d}$$

$$\overset{(A.90)}{\leq} -\theta_k \frac{S_j^k(x)}{M^*}\big(\langle \Omega S^*(x), S^*(x)\rangle - (\Omega S^*)_j(x)\big), \qquad \forall J_+(S^+(x)). \tag{A.95e}$$

Taking the sum over $x \in \mathcal{V}$ shows (5.110). □

## A.5.6. Proofs of Section 5.6.2

*Proof of Theorem 5.6.1.* Let $S^* \in \Lambda$ be a limiting point of $(S^k)_{k\geq 0}$ with $S^*(x) \in \overline{\mathcal{S}} \setminus \mathcal{S},\ \forall x \in \mathcal{V}$, by Proposition 5.5.2(iii), and let $\theta_k \in \mathbb{R}_+$, $S^{k+1} \in \mathcal{W}$ and $\widetilde{S}^k$ be determined by Algorithm 5.4 (see lines (13) and (14)), respectively. Then, by the well-known *three-point identity* [CT93, Lemma 3.1] with respect to $S^{k+1}, S^k \in \mathcal{W},\ S^* \in \overline{\mathcal{W}}$, one has

$$D_{\mathrm{KL}}(S^*, S^{k+1}) - D_{\mathrm{KL}}(S^*, S^k) = -D_{\mathrm{KL}}(S^{k+1}, S^k) - \langle \nabla f(S^{k+1}) - \nabla f(S^k), S^* - S^{k+1}\rangle. \tag{A.96}$$

Recalling step size selection 5.3 it holds $\theta_k \in (\theta_0, \frac{1}{|\lambda_{\min}(\Omega)|})$ and leveraging the DC-decomposition (A.80) with $\gamma = \frac{1}{\theta_k}$, the inclusion $\Omega S^k + \frac{1}{\theta_k}\log(\frac{S^k}{\mathbb{1}_c}) \in \partial h(S^k)$ and the strict convexity of $h(S)$ on $\mathcal{W}$ imply by the gradient inequality

$$h(S^{k+1}) - h(S^k) - \left\langle \Omega S^k + \frac{1}{\theta_k}\log\left(\frac{S^k}{\mathbb{1}_c}\right), S^{k+1} - S^k \right\rangle > 0 \tag{A.97}$$

and hence

$$\begin{aligned}
&h(S^{k+1}) - h(S^k) - \left\langle \Omega S^k + \frac{1}{\theta_k}\log\left(\frac{S^k}{\mathbb{1}_c}\right), S^{k+1} - S^k \right\rangle && \text{(A.98a)}\\
&\overset{\text{(A.80b)}}{=} \frac{1}{2}\langle S^{k+1}, \Omega S^{k+1}\rangle - \frac{1}{2}\langle S^k, \Omega S^k\rangle && \text{(A.98b)}\\
&\quad + \frac{1}{\theta_k}\left(\langle S^{k+1}, \log(S^{k+1})\rangle - \langle S^k, \log S^k\rangle - \left\langle \log\left(\frac{S^k}{\mathbb{1}_c}\right), S^{k+1} - S^k\right\rangle\right) && \text{(A.98c)}\\
&\quad - \langle \Omega S^k, S^{k+1} - S^k\rangle && \text{(A.98d)}\\
&\overset{(5.34),(2.31)}{=} J(S^k) - J(S^{k+1}) + \frac{1}{\theta_k}D_{\mathrm{KL}}(S^{k+1}, S^k) - \langle \Omega S^k, S^{k+1} - S^k\rangle. && \text{(A.98e)}
\end{aligned}$$

Therefore inequality (A.97) is equivalent to

$$-D_{\mathrm{KL}}(S^{k+1}, S^k) \leq \theta_k\big(J(S^k) - J(S^{k+1}) - \langle \Omega S^k, S^{k+1} - S^k\rangle\big). \tag{A.99}$$

Combining (A.99) and (A.96) yields

$$\begin{aligned}
D_{\mathrm{KL}}(S^*, S^{k+1}) - D_{\mathrm{KL}}(S^*, S^k) \leq \theta_k\big(J(S^k) - J(S^{k+1}) - \langle \Omega S^k, S^{k+1} - S^k\rangle\big)\\
- \langle \nabla f(S^{k+1}) - \nabla f(S^k), S^* - S^{k+1}\rangle.
\end{aligned} \tag{A.100}$$

Next, in view of Algorithm 5.4, line (14), we rewrite the last term in (A.100) in the form

$$\langle \nabla f(S^{k+1}) - \nabla f(S^k), S^* - S^{k+1}\rangle \overset{\substack{(2.35)\\ S^k, S^{k+1}\in\mathcal{W}}}{=} \langle \mathbb{1}_c + \log(S^{k+1}) - (\mathbb{1}_c + \log(S^k)), S^* - S^{k+1}\rangle \tag{A.101a}$$

$$\overset{\substack{\text{Algorithm 5.4}\\ \text{line (14)}}}{=} \langle \log(S^k) + \log(e^{\theta_k d^k}) - \log(S^k), S^* - S^{k+1}\rangle \tag{A.101b}$$

$$- \underbrace{\langle \log(\langle S^k, e^{\theta_k d^k}\rangle)\mathbb{1}_c, S^* - S^{k+1}\rangle}_{=0} \tag{A.101c}$$

$$= \quad \theta_k \langle d^k, S^* - S^{k+1}\rangle. \tag{A.101d}$$

Consequently, (A.100) becomes

$$D_{\mathrm{KL}}(S^*, S^{k+1}) - D_{\mathrm{KL}}(S^*, S^k) \tag{A.102a}$$

$$\leq \ \theta_k\big(J(S^k) - J(S^{k+1})\big) - \theta_k\langle \Omega S^k, S^* - S^k\rangle - \frac{\theta_k h_k}{2}\langle \Omega R_{S^k}(\Omega S^k), S^* - S^{k+1}\rangle \tag{A.102b}$$

$$\overset{(5.34)}{=} \theta_k\Big(2\big(J(S^*) - J(S^{k+1})\big) + J(S^{k+1}) - J(S^k) \tag{A.102c}$$

$$- \frac{h_k}{2}\langle \Omega R_{S^k}(\Omega S^k), S^* - S^{k+1}\rangle - \langle S^k, \Omega S^*\rangle - 2J(S^*)\Big). \tag{A.102d}$$

Using the inequality of Cauchy Schwarz and taking into account $S^* \in \overline{W}$, $S \in \mathcal{W}$, we estimate with $\lambda(\Omega)$ defined by (5.112b)

$$|\langle \Omega R_S(\Omega S), S^* - S\rangle| \leq \|\Omega R_S(\Omega S)\| \cdot \|S^* - S\| \leq \frac{\lambda^2(\Omega)}{2}\|S\|\sqrt{n} \leq \frac{\lambda^2(\Omega)\cdot n}{2}, \tag{A.103}$$

where the factor $\frac{1}{2}$ is due to the fact that the matrices $R_{S(x)}$ given by (3.33) are positive semidefinite with $\lambda_{\max}(R_{S(x)}) \leq \frac{1}{2}$, which easily follows from Gershgorin's circle theorem.

Using the descent step based on (5.95) and (A.52), we consider three further terms of (A.102).

$$J(S^{k+1}) - J(S^k) - \frac{h_k}{2}\langle \Omega R_{S^k}(\Omega S^k), S^* - S^{k+1}\rangle \tag{A.104a}$$

$$\overset{(5.99a)}{\leq} \theta_k c_1 \underbrace{\langle R_{S^k}(\Omega S^k), R_{S^k}(d^k)\rangle_{S^k}}_{\leq 0} - \frac{h_k}{2}\langle \Omega R_{S^k}(\Omega S^k), S^* - S^{k+1}\rangle \tag{A.104b}$$

$$\overset{(5.95)}{\leq} -\theta_k c_1(\langle R_{S^k}(\Omega S^k), R_{S^k}(\Omega S^k)\rangle_{S^k} \tag{A.104c}$$

$$+ \frac{\theta_k c_1 h_k}{2}|\langle R_{S^k}(\Omega S^k), R_{S^k}\Omega R_{S^k}\Omega S^k\rangle_{S^k}|) + \frac{h_k}{2}|\langle \Omega R_{S^k}(\Omega S^k), S^* - S^{k+1}\rangle| \tag{A.104d}$$

$$\overset{(A.51),(A.103)}{\leq} -\frac{\theta_k c_1}{2}\langle R_{S^k}(\Omega S^k), R_{S^k}(\Omega S^k)\rangle_{S^k} + \frac{\lambda^2(\Omega) n h_k}{4} \tag{A.104e}$$

$$= \ -\frac{\theta_k c_1}{2}\|\operatorname{grad} J(S^k)\|_{S^k}^2 + \frac{\lambda^2(\Omega) n h_k}{4} \tag{A.104f}$$

$$\leq \ 0, \tag{A.104g}$$

where the last inequality is holds due to assumption (5.112). Now we focus on the last remaining term occurring in (A.102). Using the index sets (5.109) with respect to the limit point $S^* \in \overline{\mathcal{W}}$ along with $S^k(x) \in \mathcal{S}$, we get

$$-\langle S^k, \Omega S^*\rangle - 2J(S^*) \overset{(5.34)}{=} -\sum_{x\in\mathcal{V}}\langle S^k(x), \Omega S^*(x)\rangle + \sum_{x\in\mathcal{V}}\langle S^*(x), \Omega S^*(x)\rangle \tag{A.105a}$$

$$= -\sum_{x\in\mathcal{V}}\sum_{j\in[c]} S_j^k(x)(\Omega S^*)_j(x) + \sum_{x\in\mathcal{V}}\underbrace{\sum_{j\in[c]} S_j^k(x)}_{=1}\langle S^*(x), \Omega S^*(x)\rangle \tag{A.105b}$$

$$= -\sum_{x\in\mathcal{V}}\sum_{j\in[c]} S_j^k(x)\big((\Omega S^*)_j(x) - \langle S^*(x), \Omega S^*(x)\rangle\big) \tag{A.105c}$$

$$\overset{(5.109)}{=} -\sum_{x\in\mathcal{V}}\Big(\sum_{j\in J_-(S^*(x))} S_j^k(x)\big((\Omega S^*)_j(x) - \langle S^*(x), \Omega S^*(x)\rangle\big) \tag{A.105d}$$

$$+ \sum_{j\in J_+(S^*(x))} S_j^k(x)\big((\Omega S^*)_j(x) - \langle S^*(x), \Omega S^*(x)\rangle\big)\Big). \tag{A.105e}$$

As a result, combining (A.104) and (A.105) for all $k \geq K$ and using $J(S^*) - J(S^{k+1}) < 0$, (A.102) becomes

$$D_{\mathrm{KL}}(S^*, S^{k+1}) - D_{\mathrm{KL}}(S^*, S^k) \leq \theta_k\Big(J(S^*) - J(S^{k+1}) - \sum_{x\in\mathcal{V}}\Big(\sum_{j\in J_-(S^*(x))} S_j^k(x)\big((\Omega S^*)_j(x)\big) \tag{A.106a}$$

$$- \langle S^*(x), \Omega S^*(x)\rangle\big) + \sum_{j\in J_+(S^*(x))} S_j^k(x)\big((\Omega S^*)_j(x) - \langle S^*(x), \Omega S^*(x)\rangle\big)\Big)\Big) \tag{A.106b}$$

By Lemma 5.6.2, there exist $\varepsilon > 0$ and $k_0 \in \mathbb{N}$ such that for all $S^k \in \mathcal{W}$ with $k \geq k_0$ and $\|S^k - S^*\| < \varepsilon$ inequality (5.110) is satisfied, where

$$Q(S) = \sum_{x\in\mathcal{V}}\sum_{j\in J_+(S^*(x))} S_j(x).$$

Introducing the mapping

$$V\colon \mathcal{W} \to \mathbb{R}_+, \qquad V(S) = D_{\mathrm{KL}}(S^*, S) + M^*\, Q(S)$$

with $M^* > 1$ as in Lemma 5.6.2, we obtain

$$V(S^{k+1}) - V(S^k) = D_{\mathrm{KL}}(S^*, S^{k+1}) - D_{\mathrm{KL}}(S^*, S^k) + M^*\big(Q(S^{k+1}) - Q(S^k)\big)$$

$$\overset{\substack{(5.109a)\\(A.106)}}{\leq} \theta_k\Big(J(S^*) - J(S^k) - \sum_{x\in\mathcal{V}}\sum_{j\in J_-(S^*(x))} S_j^k(x)\big((\Omega S^*)_j(x) - \langle S^*(x), \Omega S^*(x)\rangle\big)\Big). \tag{A.107}$$

By Lemma 5.6.1 $J(S)$ is constant on the set of limit points of the sequence $(S^k)$ and the right-hand side of (A.107) is strictly negative unless $S^k$ is a stationary point of $J(S)$. Consequently, (A.107) is *strictly* negative for all $k \geq k_0$ with $\|S^k - S^*\| < \varepsilon$. Consider $U_\delta = \{S \in \overline{\mathcal{W}}\colon V(S) < \delta\}$ with $\delta$ small enough such that $U_\delta \subset \{S \in \overline{\mathcal{W}}\colon \|S - S^*\| < \epsilon\}$. Then, as $S^* \in \Lambda$ is a limit point, there exists an index $K \geq k_0$ such that $S^K \in U_\delta$ and $(S^k)_{k\geq K} \subset U_\delta$ due to $V(S^{K+1}) < V(S^K) < \delta$ by (A.107). Therefore, for $k \geq K$ we conclude

$$0 \leq D_{\mathrm{KL}}(S^*, S^k) \leq V(S^k) \to 0 \quad \text{for} \quad k \to \infty, \tag{A.108}$$

which shows $S^k \to S^*$. □

*Proof of Theorem 5.6.2.* For $\varepsilon > 0$ let $k \in \mathbb{N}$ be such that $S^k \in B_\varepsilon(S^*)$. Then, with $S^{k+\frac{1}{2}}, S^{k+1} \in \mathcal{W}$ given by (5.96) and taking into account assumption (5.113), we have for any $x \in \mathcal{V}$ with $S^*(x) = e_{j^*(x)}$

$$\|S^{k+1}(x) - S^*(x)\|_1 = \sum_{j \in [c] \setminus j^*(x)} S_j^{k+1}(x) + 1 - S_{j^*(x)}^{k+1}(x) \tag{A.109a}$$

$$= 2 - 2S_{j^*(x)}^{k+1}(x) \tag{A.109b}$$

$$\overset{(5.96)}{=} 2 - 2\frac{S_{j^*(x)}^k(x) e^{\theta_k (\Omega S^k)_{j^*(x)}(x) + \frac{\theta_k h_k}{2} (\Omega R_{S^k}(\Omega S^k))_{j^*(x)}(x)}}{\langle S^k(x), e^{\theta_k (\Omega S^k)(x) + \frac{\theta_k h_k}{2} \Omega R_{S^k}(\Omega S^k)(x)} \rangle} \tag{A.109c}$$

$$= 2 - \frac{2S_{j^*(x)}^k(x)}{S_{j^*(x)}^k(x) + \sum_{j \neq j^*(x)} S_j^k(x) e^{-\theta_k H_j(x)}}, \tag{A.109d}$$

with the shorthand

$$H_j(x) := (\Omega S^k)_{j^*(x)}(x) - (\Omega S^k)_j(x) + \frac{h_k}{2}\big((\Omega R_{S^k}(\Omega S^k))_{j^*(x)}(x) - (\Omega R_{S^k}(\Omega S^k))_j(x)\big). \tag{A.110}$$

We consider the first two terms of the right-hand side of (A.110). Since $S^k(x) \in B_\varepsilon(S^*)$, we have

$$S_{j^*(x)}^k(x) > 1 - \frac{\varepsilon}{2}, \qquad S_j^k(x) < \frac{\varepsilon}{2} \quad \text{for all} \quad j \neq j^*(x) \tag{A.111}$$

and get

$$(\Omega S)_{j^*(x)}(x) - (\Omega S)_j(x) \overset{(5.36)}{=} \sum_{y \in \mathcal{N}(x)} \Omega(x,y) S_{j^*(x)}(y) - \sum_{y \in \mathcal{N}(x)} \Omega(x,y) S_j(y) \tag{A.112a}$$

$$= \sum_{\substack{y \in \mathcal{N}(x) \\ j^*(y) = j^*(x)}} \Omega(x,y) S_{j^*(x)}(y) + \sum_{\substack{y \in \mathcal{N}(x) \\ j^*(y) \neq j^*(x)}} \Omega(x,y) S_{j^*(x)}(y) - \sum_{\substack{y \in \mathcal{N}(x) \\ j^*(y) = j}} \Omega(x,y) S_j(y) - \sum_{\substack{y \in \mathcal{N}(x) \\ j^*(y) \neq j}} \Omega(x,y) S_j(y). \tag{A.112b}$$

Skipping the nonnegative second term and applying the constraint $S_j(y) < 1$ for indices $j^*(y) = j$, it follows with (A.111)

$$(\Omega S)_{j^*(x)}(x) - (\Omega S)_j(x) > \sum_{\substack{y \in \mathcal{N}(x) \\ j^*(y) = j^*(x)}} \Omega(x,y) S_{j^*(x)}(y) - \sum_{\substack{y \in \mathcal{N}(x) \\ j^*(y) = j}} \Omega(x,y) - \sum_{\substack{y \in \mathcal{N}(x) \\ j^*(y) \neq j}} \Omega(x,y) S_j(y) \tag{A.112c}$$

$$\overset{(A.111)}{>} (1 - \frac{\varepsilon}{2}) \sum_{\substack{y \in \mathcal{N}(x) \\ j^*(y) = j^*(x)}} \Omega(x,y) - \sum_{\substack{y \in \mathcal{N}(x) \\ j^*(y) = j}} \Omega(x,y) - \frac{\varepsilon}{2} \sum_{\substack{y \in \mathcal{N}(x) \\ j^*(y) \neq j}} \Omega(x,y) \tag{A.112d}$$

and after rewriting the last sum as $1 - \sum_{\substack{y \in \mathcal{N}(x) \\ j^*(x) = j}} \Omega(x,y)$ and using $S^*(x) = e_{j^*(x)}$

$$\geq (1 - \frac{\varepsilon}{2})\big((\Omega S^*)_{j^*(x)} - (\Omega S^*)_j\big)(x) - \frac{\varepsilon}{2}. \tag{A.112e}$$

Now we consider the last two terms of the right-hand side of (A.110), starting with the expression $R_{S^k}(\Omega S^k)$. As $\overline{B_\varepsilon(S^*)}$ is compact, the maximum

$$\rho^* = \max_{S\in\overline{B_\varepsilon(S^*)}} \rho(S), \qquad \rho(S) = \max_{x\in\mathcal{V}} \max_{l\in[c]\setminus j^*(x)} \big((\Omega S)_{j^*(x)} - (\Omega S)_l\big)(x) \tag{A.113}$$

is attained. For $j \in [c]$ with $\big(R_{S^k}(\Omega S^k)\big)_j(x) < 0$, we get

$$\begin{aligned}
\big(R_{S^k}(\Omega S^k)\big)_j(x) &= S_j^k(x)\big((\Omega S^k)_j(x) - \langle S^k(x), (\Omega S^k)(x)\rangle\big) && \text{(A.114a)}\\
&= S_j^k(x)\Big(\sum_{l\neq j} S_l^k(x)\big((\Omega S^k)_j(x) - (\Omega S^k)_l(x)\big)\Big). && \text{(A.114b)}
\end{aligned}$$

Taking into account (5.115) for $S^k \in B_\varepsilon(S^*)$, we have $(\Omega S^k)_{j^*(x)}(x) > (\Omega S^k)_l(x)$ for all $l \in [c] \setminus j^*(x)$ by (5.114) and due to $R_{S^k}(\Omega S^k)_j(x) < 0$, we conclude $j \neq j^*(x)$ in the preceding equation. Consequently, applying the second inequality in (A.111) further yields

$$\begin{aligned}
\big(R_{S^k}(\Omega S^k)\big)_j(x) &\overset{(A.111)}{>} \frac{\varepsilon}{2}\sum_{l\neq j} S_l^k(x)\big((\Omega S^k)_j - (\Omega S^k)_l\big)(x) && \text{(A.114c)}\\
&\overset{(5.113)}{\geq} \frac{\varepsilon}{2}\sum_{l\neq j} S_l^k(x)\big((\Omega S^k)_j - (\Omega S^k)_{j^*(x)}\big)(x) && \text{(A.114d)}\\
&= \frac{\varepsilon}{2}(1 - S_j^k(x))\big((\Omega S^k)_j - (\Omega S^k)_{j^*(x)}\big)(x) && \text{(A.114e)}\\
&\overset{(A.113)}{\geq} -\frac{\varepsilon}{2}\rho^*. && \text{(A.114f)}
\end{aligned}$$

In view of the last two terms of the right-hand side of (A.110), we introduce the index sets

$$\begin{aligned}
\mathcal{N}_-^j(x) &:= \{y \in \mathcal{N}(x)\colon \big(R_S(\Omega S)\big)_j(y) < \big(R_S(\Omega S)\big)_{j^*(x)}(y)\},\\
\mathcal{N}_+^j(x) &:= \{y \in \mathcal{N}(x)\colon \big(R_S(\Omega S)\big)_j(y) > \big(R_S(\Omega S)\big)_{j^*(x)}(y)\},
\end{aligned} \tag{A.115}$$

and estimate

$$\begin{aligned}
(\Omega R_{S^k}(\Omega S^k))_{j^*(x)}(x) - (\Omega R_{S^k}(\Omega S^k))_j(x) &= \sum_{y\in\mathcal{N}(x)} \Omega(x,y)\big(R_{S^k}(\Omega S^k)_{j^*(x)} - R_{S^k}(\Omega S^k)_j\big)(y) && \text{(A.116a)}\\
&\geq \sum_{y\in\mathcal{N}_+^j(x)} \Omega(x,y)\big(R_{S^k}(\Omega S^k)_{j^*(x)} - R_{S^k}(\Omega S^k)_j\big)(y). && \text{(A.116b)}
\end{aligned}$$

Regarding the term $(\cdots)$ in round brackets, using $\mathbb{1}^\top R_{S^k} = 0^\top$ and consequently $\sum_{l\in[c]}(R_{S^k}(\Omega S^k))_l(y) = 0$ for $y \in \mathcal{N}_+^j(x)$, it follows that

$$\begin{aligned}
R_{S^k}(\Omega S^k)_{j^*(x)}(y) - R_{S^k}(\Omega S^k)_j(y) &= 2(R_{S^k}(\Omega S^k))_{j^*(x)}(y) + \sum_{\substack{l\in[c]\\ l\notin\{j^*(x),j\}}} (R_{S^k}(\Omega S^k))_l(y) && \text{(A.117a)}\\
&\geq 2c \min_{l\in[c]\setminus j^*(y)} (R_{S^k}(\Omega S^k))_l(y) && \text{(A.117b)}\\
&\overset{(A.114)}{>} -\varepsilon c\rho^*. && \text{(A.117c)}
\end{aligned}$$

Consequently, applying (A.117) and $\Omega(x,y) \leq 1$, inequality (A.116) becomes

$$\Big(\big(\Omega R_{S^k}(\Omega S^k)\big)_{j^*(x)} - \big(\Omega R_{S^k}(\Omega S^k)\big)_j\Big)(x) > -\varepsilon|\mathcal{N}(x)|c\rho^*. \tag{A.118}$$

Substituting this estimate and (A.112) into (A.110) yields for any $x \in \mathcal{V}$ and $j \in [c] \setminus \{j^*(x)\}$

$$H_j(x) \geq (1-\frac{\varepsilon}{2})((\Omega S^*)_{j^*(x)} - (\Omega S^*)_j)(x) - \frac{\varepsilon}{2} - \frac{\overline{h}c}{2}\varepsilon|\mathcal{N}(x)|\rho^*, \quad \overline{h} = \max_{k\geq k_0} h_k. \tag{A.119}$$

Thus, returning to (A.109), we finally obtain for all $\varepsilon$ satisfying (5.118) and using

$$H^*(x) := \min_{j\neq j^*(x)} H_j(x) > 0 \tag{A.120}$$

the bound

$$\|S^{k+1}(x) - S^*(x)\|_1 \leq 2 - \frac{2S^k_{j^*(x)}(x)}{S^k_{j^*(x)}(x) + \sum\limits_{j\neq j^*(x)} S^k_j(x)e^{-\theta_k H^*(x)}} \tag{A.121a}$$

$$= \frac{2\big(1-S^k_{j^*(x)}(x)\big)e^{-\theta_k H^*(x)}}{S^k_{j^*(x)}(x) + \big(1-S^k_{j^*(x)}(x)\big)e^{-\theta_k H^*(x)}} \tag{A.121b}$$

$$\overset{S^k_{j^*(x)}(x)=e_{j^*(x)}}{=} \|S^k(x) - S^*\|_1 \underbrace{\frac{e^{-\theta_k H^*(x)}}{S^k_{j^*(x)}(x) + \big(1-S^k_{j^*(x)}(x)\big)e^{-\theta_k H^*(x)}}}_{=:\xi(x)<1, \text{ if } H^*(x)>0.} \tag{A.121c}$$

$$=: \|S^k(x) - S^*\|_1 \cdot \xi(x) \tag{A.121d}$$

with $\xi(x) < 1$, since $H^*(x) > 0$ by (A.120). Induction over $k > k_0$ yields

$$\|S^{k+1}(x) - S^*(x)\|_1 < \xi^{k-k_0}(x)\|S^{k_0}(x) - S^*(x)\|_1 \tag{A.122}$$

which proves (5.119). □

# List of Figures

# List of Tables

# List of Algorithms

# References


[AAL+10] B. Antony, M. Abramoff, K. Lee, P. Sonkova, P. Gupta, Y. Kwon, M. Niemeijer, Z. Hu, and M. Garvin, "Automated 3-D Segmentation of Intraretinal Layers from Optic Nerve Head Optical Coherence Tomography Images," *Progress in Biomedical Optics and Imaging - Proc.SPIE*, vol. 7626, pp. 249 –260, 2010.

[AB17] G. Acosta and J. P. Borthagaray, "A Fractional Laplace Equation: Regularity of Solutions and Finite Element Approximations," *SIAM Journal on Numerical Analysis*, vol. 55, no. 2, pp. 472–495, 2017.

[ABK+21] A. Atlas, M. Bendahmane, F. Karami, D. Meskine, and O. Oubbih, "A Nonlinear Fractional Reaction-Diffusion System Applied to Image Denoising and Decomposition," *Discrete and Continuous Dynamical Systems - B*, vol. 26, no. 9, pp. 4963–4998, 2021, ISSN: 1531-3492. DOI: 10.3934/dcdsb.2020321. [Online]. Available: /article/id/320a5457-636f-4fb6-b247-210b6e37bd70.

[AFPA07] V. Arsigny, P. Fillard, X. Pennec, and N. Ayache, "Geometric Means in a Novel Vector Space Structure on Symmetric Positive Definite Matrices," *SIAM Journal on Matrix Analysis and Applications*, vol. 29, no. 1, pp. 328–347, 2007. eprint: https://doi.org/10.1137/050637996.

[AFV18] A. F. J. Artacho, R. Fleming, and P. T. Vuong, "Accelerating the DC Algorithm for Smooth Functions," *Mathematical programming*, vol. 169, no. 1, pp. 95–118, 2018.

[AG09] P. A Absil and K. A Gallivan, "Accelerated line-search and trust-region methods," *SIAM journal on numerical analysis*, vol. 47, no. 2, pp. 997–1018, 2009.

[AGLM93] L. Alvarez, F. Guichard, P. L. Lions, and J. M. Morel, "Axioms and Fundamental Equations of Image Processing," *Arch. Rat. Mech. Anal.*, vol. 123, pp. 199–257, 1993.

[AGS10a] M. D. Abràmoff, M. K. Garvin, and M. Sonka, "Retinal Imaging and Image Analysis," *IEEE Reviews in Biomedical Engineering*, vol. 3, pp. 169–208, 2010.

[AGS10b] M. Abramoff, M. K Garvin, and M. Sonka, "Retinal imaging and image analysis," *IEEE reviews in biomedical engineering*, vol. 3, pp. 169–208, 2010, ISSN: 1937-3333 and 1941-1189.

[AJLS17] N. Ay, J. Jost, H. V. Lê, and L. Schwachhöfer, *Information Geometry*. Springer, 2017.

[AMS09] P.-A. Absil, R. Mahony, and R. Sepulchre, *Optimization Algorithms on Matrix Manifolds*. Princeton: Princeton University Press, 2009.

[AN00] S.-I. Amari and H. Nagaoka, *Methods of Information Geometry*. Amer. Math. Soc. and Oxford Univ. Press, 2000.

[AP11] B. Aksoylu and M. Parks, "Variational Theory and Domain Docomposition for Nonlocal Problems," *Applied Mathematical Computation*, vol. 217, pp. 6498–6515, 2011.

[ÅPSS17] F. Åström, S. Petra, B. Schmitzer, and C. Schnörr, "Image Labeling by Assignment," *Journal of Mathematical Imaging and Vision*, vol. 58, no. 2, pp. 211–238, 2017.

[AV10] F. Andreu-Vaillo, *Nonlocal diffusion problems / Fuensanta Andreu-Vaillo ... [at al.]*. eng, ser. Mathematical surveys and monographs ; v. 165. Providence, R.I. : Madrid: American Mathematical Society ; Real Sociedad Matemática Española, 2010, ISBN: 9780821852309.

[BB97] H. H. Bauschke and J. M. Borwein, "Legendre Functions and the Method of Random Bregman Projections," *J. Convex Analysis*, vol. 4, no. 1, pp. 27–67, 1997.

[BCM06] A. Buades, B. Coll, and J.-M. Morel, "Neighborhood Filter and PDEs," *Numer. Math.*, vol. 105, pp. 1–34, 2006.

[BCM10] ——, "Image Denoising Methods. A New Nonlocal Principle," *SIAM Review*, vol. 52, no. 1, pp. 113–147, 2010.

[BDD+21] J. Blank, K. Deb, Y. Dhebar, S. Bandaru, and H. Seada, "Generating Well-Spaced Points on a Unit Simplex for Evolutionary Many-Objective Optimization," *IEEE Transactions on Evolutionary Computation*, vol. 25, no. 1, pp. 48–60, 2021.

[BF16] A. Bertozzi and A. Flenner, "Diffuse Interface Models on Graphs for Classification of High Dimensional Data," *SIAM Review*, vol. 58, no. 2, pp. 293–328, 2016.

[BH99] M. R. Bridson and A. Häflinger, *Metric Spaces of Non-Positive Curvature*. Springer, 1999.

[Bha07] R. Bhatia, *Positive Definite Matrices*. Princeton University Press, 2007, ISBN: 978-0-691-12918-1 and 978-1-4008-2778-7 and 1-4008-2778-7.

[Bha13] ——, "The Riemannian Mean of Positive Matrices," in *Matrix Information Geometry*. Springer Berlin Heidelberg, 2013, pp. 35–51, ISBN: 978-3-642-30232-9.

[BI13] D. A. Bini and B. Iannazzo, "Computing the Karcher Mean of Symmetric Positive Definite Matrices," *Linear Alg. Appl.*, vol. 438, pp. 1700–1710, 2013.

[Bis07] C. M. Bishop, *Pattern Recognition and Machine Learning*, 5. (corr. print.), ser. Information science and statistics. New York [u.a.]: Springer, 2007, XX, 738 S.

[Bis64] R. L. Bishop, *Geometry of manifolds*, R. J. Crittenden, Ed., ser. Pure and applied mathematics; a series of monographs and textbooks ; 15. New York: Academic Press, 1964.

[BJ01] Y. Boykov and M.-P. Jolly, "Interactive graph cuts for optimal boundary & region segmentation of objects in n-d images," in *Proceedings Eighth IEEE International Conference on Computer Vision. ICCV 2001*, vol. 1, 2001, 105–112 vol.1.

[BMDG05] A Banerjee, S Merugu, I. Dhillon, and J Ghosh, "Clustering with Bregman Divergences," English, *Journal of machine learning research*, vol. 6, pp. 1705–1749, 2005.

[Bol19] B. Boll, "Dynamical Systems for Order-Preserving Image Labeling," *Heidelberg University,Master Thesis*, 2019.

[Bre67] L. Bregman, "The Relaxation Method of Finding the Common Point of Convex Sets and its Application to the Solution of Problems in Convex Programming," *USSR Computational Mathematics and Mathematical Physics*, vol. 7, no. 3, pp. 200–217, 1967.

[BS15] C. Bibiane-Schönlieb, *Partial Differential Equation Methods for Image Inpainting*. Cambridge University Press, 2015.

[BSTV18] J. Bolte, S. Sabach, M. Teboulle, and Y. Vaisbourd, "First Order Methods Beyond Convexity and Lipschitz Gradient Continuity with Applications to Quadratic Inverse Problems," *SIAM Journal on Optimization*, vol. 28, pp. 2131–2151, Jun. 2018.

[BT12] A. Beck and M. Teboulle, "Smoothing and First Order Methods: A Unified Framework," *SIAM J. Optimiz.*, vol. 22, no. 2, pp. 557–580–557–580, 2012.

[BV12] S. P. Boyd and L. Vandenberghe, *Convex Optimization*, 10. print. Cambridge: Cambridge Univ. Press, 2012, XIII, 716 S.

[BZPS22] B. Boll, A. Zeilmann, S. Petra, and C. Schnörr, "Self-Certifying Classification by Linearized Deep Assignment," *preprint arXiv:2201.11162*, 2022.

[CABM15] M. Congedo, B. Afsari, A. Barachant, and M. Moakher, "Approximate Joint Diagonalization and Geometric Mean of Symmetric Positive Definite Matrices," *PLoS ONE*, vol. 10, no. 4, e0121423, 2015.

[CAM+15] S. J. Chiu, M. J. Allingham, P. S. Mettu, S. W. Cousins, J. A. Izatt, and S. Farsiu, "Kernel Regression Based Segmentation of Optical Coherence Tomography Images with Diabetic Macular Edema," *Biomed. Opt. Express*, vol. 6, no. 4, pp. 1172–1194, 2015.

[Car13] M. P. d. Carmo, *Riemannian geometry*, 14., corrected print., ser. Mathematics: theory & applications. Boston ; Basel ; Berlin: Birkhäuser, 2013, 300 S.

[CCH06] W. R. Crum, O. Camara, and D. L. G. Hill, "Generalized Overlap Measures for Evaluation and Validation in Medical Image Analysis," *IEEE Transactions on Medical Imaging*, vol. 25, no. 11, pp. 1451–1461, 2006.

[CCN15] V. Caselles, A. Chambolle, and M. Novaga, "Total Variation in Imaging," in *Handbook of Mathematical Methods in Imaging*, O. Scherzer, Ed., Springer, 2015, pp. 1455–1499.

[CFSS16] G. Citti, B. Franceschiello, G. Sanguinetti, and A. Sarti, "Sub-Riemannian Mean Curvature Flow for Image Processing," *SIAM Journal on Imaging Sciences*, vol. 9, no. 1, pp. 212–237, 2016.

[Chu97] F. Chung, *Spectral Graph Theory*. Amer. Math. Soc., 1997.

[CIO+12] S. Chiu, J. Izatt, R. O'Connell, K. Winter, C. Toth, and S. Farsiu, "Validated Automatic Segmentation of AMD Pathology Including Drusen and Geographic Atrophy in SD-OCT Images," *Investigative ophthalmology & visual science*, vol. 53, pp. 53–61, Jan. 2012.

[CL96] F. Chung and R. P. Langlands, "A Combinatorial Laplacian with Vertex Weights," *Journal of Combinatorial Theory, Series A*, vol. 5, no. 2, pp. 316 –327, 1996, ISSN: 0097-3165.

[CLN+10] S. J. Chiu, X. T. Li, P. Nicholas, C. A. Toth, J. A. Izatt, and S. Farsiu, "Automatic Segmentation of Seven Retinal Layers in SDOCT Images Congruent with Expert Manual Segmentation," *Opt. Express*, vol. 18, no. 18, pp. 19 413–19 428, 2010.

[Coo90] G. F. Cooper, "The Computational Complexity of Probabilistic Inference Using Bayesian Belief Networks," *Artificial Intelligence*, vol. 42, no. 2, pp. 393–405, 1990.

[CR06] B. Cassin and M. Rubin, "Dictionary of eye terminology," 2006. [Online]. Available: https://books.google.de/books?id=3XKpPwAACAAJ.

[CRBD18] R. T. Q. Chen, Y. Rubanova, J. Bettencourt, and D. Duvenaud, "Neural Ordinary Differential Equations," in *Proc. NeurIPS*, 2018.

[CS16] A. Cherian and S. Sra, "Positive Definite Matrices: Data Representation and Applications to Computer Vision," in *Algorithmic Advances in Riemannian Geometry and Applications*, H. Minh and V. Murino, Eds., Springer, 2016, pp. 93–114.

[CT93] G. Chen and M. Teboulle, "Convergence Analysis of a Proximal-Like Minimization Algorithm Using Bregman Functions," *SIAM Journal on Optimization*, vol. 3, no. 3, pp. 538–543, 1993.

[CV01] T. F. Chan and L. A. Vese, "Active Contours without Edges," *IEEE Transactions on Image Processing*, vol. 10, no. 2, pp. 266–277, 2001, ISSN: 1941-0042.

[CZ97] Y. A. Censor and S. A. Zenios, *Parallel Optimization: Theory, Algorithms, and Applications*. New York: Oxford Univ. Press, 1997.

[DCA+13] P. A. Dufour, L. Ceklic, H. Abdillahi, S. Schroder, S. De Dzanet, U. Wolf-Schnurrbusch, and J. Kowal, "Graph-Based Multi-Surface Segmentation of OCT Data Using Trained Hard and Soft Constraints," *IEEE Transactions on Medical Imaging*, vol. 32, no. 3, pp. 531–543, 2013, ISSN: 1558-254X.

[DFVDVM14] A. Depeursinge, A. R. Foncubierta, D. Van De Ville, and H. Müller, "Three-Dimensional Solid Texture Analysis in Biomedical Imaging: Review and Opportunities," *Medical Image Analysis*, vol. 18, no. 1, pp. 176 –196, 2014, ISSN: 1361-8415.

[DG13] M. D'Elia and M. Gunzburger, "The Fractional Laplacian Operator on Bounded Domains as a Special Case of the Nonlocal Diffusion Operator," *Computers and Mathematics with Applications*, vol. 66, no. 7, pp. 1245–1260, 2013.

[DGLZ12] Q. Du, M. Gunzburger, R. B. Lehoucq, and K. Zhou, "Analysis and Approximation of Nonlocal Diffusion Problems with Volume Constraints," *SIAM Review*, vol. 54, no. 4, pp. 667–696, 2012.

[DGLZ13] ——, "A Nonlocal Vector Calculus, Nonlocal Volume-Constrained Problems, and Nonlocal Balance Laws," *Math. Models Meth. Appl. Sci.*, vol. 23, no. 3, pp. 493–540, 2013.

[Dic45] L. R. Dice, "Measures of the Amount of Ecologic Association Between Species," *Ecology*, vol. 26, no. 3, pp. 297–302, 1945. eprint: https://esajournals.onlinelibrary.wiley.com/doi/pdf/10.2307/1932409.

[Dre11] E. B. Dreyer, "Shields textbook of glaucoma," *JAMA*, vol. 306, no. 7, pp. 769–770, 2011, ISSN: 0098-7484 and 1538-3598.

[DTG+15] J. Duan, C. Tench, I. Gottlob, F. Proudlock, and L. Bai, "New Variational Image Decomposition Model for Simultaneously Denoising and Segmenting Optical Coherence Tomography Images," *Physics in Medicine and Biology*, vol. 60, pp. 8901–8922, Nov. 2015.

[Du19] Q. Du, *Nonlocal Modeling, Analysis, and Computation*. SIAM, 2019.

[DY99] Y. Dai and Y Yuan, "A Nonlinear Conjugate Gradient Method with a Strong Global Convergence Property," *SIAM journal on optimization*, vol. 10, no. 1, pp. 177–182, 1999.

[EFBL18] K. Ebrahimi-Fard and M. Barbero Liñán, *Discrete Mechanics, Geometric Integration and Lie-Butcher Series*, English, ser. Springer proceedings in mathematics & statistics. Cham: Springer International Publishing AG, 2018, 366 S.

[ELB08] A. Elmoataz, O. Lezoray, and S. Bougleux, "Nonlocal Discrete Regularization on Weighted Graphs: A Framework for Image and Manifold Processing," *IEEE Trans. Image Proc.*, vol. 17, no. 7, pp. 1047–1059, 2008.

[ETT15] A. Elmoataz, M. Toutain, and D. Tenbrinck, "On the $p$-Laplacian and $\infty$-Laplacian on Graphs with Applications in Image and Data Processing," *SIAM Journal on Imaging Sciences*, vol. 8, no. 4, pp. 2412–2451, 2015.

[EX17] E. E. and X. X., "Automatic Segmentation of Cross-Sectional Coronary Arterial Images," *Computer Vision and Image Understanding*, vol. 165, pp. 97–110, 2017, ISSN: 1077-3142. DOI: https://doi.org/10.1016/j.cviu.2017.11.004.

[FCW+17] L. Fang, D. Cunefare, C. Wang, R. Guymer, S. Li, and S. Farsiu, "Automatic Segmentation of Nine Retinal Layer Boundaries in OCT Images of Non-Exudative AMD Patients Using Deep Learning and Graph Search," *Biomed. Opt. Express*, vol. 8, no. 5, pp. 2732–2744, 2017.

[FM81] M. Fukushima and H. Mine, "A Generalized Proximal Point Algorithm for Certain Non-Convex Minimization Problems," *International Journal of Systems Science*, vol. 12, no. 8, pp. 989–1000, 1981.

[FRMP18] M. Fazylab, A. Ribeiro, M. Morari, and V. M. Preciado, "Analysis of Optimization Algorithms via Integral Quadratic Constraints: Nonstrongly Convex Problems," *SIAM J. Optim.*, vol. 28, no. 3, pp. 2654–2689, 2018.

[Gar13] H. Garcke, "Curvature Driven Interface Evolution," *Jahresberichte der Deutschen Mathematiker-Vereinigung*, vol. 115, no. 2, pp. 63–100, 2013.

[GASnd] M. D. Garvin, M. K. Abràmoff, and M. Sonka. (n.d). The Iowa Reference Algorithms (Retinal Image Analysis Lab, Iowa Institute for Biomedical Imaging, Iowa City, IA). https://www.iibi.uiowa.edu/oct-reference.

[GAW+09] M. K. Garvin, M. D. Abramoff, X. Wu, S. R. Russell, T. L. Burns, and M. Sonka, "Automated 3-D Intraretinal Layer Segmentation of Macular Spectral-Domain Optical Coherence Tomography Images," *IEEE Transactions on Medical Imaging*, no. 9, pp. 1436–1447, 2009.

[GAZS21] D. Gonzalez-Alvarado, A. Zeilmann, and C. Schnörr, "Quantifying Uncertainty of Image Labelings Using Assignment Flows," in *DAGM GCPR*, ser. LNCS, Springer, 2021.

[GBC16] I. Goodfellow, Y. Bengio, and A. Courville, *Deep Learning*. MIT Press, 2016.

[GGOB14] Y. van Gennip, N. Guillen, B. Osting, and A. L. Bertozzi, "Mean Curvature, Threshold Dynamics, and Phase Field Theory on Finite Graphs," *Milan Journal of Mathematics*, vol. 82, no. 1, pp. 3–65, 2014–4.

[GHL04] S. Gallot, D. Hulin, and J. Lafontaine, *Riemannian geometry*, 3. ed., ser. Universitext. Springer, 2004, XV, 322 S.

[GO07] G. Gilboa and S. Osher, "Nonlocal Linear Image Regularization and Supervised Segmentation," *Multiscale Model. Simul.*, vol. 6, no. 2, pp. 595–630, 2007.

[GO09] ——, "Nonlocal Operators with Applications to Image Processing," *Multiscale Modeling & Simulation*, vol. 7, no. 3, pp. 1005–1028, 2009.

[Gra06] L. Grady, "Random Walks for Image Segmentation," *IEEE Transactions on Pattern Analysis and Machine Intelligence*, vol. 28, no. 11, pp. 1768–1783, 2006. DOI: 10.1109/TPAMI.2006.233.

[Gra81] A. Graham, *Kronecker Products and Matrix Calculus: with Applications*. Ellis Horwood Limited, 1981.

[HAPD05] L. T. Hoai An and T. Pham Dinh, "The DC (Difference of Convex Functions) Programming and DCA Revisited with DC Models of Real World Nonconvex Optimization Problems," *Annals of Operations Res.*, vol. 133, pp. 23–46, 2005.

[Har59] P. Hartman, "On Functions Representable as a Difference of Convex Functions," *Pacific J. Math.*, vol. 9, no. 3, pp. 707–713, 1959.

[HAW+07] M. Haeker, M. Abramoff, X. Wu, R. Kardon, and M. Sonka, "Use of Varying Constraints in Optimal 3-D Graph Search for Segmentation of Macular Optical Coherence Tomography Images," *MICCAI*, vol. 10, pp. 244–51, Feb. 2007.

[HCL+19] Y. He, A. Carass, Y. Liu, B. Jedynak, S. Solomon, S. Saidha, P. Calabresi, and J. Prince, "Deep Learning Based Topology Guaranteed Surface and MME Segmentation of Multiple Sclerosis Subjects from Retinal OCT," *Biomed. Opt. Express*, vol. 10, no. 10, pp. 5042–5058, 2019.

[HFTC22] X. He, L. Fang, M. Tan, and X. Chen, "Intra- and Inter-Slice Contrastive Learning for Point Supervised OCT Fluid Segmentation," *IEEE Transactions on Image Processing*, vol. 31, pp. 1870–1881, 2022.

[Hig08] N. Higham, *Functions of Matrices: Theory and Computation*. SIAM, 2008.

[HLC+21] K. Hu, D. Liu, Z. Chen, X. Li, Y. Zhang, and X. Gao, "Embedded Residual Recurrent Network and Graph Search for the Segmentation of Retinal Layer Boundaries in Optical Coherence Tomography," *IEEE Transactions on Instrumentation and Measurement*, vol. 70, pp. 1–17, 2021.

[HLW10] E. Hairer, C. Lubich, and G. Wanner, *Geometric Numerical Integration*, Second edition, first softcover print, ser. Springer series in computational mathematics. Berlin ; Heidelberg: Springer, 2010.

[HNWxx] E. Hairer, S. P. Nørsett, and G. Wanner, *Solving Ordinary Differential Equations*, eng, ser. Springer series in computational mathematics ; ... Berlin ; Heidelberg [u.a.]: Springer, 19XX-.

[HS03] J Hofbauer and K Sigmund, "Evolutionary Game Dynamics," *Bulletin (new series) of the American Mathematical Society*, vol. 40, no. 4, pp. 479–519, 2003.

[HS87] M. Hashimoto and J. Sklansky, "Multiple-Order Derivatives for Detecting Local Image Characteristics," *Computer Vision, Graphics, and Image Processing*, vol. 39, no. 1, pp. 28 –55, 1987, ISSN: 0734-189X.

[HSL+91] D Huang, E. Swanson, C. Lin, J. Schuman, W. Stinson, W Chang, M. Hee, T Flotte, K Gregory, C. Puliafito, and a. et, "Optical Coherence Tomography," *Science*, vol. 254, no. 5035, pp. 1178–1181, 1991, ISSN: 0036-8075. eprint: https://science.sciencemag.org/content/254/5035/1178.full.pdf.

[HSPS21a] R. Hühnerbein, F. Savarino, S. Petra, and C. Schnörr, "Learning Adaptive Regularization for Image Labeling Using Geometric Assignment," *J. Math. Imaging Vision*, vol. 63, pp. 186–215, 2021.

[HSPS21b] ——, "Learning Adaptive Regularization for Image Labeling Using Geometric Assignment," *J. Math. Imaging Vision*, vol. 63, pp. 186–215, 2021.

[HT99] R. Horst and N. V. Thoai, "DC Programming: Overview," *J. Optimiz. Theory Appl.*, vol. 103, no. 1, pp. 1–43, 1999.

[HZL+22] X. Hui, P. Zhe, Z. Leixin, A. Fahim, C. Zaman, B. J. Jost, X. Weiyu, X. W. Ya, and W. Xiaodong, "Globally Optimal OCT Surface Segmentation Using a Constrained IPM Optimization," *Opt. Express*, vol. 30, no. 2, pp. 2453–2471, 2022.

[IMKNZ00] A. Iserles, H. Munthe-Kaas, S. Norsett, and A. Zanna, "Lie Group Methods," *Acta Numerica*, vol. 9, pp. 215–, Jan. 2000. DOI: 10.1017/S0962492900002154.

[Jac08] P. Jaccard, "Nouvelles recherches sur la distribution florale," *Bulletin de la Societe Vaudoise des Sciences Naturelles*, vol. 44, pp. 223–70, Jan. 1908.

[Jos17] J. Jost, *Riemannian Geometry and Geometric Analysis*, 7th. Springer-Verlag, 2017.

[KAH+15] J. Kappes, B. Andres, F. Hamprecht, C. Schnörr, S. Nowozin, D. Batra, S. Kim, B. Kausler, T. Kröger, J. Lellmann, N. Komodakis, B. Savchynskyy, and C. Rother, "A Comparative Study of Modern Inference Techniques for Structured Discrete Energy Minimization Problems," *Int. J. Computer Vision*, vol. 115, no. 2, pp. 155–184, 2015.

[KAR+22] J. Kugelman, J. Allman, S. A. Read, S. J. Vincent, J. Tong, M. Kalloniatis, F. K. C., M. J. Collins, and D. Alonso-Caneiro, "A Comparison of Deep Learning U-Net Architectures for Posterior Segment OCT Retinal Layer Segmentation," *Scientific reports*, vol. 12, no. 1, pp. 14 888–14 888, 2022.

[KBB16] W. Krichene, A. Bayen, and P. Bartlett, "Adaptive Averaging in Accelerated Descent Dynamics," in *NIPS*, 2016.

[Kjpnd] Kjpargeter, Freepik, *The muscles of the head*, http://www.freepik.com, Accessed: 2020-09-09, n.d.

[KMS97] R. Kimmel, R. Malladi, and N. Sochen, "Image Processing via the Beltrami Operator," in *Computer Vision — ACCV'98*, Springer Berlin Heidelberg, 1997, pp. 574–581.

[KRAS13] R. Kafieh, H. Rabbani, M. Abramoff, and M. Sonka, "Intra-Retinal Layer Segmentation of 3D Optical Coherence Tomography Using Coarse Grained Diffusion Map," *Medical Image Analysis*, vol. 17, pp. 907–928, Jun. 2013.

[KXCS06] Kang, L., Xiaodong, W., D. Z. Chen, and M. Sonka, "Optimal Surface Segmentation in Volumetric Images-A Graph-Theoretic Approach," *IEEE Transactions on Pattern Analysis and Machine Intelligence*, vol. 28, no. 1, pp. 119–134, 2006, ISSN: 1939-3539.

[LCC98] R. B. Lehoucq, S. D. C., and Y. C., "ARPACK Users' Guide - Solution of Large-Scale Eigenvalue Problems with Implicitly Restarted Arnoldi Methods," in *Software, Environments, Tools*, 1998.

[LCF+19] X. Liu, J. Cao, T. Fu, Z. Pan, W. Hu, K. Zhang, and J. Liu, "Semi-Supervised Automatic Segmentation of Layer and Fluid Region in Retinal Optical Coherence Tomography Images Using Adversarial Learning," *IEEE Access*, vol. 7, pp. 3046–3061, 2019, ISSN: 2169-3536.

[Lee13] J. M. Lee, *Introduction to Smooth Manifolds*. Springer, 2013.

[Lin04] T. Lindeberg, "Feature Detection with Automatic Scale Selection," *International Journal of Computer Vision*, vol. 30, pp. 79–116, 2004.

[LT18] H. A. L.T. and P. D. T., "DC Programming and DCA: Thirty Years of Developments," English, *Mathematical programming*, vol. 169, no. 1, pp. 5–68, 2018.

[Mas01] R. H. Masland, "The Fundamental Plan of the Retina," *Nature neuroscience*, vol. 4, no. 9, pp. 877–886, 2001.

[MB06] M. Moakher and P. G. Batchelor, "Symmetric Positive-Definite Matrices: From Geometry to Applications and Visualization," in *Visualization and Processing of Tensor Fields*, Berlin, Heidelberg: Springer, 2006, pp. 285–298, ISBN: 978-3-540-31272-7.

[MBO94] B. Merriman, J. Bence, and S. Osher, "Motion of Multiple Junctions: A Level Set Approach," *J. Comp. Physics*, vol. 112, no. 2, pp. 334–363, 1994.

[MBP+21] S. Minaee, Y. Y. Boykov, F. Porikli, A. J. Plaza, N. Kehtarnavaz, and D. Terzopoulos, "Image Segmentation Using Deep Learning: A Survey," *IEEE Trans. Pattern Anal. Mach. Intell., https://ieeexplore.ieee.org/document/9356353*, 2021.

[MT04] M. M. Meerschaert and C. Tadjeran, "Finite Difference Approximations for Fractional Advection–Dispersion Flow Equations," *Journal of Computational and Applied Mathematics*, vol. 172, no. 1, pp. 65–77, 2004.

[NVd+17] J. Novosel, K. A. Vermeer, J. H. de Jong, Z. Wang, and L. J. van Vliet, "Joint Segmentation of Retinal Layers and Focal Lesions in 3-D OCT Data of Topologically Disrupted Retinas," *IEEE Transactions on Medical Imaging*, vol. 36, no. 6, pp. 1276–1286, 2017, ISSN: 1558-254X.

[NW06] J. Nocedal and S. J. Wright, *Numerical Optimization*, 2nd ed. Springer, 2006.

[OS88] S. Osher and J. Sethian, "Fronts propagating with curvature-dependent speed: Algorithms based on Hamilton-Jacobi formulations," *J. Comp. Physics*, vol. 79, no. 1, pp. 12–49, 1988.

[PC08] S. Peyré G.and Bougleux and L. Cohen, "Non-local regularization of inverse problems," pp. 57–68, 2008.

[Pet05] D. Petz, "Information Geometry and Statistical Inference," in *Proceedings of the 2nd International Symposium on Information Geometry and its Applications, Tokyo,Japan*, 2005, pp. 162–169.

[PFAE06] X. Pennec, P. Fillard, N. Ayache, and P. Epidaure, "A Riemannian Framework for Tensor Computing," *International Journal of Computer Vision*, vol. 66, pp. 41–66, Jan. 2006.

[PFS+15] J. Portegies, R. H. Fick, G. Sanguinetti, S. Meesters, G Girard, and R Duits, "Improving fiber alignment in hardi by combining contextual pde flow with constrained spherical deconvolution," *PloS one*, vol. 10, no. 10, e0138122–e0138122, 2015.

[PLT18] D. N. Phan, H. M. Le, and H. A. L. Thi, "Accelerated difference of convex functions algorithm and its application to sparse binary logistic regression," in *Proceedings of the Twenty-Seventh International Joint Conference on Artificial Intelligence, IJCAI-18*, International Joint Conferences on Artificial Intelligence Organization, Jul. 2018, pp. 1369–1375.

[PPMV18] G. Peyman, R. Priyanka, K. P. Mohana, and L. Vasudevan, "OCTID: Optical Coherence Tomography Image Database," *CoRR*, vol. abs/1812.07056, 2018. arXiv: 1812.07056. [Online]. Available: http://arxiv.org/abs/1812.07056.

[PSA88] S. P.K., S. S., and W. A.K.C., "A Survey of Thresholding Techniques," *Computer Vision, Graphics, and Image Processing*, vol. 41, no. 2, pp. 233–260, 1988.

[QB06] H. A. Quigley and A. T. Broman, "The Number of People with Glaucoma Worldwide in 2010 and 2020," *British Journal of Ophthalmology*, vol. 90, no. 3, pp. 262–267, 2006.

[QLD+10] G. Quellec, K. Lee, M. Dolejsi, M. K. Garvin, M. D. Abramoff, and M. Sonka, "Three-Dimensional Analysis of Retinal Layer Texture: Identification of Fluid-Filled Regions in SD-OCT of the Macula," *IEEE Transactions on Medical Imaging*, vol. 29, no. 6, pp. 1321–1330, 2010, ISSN: 1558-254X.

[RCK+17] A. Roy, S. Conjeti, S. Karri, D. Sheet, A. Katouzian, C. Wachinger, and N. Navab, "ReLayNet: Retinal Layer and Fluid Segmentation of Macular Optical Coherence Tomography Using Fully Convolutional Networks," *Biomed. Opt. Express*, vol. 8, no. 8, pp. 3627–3642, 2017.

[RDS17] F. Rathke, M. Desana, and C. Schnörr, "Locally Adaptive Probabilistic Models for Global Segmentation of Pathological OCT Scans," in *MICCAI*, vol. 10433, Springer, 2017, pp. 177–184, ISBN: 978-3-319-66181-0.

[RFB15] O. Ronneberger, P. Fischer, and T. Brox, "U-Net: Convolutional Networks for Biomedical Image Segmentation," in *MICCAI*, Cham: Springer International Publishing, 2015, pp. 234–241, ISBN: 978-3-319-24574-4.

[Roc70] R. T. Rockafellar, *Convex Analysis*, eng, ser. Princeton mathematical series. Princeton Univ. Press, 1970, XVIII, 451 Seiten, ISBN: 0-691-08069-0 and 978-0-691-08069-7.

[ROF92] L. Rudin, S. Osher, and E. Fatemi, "Nonlinear Total Variation Based Noise Removal Algorithms," *Physica D*, vol. 60, pp. 259–268, 1992.

[RSS14] F. Rathke, S. Schmidt, and C. Schnörr, "Probabilistic Intra-Retinal Layer Segmentation in 3-D OCT Images Using Global Shape Regularization," *Medical Image Analysis*, vol. 18, no. 5, pp. 781–794, 2014.

[RW10] R. T. Rockafellar and R. J.-B. Wets, *Variational analysis*, eng, Corr. 3. printing. [Softcover version of original hardcover edition 1998], ser. Die Grundlehren der mathematischen Wissenschaften in Einzeldarstellungen ARRAY(0x557fea673338). Heidelberg ; Berlin: Springer, 2010, XII, 734 S. ISBN: 978-3-642-08304-4 and 3-642-08304-8.

[SACO22] N. Sharp, S. Attaiki, K. Crane, and M. Ovsjanikov, "DiffusionNet: Discretization Agnostic Learning on Surfaces," *ACM transactions on graphics*, vol. 41, no. 3, pp. 1–16, 2022.

[SAS21a] F. Savarino, P. Albers, and C. Schnörr, "On the Geometric Mechanics of Assignment Flows for Metric Data Labeling," *CoRR abs/2111.02543*, 2021.

[SAS21b] ——, "On the Geometric Mechanics of Assignment Flows for Metric Data Labeling," in *Scale Space and Variational Methods in Computer Vision (SSVM)*, A. Elmoataz, J. Fadili, Y. Quéau, J. Rabin, and L. Simon, Eds., ser. LNCS, vol. 12679, 2021, pp. 398–410.

[SBG+13] Q. Song, J. Bai, M. K. Garvin, M. Sonka, J. M. Buatti, and X. Wu, "Optimal Multiple Surface Segmentation With Shape and Context Priors," *IEEE Transactions on Medical Imaging*, vol. 32, no. 2, pp. 376–386, 2013, ISSN: 1558-254X.

[SBS21a] D. Sitenko, B. Boll, and C. Schnörr, "Assignment Flow For Order-Constrained OCT Segmentation," *Int. J. Computer Vision*, vol. 129, pp. 3088–3118, 2021.

[SBS21b] ——, "Assignment Flows and Nonlocal PDEs on Graphs," in *DAGM GCPR*, ser. LNCS, Springer, 2021.

[SBS23] D. Sitenko, B. Boll, and C. Schnörr, "A Nonlocal Graph-PDE and Higher-Order Geometric Integration for Image Labeling," *SIAM J. Imaging Science, in press*, 2023.

[Sch15] C.-B. Schönlieb, *Partial Differential Equation Methods for Image Inpainting*, ser. Cambridge Monographs on Applied and Computational Mathematics. Cambridge University Press, 2015.

[Sch20] C. Schnörr, "Assignment Flows," in *Variational Methods for Nonlinear Geometric Data and Applications*, P. Grohs, M. Holler, and A. Weinmann, Eds., Springer, 2020, pp. 235–260.

[Sit20] Sitenko, D. and Boll, B. and Schnörr, C., "Assignment Flow for Order-Constrained OCT Segmentation," in *GCPR*, 2020, pp. 58–71.

[Sra12] S. Sra, "A New Metric on the Manifold of Kernel Matrices with Application to Matrix Geometric Means," in *Advances in Neural Information Processing Systems 25*, Curran Associates, Inc., 2012, pp. 144–152.

[Sra16] Sra, S., "Positive Definite Matrices and the S-Divergence," *Proceedings of the American Mathematical Society*, vol. 144, no. 7, pp. 2787–2797, 2016, ISSN: 0002-9939 and 1088-6826.

[SS21] F. Savarino and C. Schnörr, "Continuous-Domain Assignment Flows," *Europ. J. Appl. Math.*, vol. 32, no. 3, pp. 570–597, 2021.

[SSR15] K. Sirinukunwattana, D. R. Snead, and N. M. Rajpoot, "A Novel Texture Descriptor for Detection of Glandular Structures in Colon Histology Images," in *Medical Imaging: Digital Pathology*, vol. 9420, SPIE, 2015, pp. 186 –194.

[TD14] X. Tian and Q. Du, "Asymptotycally Compatible Schemes and Applications to Robust Discretizations," *SIAM J. Numerical Analysis*, vol. 52, pp. 1641–1665, 2014.

[Teb07] M. Teboulle, "A Unified Continuous Optimization Framework for Center-Based Clustering Methods," *J. Mach. Learn. Res.*, vol. 8, pp. 65–102, 2007.

[TPM06] O. Tuzel, F. Porikli, and P. Meer, "Region Covariance: A Fast Descriptor for Detection and Classification," in *Proc. ECCV*, vol. 3952, 2006, pp. 589–600.

[TS16] P. Turaga and A. Srivastava, Eds., *Riemannian Computing in Computer Vision*. Springer, 2016.

[VMN+18] P. L. Vidal, J. de Moura, J. Novo, M. G. Penedo, and M. Ortega, "Intraretinal Fluid Identification via Enhanced Maps Using Optical Coherence Tomography Images," *Biomed. Opt. Express*, vol. 9, no. 10, pp. 4730–4754, 2018.

[Wei98] J. Weickert, *Anisotropic Diffusion in Image Processing*, eng. B.G. Teubner, 1998, XII, 170 S. ISBN: 3-519-02606-6 and 978-3-519-02606-8.

[WJ05] Y. Wang and Q. Ji, "A dynamic conditional random field model for object segmentation in image sequences," in *2005 IEEE Computer Society Conference on Computer Vision and Pattern Recognition (CVPR'05)*, vol. 1, 2005, 264–270 vol. 1.

[WJ08] M. Wainwright and M. Jordan, "Graphical Models, Exponential Families, and Variational Inference," *Found. Trends Mach. Learn.*, vol. 1, no. 1-2, pp. 1–305, 2008.

[WS01] J Weickert and C Schnorr, "Variational optic flow computation with a spatio-temporal smoothness constraint," *Journal of mathematical imaging and vision*, vol. 14, no. 3, pp. 245–255, 2001.

[WW20] M. Welk and J. Weickert, "PDE Evolutions for M-Smoothers in One, Two, and Three Dimensions," *Journal of Mathematical Imaging and Vision*, vol. 63, no. 2, pp. 157–185, 2020.

[YAN82] M. YANOFF, "Ocular Pathology," *A Text and Atlas*, pp. 513–514, 1982.

[YHSS11] A. Yazdanpanah, G. Hamarneh, B. R. Smith, and M. V. Sarunic, "Segmentation of Intra-Retinal Layers From Optical Coherence Tomography Images Using an Active Contour Approach," *IEEE Transactions on Medical Imaging*, vol. 30, no. 2, pp. 484–496, 2011, ISSN: 1558-254X.

[YS20] L. Y. and S. Z. S., "Seismic Horizon Tracking Using a Deep Convolutional Neural Network," *Journal of Petroleum Science and Engineering*, vol. 187, p. 106 709, 2020, ISSN: 0920-4105.

[ZFW+07] R. Zawadski, A. R. Fuller, D. Wiley, B. Hamann, S. Choi, and J. Werner, "Adaptation of a Support Vector Machine Algorithm for Segmentation and Visualization of Retinal Structure in Volumetric Optical Coherence Tomography Data Sets," *J. Biomed. Opt.*, vol. 12, no. 4, 2007.

[ZPS21] A. Zeilmann, S. Petra, and C. Schnörr, "Learning Linear Assignment Flows for Image Labeling via Exponential Integration," in *Scale Space and Variational Methods in Computer Vision (SSVM)*, A. Elmoataz, J. Fadili, Y. Quéau, J. Rabin, and L. Simon, Eds., ser. LNCS, vol. 12679, 2021, pp. 385–397.

[ZPS22] ——, "Learning Linearized Assignment Flows for Image Labeling," *J. Math. Imag. Vision*, vol. in press (preprint arXiv:2108.02571), 2022.

[ZRS18] A. Zern, K. Rohr, and C. Schnörr, "Geometric Image Labeling with Global Convex Labeling Constraints," in *Energy Minimization Methods in Computer Vision and Pattern Recognition*, Springer International Publishing, 2018, pp. 533–547.

[ZSPS20] A. Zeilmann, F. Savarino, S. Petra, and C. Schnörr, "Geometric Numerical Integration of the Assignment Flow," *Inverse Problems*, vol. 36, no. 3, 034004 (33pp), 2020.

[ZWC18] M. Zhao, H. Wang, and A. Cheng, "A Fast Finite Difference Method for Three-Dimensional Time-Dependent Space-Fractional Diffusion Equations with Fractional Derivative Boundary Conditions," *J. Sci. Comput.*, vol. 74, no. 2, pp. 1009–1033, 2018.

[ZZPS20a] A. Zern, M. Zisler, S. Petra, and C. Schnörr, "Unsupervised Assignment Flow: Label Learning on Feature Manifolds by Spatially Regularized Geometric Assignment," *Journal of Mathematical Imaging and Vision*, vol. 62, no. 6–7, pp. 982–1006, 2020.

[ZZPS20b] M. Zisler, A. Zern, S. Petra, and C. Schnörr, "Self-Assignment Flows for Unsupervised Data Labeling on Graphs," *SIAM Journal on Imaging Sciences*, vol. 13, no. 3, pp. 1113–1156, 2020.

[ZZS20] A. Zern, A. Zeilmann, and C. Schnörr, "Assignment Flows for Data Labeling on Graphs: Convergence and Stability," *CoRR abs/2002.11571*, 2020. arXiv: 2002.11571.